COMMUNICATIONS

COMMUNICATIONS

Dear Readers,

This issue of the Communications – Scientific Letters of the University of Zilina is oriented on the current topics of electrical engineering and information technologies. Fast development in these areas forces many researchers and scientific workers to publish their results. This is a very good opportunity to dissipate these results to the readers of this journal. This issue consists of 16 papers focused on control engineering, biomedical engineering, digital technologies, multimedia technologies, telecommunications, electrical power systems, electric drives and power electronic systems.

It's a pleasure for the Editorial Board members to bring 16 selected and reviewed contributions.

Allow me to express my thanks to the authors, colleagues, reviewers and those who contributed and prepared this issue of the Communications – Scientific Letters of the University of Zilina.

Pavol Rafajdus

Adam Horvath - Tamas Berczes *

SPECTRUM RENTING WITH TWO FINITE SOURCE POOLS IN MOBILE CELLULAR NETWORKS

Spectrum renting is a technique for improving the efficiency of spectrum usage and alleviating the scarcity of the available spectrum in mobile cellular networks. Since the first proposal of spectrum pooling, several works have been done in this area.

In this paper, we propose a finite-source queuing model in which service providers may rent each other's unutilized frequency bands. Our model contains two source pools: one for subscribers generating fresh calls in the investigated mobile cell, and another for modeling handover calls. The model considers the traveling of subscribers over the borders of the investigated mobile cell, too. Moreover, we take into account the retrial phenomenon caused by the impatience of subscribers. It has been already shown in the literature that the use of spectrum renting improves the main performance indices while the average profit rate increases. In this paper, we show how these parameters change with respect to the protection of handover calls.

Keywords: *Spectrum renting, finite-source, retrial queues, handover, impatience.*

1. Introduction

Similarly to many related research fields (see [1], [2], [3] and [4]), the efficient usage of means is always a crucial task. The basic idea of spectrum renting was first proposed by Mitola [5], to aid the efficient usage of the available radio spectrum. Since the Federal Communications Commission's Spectrum Policy Task Force [6] proposed the dynamic/liberalized access to the spectrum in 2002, many researchers have dealt with the realization of spectrum renting [7], [8], [9], [10] and [11]. Besides, some queuing models for spectrum renting were also proposed. In [12] and [13], the authors assume that the speech channels can be rented in one unit, which is not a valid assumption, since each block of speech channels should be controlled by a single network operator [14]. Do et al. considered first this technology aspect in their infinite-source model [14], but they did not consider the retrial phenomenon in their model. In [15], an opportunistic spectrum access model was proposed based on a high-level cooperation between two competing service providers (the aspects of cooperation can open new directions in this area [16]). However, the handover process and the impatience of the users were not touched in that paper.

The retrial queues have been widely studied, too, for the evaluation of the resource contention problem in mobile cellular networks. The works in this area can be classified based on the number of traffic sources. Infinite-source models were presented, e.g., in [17], [18], [19], [20] and [21], while finite-source works can be found, e.g., in [22], [23], [24], [25] and [26]. The assumption on the infinite number of sources may lead to some efficient algorithms [27]. However, the fact that the number of subscribers in a specific mobile cell is finite, justifies the construction of finite-source models. In [27], the authors proposed the use of the retrial queues to model spectrum renting. The model considers the finite size of the subscribers' population, their impatience, and has a queue for the subscribers who requested the outbound service. Moreover, the authors took the renting fee into account, too, for the optimization of the renting process. As it was mentioned in that paper, several model variants could be derived from [27] to investigate additional aspects of spectrum renting.

Based on [27], we set up a finite-source queuing model with two source pools. The additional source pool allows us to investigate also the handover calls, which were not mentioned in [27]. Moreover, our model considers the traveling of subscribers by modeling the transitions over the borders of the investigated mobile cell.

The rest of the paper is organized as follows. Section II introduces the key aspects of our model. Section III describes our system model while the mathematical background is presented in Section IV. The numerical results are provided in Section V. Finally, Section VI concludes the paper.

* [1]Adam Horvath, [2]Tamas Berczes
[1]University of West Hungary, Institute of Informatics and Economics, Sopron, Hungary
[2]University of Debrecen, Faculty of Informatics, Debrecen, Hungary
Email: berczes.tamas@inf.unideb.hu
Email: horvath@inf.nyme.hu

2. Background

In this section, we give a short overview of the key aspects which we took into account in our model: the organization of speech channels, the spectrum renting, the impatience of subscribers and the handover process.

- In mobile cellular networks, service providers get exclusive access to certain frequency bands on spectrum auctions held by the government. Each service provider divides its coverage area to regular shaped cells, and assigns a number of frequency bands to each cell. Using different multiple access techniques, each frequency band hosts regularly 8 full-rate or 16 half-rate speech channels. Such techniques are the Frequency and the Time Division Multiple Access (FDMA, TDMA [28]), the Code Division Multiple Access (CDMA [29]), or for long term evolution (LTE) systems, the Orthogonal Frequency Division Multiple Access (OFDMA [30]). Therefore, a finite number of speech channels is available in each cell.
- Since the right to frequency usage is expensive, improving the utilization in mobile cellular networks is a critical task. Spectrum renting can be used for alleviating the negative effects of temporary capacity shortages [9], [14], [15]. With spectrum renting, service providers may rent each other's unutilized frequency bands to reduce the blocking probability of calls.
- As it was mentioned in the literature [14], [23] and [31], behavioral psychology of using the mobile cellular network services includes repeated attempts and abandonments. When a call is not admitted due to all channels are occupied, the subscriber initiates a repeated attempt later. The abandonment means that after a certain time, the subscribers gives up without being served.
- When the signal strength of a base station, which a traveling user is connected to, decreases below a certain value, another base station with appropriate signal strength must be chosen for serving the ongoing call. This process is termed as handover. Since the break of the connection is annoying for traveling subscribers, a protection procedure must be applied for handover calls (e.g., the well-known guard channel policy [32]).

3. System model

Figure 1 illustrates our system model. The model incorporates the handover process with fractional guard channel (FGC) policy, an orbit for the impatient users, and the blocks of channels, considering the own and the rented blocks, too. Moreover, the model contains two finite sources *i*) for generating the fresh calls within the bounds of the investigated mobile cell, and *ii*) for the handover calls.

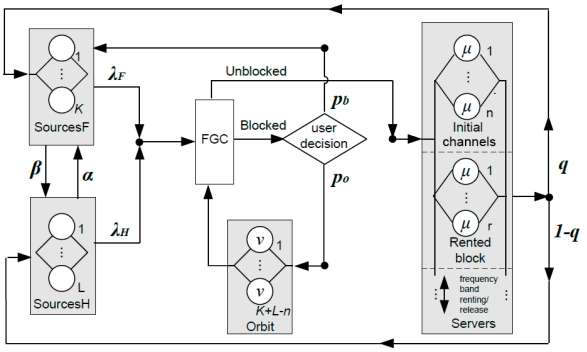

Fig. 1 The system model of the retrial queue

A. Model Operation

From the mobile cell's point of view, a finite number of K subscribers belongs to one mobile cell, generating fresh calls. Being in the *SourcesF* state, each subscriber initiates a fresh call with rate λ_F.

Similarly, a finite number of L subscribers belongs to the investigated mobile cell, being physically out of the cell, generating handover calls. So, the handover calls are generated from state *SourcesH* with rate λ_H on the average by each subscriber.

During the idle periods, the subscribers may leave the investigated mobile cell with rate β, moving from state *SourcesF* to *SourcesH*. Certainly, the subscribers may move into the investigated mobile cell with rate α, changing their state from *SourcesH* to *SourcesF*.

In order to protect the handover calls, a FGC policy is applied for the incoming calls. If a call is admitted, a channel is immediately allocated for it, either in an own frequency band, or in a rented one (state Servers in Fig. 1). The call duration is exponentially distributed with parameter μ, after which the channel is released and the subscriber returns either to the *SourcesF* state with probability q, or to the *SourcesH* state with probability $1 - q$.

If the call is not admitted, the subscriber has two options: i) he/she joins the orbit (state *Orbit* in Fig. 1) with probability p_o, and retries to get a free channel with retrial rate ν; or ii) he/she gives up and becomes idle with probability $p_b = 1 - p_o$.

B. Decision about Renting and Releasing a Frequency Band

Do et al. proposed two thresholds for the number of free channels in [14] to determine when to rent and release frequency bands, and we apply their approach in our model. When the number of free channels decreases to a certain t_1 value, the network operator initiates the frequency renting procedure. The frequency renting is successful in our model with probability p_r, while it fails with probability $p_f = 1 - p_r$. In the latter case, the

network operator retries to rent a frequency band with rate n_r as long as the number of free channels does not exceed t_1.

On the other hand, when the number of free channels increases to $t_2 + r$, then the block of r channels are given back to the owner after an exponentially distributed release time with mean μ_r.

To find the appropriate parameter setting, we have to take into account the blocking probability of fresh calls and handover calls, and the renting fee. To facilitate this decision, we take into account the average profit rate, too, in our investigations.

C. Fractional Guard Channel Policies

In order to minimize the interruption of ongoing calls, network operators exclusively reserve some channels for handover calls [32]. A generalization of this concept is the FGC policy proposed in [33]. To ease the further negotiation, we collected the notations in Table 1.

Notations Table 1

Parameter	Description
$I(t)$	The number of occupied channels in a specific cell.
$J(t)$	The number of rented frequency bands.
$\beta_{i,j}$	The probability of accepting a call for $I(t) = i$ and $J(t) = j$.
n	The number of own channels.
r	The number of channels per block.
N_j	The number of available channels ($N_j = n + jr$ for $J(t) = j$).
g	The real number of guard channels.

Note that in case of a handover call, $\beta_{i,j} = 1$. Based on [34], several FGC policy variants can be distinguished. Since Do et al. showed in [14] that the Limited average FGC (LFGC) is the most convenient for protecting handover calls, we applied this policy and the Non Prioritization Scheme (NPS) in this paper. These policies can be defined as follows [35]:

- *Limited average FGC (LFGC)*, where
- $$\beta_{i,j} = \begin{cases} 1, if\ 0 \le i \le N_j - \lfloor g \rfloor - 2, \\ 1 - g + \lfloor g \rfloor, if\ i = N_j - \lfloor g \rfloor - 2, \\ 0\ else. \end{cases}$$
- *Non Prioritization Scheme (NPS)*, where $\beta_{i,j} = 1$.

4. Mathematical Background

In this section, we describe the mathematical background of our work. We introduce the following notations in order to ease the further negotiation.

- $k(t)$ is the number of active sources being in the investigated mobile cell at time instant t,
- $l(t)$ is the number of active sources with the possibility of generating handover calls at time instant t,
- $s(t)$ denotes the number of occupied channels in the investigated cell at time instant t,
- $b(t)$ ($0 \le b(t) \le m$) is the number of rented frequency bands at time instant t,
- $o(t)$ is the number of calls in the orbit at time instant t,
- $u(t)$ ($u(t) \in \{0,1\}$) indicates whether there is an unsatisfied block rental retrial at time instant t.

Note that $l(t) = K + L - k(t) - s(t) - o(t)$.

In Table 2, we present the main parameters of our model while a complete list of parameters including numerical values is detailed later in Table 3 (see Section V).

Overview of the main parameters Table 2

Parameter	Maximum	Value at time t	Mean
Nr. of users in *SourcesF*	K	$k(t)$	$\overline{K}$
Nr. of users in *SourcesH*	L	$l(t)$	$\overline{L}$
Orbit size	$O = K - n$	$o(t)$	$\overline{O}$
Nr. of busy channels	$n + m \times r$	$s(t)$	$\overline{S}$
Nr. of rented bands	m	$b(t)$	$\overline{B}$
Retrial rate of renting	1	$u(t)$	$\overline{U}$
Fresh call gen. rate	$\lambda_F K$	λ_F	
Handover call gen. rate	$\lambda_H L$	λ_H	
Service rate		μ	
Retrial rate		ν	
Rate of leaving the cell		α	
Rate of moving into the cell		β	

To preserve the mathematical tractability, we assume that all inter-event times (including request generation time, impatience time, service time, retrial time, and times related to the spectrum renting) are exponentially distributed and can be characterized by their rate parameter[1]. Therefore, the system is modeled by a five-dimensional Continuous-Time Markov Chain (CTMC)

[1] *This modeling simplification is frequently applied in the performance evaluation of wireless cellular networks, see e.g. [31], [36] or [37].*

$[s(t),\ k(t),\ b(t),\ o(t),\ u(t)]$. The steady state probabilities are denoted

$$p_{s,k,b,o,u} = \lim_{t\to\infty} \Pr(s(t)=s, k(t)= \\ = k, b(t)=b, o(t)=o, u(t)=u) \quad (1)$$

The underlying CTMC is driven by the following types of events:

a) the arrival of fresh calls and handover calls,
b) the retrials of calls,
c) the departure of calls,
d) the request and retrial process for renting spectrum,
e) the release of the rented spectrum.

Since the underlying CTMC is irreducible and its state space is finite, the steady state probabilities surely exist. Taking into account that the state space of this CTMC is very large, it is difficult to determine the performance indices of the system in a traditional way of solving the steady-state equations. Therefore, we use the *MOSEL-2* software tool to generate the underlying Markov chain and its transition rate matrix directly based on a high-level model description, computing the stationary distribution, and deriving performance measures from them, such as

- mean number of rented frequency bands
$$\overline{B} = \sum_{u=0}^{1}\sum_{b=u}^{m}\sum_{s=0}^{n+(b-u)\times r}\sum_{k=0}^{K+L}\sum_{o=0}^{K+L-n} bP(s,k,b,o,u),$$
- mean number of busy channels
$$\overline{S} = \sum_{u=0}^{1}\sum_{b=u}^{m}\sum_{s=0}^{n+(b-u)\times r}\sum_{k=0}^{K+L}\sum_{o=0}^{K+L-n} sP(s,k,b,o,u),$$
- mean orbit size
$$\overline{O} = \sum_{u=0}^{1}\sum_{b=u}^{m}\sum_{s=0}^{n+(b-u)\times r}\sum_{k=0}^{K+L}\sum_{o=0}^{K+L-n} oP(s,k,b,o,u),$$
- mean number of sources generating fresh calls
$$\overline{K} = \sum_{u=0}^{1}\sum_{b=u}^{m}\sum_{s=0}^{n+(b-u)\times r}\sum_{k=0}^{K+L}\sum_{o=0}^{K+L-n} kP(s,k,b,o,u),$$
- mean number of sources generating handover calls
$\overline{L} = K + L - \overline{S} - \overline{K} - \overline{O}$,
- mean system throughput
$\overline{\lambda} = (\overline{K} + \overline{L})\lambda$,
- mean time spent in the orbit
$$\overline{T_O} = \frac{\overline{O}}{\overline{\lambda}}.$$

The last equation can be derived as follows. Let λ_O denote the throughput of the orbit. Using Little's Low, the mean time spent in the orbit by each request is $\overline{T_O^v} = \frac{\overline{O}}{\lambda_O}$. The mean number of visits in the orbit by each request is $e_O = \frac{\lambda_O}{\overline{\lambda}}$. So the overall mean time spent in the orbit can be computed as

$$\overline{T_O} = e_O \overline{T_O^v} = \frac{\lambda_O}{\overline{\lambda}} \frac{\overline{O}}{\lambda_O} = \frac{\overline{O}}{\overline{\lambda}}.$$

5. Numerical results

The *MOSEL-2* tool uses a high-level modeling language that provides a very convenient way for system description [38]. It focuses on the formal system description and exploits the power of various existing and well-tested packages (*MOSES* [39], *SPNP* [40] and [41] and *TimeNET* [42]) for numerical evaluation.

In Table 3, we collected the parameter settings we used in our investigations. As we mentioned above, we use the exponential distribution for modeling the channel holding times, which follow the lognormal distribution [43]. To get a mathematically tractable model, we also used the exponential distribution for channel holding times with the mean of 53.22s, which was determined observing real data traffic [43].

The applied parameter setting — Table 3

Parameter	Symbol	Value
Normalized traffic intensity	$\rho_0 = \frac{K\lambda}{n\mu}$	[0.1 .. 0.9]
Fresh call generation rate	λ_F	$\frac{2}{3}\lambda$
Handover call generation rate	λ_H	$\frac{1}{3}\lambda$
Initial nr. of subscribers in SourcesF	K	100
Initial nr. of subscribers in SourcesH	L	50
Real number of reserved channels	g	2.9
Retrial rate	v	1
Prob. that subscriber gives up	p_b	0.5
Impatience rate	η	1/300
Prob. that imp. user goes back to orbit	p_O	0.5
No. of channels per block	r	8
Number of channels without renting	n	$2 \times r$
Service rate	μ	1/53.22
Rate of moving into the cell	α	0.45
Rate of leaving the cell	β	0.55
Block renting threshold	t_1	3
Block renting rate	λ_r	0.2
Block release threshold	t_2	6
Block release rate	μ_r	1
Prob. for successful renting	p_r	0.8
Block rental retrial rate	v_r	1/7

In the following figures, we depict the results applying LFGC policy for protecting the handover calls, and the case when no protection was applied (NPS). Moreover, Figures 2 - 5 show the results besides the use of spectrum renting, and the no renting case, when p_r = 0. The results clearly show that the possibility of spectrum renting significantly decreases the blocking probabilities. Accordingly, the mean orbit size also decreases applying spectrum renting. Finally, the use of spectrum renting increases the average profit rate (APR), which is an evident financial advantage.

In the following, we focus on the results concerning the handover calls' protection since touching this aspect is a remarkable novelty in our contribution.

Figures 2 and 3 show the blocking probabilities of fresh and handover calls, respectively, as a function of the normalized traffic intensity. We can observe that applying LFGC policy, we obtain an increased protection for handover calls while the price of this protection is the increased blocking probability of fresh calls compared to the case when NPS is used.

In Fig. 4, the mean orbit size in shown. Since the subscribers rapidly leave this state (either due to retrial or giving up), the number of subscribers is relatively low in the orbit even if the traffic increases. Due to the increased blocking probability caused by protecting handover calls, the mean orbit size is higher when LFGC policy was applied than in case of NPS.

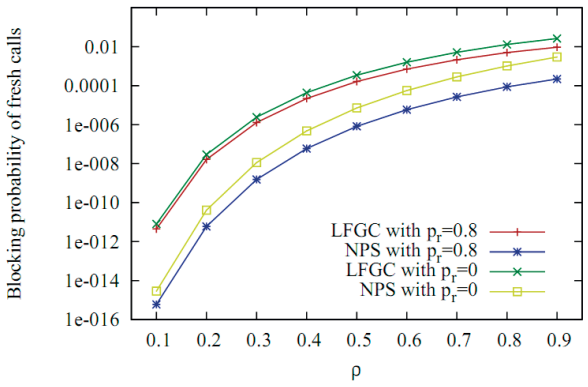

Fig. 2 Blocking probability of fresh calls as a function of the normalized traffic intensity

To measure the financial effect of the handover calls' protection, we illustrated the APR as a function of the normalized traffic in Fig. 5. Besides the case of NPS, we depicted two graphs with different values of LFGC parameter g. We can realize that protecting the handover calls has little impact on APR when number of guard channels is 2.9. Using g = 6.3, the difference between the investigated policies becomes significant as the normalized load increases (the protection of handover calls with relatively high number of guard channels must be paid). However, the operators are able to fine-tune the value of g in view of the expected profit, too.

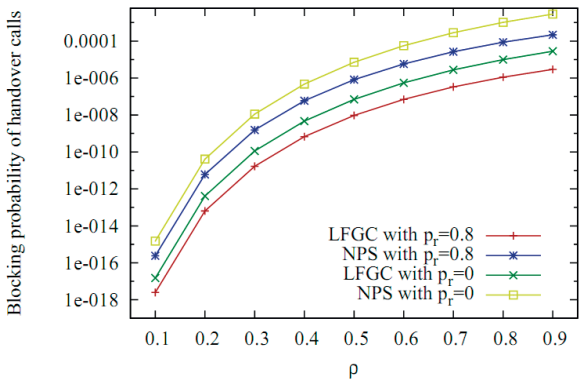

Fig. 3 Blocking probability of handover calls as a function of the normalized traffic intensity

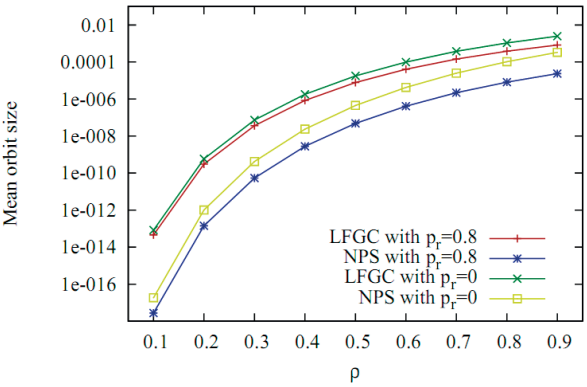

Fig. 4 The mean orbit size as a function of the normalized traffic intensity

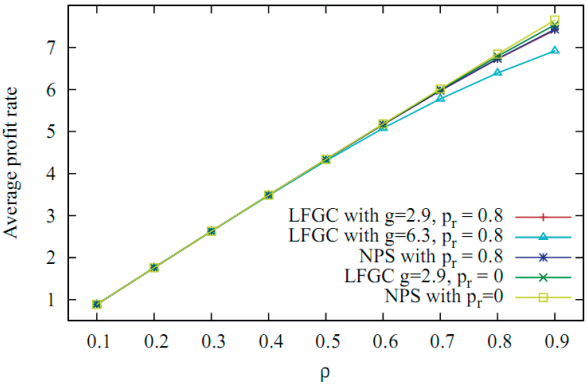

Fig. 5 The average profit rate as a function of the normalized traffic intensity

For the more precise investigation of LFGC parameter *g*, we investigated the above mentioned performance indices as a function of *g* (see Figs. 6 - 9). To ease the comparison with the case of NPS, we also represent the constant values of NPS policy in Figures 6 - 9. As we can see in Figs. 6 and 7, the operators should find a trade-off between the blocking probabilities of fresh calls and handover calls, while the effect of the value of *g* on the APR is not significant in this scenario until *g* increases to around 4 (Fig. 9).

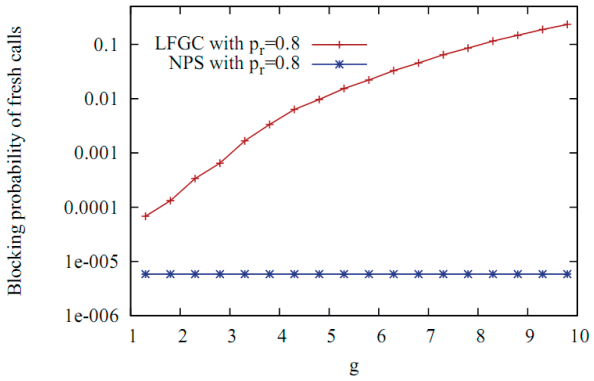

Fig. 6 The blocking probability of fresh calls as a function of the number of guard channels

6. Conclusions

In this paper, we described a queuing model with finite number of subscribers for modeling spectrum renting. The results showed that applying spectrum renting, the blocking probabilities decrease while the increasing value of APR justifies the financial benefits of spectrum renting. To the best of our knowledge, our model is the first finite-source queuing model for modeling spectrum renting in wireless cellular networks that incorporates the handling of handover calls' protection, together with modeling the subscribers' mobility and the retrial phenomenon caused by the impatience of subscribers. Our investigations showed that with appropriate parameter setting, the mobile operators can make a trade-off between the blocking probability of fresh calls and handover calls while the average profit rate can be preserved by controlling the number of guard channels.

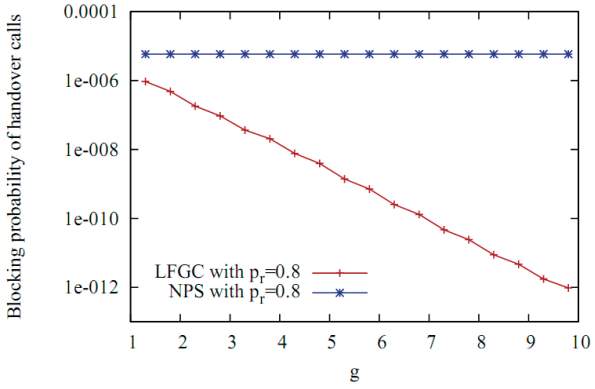

Fig. 7 The blocking probability of handover calls as a function of the number of guard channels

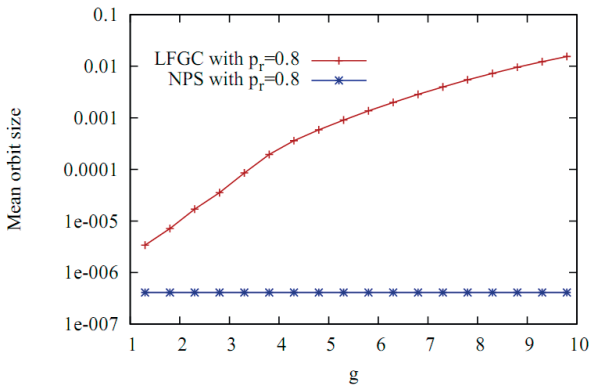

Fig. 8 The mean orbit size as a function of the number of guard channels

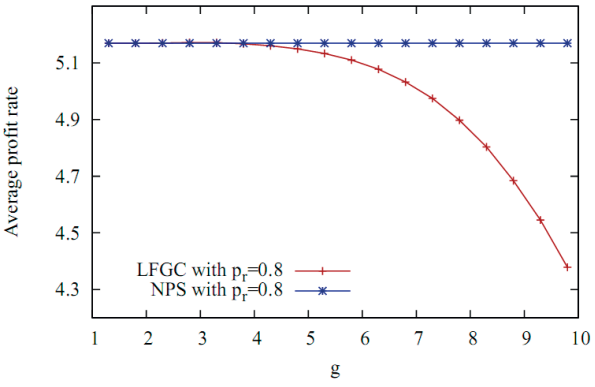

Fig. 9 The average profit rate as a function of the number of guard channels

Acknowledgment

The authors thank Prof. Tien Van Do, Department of Networked Systems and Services, Budapest University of

Technology and Economics, for his professional support during the preparation of this paper.

The work of Tamas Berczes was supported by the TAMOP 4.2.2. C11/1/KONV20120001 project. The project has been supported by the European Union, co-financed by the European Social Fund.

The research of Adam Horvath was supported by the European Union and the State of Hungary, co-financed by the European Social Fund in the framework of TAMOP 4.2.4. A/211120120001 "National Excellence Program".

References

[1] RADOS, I., SCHWARTZ, L.: The Worst Availability as a Parameter for Designing and Reporting on the Network Performances, *Communications - Scientific Letters of the University of Zilina*, vol. 13, No. 1, pp. 60-66, 2011.

[2] LYKOURGIOTIS, A., KOTSOPOULOS, S.: Protocols Performance in Next Generation Networks, *Communications - Scientific Letters of the University of Zilina*, vol. 13, No. 2A, pp. 13-18, 2011.

[3] CHEN, Y., HALBAUER, H., SAUR, S., SCHAICH, F.: WiMax Performance Impacts in Multi-cell Deployments, *Communications - Scientific Letters of the University of Zilina*, vol. 10, No. 4, 2008.

[4] VARDAKAS, J. S., VASSILAKIS, V. G, LOGOTHETIS, M. D.: Performance Modeling and Analysis of Passive Optical Networks for Poisson Traffic, *Communications - Scientific Letters of the University of Zilina*, vol. 10, no. 4, pp. 38-44, 2008.

[5] MITOLA, J. III: *Cognitive Radio for Flexible Mobile Multimedia Communications,* Mobile Multimedia Communications*,* MoMuC'99 - IEEE Intern. Workshop, pp. 3-10, IEEE, 1999.

[6] KOLODZY, P.: Spectrum Policy Task Force, *Communications*, docket No. 02-135, 2002.

[7] BUDDHIKOT, M. M.: *Understanding Dynamic Spectrum Access: Models, Taxonomy and Challenges,* 2nd IEEE Intern. Symposium on New Frontiers in Dynamic Spectrum Access Networks, DySPAN 2007, pp. 649-663, 2007.

[8] GANDHI, S., BURAGOHAIN, C., CAO, L., ZHENG, H., SURI, S.: Towards Realtime Dynamic Spectrum Auctions, *Computer Networks*, vol. 52, No. 4, pp. 879-897, 2008.

[9] PEHA, J. M.: *Sharing Spectrum through Spectrum Preform and Cognitive Radio,* Proc. of the IEEE, vol. 97, pp. 708-719, 2009.

[10] JABBARI, B., PICKHOLTZ, R., NORTON, M.: Dynamic Spectrum Access and Management Dynamic SpectrumM, *IEEE Wireless Communications*, vol. 17, pp. 615, aug. 2010.

[11] WEISS, T. A., JONDRAL, F.: Spectrum Pooling: An Innovative Strategy for the Enhancement of Spectrum Efficiency, *IEEE Communications Magazine*, vol. 42, pp. 8-14, March 2004.

[12] TZENG, S.-S.: Call Admission Control Policies in Cellular Wireless Networks with Spectrum Renting, *Computer Communications*, vol. 32, No. 18, pp. 1905-1913, 2009.

[13] TZENG, S.-S., HUANG, C.-W.: Threshold Based Call Admission Control for QoS Provisioning in Cellular Wireless Networks with Spectrum Renting, *Novel Algorithms and Techniques in Telecommunications and Networking*, pp. 17-22, Springer: Berlin: Heidelberg, 2010.

[14] DO, T. V., DO, N. H., CHAKKA, R.: A New Queueing Model for Spectrum Renting in Mobile Cellular Networks, *Computer Communications*, vol. 35, No. 10, pp. 1165-1171, 2012.

[15] HORVATH, A.: Applying Opportunistic Spectrum Access in Mobile Cellular Networks, *Infocommunications J.*, vol. 5, No. 2, pp. 36-40, 2013.

[16] VODAK, J., SOVIAR, J., LENDEL, V.: Identification of the Main Aspects of Cooperation Management and the Problems Arising from their Misunderstanding," *Communications - Scientific Letters of the University of Zilina*, vol. 16, No. 3, pp. 93-101, 2014.

[17] MARSAN, M. A., CAROLIS, G. D., LEONARDI, E., LO CIGNO, R., MEO, M.: Efficient Estimation of Call Blocking Probabilities in Cellular Mobile Telephony Networks with Customer Retrials, *IEEE J. on Selected Areas in Communications*, vol. 19, No. 2, pp. 332-346, 2001.

[18] ARTALEJO, J. R.: Accessible Bibliography on Retrial Queues: Progress in 2000-2009, *Mathematical and Computer Modelling*, vol. 51, no. 9-10, pp. 1071-1081, 2010.

[19] DO, T. V.: An Efficient Solution to a Retrial Queue for the Performability Evaluation of DHCP, *Computers & OR*, vol. 37, No. 7, pp. 1191-1198, 2010.

[20] DO, T. V.: A New Computational Algorithm for Retrial Queues to Cellular Mobile Systems with Guard Channels, *Computers & Industrial Engineering*, vol. 59, No. 4, pp. 865-872, 2010.

[21] TRAN-GIA, P., MANDJES, M.: Modeling of Customer Retrial Phenomenon in Cellular Mobile Networks, *IEEE J. on Selected Areas in Communications*, vol. 15, No. 8, pp. 1406-1414, 1997.

[22] ARTALEJO, J. R., LOPEZ-HERRERO, M. J.: The Single Server Retrial Queue with Finite Population: A BSDE Approach, *Operational Research*, vol. 12, No. 2, pp. 109-131, 2012.

[23] WUECHNER, P., SZTRIK, J., DE MEER, H.: Finite-source M/M/S Retrial Queue with Search for Balking and Impatient Customers from the Orbit, *Computer Networks*, vol. 53, No. 8, pp. 1264-1273, 2009.

[24] ZHANG, F., WANG, J.: Stochastic Analysis of a Finite Source Retrial Queue with Spares and Orbit Search, *Measurement, Modelling, and Evaluation of Computing Systems and Dependability and Fault Tolerance*, No. 7201 of Lecture Notes in Computer Science, pp. 1630, Springer, 2012.

[25] GHARBI, N., DUTHEILLET, C.: An Algorithmic Approach for Analysis of Finite-source Retrial Systems with Unreliable Servers, *Computers & Mathematics with Applications*, vol. 62, No. 6, pp. 2535-2546, 2011.

[26] ALMASI, B., ROSZIK, J., SZTRIK, J.: Homogeneous Finite-source Retrial Queues with Server Subject to Breakdowns and Repairs, *Mathematical and Computer Modelling*, vol. 42, No. 5-6, pp. 673-682, 2005.

[27] DO, T. V., WUECHNER, P., BERCZES, T., SZTRIK, J., MEER, H. D.: A New Finite-Source Queueing Model for Mobile Cellular Networks Applying Spectrum Renting, *Asia Pacific J. of Operational Research (APJOR)*, vol. 31, No. 2, 2013.

[28] Y.-B. LIN and I. CHLAMTAC, Wireless and Mobile Network Architectures, *Wiley Computer Publishing*, John Wiley & Sons, Inc., 2001.

[29] RAPPAPORT, T. S.: Wireless Communications, *Principles and Practice,* Prentice-Hall, 2002.

[30] COX, C.: Orthogonal Frequency Division Multiple Access, in *An Introduction to LTE: LTE, LTE-Advanced, SAE and 4G Mobile Communications*, *John Wiley & Sons, Ltd*, Chichester, UK. 2012.

[31] PEREL, N., YECHIALI, U.: Queues with Slow Servers and Impatient Customers, *European J. of Operational Research*, vol. 201, No. 1, pp. 247-258, 2010.

[32] GUERIN, R.: Queueing-blocking System with Two Arrival Streams and Guard Channels, *IEEE Transactions on Communications*, vol. 36, No. 2, pp. 153-163, 1988.

[33] RAMJEE, R., TOWSLEY, D., NAGARAJAN, R.: On Optimal Call Admission Control in Cellular Networks, *Wireless Networks*, vol. 3, No. 1, pp. 29-41, March 1997.

[34] CRUZ-PEREZ, F. A., ORTIGOZA-GUERRERO, L.: Fractional Resource Reservation in Mobile Cellular Systems, *Resource, Mobility, and Security Management in Wireless Networks and Mobile Communications*, pp. 335-362, Oct 2006.

[35] DO, T. V.: Solution for a Retrial Queueing Problem in Cellular Networks with the Fractional Guard Channel Policy, *Mathematical and Computer Modelling*, vol. 53, No. 11-12, pp. 2058-2065, 2011.

[36] ARTALEJO, J. R., GOMEZ-CORRAL, A.: *Retrial Queueing Systems: A Computational Approach,* Springer, 2008.

[37] TRAN-GIA, P., MANDJES, M.: Modeling of Customer Retrial Phenomenon in Cellular Mobile Networks, *IEEE J. of Selected Areas in Communications*, vol. 15, pp. 14061414, 1997.

[38] WUECHNER, P., DE MEER, H., BARNER, J., BOLCH, G.: *A Brief Introduction to MOSEL-2*, *Proc. of MMB 2006 Conference,* University of Erlangen, VDE Verlag, 2006.

[39] GREINER, S., BOLCH, G.: *Modeling Production Lines with Blocking, Batch Processing and Unreliable Machines Using the Markov Analyzer MOSES,* Proc. European Simulation Symp. - ESS '95, pp. 303-309, 1995.

[40] CIARDO, G., MUPPALA, J. K., TRIVEDI, K. S.: SPNP: Stochastic Petri Net Package, *PNPM*, pp. 142-151, IEEE Computer Society, 1989.

[41] HIREL, C., TUFFIN, B., TRIVEDI, K. S.: *SPNP: Stochastic Petri Nets. Version 6.0,* Proc. of the 11th Intern. Conference on Computer Performance Evaluation: Modelling Techniques and Tools, pp. 354-357, Springer-Verlag, London, UK, 2000.

[42] GERMAN, R., KELLING, C., ZIMMERMANN, A., HOMMEL, G., BERLIN, T. U., ROBOTIK, F. P. U.: TimeNET - A Toolkit for Evaluating Non-Markovian Stochastic Petri Nets, *Performance Evaluation*, vol. 24, pp. 69-87, 1995.

[43] JEDRZYCKI, C., LEUNG, V.: *Probability Distribution of Channel Holding Time in Cellular Telephony Systems,* Vehicular Technology Conference, 1996. 'Mobile Technology for the Human Race', IEEE 46th, 1996.

Milan Smetana - Klara Capova *

BIOMATERIAL REAL CRACKS EVALUATION BY EDDY CURRENT TESTING METHOD

The paper deals with identification of real biomaterial`s cracks using electromagnetic non-destructive sensing. Advanced types of the magnetic field sensors are used for this purpose. New modular eddy current probe is used for the evaluation. Harmonic excitation is used for the excitation of the eddy currents. The real biomaterial stress corrosion cracks (SCC) and fatigue cracks (FC) are inspected. Gained results are discussed and presented in the paper. The main aim of the paper is to compare the sensitivity of the various magnetic field sensors under the same conditions.

Keywords: *Nondestructive evaluation; inductance coil sensor, fluxgate magnetometer; GMR sensor; AMR sensor, biomaterial stress-corrosion and fatique cracks.*

1. Introduction

Increased R&D activities in the field of non-destructive evaluation (NDE) have been motivated by the need for precise evaluation of materials for the assessment of the expected life of system components. System health monitoring (SHM) and condition based maintenance (CBM) are of high interest nowadays in order to sustain safety, reliability and quality of various processes. They come out from the so-called damage tolerance approach where an inspected element is actively used up to a certain point beyond which the structural integrity of a device could be affected. CBM and SHM systems include three phases: detection, diagnosis and prediction. The first two phases are inherently associated with non-destructive evaluation (NDE) of materials. NDE of materials is based on numerous physical principles and phenomena [1] and [2]. NDE techniques are widely used in a range of industries for the inspection of various complex structures. The periodic inspection of components and devices ensures their safe, effective and long-term operation. New methods and devices are still being developed and designed to tackle gradually increasing demands for reliable detection and precise characterization of material discontinuities. Increased R&D activities in the field of non-destructive evaluation (NDE) have been motivated by the need for precise evaluation of cracks and flaws for the assessment of the expected life of mechanical components. Nowadays, evaluation of stress corrosion cracks (SCC) and fatigue cracks (FC) in real biological environment is one of the most important problems, Fig. 1. These cracks strongly affect the structural integrity of the material or biomaterial objects. Biomaterials are materials used to manufacture prostheses, implants, and surgical instruments.

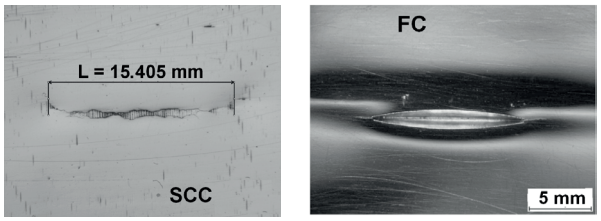

Fig. 1. Microscopy images of the inspected cracks

Designed not to provoke rejection by our bodies (skin, blood, bone, etc.), they can be natural (collagen, cellulose, etc.) or synthetic (metallic, alloy, ceramic, plastic, and others). Human body is a very aggressive corrosive environment and arising probability of the SCC or FC cracks is very high. However, evaluation of the SC cracks is quite difficult because they are partially conductive, Fig. 2.

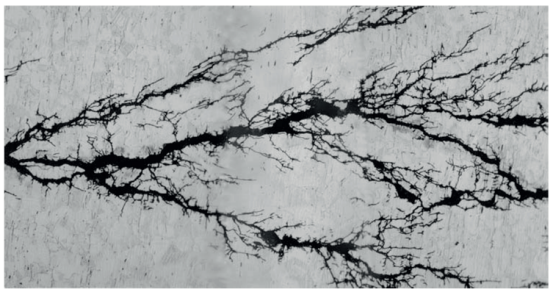

Fig. 2.Internal structure of the SC crack (after destructive evaluation)

* **Milan Smetana, Klara Capova**
Department of Electromagnetic and Biomedical Engineering, Faculty of Electrical Engineering, University of Zilina, Slovakia
E-mail: milan.smetana@fel.uniza.sk

2. Eddy current evaluation

In recent years, electromagnetic methods, especially eddy current testing (ECT), have attracted increasing attention. The ECT method is theoretically well known and widely utilized in the practice. Eddy current testing is used to ensure pre-service quality and to assess in-service health of industrial components made of electrically conducting materials, by way of detection and characterization of defects or discontinuities. Eddy current probe is the main link between the eddy current instrument and the component under test. Success of eddy current testing for a specific inspection application depends on sensor, instrument and optimization of test parameters. The probe plays two important roles: it induces the eddy currents, and it senses the distortion of their flow caused by defects. Design and development of eddy current probes is very important as it is the probe that dictates the probability of detection and the reliability of characterization, [3], [4], [5], [6] and [7]. Traditional eddy current testing method based on excitation-detection coils is fundamentally limited by the poor sensitivity of the detection coils at low frequencies, [8]. Nowadays comes to the fore the use of different types of detection elements such as Hall sensors, SQUID, GMR, AMR, Fluxgate and other to increase a detection sensitivity. The shape, cross-section, size and configuration of coils and sensing elements are varied to design an eddy current probe for a specific application, [4] and [5]. Among these, the magneto-resistive (MR) sensors offer a good trade-off in terms of performance versus cost. They have small dimensions, high sensitivity over a broad range of frequency (from hertz to megahertz domains), low noise; they operate at room temperature, and are inexpensive. It has been demonstrated that the MR probes perform better than conventional probes for low-frequency applications, e.g. when detecting deeply buried flaws. This is because the electromagnetic sensors are sensitive to the magnitude of the magnetic field. In the case of inductive-based probes, the output voltage is proportional to the time variation of the magnetic field; therefore, their sensitivity is reduced at low frequencies. Although their sensitivities are comparable, GMR sensors have better directional property than AMR sensors. Both types of sensors detect the component of the magnetic field vector along their sensitive axis. In the case of GMR sensors, fields applied perpendicularly to the sensitive axis have negligible effect on their output. In contrast, the sensitivity of AMR-based probes is lowered by a field perpendicular to the sensitive axis, which, at high values, can even "flip" the sensor response [4]. This property is particularly important in the coil-crack interaction problems where the electromagnetic field has a complex three-dimensional (3-D) distribution. The directional property of GMR sensor can be used in a difficult problem encountered in NDE, e. g, detection of edge cracks [8]. It is shown that by properly orienting the sensitive axis, the probe will be insensitive to the edge. Additionally, the presence of the edge enhances the sensitivity and resolution of the GMR probe to cracks initiating perpendicular to this edge. The main objective in these strategies is to detect the weak magnetic fields from the defects rather than the traditional measurement of the impedance changes. When more than one sensor is used and data fusion methods are adopted to combine the sensors data then it forms a comprehensive global picture of investigated regions. This article deals with comparison of the four sensing elements: inductance coil, GMR, AMR and fluxgate sensor, in eddy current evaluation under the same conditions. The harmonic excitation is used to drive the eddy currents. The sensitivity and the resolution of the sensors are concerned. The reason for this comparison is to show which of these sensors is able to provide higher probability of detection and to give response signal with higher information rate for accurate characterization of defects.

3. Experimental set-up

The SUS 316L plate specimen with a thickness of h_1 = 10 mm is inspected from the near-side. The material has the conductivity of σ = 1.4 MS/m and the relative permeability of μ_r = 1. Every specimen contains one SCC and FC crack, located in the middle of the specimen, respectively, Fig. 3. The SCC cracks were made using corrosive environment ($MgCl_2$) and static load with various exposure times.

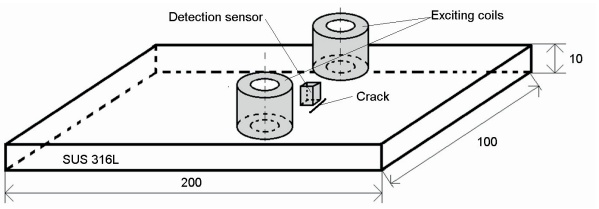

Fig. 3. Configuration of the plate specimen with the crack

New ECT probe is designed for this study. It consists of two exciting coils that are positioned normally to the surface of inspected material apart from each other. The coils are connected in series but magnetically opposite to decrease coupling between the exciting system and the sensing element. High sensitivity of a pick-up circuit can be adjusted in such case. The exciting coils are driven by the harmonic current with various frequencies. Four sensing elements with appropriate dimensions, the inductance coil, the fluxgate magnetometer, the GMR sensor and the AMR sensor, shown in Fig. 4, are used to pick-up the response signal.

The inductance coil is a classical type without the ferrite core. The fluxgate magnetometer is the commercial one made by Canon. The GMR and AMR sensor are the commercial ones made by Sensitec GmbH. Measured component of the magnetic field in given direction is converted to the output voltage signal. Each inspection is performed four-times, once with the inductance coil and then with the fluxgate magnetometer and the GMR and AMR sensor, respectively. Realized modular probe with

the sensing elements is shown in Fig. 5. Configuration of the experimental set-up is shown in Fig. 6 (SG - signal generator, PA - power amplifier, EC – excitation coils, SD – sensing device, XYZ – linear positioning system, SC – stage controller, DAC – data acquisition card, LI – lock-in amplifier, PC – personal computer).

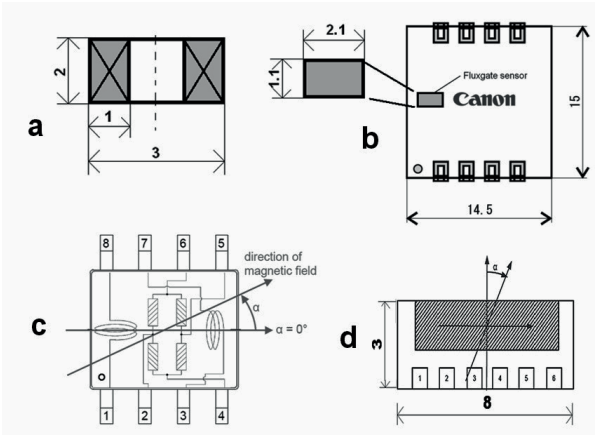

Fig. 4. Package outline of the sensing elements: inductance coil (a), fluxgate sensor (b), AMR sensor (c), GMR sensor (d)

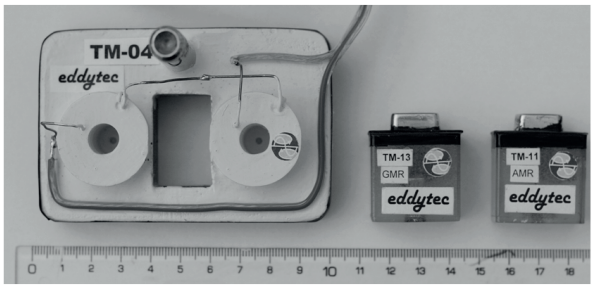

Fig. 5. Designed modular ECT probe (left) with the sensing elements (right)

Measured data are acquired using the data acquisition card with resolution of 16bits/channel, 25kS/sec. User interface for data manipulation, controlling the stage and processing the data is created using the LabVIEW development environment. One dimensional scanning is performed over each crack along its length in a range <-30 mm, 30 mm> relative to a crack center. The sensing elements are positioned in the middle between the exciting coils. Layout of the probe is shown in Fig. 7. Two exciting coils with self-inductances of L_1 = 2.24 mH, L_2 = 2.23 mH are driven by the harmonic current with an effective value of I = 0.7 A. The inductance receiver coil has N = 600 number of turns and it is wound from a copper wire with a diameter of Ø = 0.05 mm.

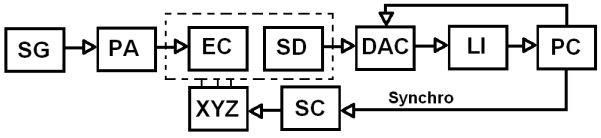

Fig. 6. Flowchart of the experimental setup

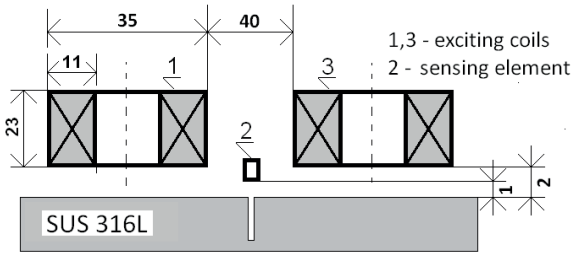

Fig. 7. Configuration of the designed and realized ECT probe

4. Experimental results

Results of the realized experiments are presented in this section. The SUS316L plate specimen with a thickness of h = 10 mm is inspected from the near-side. Figures 8 - 17 display the sensors' response signals magnitude on the probe position relative to the crack center for the near side inspection. Several waveforms for different frequencies are displayed for every graph. It can be observed that the experimental results using various sensing elements have approximately comparable information value. The sensitivities of the sensors are quite similar when comparing the results in the relative scale. The individual signals for all the excitation frequencies are separated from each other using both types of sensing elements.

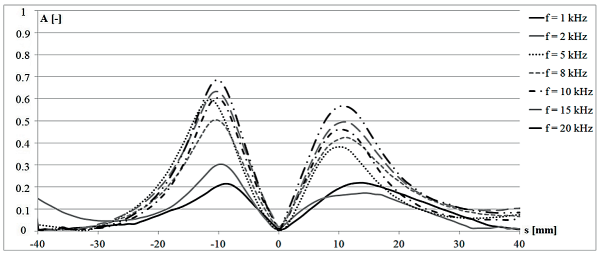

Fig. 8. Experimental results: GMR sensor, SC crack (load force F = 1.2 kN, t = 12 hours)

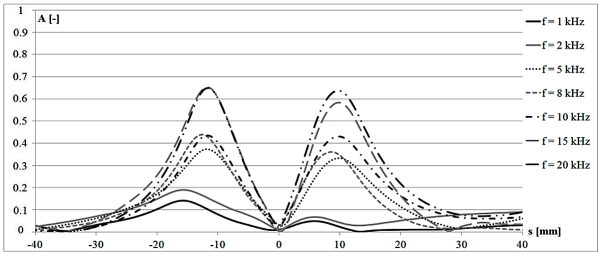

Fig. 9. Experimental results: inductance sensor, SC crack (load force F = 1.2 kN, t = 12 hours)

Further, it can be observed that approximately the same resolution is obtained with all the magnetic field sensors. It

seems that when an ECT probe is constructed in such a way that the direct coupling between the exciting system and the pick-up system is minimized all the sensing elements have comparable sensitivity and resolution. The results show that the higher the excitation frequency the higher the amplitude of the differential response signal.

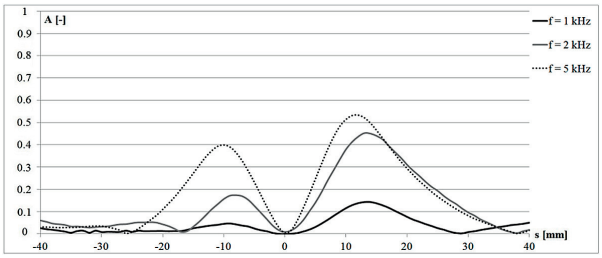

Fig. 10. Experimental results: fluxgate sensor, SC crack (load force F = 1.2 kN, t = 12 hours)

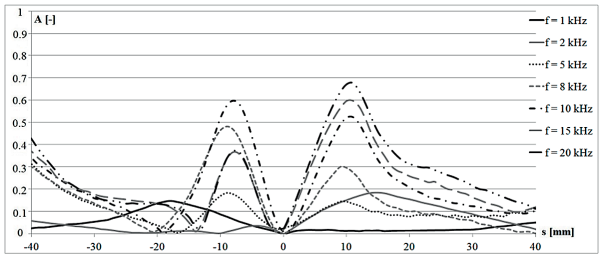

Fig. 11. Experimental results: GMR sensor, SC crack (load force F = 1.8 kN, t = 6 hours)

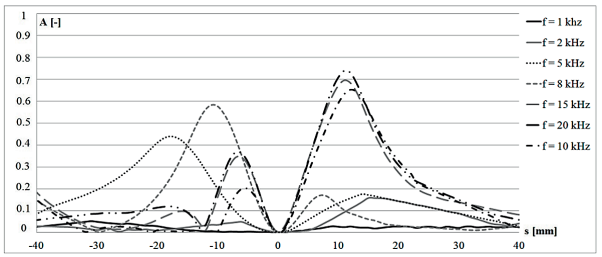

Fig. 12. Experimental results: inductance sensor, SC crack (load force F = 1.8 kN, t = 6 hours)

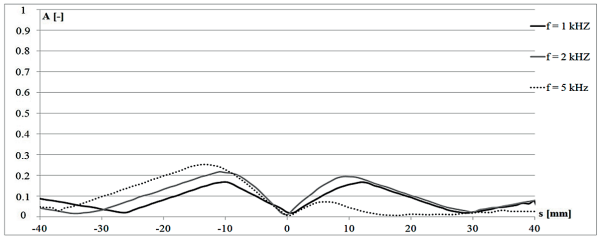

Fig. 13. Experimental results: fluxgate sensor, SC crack (load force F = 1.8 kN, t = 6 hours)

The results for the fluxgate sensor represent only three individual waveforms because its upper frequency range was approximately f_{max} = 3.4 kHz. All the sensed signals for one excitation frequency are shown in Fig. 16 to see the sensitivity of the sensors. It can be seen that the highest sensitivity was obtained using the GMR sensor. However, the length of the defect can be clearly detected observing the local peaks of the individual signals.

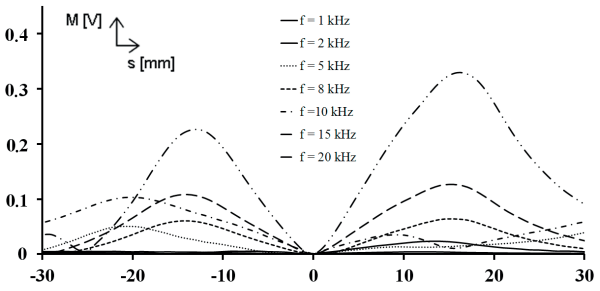

Fig. 14. Experimental results - AMR sensor, FC crack

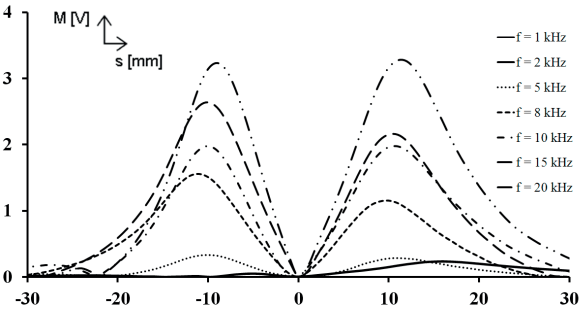

Fig. 15. Experimental results - GMR sensor, FC crack

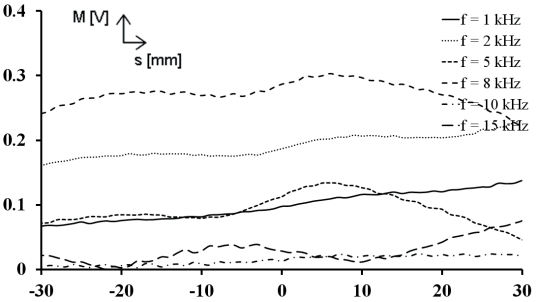

Fig. 16. Experimental results - AMR sensor (left), SCC crack (load force F=1.8 kN, t=12hours)

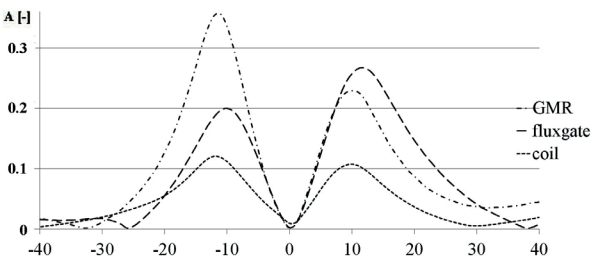

Fig. 17. Experimental results: SC crack, (load force F = 1.2 kN, t = 24 hours), excitation frequency f = 1kHz

5. Conclusion

The article presented the design and performances of the eddy current probe in non-destructive inspection under harmonic excitation. Realized experiments were carried out to evaluate sensitivity and resolution of the four different sensors under the same conditions. Austenitic steel plates with presence of stress-corrosion crack and fatique crack were evaluated, respectively. According to the results it can be concluded that the four sensors have almost equal performances under the same conditions. Evaluated stress-corrosion and fatique cracks made under different conditions present real biomaterial's cracks that may occur in conductive prosthetic replacements *in vivo*. Because of complicated SCC`s internal structure and partially conductive character, their detection and especially evaluation is quite difficult. On the other hand, based on the results, it can be seen that such types of material defects can be detected also at relatively low frequencies. Information value of the useful signals increase with higher excitation frequency. It can be concluded that even when the four different sensors exhibit almost similar performances, it is recommended to use the GMR sensor, because of its parameters (low noise, very high sensitivity in the senstive axis, cost etc.)

Further work of the authors will address the behaviour of other types of multi-axis sensing elements under various types of excitations.

Acknowledgment

The authors wish to express their thanks to prof. Peter Palcek and his co-workers of Department of Mechanical Engineering, University of Zilina, for the cooperation. This work was supported by the Slovak Research and Development Agency under the contracts No. APVV-0349-10.

References

[1] REIG, C., CUBBELS-BELTRAN, M. D., MUNOZ RAMIREZ, D.: *Magnetic Field Sensors Based on Giant Magnetoresistance (GMR) Technology: Applications in Electrical Current Sensing*, Sensors 2009, ISSN 1424-8220, pp. 7920 - 7924

[2] BETTA, G., FERRIGNO, L., LATACCA M.: GMR - Based ECT Instrument for Detection and Characterization of Crack on Planar Specimen: A Hand-held Solution, *IEEE Transactions on Instrumentation and Measurement*, vol. 61, No. 2, February 2012, pp. 505-512

[3] RIPKA, P.: *Advances in Fluxgate Sensors, ScienceDirect, Sensors and Actuators A 106*, 2003, pp. 8-14

[4] PERNISOVA, V., CAPOVA, K., SMETANA, M., STRAPACOVA, T.: *Biomaterial Real Defects Evaluation Using Advanced Detection Sensors*, Proc. of Intern. workshop on Electromagnetic non-destructive evaluation, 2013, Bratislava, ISBN 978-80-554-0713-5

[5] JANOUSEK, L.: *Impact of Selected Parameters on Eddy Current Attenuation in Conductive Materials*, 2012, Proc. of 9th Intern. Conference, ELEKTRO 2012, art. No. 6225656

[6] JANOUSEK, L., REBICAN, M. I., SMETANA, M., STRAPACOVA, T., DUCA, A., PERNISOVA, V.: Recent Innovative Solutions in Eddy Current Non-destructive Diagnosis, *Communications - Scientific Letters of the University of Zilina*, vol. 15, No. 2, 2013, pp. 102-108, ISSN: 13354205

[7] STRAPACOVA, T., CAPOVA, K., SMETANA, M.: Biomaterials Inhomogeneities Detection by Electromagnetic Methods. *Communications - Scientific Letters of the University of Zilina*, vol. 13, No. 1, 2011, pp. 32-36, ISSN 1335-4205.

[8] JANOUSEK, L.: Effect of Exciting System Configuration on Eddy Currents Distribution in Non-destructive Evaluation of Materials, 2013, *Przeglad Elektrotechniczny* 89(3A) , pp. 256-258.

Ladislav Janousek - Mihai Rebican - Milan Smetana - Anton Duca *

PROGRESS IN THREE-DIMENSIONAL NON-DESTRUCTIVE ASSESSMENT OF REAL CRACKS FROM EDDY CURRENT TESTING SIGNALS

Enhancement in three-dimensional non-destructive evaluation of real cracks from two-dimensional simulated eddy current testing signals is reported in the paper. A new uniform eddy current testing probe is employed for the inspection. All three spatial components of the perturbation electromagnetic field are acquired during two-dimensional scan of the probe. The ECT signals due to partially conductive cracks are simulated by a fast forward FEM-BEM solver using a database. Two crack models are proposed for the inversion using the tabu search stochastic method. The former model has a cuboid shape and the latter one reflects a more complex geometry. Numerical results of the three-dimensional reconstruction of partially conductive cracks from simulated two-dimensional signals are presented and discussed in the paper.

Keywords: *Non-destructive evaluation, eddy currents, partially conductive cracks, diagnosis, stochastic method, tabu search.*

1. Introduction

New approaches such as System Health Monitoring and Condition Based Maintenance are nowadays employed for assessment of structural integrity of various components and structures. The modern methods follow three consecutive phases – detection of non-homogeneities, their diagnosis and prognosis of their further development. The first two phases are inherently associated with Non-Destructive Evaluation (NDE) of materials. Enhancing NDE methods is therefore very important for accomplishing their challenging missions.

NDE techniques are based on numerous physical principles and phenomena. Eddy current testing (ECT) is one of the widely utilized electromagnetic NDE methods. ECT works based on an interaction of time-varying electromagnetic field with a conductive body according to the Faraday's electromagnetic induction law. There are many advantages such as high sensitivity for surface breaking defects, high inspection speed, contact-less inspection, versatility, maturity of numerical means that account for continuously enlarging application area of the ECT mainly in nuclear, petrochemical and aviation industries [1]. On the other hand, ECT is a relative method and the inverse problem is ill-posed [2]. Therefore, evaluating dimensions of a detected defect from ECT response signals can be quite difficult [3]. ECT instruments provide raw data with limited or absent capability of interpreting quantitatively the data [4]. Typically, evaluation relies on calibrated curves measured on pre-fabricated etalons and on the skills of an operator. Recently, the progress in powerful computers has allowed developing of automated procedures to make decisions. Quite satisfactory results are reported by several groups for automated evaluation of artificial slits [3] and even for several parallel notches [5]. However, evaluation of real cracks, especially stress corrosion cracking (SCC), from ECT response signals remains still very difficult.

SCCs are quite different comparing to artificial slits or even to other types of real defects. Cross sections of SCC frequently show branched structure and group of cracks usually occur in what is known as a colony. The local opening of SCC is usually very small, e.g. tens of micrometers; however a damaged region itself is much broader. SCC contains many unbroken ligaments both in depth and opening directions, which makes SCC partially conductive [6]. In the case of artificial electro-discharge machined (EDM) notches, the width is usually considered fixed in the inversion process of ECT signals. However, for cracks with non-zero conductivity the width affects the signal and it has to be considered unknown during reconstruction [7]. It means that the additional variable should be taken into account for evaluation of a detected SCC which considerably increases ill-posedness of the inverse problem [2]. Thus, many unsatisfactory results are reported when the automated procedures originally developed for non-conductive cracks are employed in the evaluation of SCCs. It is stated that one of the possible reasons is lack of sufficient information [3].

* [1]**Ladislav Janousek,** [2]**Mihai Rebican,** [1]**Milan Smetana,** [2]**Anton Duca**
[1]Department of Electromagnetic and Biomedical Engineering, Faculty of Electrical Engineering, University of Zilina, Slovakia
[2]Faculty of Electrical Engineering, University Politehnica of Bucharest, Bucharest, Romania
E-mail: ladislav.janousek@fel.uniza.sk

Common eddy current probes are designed in such a way that they sense only one component of the perturbation electromagnetic field. Usually, the most significant component is used for the evaluation. However, curved paths of eddy currents provide more information in principle.

Several studies of authors focused on enhancing information level of eddy current testing signals [8] - [10]. The original idea is based on sensing of all three spatial components of the perturbation electromagnetic field. The studies have revealed that the uncertainty in cracks' evaluation is reduced when the enriched information is utilized for the purpose. Promising results create new challenges concerning development of automatic procedures for diagnosis of real cracks.

The authors have already developed an algorithm for reconstruction of multiple slits from ECT signals by means of a stochastic optimization method, such as tabu search [5]. The reconstruction of multiple slits was done in three-dimensions. Therefore, the scheme is also appropriate for reconstruction of a partially conductive crack when the width has to be considered as variable.

This paper presents enhanced procedure for diagnosis of real cracks from simulated eddy current testing response signals. The tabu search is applied for the three-dimensional reconstruction of partially conductive cracks. Uniqueness of the proposal lies in the utilization of two-dimensional response signals for the 3D inversion. Moreover, all the three spatial components of the perturbation electromagnetic field are taken as the response signals in order to tackle severe problem connected with diagnosis of partially conductive cracks.

2. Numerical model

A plate specimen having the electromagnetic parameters of a stainless steel SUS316L is inspected in this study. The specimen has a thickness of t = 10 mm, a conductivity of σ = 1.35 MS/m and a relative permeability of $\mu_r = 1$. A single surface breaking crack appears in the plate. It is modelled as a cuboid having different electromagnetic properties from the base material. Configuration of the plate (region Ω_0) with the crack (region Ω_1) is shown in Fig. 1. The crack region Ω_1 (22×2×10 mm^3) is uniformly divided into a grid composed of $n_x \times n_y \times n_z$ (11×5×10) cells defining a possible crack geometry. The dimensions of each cell are 2.0×0.4×1.0 mm^3.

A new eddy-current probe proposed by the authors is employed for the near-side inspection of the plate [10]. It consists of two circular exciting coils positioned apart from each other and oriented normally regarding the plate's surface. The circular coils are connected in series but magnetically opposite to induce uniformly distributed eddy currents in the plate. The exciting coils are supplied from a harmonic source with a frequency of 5 kHz and the current density 1 A/mm^2. A detection system of the probe is composed of three small circular coils oriented along three axes perpendicularly to each other [8]. The detection system is located in the centre between the exciting coils to gain high sensitivity as the direct coupling between the exciting coils and the detectors is minimal at this position. Configuration of the new probe is shown in Fig. 2. Dimensions of the detecting coils are as follows: an inner diameter of 1.2 mm, an outer diameter of 3.2 mm and a winding height of 0.8 mm.

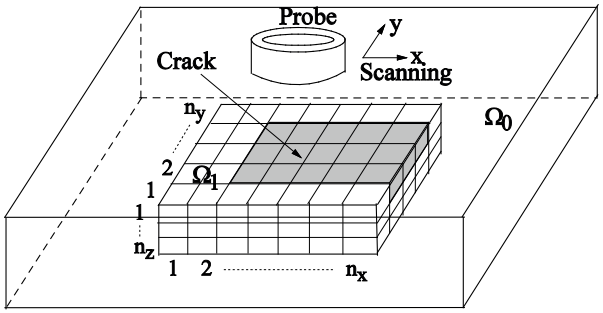

Fig. 1 Configuration of plate specimen with crack region

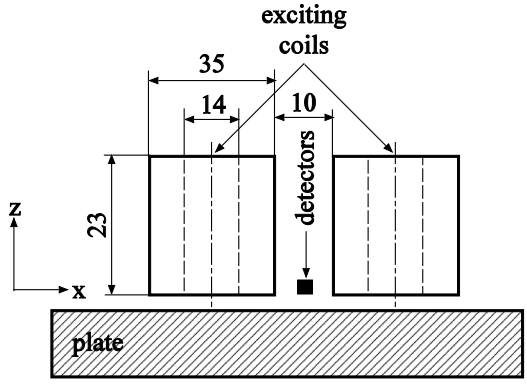

Fig. 2 ECT probe configuration

Two-dimensional scanning, so called C-scan, is performed over the cracked surface with a lift-off of 1 mm. The real and imaginary parts of the induced voltages in all three detecting coils corresponding to three spatial components of the perturbation electromagnetic field are sensed and recorded during the inspection.

3. Crack reconstruction

The fast-forward FEM-BEM analysis solver using database [11] is adopted here for the ECT response signals simulation. Actually, a version of the database algorithm upgraded by the authors in previous works [5] for the computation of the ECT signals due to multiple cracks is used in this paper. The database is designed for a three-dimensional defect region and not as usually

for a two-dimensional one where a crack width is considered fixed. Thus, the ECT response signals can be simulated also for partially conductive cracks with variable width using the same database generated in advance. The area of the simulated two-dimensional ECT signals has surface dimensions of 100×28 mm^2. The number of scanning points in the two directions is 50 and 70, respectively.

Tabu search is employed for the three-dimensional diagnosis of a detected crack [5]. The error function ε to be minimized is defined as:

$$\varepsilon = \frac{\sum_{i=1}^{n} \left| \Delta V_{ix}(c) - \Delta V_{ix}^{m} \right|^2}{\sum_{i=1}^{n} \left| \Delta V_{ix}^{m} \right|^2} + \frac{\sum_{i=1}^{n} \left| \Delta V_{iy}(c) - \Delta V_{iy}^{m} \right|^2}{\sum_{i=1}^{n} \left| \Delta V_{iy}^{m} \right|^2} + \frac{\sum_{i=1}^{n} \left| \Delta V_{iz}(c) - \Delta V_{iz}^{m} \right|^2}{\sum_{i=1}^{n} \left| \Delta V_{iz}^{m} \right|^2},$$

where c is the crack parameter vector, ΔV_i and ΔV_i^m are the simulated (reconstructed) and true (measured) induced pick-up voltages of the coils at the i-th scanning point respectively, and n is the number of scanning points. It should be noted that the real and the imaginary parts of each spatial component (X, Y and Z according to the coordinate system shown in Figs. 1 and 2) of the perturbation electromagnetic field are employed for the inversion.

Two three-dimensional crack models shown in Fig. 3 are employed in the inversion. The partial conductivity of both crack models is considered uniform.

In the first model shown in Fig. 3a, the crack has a cuboid shape. The crack parameter vector c consists of 6 integers, $c = [ix_1, ix_2, iy_1, iy_2, iz, s]$, where ix_1 and ix_2 are the indices of the first and last cells of the crack along the length of crack, iy_1 and iy_2 are the indices of the first and last cells of the crack along the width of crack, iz is the number of cells of the crack along the depth of crack, and $\sigma_c = s\%\sigma$ (σ_c – the conductivity of crack, σ - the conductivity of base material). In Fig. 3a, for a uniform grid with 13×5×10 cells, the parameter vector is c = [6, 13, 1, 3, 4 and 20]. Thus, 8×3×4 cells form the crack, and the crack conductivity is $\sigma_c = 20\%\sigma$.

The second crack model shown in Fig. 3b adopts a more complex shape. The crack depth is considered as variable along the crack length. The crack parameter vector c consists of n_x+3 integers, $c = [iz_1, iz_2, \ldots, iz_{nx}, iy_1, iy_2, s]$, where iz_k, k = 1, nx is the number of cells of the crack along the depth of crack, iy_1 and iy_2 are the indices of the first and last cells of the crack along the width of crack, and $\sigma_c = s\%\sigma$ (σ_c – the conductivity of crack, σ - the conductivity of base material). In Fig. 3b, for a uniform grid with 13×5×10 cells, the parameter vector contains 16 integers, as c = [0,0,0,0,0,8,4,1,2,5,3,6,4,1,3,30]. Thus, (8+4+ 1+2+5+3+6+4)×3 cells form the crack, and the crack conductivity is $\sigma_c = 30\%\sigma$.

In the both models, the cracks have the same orientation. The width of crack can have the values: 0.4, 0.8, 1.2, 1.6, 2 mm.

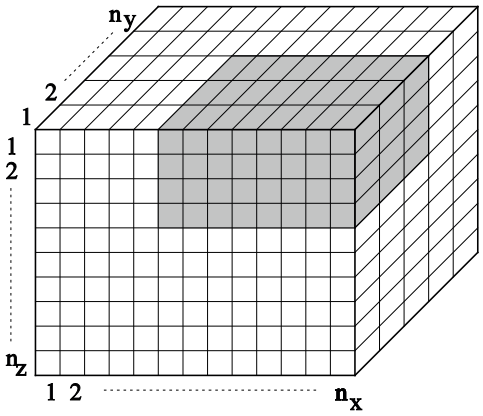

a) cuboid shape of crack (model 1)

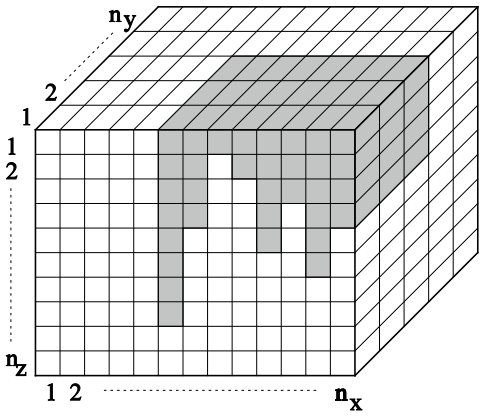

b) complex shape of crack (model 2)

Fig. 3 Crack region division

In this paper, the simulated signals are affected by added noise before the inversion process in order to prove the validity and robustness of the proposed approach. The perturbed signal is computed as:

$$\left(\Delta V_i^m\right)_{ms} = \Delta V_i^m \left(1 \pm ns\%\right),$$

where ΔV_i^m and $\left(\Delta V_i^m\right)_{ns}$ are the initial and the perturbed true signals at the i-th scanning point respectively, ns is a random value of an imposed maximum noise level.

Figure 4 shows the simulated ECT signal (Fig. 4a) and the perturbed ECT signal (Fig. 4b) for Z-component when a noise of maximum level 40% is added, for a partially conductive crack with a cuboid shape (l_c = 6mm, w_c = 0.8mm, d_c = 4mm, s_c = 5% of σ).

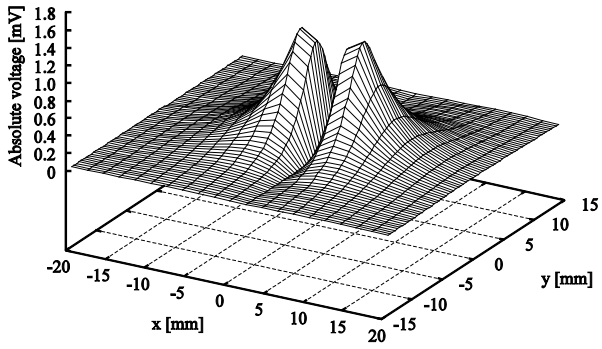

a) unperturbed simulated signal

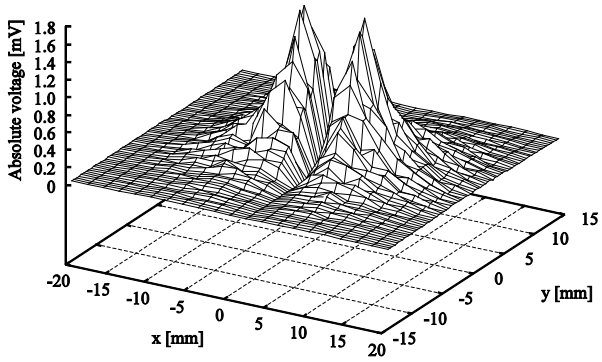

b) simulated signal perturbed with noise

Fig. 4 Simulated ECT response signal

5. Results and discussions

In Table 1 the numerical results of the reconstruction are presented when a partially conductive crack is modelled as a cuboid shape, Fig. 3a. The column denoted as "Real" gives the true dimensions ($l_c \times w_c \times d_c$) and partial conductivity (σ_c in % of σ) of the crack. The results of the diagnosis are provided in the column labelled as "Reconstructed" for various maximum levels of the noise added to simulated ECT signals. The error function $\varepsilon(c)$ of the diagnosis are reported, too. Five numerical simulations were performed for each crack reconstruction, with different random initializations of the tabu search initial population.

The time required for reconstruction of one crack is approximately 90-120 minutes. When there is no noise added to signal, the reconstructed crack is the same with the real crack (the error function ε = 0) for each random initial population. In the case of diagnosis from signals perturbed by noise (maximum noise level = 10, 20, 30, 40%), for the most random initial populations, the crack is exactly reconstructed even if the maximum level of noise is high (30, 40%). For one random initial population and for a perturbed signal by added noise of highest level, i.e. 40%, the result is slightly different (the last column in Table 1): the length and depth are equal to the true values; the width and partial conductivity are estimated not exactly but with good precision (the width is different with the minimum value of 0.4 mm). However, the last two parameters are not very important from structural integrity point of view. The results clearly show

Reconstruction of partially conductive cracks, crack model 1 Table 1

Crack	Real	Reconstructed					
Noise (%)		0	10	20	30	40	40
l_c [mm]	6.0	6.0	6.0	6.0	6.0	6.0	6.0
w_c [mm]	0.8	0.8	0.8	0.8	0.8	0.8	1.2
d_c [mm]	4.0	4.0	4.0	4.0	4.0	4.0	4.0
σ_c [%]	5	5	5	5	4	4	9
$\varepsilon \cdot 10^{-3}$	-	0	11	21	32	42	45

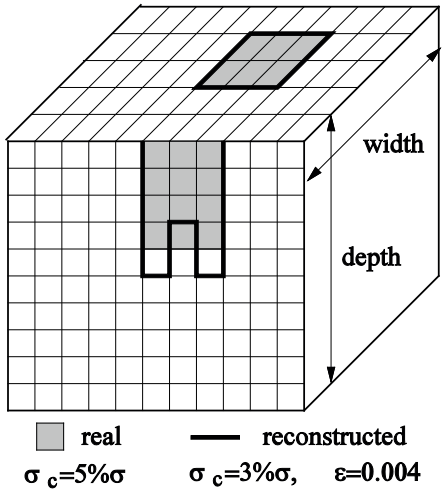

a) crack signal without noise

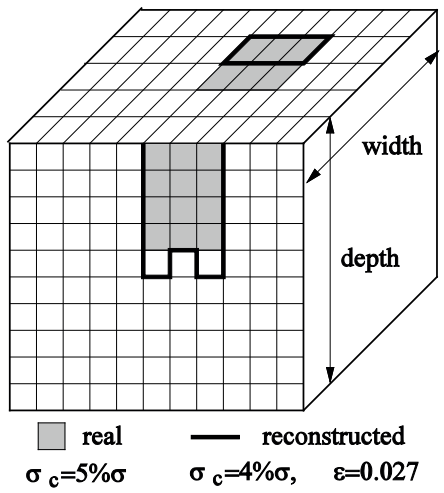

b) crack signal with added noise of 20%

Fig. 5 Reconstruction of a partially conductive crack, crack model 2

that the crack parameters are estimated quite precisely from the noisy ECT signals using the proposed approach for various random initial populations.

Figure 5 shows the results of three-dimensional diagnosis of the partially conductive crack described in Table 1 (column "Real") from 2D ECT signals without noise (Fig. 5a) and with added noise of maximum level 20% (Fig. 5b) when the complex crack model (Fig. 3b) is employed for the inversion. One diagnosis takes around 5-7 hours. In the case of the reconstruction from signal without noise, the crack is precisely localized and also its length and width are exactly estimated. The depth profile does not perfectly copy the true one. However, the maximum depth is accurately assessed. But, for the reconstruction from signal with added noise of maximum level of 20%, the width is smaller with a minimum value of 0.4 mm than the real width.

The presented results proved effectiveness of the enhanced approach of three-dimensional diagnosis of partially conductive cracks, even if cracks with complex shape and signals with added noise are considered. ECT response signals gained during C-scan together with acquiring all three spatial components of the perturbation electromagnetic field significantly improve the preciseness of inversion process using tabu search stochastic method.

6. Conclusion

Enhanced technique for three-dimensional diagnosis of partially conductive cracks was presented in the paper. A special eddy current probe driving uniformly distributed eddy currents was used for the inspection of a plate specimen. A detection system of the probe was designed in such a way that all three spatial components of the perturbation electromagnetic field were acquired. The tabu search stochastic method was employed for the reconstruction of partially conductive cracks profile from eddy current response signals gained during the C-scan of the probe. Two crack models were proposed: a crack with cuboid shape and the other one with more complex shape. The length, depth, width and conductivity of the crack were considered unknown in the inversion process. The conductivity of the crack was uniform. The presented results proved that the proposed approach allows quite precisely reconstructing three-dimensional profile of a crack together with its partial conductivity from ECT response signals even with added noise.

Further work of the authors will concern more realistic shapes of cracks and validation with measured data from natural cracks (SCC).

Acknowledgement

This work was supported by the Slovak Research and Development Agency under the contracts No. APVV-0349-10 and APVV-0194-07.

This work was co-funded by a Slovakia-Romania joint grant by the Slovak Research and Development Agency under the contract No. SK-RO-0011-12 and the ANCS under the Grant No. 654/2013.

References

[1] JANOUSEK, L., MAREK, T., GOMBARSKA, D.: Eddy Current Non-destructive Evaluation of Conductive Materials, *Communications - Scientific Letters of the University of Zilina*, No. 1, pp. 29-33, 2006.

[2] YUSA, N., HUANG, H., MIYA, K.: Numerical Evaluation of the Ill-posedness of Eddy Current Problems to Size Real Cracks, *NDT&E International*, vol. 40, pp. 185-191, 2007.

[2] JANOUSEK, L., SMETANA, M.: Uncertainty in Depth Evaluation of Partially Conductive Cracks from Eddy Current Testing Signals, *Communications - Scientific Letters of the University of Zilina*, vol. 13, pp. 55-60, 2011.

[4] RUBINACCI, G., TAMBURINO, A., VENTRE, S.: Fast Numerical Techniques for Electromagnetic Nondestructive Evaluation, *Nondestructive Testing and Evaluation*, vol. 24, pp. 165-194, 2009.

[5] REBICAN, M., CHEN, Z., YUSA, N., JANOUSEK, L., MIYA, K.: Shape Reconstruction of Multiple Cracks from ECT Signals by Means of a Stochastic Method, IEEE Transactions on Magnetics, vol. 42, pp. 1079-1082, 2006.

[6] YUSA, N., MIYA, K.: Discussion on the Equivalent Conductivity and Resistance of Stress Corrosion Cracks in Eddy Current Simulations, *NDT&E International*, vol. 42, pp. 9-15, 2009.

[7] CHEN, Z., REBICAN, M., YUSA, N., MIYA, K.: Fast Simulation of ECT Signal Due to a Conductive Crack of Arbitrary width, *IEEE Transactions on Magnetics*, vol. 42, pp. 683-686, 2006.

[8] JANOUSEK, L., SMETANA, M., CAPOVA, K.: Enhancing Information Level in Eddy-current Non-destructive Inspection, *Intern. J. of Applied Electromagnetics and Mechanics*, vol. 33, pp. 1149-1155, 2010.

[9] JANOUSEK, L., SMETANA, M., ALMAN, M.: Decreasing Uncertainty in Size Estimation of Stress Corrosion Cracking from Eddy-current Signals, *Studies in Applied Electromagnetics and Mechanics*, vol. 35, pp. 53-60, 2011.

[10] JANOUSEK, L., SMETANA, M., ALMAN, M.: Decline in Ambiguity of Partially Conductive Cracks' Depth Evaluation from Eddy Current Testing Signals, *Intern. J. of Applied Electromagnetics and Mechanics*, vol. 39, pp. 329-334, 2012.

[11] CHEN, Z., MIYA, K., KUROKAWA: Rapid Prediction of Eddy Current Testing Signals Using A - ϕ Method and Database, *NDT&E International*, vol. 32, pp. 29-36, 1999.

Matej Pacha - Jiri Stepanek *

IMPACT OF PARALLEL OPERATION OF AC TRACTION MOTORS ON LOCOMOTIVE PERFORMANCE

Presented paper deals with common problems of parallel operation of AC traction motors and presents some methods to investigate the basic impacts of the concept. A complex simulation model is introduced as well as results of simulations. Based on the results, a conclusion is made on locomotive performance impact.

Keywords: *Traction drive, AC traction motor, parallel operation, tilting, adhesion.*

1. Introduction

In many railway applications, AC induction traction motors are preferred as the best cost-effective solution for a modern locomotive. On the other hand, due to converter and AC motor prices, the investments are still higher than the DC traction drive application. Possible solution is to reduce number of traction converters and to use parallel connection of traction drives.

Unfortunately, parallel operation of AC induction machines introduces some problems with a vector control implementation and anti-wheel slip control. In addition, impact of bogies and locomotive frame tilting cannot be neglected. Finally, adhesion phenomenon should be considered, which leads to a very complex problem. Manufacturers and customers should consider investments vs. maintenance needs based on the impact of the solution. Based on the previous simulations in [1] and theory published e.g. in [2], locomotive performance is affected and thus should be expressed. Detailed analysis of parallel operation of AC traction motors is introduced below. Static simulation model is introduced, considering tilting forces, adhesion model and traction motors model, all in one complex simulation.

2. Simulation model

Energy analysis of a train movement helps us to focus on reasonable train operation types for hybrid drive applications. The key parameter is a kinetic energy, being developed with each acceleration and lost when braking [3] and [4].

A. Tilting Model of a Locomotive

Tilting phenomenon is well known and it is well described in [2] and [3]. Manufacturers introduced many systems how to lower the impact of tilting, e.g. levers, pneumatic cylinders, etc. The worst and the most generic wheel set involves no such systems. For 4-axle locomotive, the setup is shown in Fig. 1. Forces F_1 to F_4 are forces on wheels produced by traction drives, F_{12} and F_{34} are forces on pivots. Gravitation force G is divided in two on pivots G_{p1} and G_{p2}. The reaction forces on axles are F_{n1} to F_{n4}. F_t is traction force on a coupler.

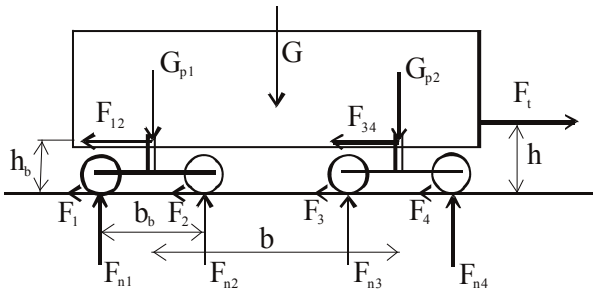

Fig. 1 Forces definition of a wheel set

Using static torque analysis, following equations (1) - (6) can be obtained.

$$F_{n1} = \frac{G_{p1}}{2} - (F_1 + F_2) \cdot \frac{h_p}{b_p} \tag{1}$$

* [1]Matej Pacha, [2]Jiri Stepanek
[1]Faculty of Electrical Engineering, University of Zilina, Slovakia
[2]CZ LOKO, a.s., Ceska Trebova, Czech Republic
E-mail: matej.pacha@fel.uniza.sk

$$F_{n2} = \frac{G_{p2}}{2} - (F_1 + F_2) \cdot \frac{h_p}{b_p} \quad (2)$$

$$F_{n3} = \frac{G_{p2}}{2} - (F_3 + F_4) \cdot \frac{h_p}{b_p} \quad (3)$$

$$F_{n4} = \frac{G_{p2}}{2} - (F_3 + F_4) \cdot \frac{h_p}{b_p} \quad (4)$$

$$G_{p1} = \frac{G}{2} - (F_1 + F_2 + F_3 + F_4) \cdot \frac{h_p - h}{b} \quad (5)$$

$$G_{p2} = \frac{G}{2} - (F_1 + F_2 + F_3 + F_4) \cdot \frac{h_p - h}{b} \quad (6)$$

The simulation model can be easily programmed in MATLAB Simulink, shown in Figs. 2 and 3.

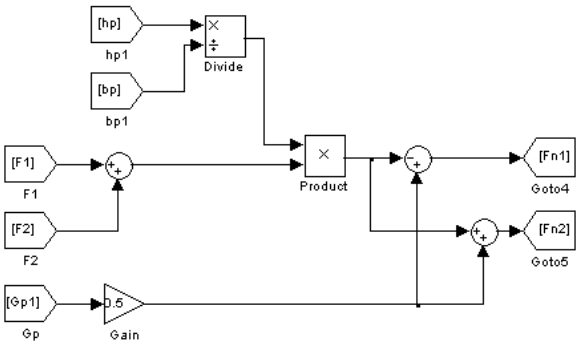

Fig. 2 Bogie (or two axle) tilting model in MATLAB Simulink (1) and (2) II.

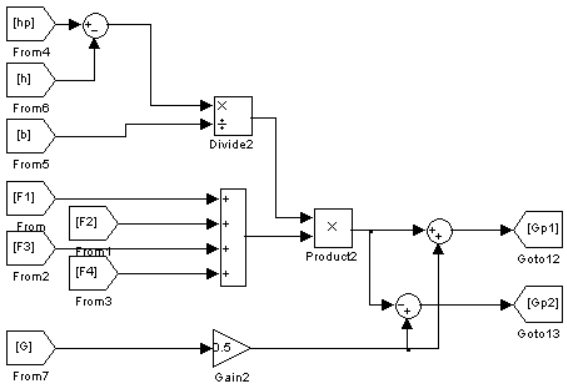

Fig. 3 Frame tilting model in MATLAB Simulink (5) and (6)

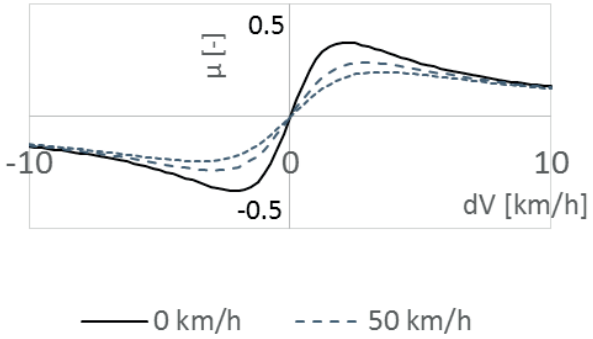

Fig. 4 Slip characteristics for different train speeds

B. *Model of Adhesion*

To simulate adhesion conditions of each axle, the slip model presented in [1] is introduced. In adhesive force transmission, some difference between a vehicle speed and a wheel speed is needed (a wheel creep [2]). There is a maximal adhesive force $F_{adh(max)}$ that can be transmitted to the rail. Passing this maximum causes the more force is put on the wheel acceleration and the tractive force transmitted decreases (a wheel slip). The slip characteristics [2] and [5] can be described by (7) where μ is relative adhesive force in N/kN, K is a slope coefficient, φ_a is maximal relative adhesive force and Δv is actual wheel slip.

$$\mu = \frac{2K\varphi_a^2 \Delta v}{\varphi_a^2 \Delta v^2 + K^2} \quad (7)$$

Impact of adhesion conditions on the shape is given by φ_a (8) [2], which is shown in Fig. 4,

$$\varphi_a = c_w \cdot \left(\frac{7.5}{V + 44} + 0.161 \right) \quad (8)$$

where c_w is a weather coefficient and V is a train speed in km/h. Low values of c_w have similar impact as high speeds.

Based on measurements in [4], there is a cleaning effect of the first axle of the locomotive. Assuming the first axle of the locomotive is the most lightened, the wheel creep is very intensive, thus power losses of the creeping wheels are higher. To conclude, the power losses cause the rail to be cleaner, thus, the second axle operates on better adhesion conditions. The situation can be transferred to the rest of the axles. Finally, a set of correction factors can be used to model this cleaning effect. For 4-axle locomotive, the cleaning effect coefficients are shown in Table 1. If an independent force control is applied, the overall adhesion utilization is actually higher than 1 [2] and [4]. In parallel operation/control of traction motors, the adhesion utilization is limited to the weakest axle in the wheel set.

The model is shown in Fig. 5. Adhesion limit is computed based on the train speed using (8) – block umax where g1 block is cleaning effect coefficient from Table 1. Finally, output axle force Fa1 is computed using (7) in block Slip.

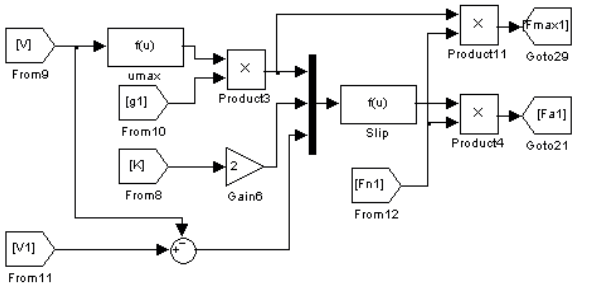

Fig. 5 Adhesion model in MATLAB - Simulink

CleaninG Effect Correction [1] Table 1

Axle	Correction	Error
1	1	-
2	1.232	±0.057
3	1.313	±0.192
4	1.512	±0.263

C. Model of Traction Motors

Dealing with modern locomotives, AC induction motors (ATM) are the most common traction motors used. As far as the simulation is static, a dynamic model is not necessary. Static model of ATM is needed because of parallel operation of multiple motors where the output voltage and frequency is common for all the motors in the group. ATMs in parallel operation are usually controlled by a vector control algorithm, either single motor, or weighted multiple motor algorithm. Advantages of weighted control can be found in [6]. Nevertheless, in a quasi-static state, the output is still the voltage and the frequency. While one ATM can operate on its optimum, another can be overloaded or unloaded.

The model (Fig. 6) can be described by following equations (9) – (13). Parameters and variables used are:

T_e ... *torque*
m ... *number of phases*
Ω_S ... *sync. angular speed*
s ... *rotor slip*
R_R ... *rotor resistance*
R_S ... *stator resistance*
X_R ... *rotor reactance*
X_S ... *stator reactance*
I_R ... *rotor current*
I_S ... *stator current*
U_i ... *back EMF voltage*
U_{1f} ...*input voltage*
X_μ ... *parallel reactance*
Z_{AB} ... *subcircuit impedance*
j ... *complex component*

Using concrete ATM parameters, input voltage and frequency, electromechanical characteristics can be obtained. These characteristics are suitable for our simulation. While the ATMs are supplied by constant voltage and frequency, the train speed can be forced – decreased from synchronous speed (thus zero torque developed) to the speed of maximal tractive force, thus observing the wheel creep area. The wheel slip occurrence is a dynamic state which should be computed using dynamic simulation.

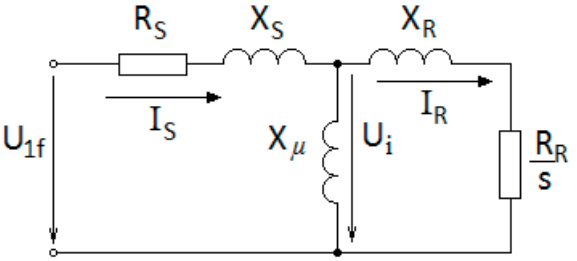

Fig. 6 AC Induction machine model scheme

$$T_e = \frac{m}{\Omega_s} \cdot \frac{R'_R}{s} \cdot I'^2_R \tag{9}$$

$$I'_R = \frac{|\vec{U}_i|}{\sqrt{\left(\frac{R'_R}{s}\right)^2 + X'^2_R}} \tag{10}$$

$$\vec{U}_i = \vec{U}_{1f} - \vec{I}_S \cdot (R_S + j \cdot X_S) \tag{11}$$

$$\vec{I}_S = \frac{\vec{U}_{1f}}{\vec{Z}_{AB} + R_S + j \cdot X_S} \tag{12}$$

$$\vec{Z}_{AB} = \frac{1}{\frac{-j}{X\mu} + \frac{1}{\frac{R'_R}{s} + j \cdot X'_R}} \tag{13}$$

Figure 7 shows the active part of electromechanical characteristics of ATM for diesel-electric locomotives of 450 kW rated power, operating at 200 rpm of synchronous speed. Motor parameters are marked as confidential. The characteristics are recalculated considering a gearbox ratio and a wheel diameter respectively.

D. Overall Simulation Model

Following the Introduction, the main purpose of this model is to make a complex simulation of a traction drive considering tilting forces, adhesion conditions and motor characteristics, to investigate impacts of parallel ATM operation on wheel's wear and traction characteristics, including adhesion.

Traction drive is modelled as steady state set of four ATMs in parallel operation (all motors supplied by the same voltage and frequency), but with different load and speed. Tilting forces are computed based on a static model of the wheel set of Bo'Bo' (4-axles in 2 bogies setup) locomotive. Adhesion model is made of four independent slip characteristics, one for each axle. There

is an algebraic loop preventing integrator using a small time constant to avoid an impact on the computation (Fig. 8).

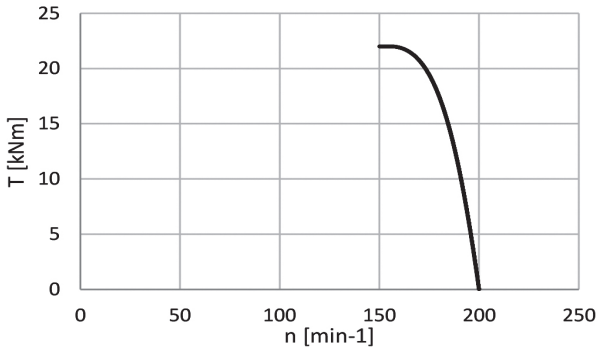

Fig. 7 Electromechanical characteristics of ATM (450 kW) @ 200 RPM of synchronous speed

The whole simulation is driven by a vehicle speed instead of time, thus no dynamic effects are simulated. Since two main effects – axle wear and traction characteristics impacts – are investigated, additional calculations are made. The first one is a power drop on the wheel-to-rail contact, pointing at the level of wheel wear (wheel slip percentage can be used as well) [7] and [8]. The more power the more wheel wear. The second one is locomotive adhesion utilization coefficient (14),

$$\varepsilon = \frac{MIN(F_{imax})}{\varphi_a \cdot n \cdot G} \tag{14}$$

where MIN(F_{imax}) is a minimum of maximal tractive forces on wheels, n is number of axles and G is gravity force of the locomotive. The model can be also extended or used in time-domain simulation with dynamic analysis as in [9].

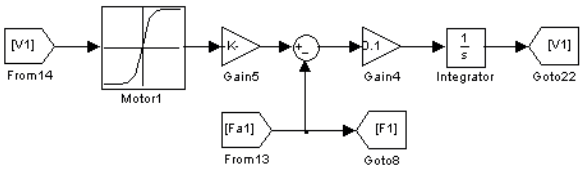

Fig. 8 Connection between ATM characteristics, traction force and axle speed

3. Simulation results

Simulation introduces 4-axle wheel-set configuration with considering the cleaning effect of the creeping wheels. All 4 traction motors are driven from single traction converter. Wheel set dimensions used in the simulations correspond to a common 4-axle diesel-electric locomotive (where h < h_b). Conclusion is made based on relative results.

As described in Table 1, the cleaning effect grows from the first to the last axle of the wheel set in direction of movement. Following charts show the simulation considering the coefficients from Table 1.

In Fig. 9, Axles No. 2 and No. 4 are in charge while axles No. 1 and No. 3 are lightened. The smaller difference between axles 2 and 4 is caused by the cleaning effect and resulting axle forces.

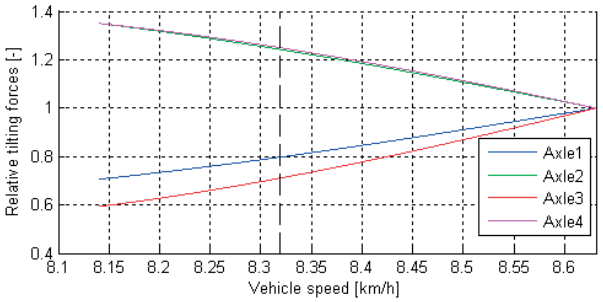

Fig. 9 Relative tilting forces including cleaning effect, using h < $_h$b

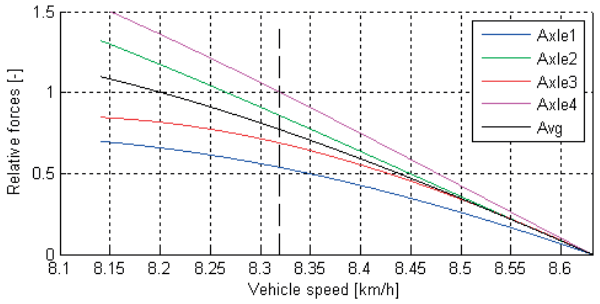

Fig. 10 Relative axle forces (1 = nominal value), excluding cleaning effect, using h <hb

Figure 10 shows the most loaded ATM is on 4th axle. Obviously, the reason is the cleaning effect of the first axles creeping. The overall tractive force is at 77.06% of nominal if none of the ATMs is overloaded. This means, the locomotive performance is lower than expected. In case of the currents are not measured separately for each ATM, overloading of ATMs can be caused by setting the locomotive output to the "rated" force (theoretically computed).

4. Conclusion

The article introduces a complex static simulation model of 4-axle locomotive traction drive in speed domain. The model connects several aspects of AC traction drive simulation in parallel operation.

The simulation model is based on static tilting model of 4-axle diesel-electric locomotive, which can be used for electric locomotives as well. Nevertheless, the AC traction drive with

parallel operation is much more typical solution for diesel-electric concepts. The model considers individual axle forces and introduces independent adhesion models, including the cleaning effect of creeping wheels.

AC traction drive is modelled as a static characteristic of induction traction motor, which fits the static simulation needs.

Tilting forces create different adhesion conditions for each axle. The first axle in the movement direction is always lightened, while second, etc. is more loaded. If an individual traction drive control is used, overall traction force can be even higher than with a common traction drive [4]. In a parallel traction drive operation, natural electro-mechanical characteristics of the drive should be taken into account. In case of induction traction motors operating at common (constant) voltage and frequency, one of the motors operates at higher load (usually up to nominal) while the other motors operate at lower load. The overall tractive force is then lower, about 77% of the ideal value. This is even lower than the theoretical value of the DC traction drive 83% [4].

The main concern is connected with different performance of the motors commonly driven. If none of the motors is overloaded, the last motor (in the movement direction) operates on its rated current and the other motors' load is reduced due to higher wheel creep. Locomotive performance data should be reduced if traction motors operate in parallel. To keep the locomotive performance higher, the traction drive configuration should involve at least two groups of parallel driven traction motors with independent wheel creep control [10].

Acknowledgment

Authors would like to thank CZ LOKO Company for input data and consultations. The article has been supported by project VEGA 1/0794/14.

References

[1] PACHA, M., STEPANEK, J.: *Modelling of Parallel Operation of AC Traction Motors Considering Adhesion and Tilting*. Proc. of Intern. Conference Elektro, 2014 , pp. 352-357, May 2014

[2] DANZER, J.: *Electric Traction / Elektricka trakce (in Czech),* ZCU Plzen, vol. 7, November 2008.

[3] IWNICKI, S.: *Handbook of Railway Vehicle Dynamics* CRC Press, Taylor & Francis Group, Boca Raton, 2006.

[4] DANZER, J.: Wheelslip on bogie with AC Traction Motors / Skluz podvozku s asynchronnimi trakcnimi motory (in Czech), *Elektrotechnicky obzor* 80, 1991, pp. 1-12.

[5] POLACH, O.: Contact of Wheel and Rail in Computer Simulation of Vehicle Dynamics and Axle Drive Dynamics, *Communications - Scientific Letters of the University of Zilina,* vol. 1, 2001, pp. 11-17, ISSN 1335-4205.

[6] SKUDENLY, H.-CH., WEINHARDT, M.: *An Investigation of the Dynamic Response of Two Induction Motors in a Locomotive Truck Fed by a Common Inverter*, Industry Applications, IEEE Transactions, vol. IA-20, No.1, pp.173-179, Jan. 1984.

[7] BOSSO, N., ZAMPIERI, N.: *Experimental and Numerical Simulation of Wheel-Rail Adhesion and Wear Using a Scaled Roller Rig and a Real-Time Contact Code*, Hindawi Publishing Corporation [online], 2014, Article ID 385018, p. 14.

[8] KUMAR, S., ALZOUBI, M. F., ALLSAYYED, N. A.: *Wheel/rail Adhesion Wear Investigation Using a Quarter Scale Laboratory Testing Facility*, Railroad Conference, 1996, Proc. of the 1996 ASME/IEEE Joint, pp. 247-254, Apr-May 1996.

[9] ONDROVA, Z.: Dynamic Analysis of a 4-axles Railway Vehicle Model, *Communications - Scientific Letters of the University of Zilina*, vol. 2, 2009, pp. 65-69, ISSN 1335-4205.

[10] YAMASHITA, M., SOEDA, T.: *A Novel Slip Control Method Considering Axle-weight Transfer for Electric Locomotive*, Vehicle Power and Propulsion Conference (VPPC), 2010 IEEE , pp.1,6, 1-3 Sept. 2010.

Volodymyr Yaskiv - Alexander Abramovitz - Keyue Smedley - Anna Yaskiv *

MAGAMP REGULATED ISOLATED AC-DC CONVERTER WITH HIGH POWER FACTOR

This paper evaluates the performance of magnetic amplifier regulator in isolated off-line power supplies with power factor correction stage. A research of operation modes of power converter, based on high frequency magnetic amplifiers, with power factor correction was conducted for the first time. Simplified controller circuitry is suggested and analyzed. Experimental results are reported.

Keywords: *Magnetic device, power supply, power factor correction, soft switching, efficiency.*

1. Introduction

Advances in low-loss magnetic materials continue to maintain an interest in a well founded power control technology - the magnetic amplifier (MagAmp) [1] and [2]. Numerous topologies for MagAmp regulator schemes were proposed in literature [3] - [5]. The main advantages of MagAmp are its simplicity and ruggedness. MagAmp can be controlled by relatively simple control circuitry and can provide good output regulation under wide load variations [6] and has good dynamic characteristics [7] - [10]. Studies showed that at 10 kW and 10 kHz the IGBT converter losses are about 100 W, whereas with a Magamp design the losses are as low as 25 W. At 80 kHz the IGBT losses are about 355 W while with a Magamp design they are only about 25 W [11]. Better efficiency also implies weight reduction of cooling system. Moreover, contrast with the abrupt switching of the semiconductor switch, MagAmp has a smooth switching trajectory dictated by the hysteresis loop. Consequently, MagAmp has soft switching properties and, hence, generates lower electro-magnetic interference. In addition, MagAmp switch requires neither snubbers [12] nor over-voltage, nor short circuit protection circuitry. On top of that, MagAmp regulator can facilitate zero voltage soft switching of the active devices of the driving power stage [13]. Recently, front end multiple output LLC resonant converter with MagAmp post regulation was demonstrated operating at 110 kHz [14] and [15]. However, MagAmp is known to operate at even higher switching frequencies up to several hundred kHz [16] and [17]. Therefore, application of high-frequency MagAmps is a viable solution for implementing converters with multiple isolated high-current regulated outputs.

Recent regulations regarding the line current quality have made Power Factor Correctors (PFC) a standard utility interface stage for most electronic equipment that uses ac-line power. However, the high output voltage of the PFC corrected rectifiers requires down-stream dc-dc converter having larger step down ratio. This also increases the voltage stress on the semiconductor switches. Clearly, operation at higher voltage has an effect on the overall efficiency of the off line ac-dc converter.

This paper describes an isolated, MagAmp regulated ac-dc converter with good dynamic characteristics and high power factor within a wide range of the load current. A simple MagAmp control circuit is proposed. The objective of this paper is to reevaluate the performance of MagAmp regulated power stage in off-line (grid connected) applications. Experimental results are reported.

2. General concept

In order to achieve low-harmonic line current, isolation capability and dc output regulation a three stage approach is considered as shown in Fig. 1 [18]. One Cycle Controlled (OCC) Power Factor Pre-regulator is applied to attain high power factor utility interface, transformer isolated self oscillating half-bridge power oscillator implements an isolated high frequency link, whereas MagAmp post-regulator is employed to provide output voltage regulation.

* [1]Volodymyr Yaskiv, [2]Alexander Abramovitz, [3]Keyue Smedley, [1]Anna Yaskiv
[1]Department of Testing Instruments and Radio Computer Systems, Ternopil Ivan Puluj National Technical University, Ternopil, Ukraine
[2]Department of Electrical and Electronics Engineering, Sami Shamoon College of Engineering, Beer-Sheva, Israel
[3]Department of Electrical Engineering and Computer Science, University of California, Irvine, USA
E- mail: yaskiv@yahoo.com

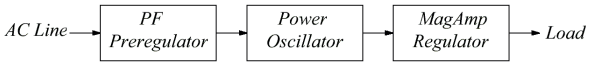

Fig. 1 Block diagram of the proposed ac-dc converter

The purpose of the PF pre-regulator is twofold [18]. First, is to provide a near sinusoidal line current and reduce line harmonics and secondly, to provide the pre-stabilized dc voltage for the Power Oscillator. The PF pre-regulator output voltage is supported by large reservoir capacitance, designed to provide a sufficient holding time in case of utility sag. The Power Oscillator stage is fed by the output voltage of the PF pre-regulator and drives the step-down isolating transformer with a high voltage, high frequency square wave excitation signal. High frequency operation allows miniaturization of the power transformer size, weight and cost. Due to the self-oscillating nature of the circuit neither bootstrap drivers nor auxiliary power supply are needed. The MagAmp post-regulator is implemented at the power transformer secondary and provides regulation of the output voltage. Since the MagAmp control circuits are implemented entirely on the secondary side, there is no need for isolated feedback path, which further simplifies the circuitry [18].

2.1 The PF pre-regulator stage

The proposed high power factor pre-regulator uses a boost power stage and OCC method to regulate the output voltage and shape the line current [18] and [19]. The diagram of the PF Pre-regulator with a boost power stage and OCC controller is shown in Fig. 2. Here, the downstream power stages are represented by the equivalent load resistor R_L. Theoretically, under the OCC control the boost converter exhibits resistive input characteristic. As a result, the line current is in phase with the input voltage and harmonic free. Therefore, the power factor of the OCC controlled rectifier equals unity. By keeping the PF pre-regulator output voltage V_O at a constant level, the voltage feedback loop establishes the power balance so that the average ac power drawn from the line equals the dc power demands of the load. To attain this control objective, the error amplifier signal V_m is modulated to adjust the average power flow. The advantages of the OCC control method are the simple and low cost PF Pre-regulator circuitry as well as good and reliable performance [18]. Detailed description of the controller and design procedure of OCC high PF rectifier can be found in [20].

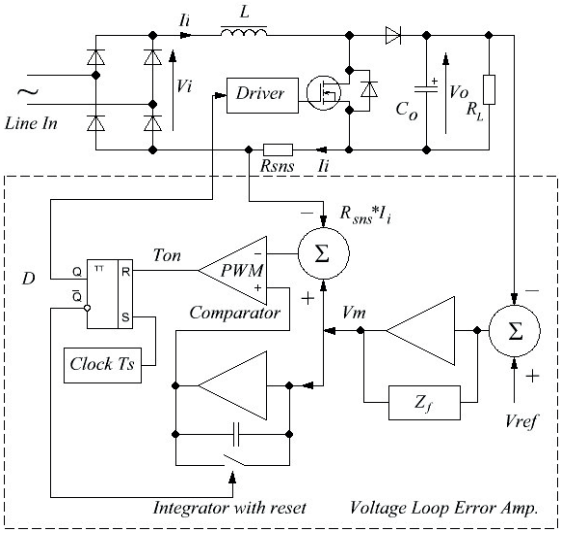

Fig. 2 Block diagram of the OCC controlled PF pre-regulator Boost rectifier

2.2 The power oscillator stage

The Power Oscillator, shown in Fig. 3, is a modified self-oscillating half-bridge circuit derived from [4]. The circuit is comprised of power transistors Q1 and Q2, free-wheeling diodes D9 and D10, splitting capacitors C5 and C6, which are also used as the hold-up capacitors, and the power transformer T2. The drive signal is obtained by the feedback transformer T3 placed in parallel to the oscillator output. The drive transformer T1 has two split anti-phase drive windings N1 for each power transistor and a proportional base drive winding N2. The advantage of the half-bridge stage is that it applies only half of the supply voltage to the transformer primary and so provides additional voltage step down. This allows lowering the transformer turn ratio as well as transformer's primary magnetizing inductance.

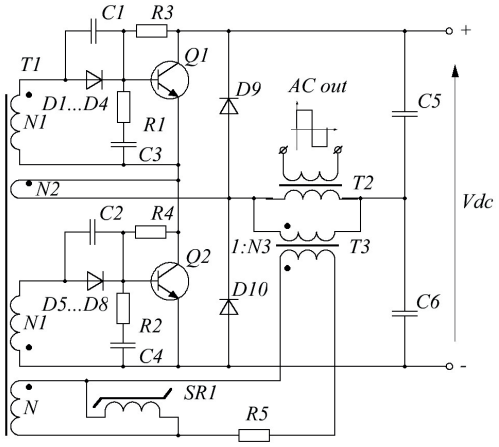

Fig. 3 Schematic diagram of the Power Oscillator

The oscillator cycle is determined by the time required for the saturable reactor, SR1, to slew from positive to negative saturation and then back again to positive saturation and is a function of SR1 parameters, that is, number of turns, effective core cross section area and maximum flux density of the saturable reactor SR1, N_{SR}, A, B_{max}, and applied voltage. The voltage across SR1 equals the voltage across five conducting diodes $5V_{on}$ reflected towards the saturable reactor via the drive transformer with turns ratio of $\frac{N}{N_1}$. Therefore, the approximate expression for the oscillator frequency can be derived as:

$$f_s = \frac{5NV_{on}}{4N_1N_{SR}AB_{\max}} \quad (1)$$

The advantage of the proposed scheme is that the saturable reactor SR1 keeps the positive and negative half-cycles of the oscillator's output voltage waveform in perfect balance. This prevents saturating the power transformer. Thus, no dc blocking capacitor is needed at the transformer's primary.

2.3 A quick review of MagAmp post-regulator and control circuit

The MagAmp post-regulator is implemented as a push-pull full-wave circuit [5] at the secondary of the power transformer, T, as shown in Fig. 4. The post-regulator is comprised of a pair of the MagAmp switches SR1 and SR2; power rectifier diodes D1-D2; a free-wheeling diode DFW and a second order LC output filter.

As compared to a single ended MagAmp circuit, the push-pull MagAmp configuration has the advantages of the symmetrical operation and doubled dc output voltage.

Here, both MagAmp switches operate with current reset. The reset current I_R is provided by the controller as discussed below. The steering diodes DR1 and DR2 naturally steer the reset current I_R towards the device to be reset. Each MagAmp is wound using two parallel strands of litz wire on the same core. The parallel connection of the MagAmp windings lowers the equivalent resistance of the conduction path and accordingly, lowers the power losses of the power stage under high load current.

There are different approaches to control circuit design [21]. The proposed MagAmp control circuit is shown in Fig. 5. This circuit is a simplification of that used in [9]. The circuit is fed directly by the output voltage, Vout. Resistor divider R1, R2 determines the feedback ratio, breakdown diode D8 provides the voltage reference, whereas the PNP transistor Q3 realizes a transconduction error amplifier, Gm. The compensation network is constituted of R_{e1}, R_{e2}, C_e. The collector current of Q3 is applied to MagAmp switches as the reset current I_R.

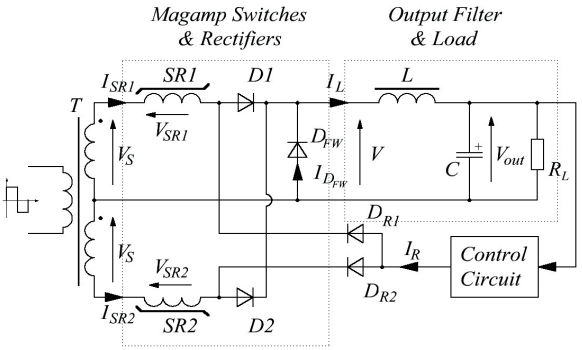

Fig. 4 Push-pull MagAmp regulator circuit

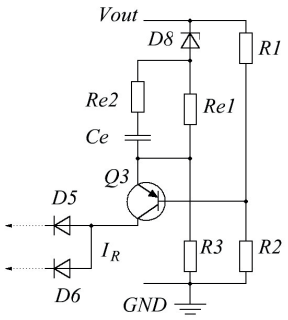

Fig. 5 MagAmp control circuit

Under closed loop action, assuming also that the voltage drop across Re1 is negligible, the converter's steady state output voltage is established according to:

$$V_{out} = \left(V_z + V_{EBon}\right) \cdot \left(1 + \frac{R_2}{R_1}\right), \quad (2)$$

Vz is the breakdown voltage of D8 and V_{EBon} is the ON voltage of Q3 emitter – base junction.

2.4 Derivation of approximate MagAmp large signal relationships

In the blocking state the MagAmp has to sustain the pulse voltage V_p with only a negligible current *i* flowing through the device. Thus, according to the Faraday's law:

$$V_p = \frac{d\lambda}{dt} = \left(\frac{d\lambda}{di}\right)\frac{di}{dt}, \quad (3)$$

where λ is the flux linkage.

Due to the hysteresis of the core material, $\left(\frac{d\lambda}{di}\right)$ is a non linear function. However, modern materials recommended for implementation of MagAmps have a relatively sharp hysteresis loop. The sharpness property allows defining the *average*

permeability $\mu = \mu_0 \mu_r$ of the MagAmp core along the steep segment of the B-H curve. This linearization of the B-H curve is useful to obtain simple approximate results to facilitate easy design of the converter. Relying on the assumption above, a simple approximate model of the MagAmp regulator is derived introducing the *average* inductance of the MagAmp defined as:

$$L_{SR} = \frac{\overline{d\lambda}}{di} = N_{ma}^2 \frac{\mu A_e}{l_e} \tag{4}$$

where A_e is the MagAmp core effective cross area; l_e is the MagAmp core effective length; N_{ma} is the number of turns of the MagAmp.

Rearranging (3) and applying (4), the MagAmp blocking time, Δt can be expressed as:

$$\Delta t = L_{SR} \frac{\Delta I}{V_p} = L_{SR} \frac{I_{\max} + I_R}{V_p} \tag{5}$$

where:

$$\Delta I = I_{\max} - (-I_R) \tag{6}$$

is the current swing from the reset operating point R established by the (negative) reset current ($-I_R$) to the maximum (positive) current $I_{\max}$ on the verge of MagAmp saturation, approximated by:

$$I_{\max} = \frac{H_{\max} l_e}{N_{ma}} = \frac{B_{\max} l_e}{\mu N_{ma}} \tag{7}$$

Here, $B_{\max}$ is the maximum flux density of the MagAmp core material.

As shown in Fig. 5, MagAmp switches operate in a complementary fashion either in the positive or negative half cycle. Once saturated at instance Δt, the MagAmp remains in saturation till the rest of the half-cycle $\frac{1}{2}T_s$. Thus, the MagAmp allows the voltage to appear at the input terminals of the output filter for the duration of:

$$T_{on} = \frac{1}{2}T_s - \Delta t = \frac{1}{2}T_s - \frac{L_{SR}}{V_p} I_{\max} - \frac{L_{SR}}{V_p} I_R \tag{8}$$

Hence, the average voltage applied to the input terminals of the output filter by the push-pull MagAmp stage is:

$$V_{av} = \frac{2}{T_s}(V_p T_{on}) = V_p - 2 f_s L_{SR} I_{\max} - 2 f_s L_{SR} I_R = \\ = V_{av\max} - 2 f_s L_{SR} I_R \tag{9}$$

where $f_s = \frac{1}{T_s}$ is the switching frequency, and $V_{av\max}$ is the maximum average voltage that could be attained with zero reset current:

$$V_{av\max} = V_p - f_s L_{SR} I_{\max} = V_p - 2 f_s N_{ma} A_e B_{\max} \tag{10}$$

Equations (9), (10) constitute a simple approximate average large signal behavioral model of the MagAmp switch. More accurate model of MagAmp was derived in [10] and [11], however, the relative complexity of those makes it inconvenient to be used by a circuit designer.

2.5 Control loop small signal relationships

The MagAmp controller is implemented entirely on the secondary side of the power transformer and employs a single voltage loop. Average model of MagAmp control loop after [9] is shown in Fig. 6. Here, $H_{ma}(s)$ is the average MagAmp small signal transfer function, $H_d(S)$ is the MagAmp delay transfer function and $H_f(S)$ is the output filter transfer function. The voltage reference V_{ref}, the feedback β, the summer and the error amplifier transfer function $G_m(S)$, are implemented by the controller circuitry. The resulting MagAmp post-regulator loop-gain, see Fig. 8, is obtained as:

$$G_L(S) = \beta G_m(S) H_{ma}(S) H_d(S) H_f(S) = \\ = \left(\frac{R_1}{R_1 + R_2}\right)\left(-\frac{1}{R_E}\right)\left(\frac{1 + \frac{S}{\omega_z}}{1 + \frac{S}{\omega_p}}\right)(-2 f_s L_{SR})\left(\frac{1 - \frac{S}{4 f_s}}{1 + \frac{S}{4 f_s}}\right) \times \\ \times \frac{1}{1 + \frac{1}{Q}\left(\frac{S}{\omega_n}\right) + \left(\frac{S}{\omega_n}\right)^2} \tag{11}$$

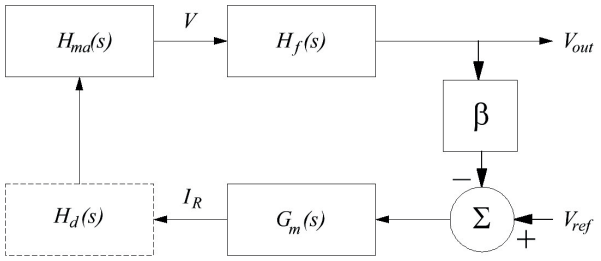

Fig. 6 Average model of MagAmp control loop

3. Experimental results

The experimental converter circuit was built and tested. The converter was designed to operate from the universal line 90-240 Vac and provide 24 Vdc output at 10 A load current. The switching frequency of the power factor pre-regulator was 85 kHz whereas the isolation stage half-bridge was operated at 50 kHz. The converter exhibited stable and reliable operation within the entire load and line range. The experimental characteristics of the proposed converter were obtained for 230 Vac, 115 Vac, 90 Vac line, whereas the load power was varied in the 10%-100% range.

3.1 Experimental steady state characteristics

Steady state characteristics of the experimental converter are presented in Figs. 7 and 8.

Fig. 7 Power Factor as function of line voltage and output power

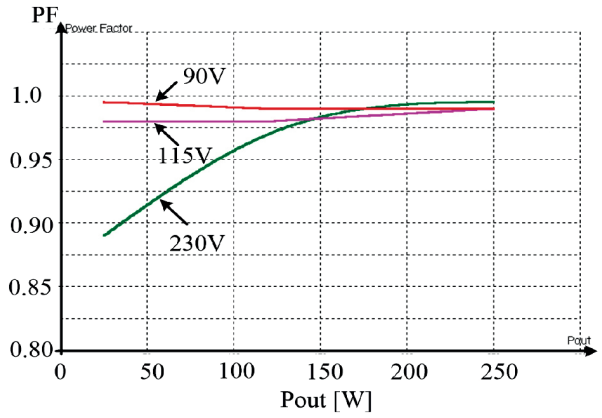

Fig. 8 Overall efficiency of the experimental converter

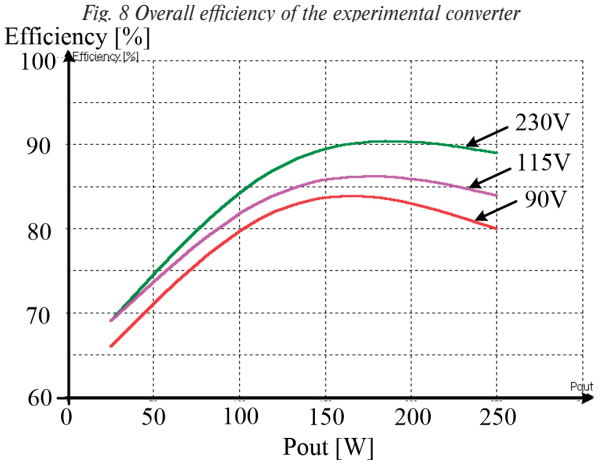

as function of output power and line voltage.

3.2 Experimental waveforms

Experimental waveforms of MagAmp regulator and line voltage and current are presented in Figs. 9 and 10 respectively.

(a)

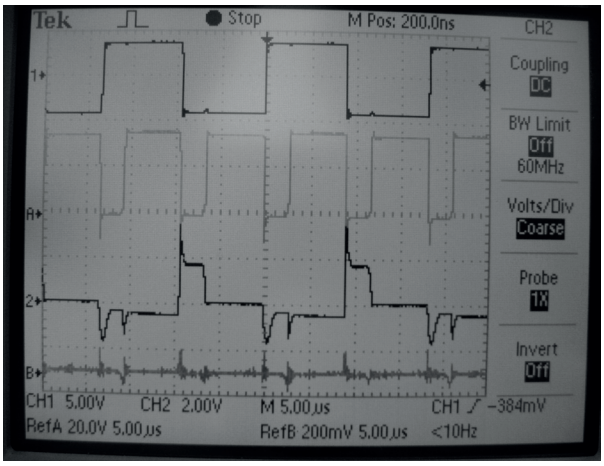

(b)

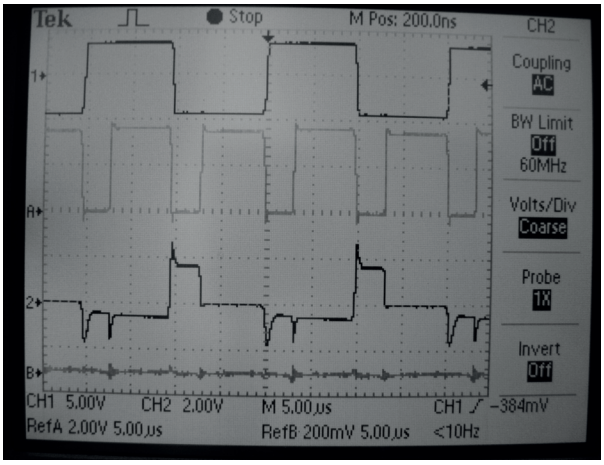

(c)

Fig. 9 Experimental waveforms of MagAmp regulator under different loading conditions: Pout=240 W(a); Pout=120 W (b); Pout=25 W (c). Ch1: Power transformer secondary voltage (50 V/Div); Ch2: Magamp voltage (50 V/Div); Ref. A: Input voltage of output filter (20 V/Div); Ref. B: Output voltage ripples (200 mV/Div). Horizontal scale 5 uSec.

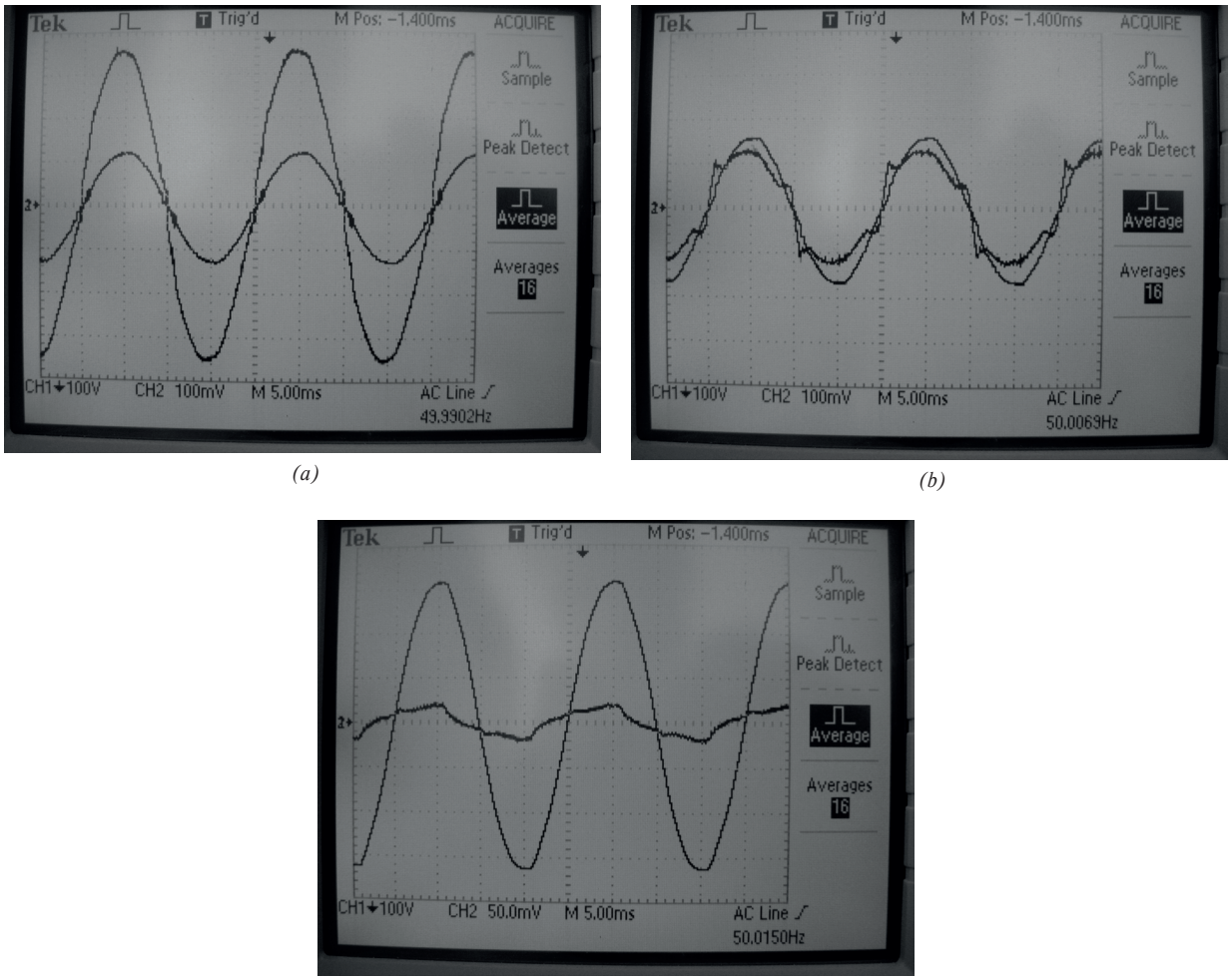

(a) *(b)* *(c)*

Fig. 10 Experimental waveforms of line voltage and current: (a) Pout=240 W, V_{line}=90 Vrms, Ch2: Line current (1.33 Amp/Div); (b) Pout=120 W, V_{line}=115 Vrms, Ch2: Line current (1.33 Amp/Div); (c) Pout=25 W, V_{line}=90 Vrms, Ch2: Line current (0.67 Amp/Div). Ch1: Line voltage (100 V/Div); Horizontal scale 5 mSec.

4. Conclusion

This paper reevaluated the performance of MagAmp regulated, isolated, ac-dc converter with high power factor pre-regulator. A simple MagAmp control circuit was proposed.

The experimental converter was designed to provide 24 Vdc at 10 A output and provided adequate characteristics within a wide range of the load current. Under full load a 0.1 V output ripple in the steady state was observed. The overall efficiency of the converter reached peak value of 91% at medium power level. The experimental data suggests that the PF pre-regulator stage conduction losses have a severe impact on the converter efficiency, which deteriorates as the line voltage is lowered. Particularly under light load conditions the efficiency drops to the minimum of 65% as the controller power and switching losses become comparable to the load power.

As can be seen from the experimental waveforms, MagAmp created favorable switching conditions to the power oscillator transistors so that no overshoot or ringing was observed in the power oscillator waveform. The regulator circuits are implemented entirely on the low voltage secondary side so that no isolated feedback circuits are required. Simplicity, ruggedness and reliability as well as soft switching make MagAmp a viable solution for implementing converters with multiple isolated high-current regulated outputs.

References

[1] *Mag Amp Cores and Materials,* Technical Bulletin, BULLETIN SR-4, Magnetics Inc., available on line at: http://www.mag-inc.com/design/technical-documents.

[2] MAMANO, B.: *Magnetic Amplifier Control, for Simple, Low-cost, Secondary Regulation*, Unitrode corp. slup129.

[3] JAMERSON, C., CHEN, D. Y.: Magamp Post Regulators for Symmetrical Topologies with Emphasis on Half-bridge Configuration, *IEEE Transactions on Power Electronics*, 1993, 8(1), pp. 26-29.

[4] WEN, C. C., CHEN, C. L., CHEN, W., JIANG, J.: *Magamp Post Regulation for Flyback Converter,* Proc. of IEEE Power Electron. Spec. Conf., 2001, pp. 333-338.

[5] CHEN, W., HAN, J., WEN, C. C.: *Bi-directional Resetting Scheme of the Magamp Post-regulator*, Proc. of IEEE Appl. Power Electron. Conf., 2002, pp. 838-842.

[6] LEE, J., CHEN, D. Y., JAMERSON, *C.: Magamp Post Regulators-practical Design Considerations to Allow Operation under Extreme Loading Conditions*, Proc. of IEEE APEC, 1988, pp. 368-376.

[7] LEE, J., CHEN, D. Y., WU, Y. P., JAMERSON, C.: Modeling of Control Loop behavior of Magamp Post Regulators, *IEEE Trans. Power Electron*., vol. 5, pp. 476-483, Oct. 1990.

[8] YANG, C. H., CHEN, D. Y., JAMERSON, C., WU, Y. P.: Stabilizing Magamp Control Loop by Using an Inner-loop Compensation, *IEEE Trans. Power Electron.*, vol. 6, pp. 419-429, July 1991.

[9] JOVANOVIC, M. M., HUBER, L.: Small-signal Modeling of Magamp PWM Switch", *IEEE Trans. on Power Electr.,* vol. 14, No. 5, Sep. 1999, pp. 882-889.

[10] CHEN, Y.-T., CHEN, D. Y.: Small-Signal Modeling of Magnetic Amplifier Post Regulators with Current-Mode Control, *IEEE Trans on Ind. Electr.,* vol. 47, No. 4, Aug. 2000, pp. 821-831.

[11] AUSTRIN, L., FIGUEROA-KARLSTROM, E., ENGDAHL, G.: *Evaluation of Switching Losses in Magnetic Amplifiers as an Alternative to IGBT Switching Technologies,* 4th IET Intern. Conference on Power Electronics, Machines and Drives (PEMD 2008) York, April 2008, pp. 250-254.

[12] DUDRIK, J., BODOR, M., TRIP, N. D.: Operation Analysis of Soft Switching PWM DC-DC Converter with Secondary Snubber, *Communications - Scientific Letters of the University of Zilina*, No. 3, 2013.

[13] WATSON, R., LEE, F. C.: Analysis, Design, and Experimental Results of a 1kW ZVS FB PWM Converter Employing Magamp Secondary-side Control, *IEEE Transactions on Industrial Electronics*, 1998, 45(5), pp 806-814.

[14] HANG, L. J., GU, Y. L., LU, Z. Y., QIAN, Z. M., XU, D. H.: *Magamp Post Regulation for LLC Series Resonant Converter with Multi-output*, Proc. of IEEE IECON, Nov. 2005, pp. 628-632.

[15] HANG, L., WANG, S., GU, Y., YAO, W., LU, Z.: High Cross Regulation Multi-output LLC Series Resonant Converter with Magamp Post-regulator, *IEEE Trans. Ind. Electr.* vol. 58, No. 9, pp. 3905-3913, 2011.

[16] FISHER, R., NGO, K., KUO, M.: *A 500 kHz, 250 W DC-DC Converter with Multiple Outputs Controlled by Phase-Shifted PWM and Magnetic Amplifiers*, Proc. of High Frequency Power Conversion Conference, pp. 100-110, May 1988.

[17] HIRAMATSU R., MULLET, C. E.: *Using Saturable Reactor Control in 500 kHz Converter Design,* Proc. of the Tenth National Solid-State Power Conversion Conference, Powercon 10 record, pp. F-2.1-F-2.10.

[18] YASKIV, V.; ABRAMOVITZ, A.; SMEDLEY, K.: *MagAmp Power Converters with Low Level EMI,* Proc. of Experience on Designing and Application of CAD Systems in Microelectronics (CADSM), 2013 12th Intern. Conference on the 19-23 February, 2013, pp. 388-395.

[19] LAI, Z., SMEDLEY, K.: A Family of Continuous-Conduction-Mode Power-Factor-Correction Controllers Based on the General Pulse-Width Modulator, *IEEE Trans. on Power Electronics*, vol. 13, pp. 501-510, 1998.

[20] BROWN, R., SOLDANO, M.: *One Cycle Control IC Simplifies PFC Designs,* Proc. of APEC '05 Conf., Austin, TX, 6-10 March, 2005 vol. 2, pp. 825-829.

[21] DRGONA, P., PRIKOPOVA, A., FRIVALDSKY, M., PRIECINSKY, M.: Simulation Based Method for Design and Application of Digital Control System, *Communications - Scientific Letters of the University of Zilina*, vol. 2A, 2011.

Oleg V. Chernoyarov - Martin Vaculik - Armen Shirikyan - Alexandra V. Salnikova *

STATISTICAL ANALYSIS OF FAST FLUCTUATING RANDOM SIGNALS WITH ARBITRARY-FUNCTION ENVELOPE AND UNKNOWN PARAMETERS

We find a new expression for the solving statistics of fast fluctuating Gaussian pulses with arbitrary-function envelope, based on which we can receive much simpler processing algorithms of random signals with unknown parameters in comparison with available analogues. For example, the synthesis and analysis of maximum likelihood detector and measurer of a high-frequency random pulse with unknown time parameter is carried out. The asymptotically exact expressions for detection and estimation characteristics including anomalous effects are presented. By methods of statistical computer modeling the adequacy of the considered analytical approach of the statistical analysis of random pulsed signals is corroborated, the working capacity of offered detector and measurer is established, and applicability borders of asymptotically exact formulas for their characteristics are also defined.

Keywords: *Fast fluctuating random signal, maximum likelihood method, solving statistics, signal detection and estimation, local Markov approximation method, statistical modeling.*

1. Introduction

In a number of practical appendices of statistical radio engineering and radio physics it is necessary to solve a processing problem of random pulsed signals with unknown parameters against hindrances. In [1 - 5, etc.] the detection and measurement tasks of random Gaussian pulses with rectangular or close to the rectangular envelope are considered in the conditions of various parametrical prior uncertainty. However, a received signal waveform can essentially differ from the rectangular often enough. Thereupon, it is of interest to find the optimal receiver structure for random Gaussian pulse with arbitrary-function envelope.

2. The output signal of the maximum likelihood receiver of a random Gaussian pulse

As a random Gaussian pulse with arbitrary-function envelope, we will understand a multiplicative combination taking a form of:

$$s(t)=\xi(t)f[\gamma(t-\lambda_0)]I\left(\frac{t-\lambda_0}{\tau_0}\right),$$
$$I(x)=\begin{cases}1, & |x|\le 1/2\\ 0, & |x|>1/2.\end{cases} \qquad (1)$$

Here λ_0 is the appearance time, τ_0 is the duration of a pulse, $\xi(t)$ is the stationary Gaussian random process, $f(t)$ is the determined function (envelope), which is describing the pulse form and is normalized so that $\max f(t)=1$, and γ is a scaling multiplier. We will designate $a_0=\langle\xi(t)\rangle$ as mathematical expectation,

$B_\xi(t_2-t_1)=\langle[\xi(t_1)-\langle\xi(t_1)\rangle][\xi(t_2)-\langle\xi(t_2)\rangle]\rangle$ - as covariance function and

$G_\xi(\omega)=\int_{-\infty}^{\infty}B_\xi(t)\exp(-j\omega\tau)d\tau$ - as spectral density (SD) of the process $\xi(t)$.

Let us consider that fluctuations $\xi(t)$ are "fast", that is, the pulse duration τ_0 and the characteristic changing time Δt of the function $f(t)$ essentially exceed the correlation time of the process $\xi(t)$, so the following conditions are satisfied:

$$\tau_0 >> 2\pi/\Omega_0,\ \Delta t >> 2\pi/\Omega_0. \qquad (2)$$

Here Ω_0 - bandwidth of the process $\xi(t)$. Hindrances and $n(t)$ registration errors will be approximated by Gaussian white noise with the one-sided SD N_0.

* [1]Oleg V. Chernoyarov, [2]Martin Vaculik, [3]Armen Shirikyan, [4]Alexandra V. Salnikova
[1]National Research University "Moscow Power Engineering Institute", Moscow, Russia
[2]Department of Telecommunications and Multimedia, University of Zilina, Slovakia
[3]University of Cergy-Pontoise, Cergy-Pontoise, France
[4]Voronezh State University of Architecture and Civil Engineering, Voronezh, Russia
E-mail: o_v_ch@mail.ru

For the signal (1) detection and measurement, we will use a maximum likelihood method [1, 6 and 7]. According to [6], the maximum likelihood receiver (MLR) should form the logarithm of the functional of likelihood ratio (FLR) $L(\vec{\vartheta})$ as function of current values $\vec{\vartheta}$ of set of unknown parameters $\vec{\vartheta}_0$ (let us accept for further that true value of parameter is designated with the subindex "0", and its current value – without the subindex). Any signal (1) parameters (appearance time, duration, mathematical expectation, etc) can be vector $\vec{\vartheta}_0$ components.

Let the realization $x(t) = s(t) + n(t)$ or $x(t) = n(t)$ be received to the MLR input. Then, in concordance with [1 and 4], the logarithm of FLR can be presented as

$$L(\vec{\vartheta}) = \frac{1}{N_0}\int_0^T\int_0^T x(t_1)x(t_2)Q(t_1,t_2)dt_1dt_2 + \int_0^T x(t)V(t)dt - \frac{1}{2}\int_0^T a_s(t)V(t)dt - \frac{1}{2}\int_0^1 d\chi\int_0^T \tilde{Q}(t,t,\chi)dt. \quad (3)$$

Here, $a_s(t) = \langle s(t)\rangle = a\,f[\gamma(t-\lambda)]I[(t-\lambda)/t]$,

$$V(t) = \frac{2}{N_0}\left[a_s(t) - \int_0^T a_s(t')Q(t,t')dt'\right], \quad (4)$$

$Q(t_1,t_2) = \tilde{Q}(t_1,t_2,1)$, and function $\tilde{Q}(t_1,t_2,\chi)$ satisfies the following integral equation:

$$\frac{N_0}{2}\tilde{Q}(t_1,t_2,\chi) + \chi\int_0^T \tilde{Q}(t_1,t_2,\chi)B_s(t,t_2)dt = B_s(t_1,t_2), \quad (5)$$

where

$$B_s(t_1,t_2) = \langle[s(t_1)-a_s(t_1)][s(t_2)-a_s(t_2)]\rangle = B_\xi(t_2-t_1)f[\gamma(t_1-\lambda)]f[\gamma(t_2-\lambda)]I\left(\frac{t_1-\lambda}{\tau}\right)I\left(\frac{t_2-\lambda}{\tau}\right) \quad (6)$$

is the covariance function of signal $s(t)$. If some signal (1) parameter is known, then in Eqs. (3)-(6) its true value should be used instead of current value.

We will try solution of Eq. (5) in a form structurally similar to Eq. (6), i.e.

$$\tilde{Q}(t_1,t_2,\chi) = \tilde{Q}_0(t_1,t_2,\chi)f[\gamma(t_1-\lambda)]f[\gamma(t_2-\lambda)]I[(t_1-\lambda)/\tau]I[(t_2-\lambda)/\tau]. \quad (7)$$

Substituting Eqs. (6), (7) in Eq. (5), we come to the equation of a form

$$\frac{N_0}{2}\tilde{Q}_0(t_1,t_2,\chi) + \chi\int_{\lambda-\tau/2}^{\lambda+\tau/2}[\gamma(t-\lambda)]\tilde{Q}_0(t_1,t,\chi)B_\xi(t_2-t)dt = B_\xi(t_2-t_1). \quad (8)$$

Solving Eq. (8) by Fourier transformation method [8], with a variable $\Delta = t_2 - t_1$ and taking into account the ratios (2), we come to

$$\tilde{Q}_0(t_1,t_2,\chi) = \frac{1}{2\pi}\int_{-\infty}^{\infty}\frac{G_\xi(\omega)\exp[j\omega(t_2-t_1)]}{N_0/2 + \chi f^2[\gamma(t_1-\lambda)]G_\xi(\omega)}d\omega. \quad (9)$$

In terms of Eq. (9), we specify expressions for the summands entering the logarithm of FLR (3). Using Eqs. (7), (9), we can present last summand in Eq. (3) as

$$\frac{1}{2}\int_0^1 d\chi\int_0^T \tilde{Q}(t,t,\chi)dt = \frac{1}{4\pi}\int_{-\tau/2}^{\tau/2}\int_{-\infty}^{\infty} ln\left[1 + \frac{2f^2(\gamma t)G_\xi(\omega)}{N_0}\right]d\omega dt. \quad (10)$$

Further, we set $\chi = 1$ in Eq. (9) and then substitute Eq. (9) into Eq. (7), and Eq. (7) into Eq. (4), and so, after corresponding transformations for the function $V(t)$, we come to

$$V(t) \approx \frac{2a}{N_0[1+qf^2(\gamma(t-\lambda))]}f[\gamma(t-\lambda)]I\left(\frac{t-\lambda}{\tau}\right), \quad (11)$$

where $q = 2G_\xi(0)/N_0$. Now, after substituting Eq. (9) into Eq. (7) and then Eqs. (7), (10), (11) into Eq. (3), we receive the following expression for the logarithm of FLR for the random Gaussian pulse with arbitrary-function envelope:

$$L(\vec{\vartheta}) = L_1(\vec{\vartheta}) + L_2(\vec{\vartheta}) - L_3(\vec{\vartheta}), \quad (12)$$

$$L_1(\vec{\vartheta}) = \frac{1}{N_0}\int_{\lambda-\tau/2}^{\lambda+\tau/2} x(t_1)x(t_2)f[\gamma(t_1-\lambda)]f[\gamma(t_2-\lambda)]Q_0(t_1,t_2)dt_1dt_2,$$

$$L_2(\vec{\vartheta}) = \frac{2a}{N_0}\left\{\int_{\lambda-\tau/2}^{\lambda+\tau/2}\frac{f[\gamma(t-\lambda)]x(t)dt}{1+qf^2[\gamma(t-\lambda)]} - \frac{a}{2}\int_{-\tau/2}^{\tau/2}\frac{f^2(\gamma t)dt}{1+qf^2(\gamma t)}\right\},$$

$$L_3(\vec{\vartheta}) = \frac{1}{4\pi}\int_{-\tau/2}^{\tau/2}\int_{-\infty}^{\infty} ln\left[1 + \frac{f^2(\gamma t)G_\xi(\omega)}{N_0}\right]d\omega dt.$$

Here, $Q_0(t_1,t_2) = \tilde{Q}_0(t_1,t_2,1)$.

The formula (12) is essentially simplified if SD $G_\xi(\omega)$ allows for rectangular approximation [4]:

$$G_\xi(\omega) = (d_0/2)I(\omega/\Omega_0) \quad (13)$$

for low-frequency (LF) process $\xi(t)$ and

$$G_\xi(\omega) = (d_0/2)\{I[(v_0-\omega)/\Omega_0] + I[(v_0+\omega)/\Omega_0]\} \quad (14)$$

for high-frequency (HF) process $\xi(t)$ with a central frequency v_0. Here d_0 is SD magnitude. Such kind of approximation of the SD form can be used if real SD rapidly decreases outside of the bandwidth Ω_0. With the realization of Eq. (13) or (14), the first summand in Eq. (12) can be written down in a form:

$$L_1(\vec{\vartheta}) = \frac{d}{N_0}\int_{-\infty}^{\infty} \tilde{y}^2(t)dt, \tag{15}$$

where

$$\tilde{y}(t) = \int_{-\infty}^{\infty} \tilde{x}(t')h(t-t')dt',$$
$$\tilde{x}(t) = \frac{x(t)}{\sqrt{N_0 + df^2[\gamma(-\lambda]}} f[\gamma(t-\lambda)]I\left(\frac{t-\lambda}{\tau}\right), \tag{16}$$

$h(t)$ is the function, the spectrum $H(\omega)$ of which satisfies the condition

$$|H(\omega)|^2 = 2G_{\xi}(\omega)/d_0, \tag{17}$$

and d is current value of the SD magnitude (in a case when the parameter d_0 is unknown).

As follows from the last parity, if inequalities (2) hold, then the duration of the pulse response $h(t)$ is much less than the signal $s(t)$ (1) duration and the characteristic changing time Δt of the function $f(t)$. Then the filter response $\tilde{y}(t)$ (16) allows representation:

$$\tilde{y}(t) \approx \frac{y(t)}{\sqrt{N_0 + df^2[\gamma(t-\lambda)]}} f[\gamma(t-\lambda)]I\left(\frac{t-\lambda}{\tau}\right),$$
$$y(t) = \int_{-\infty}^{\infty} x(t')h(t-t')dt'. \tag{18}$$

Indeed, the duration of the transient processes in the filter with the pulse response $h(t)$ (16) has an order of magnitude $2\pi/\Omega$. Therefore, the right and the left parts of the approximate equality (18) can differ essentially only in time intervals of an order $2\pi/\Omega$. in the neighborhood of the points $t = \lambda - \tau/2$ and $t = \lambda + \tau/2$. Still we can neglect this difference considering that Eq. (18) enters the logarithm of FLR under integral sign while executing ratios (2). Substituting Eq. (18) into Eq. (15) we have:

$$L_1(\vec{\vartheta}) = \frac{d}{N_0}\int_{\lambda-\tau/2}^{\lambda+\tau/2} \frac{f^2[\gamma(t-\lambda)]y^2(t)}{N_0 + df^2[\gamma(t-\lambda)]}dt. \tag{19}$$

In view of Eqs. (13), (14), we will transform summand $L_3(\vec{\vartheta})$ into a form:

$$L_3(\vec{\vartheta}) = \frac{\varepsilon\Omega}{4\pi}\int_{-\tau/2}^{\tau/2} \ln\left[1 + \frac{d}{N_0}f^2(\gamma t)\right]dt, \tag{20}$$

where $\varepsilon = 1$ or $\varepsilon = 2$ for LF or HF process $\xi(t)$ correspondingly.

Applying Eqs. (19), (20) in Eq. (12) for the logarithm of FLR for the Gaussian pulse with the arbitrary-function envelope and band SD, we receive:

$$L(\vec{\vartheta}) = \frac{q}{N_0}\int_{\lambda-\tau/2}^{\lambda+\tau/2} \frac{f^2[\gamma(t-\lambda)]y^2(t)}{1 + qf^2[\gamma(t-\lambda)]}dt + \frac{2a}{N_0}$$
$$\int_{\lambda-\tau/2}^{\lambda+\tau/2} \frac{f[\gamma(t-\lambda)]x(t)}{1 + qf^2[\gamma(t-\lambda)]}dt - L_0(\vec{\vartheta}),$$

$$L_0(\vec{\vartheta}) = \frac{a^2}{N_0}\int_{-\tau/2}^{\tau/2} \frac{f^2(\gamma t)}{1 + qf^2(\gamma t)}dt + \frac{\Omega}{4\pi}$$
$$\int_{-\tau/2}^{\tau/2} l\ln[1 + qf^2(\gamma t)]dt,$$

if process $\xi(t)$ is LF, and

$$L(\vec{\vartheta}) = \frac{q}{N_0}\int_{\lambda-\tau/2}^{\lambda+\tau/2} \frac{f^2[\gamma(t-\lambda)]y^2(t)}{1 + qf^2[\gamma(t-\lambda)]}dt - L_0(\vec{\vartheta}),$$
$$L_0(\vec{\vartheta}) = \frac{\Omega}{2\pi}\int_{-\tau/2}^{\tau/2} l\ln[1 + qf^2(\gamma t)]dt' \tag{21}$$

if process $\xi(t)$ is HF. Here, $q = d/N_0$.

3. Properties of the output signal of the maximum likelihood receiver of a random Gaussian pulse with unknown appearance time

For the definiteness of the further calculations we will refer to the process $\xi(t)$ as to a bandpass HF random process (14) and we will select pulse appearance time λ_0 as unknown parameter (other signal parameters are supposed to be known).

In the presence of a useful signal (1), (14), the term

$$M(\lambda) = \int_{\lambda-\tau_0/2}^{\lambda+\tau_0/2} \frac{f^2[\gamma(t-\lambda)]y^2(t)}{1 + q_0f^2[\gamma(t-\lambda)]}dt \tag{22}$$

of the functional $L(\vec{\vartheta}) = L(\lambda)$, depending on the realization of the observable data $x(t)$, can be presented as the sum of regular and noise functions [6]: $M(\lambda) = S(1) + N(1)$, where $S(1) = \langle M(\lambda)\rangle$ is regular function, $N(1) = M(\lambda) - \langle M(\lambda)\rangle$ is noise function, $q_0 = d_0/N_0$, $l = \lambda/\tau_0$ is current value of the dimensionless parameter $l_0 = \lambda_0/\tau_0$, and the averaging is executed through all possible realizations $x(t)$ with the fixed λ_0 value. While executing the ratios (2), for regular function and covariance function of noise function we receive

$$S(1) = \mu d_0 C(l - l_0) + Sn,$$
$$\langle N(l_1)N(l_2)\rangle = \mu N_0^2[R_1(l_1, l_2, l_0) + R_2(l_1, l_2)], \tag{23}$$

where

$$C(x) = \int_{1/2+\max(0,x)}^{1/2+\min(0,x)} g_{21}(\tilde{t} - x)f^2(\tilde{\gamma}\tilde{t})d\tilde{t},$$
$$S_N = \mu N_0 G_{21}(1/2),$$
$$R_1(l_1, l_2, l_0) = \int_{1/2+\max(0, l_1-l_0, l_2-l_0)}^{1/2+\min(0, l_1-l_0, l_2-l_0)} g_{21}(\tilde{t} - l_1 + l_0)$$
$$g_{21}(\tilde{t} - l_2 + l_0)[(1 + q_0f^2(\tilde{\gamma}\tilde{t}))^2 - 1]d\tilde{t},$$
$$R_1(l_1, l_2) = \int_{1/2+\max(l_1, l_2)}^{1/2+\min(l_1, l_2)} g_{21}(\tilde{t} - l_1)g_{21}(\tilde{t} - l_2)d\tilde{t},$$

$x \in [X_1, X_2]$, possesses drift coefficient

$$g_{nmn}(\tilde{t}) = \frac{f^m(\tilde{\gamma}\tilde{t})}{[1 + q_0 f^2(\tilde{\gamma}t)]^n},$$
$$G_{mn}(\tilde{t}) = \int_{-\tilde{t}}^{\tilde{t}} g_{mn}(\tilde{t})d\tilde{t}, \quad (24)$$
$$\mu = \tau_0\Omega_0/2\pi, \tilde{\gamma} = \gamma\tau_0, \tilde{t} = t/\tau_0.$$

If the useful signal (1), (14) is absent, then, both for regular function and covariance function of noise function of the functional (22), we have

$$S(l) = S_N, \langle N(l_1)N(l_2)\rangle = \mu N_0^2 R_2(l_1, l_2). \quad (25)$$

4. The appearance time estimate of the random Gaussian pulse

Let us state that the signal (1), (14) is present with the probability 1. Then, according to [1 and 6], the maximum likelihood estimate (MLE) λ_m of appearance time λ_0 will be defined as

$$\lambda_m = \arg\sup_{\lambda\in[\Lambda_1,\Lambda_2]} L(\lambda) = \arg\sup_{\lambda\in[\Lambda_1,\Lambda_2]} M(\lambda). \quad (26)$$

The block diagram of the measurer (26) is shown in Fig. 1 where the designations are the following: 1 is the switch that is open for time $[\Lambda_1 - \tau_0/2, \Lambda_2 + \tau_0/2]$; 2 is a filter with transfer function $H(\omega)$ (14), (17); 3 is the squarer; 4 is the filter matched with the signal $f^2(\gamma t)I(t/\tau_0)/[1 + q_0 f^2(\gamma t)]$; 5 is the extremator that fixes the location of the greatest maximum of the input signal as an estimate λ_m. As appears from Fig. 1, synthesized optimal receiver of HF random pulse with arbitrary-function envelope and unknown appearance time has a single-channel structure, unlike alternative multichannel variants presented in the current researches [2, etc.].

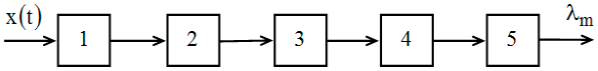

Fig. 1 The optimal measurer of appearance time of HF random pulse

Let us find the characteristics of MLE λ_m. During the analysis process, we find it expedient to divide all the estimates into the two classes: reliable and anomalous [6]. The estimate $l_m = \lambda_m/\tau_0$ is reliable, if it is within the interval limits $\Gamma \equiv [l_0 - 1, l_0 + 1]$ where the regular function (23) is distinct from S_N. If MLE l_m is out of an interval Γ_S, i.e. $l_m \in \Gamma_N = \Gamma \setminus \Gamma_S$, $\Gamma \equiv [\tilde{\Lambda}_1, \tilde{\Lambda}_2]$, $\tilde{\Lambda}_{1,2} = \Lambda_{1,2}/\tau_0$, then the estimate and the corresponding estimate error are designated as anomalous [6]. It is necessary to consider the anomalous errors if the length of the prior interval $[\Lambda_1, \Lambda_2]$ of the possible values of appearance time λ_0 is much greater than signal (1) duration τ_0, i.e. the following condition holds

$$m = \tilde{\Lambda}_2 - \tilde{\Lambda}_1 >> 1. \quad (27)$$

According to [6], while executing ratio (27), the conditional bias $b(l_m | l_0) = \langle l_m - l_0\rangle$ and variance $V(l_m | l_0) = \langle (l_m - l_0)^2\rangle$ of MLE l_m, with the allowance for the anomalous errors, can be written down as follows:

$$b(l_m | l_0) = P_0 b_0(l_m | l_0) + (1 - P_0)[(\tilde{\Lambda}_1 + \tilde{\Lambda}_2)/2 - l_0],$$
$$V(l_m | l_0) = P_0 V_0(l_m | l_0) + (1 - P_0)$$
$$[(\tilde{\Lambda}_1^2 + \tilde{\Lambda}_1\tilde{\Lambda}_2 + \tilde{\Lambda}_2^2)/3 - l_0(\tilde{\Lambda}_1 + \tilde{\Lambda}_2) + l_0^2]. \quad (28)$$

Here, $b_0(l_m | l_0)$, $V_0(l_m | l_0)$, $P_0 = P[|l_m - l_0| \le 1]$ are, correspondingly, conditional bias, conditional variance and probability of a reliable estimate l_m (26).

While determining $b_0(l_m | l_0)$, $V_0(l_m | l_0)$ and P_0, we will be limited to a condition of a high posterior accuracy when the output signal-to-noise ratio (SNR) z^2 of the algorithm (26) is sufficiently great, i.e.

$$z^2 = [S(l_0) - S_N]^2/\langle N^2(l_0)\rangle =$$
$$\mu q_0^2 \left[\int_{-1/2}^{1/2} \frac{f^4(\tilde{\gamma}\tilde{t})d\tilde{t}}{1 + q_0 f^2(\tilde{\gamma}\tilde{t})}\right]^2 \Big/ \int_{-1/2}^{1/2} f^4(\tilde{\gamma}\tilde{t})d\tilde{t} >> 1. \quad (29)$$

The inequality (29) is valid with ratios (2) executed and when the values of q_0 are not too small.

We will presuppose that $f(\tilde{\gamma}\tilde{t})$ does not vanish in points $\tilde{t} = \pm 1/2$, i.e. the useful signal (1) is discontinuous (for a continuous signal the results received in [5] can be used at their obvious generalization). Similarly to [6], it can be shown that MLE l_m converges in a mean square to a true value of the estimated parameter l_0 with the increase of z^2. Hereupon, for the definition of the characteristics of the reliable estimate l_m under $z^2 >> 1$, it is sufficient to investigate the behavior of the functional $M(l)$ (22) in a small neighborhood of the point $l = l_0$. We will designate $\Delta = \max\{|l_1 - l_0|, |l_2 - l_0|, |l_1 - l_2|\}$. Then, taking into account the ratios (2) under $\Delta \to 0$, the following asymptotic expansions are true for Eqs. (23):

$$S(l) = \mu d_0[G_{14}(1/2) + g_{41}(1/2)\min(0, l - l_0) -$$
$$- g_{41}(-1/2)\max(0, l - l_0)] + S_N + o(\Delta), \quad (30)$$

$$\langle N(l_1)N(l_2)\rangle = \mu N_0^2\{G_{40}(1/2) + g_{42}(1/2)\min$$
$$(l_1 - l_0, l_2 - l_0) - g_{42}(-1/2)\max(l_1 - l_0, l_2 - l_0) +$$
$$+[g_{40}(1/2) - g_{42}(1/2)] - \min(0, l_1 - l_0, l_2 - l_0) -$$
$$-[g_{40}(-1/2) - g_{42}(-1/2)]\max(0, l_1 - l_0, l_2 - l_0)\} + o(\Delta),$$

where $o(\Delta)$ denotes the higher-order infinitesimal terms

compared with Δ and $g_{mn}(\tilde{t})$, $G_{mn}(\tilde{t})$ are defined according to Eqs. (24).

Using results [9 and 10], on the basis of regular and noise functions properties (30) of solving statistics (22) for conditional bias $b_0(l_m \mid l_0)$, conditional variance $V_0(l_m \mid l_0)$ and probability of a reliable estimate l_m we find $b_0(l_m \mid l_0) \approx 0$,

$$V_0(l_m \mid l_0) = 13\{f^4(\tilde{\gamma}/2)f(-\tilde{\gamma}/2)[1+q_0 f^2(\tilde{\gamma}/2)]^2\} \times \\ \times\{f^4(-\tilde{\gamma}/2)+f^4(\tilde{\gamma}/2)[1+q_0 f^2(-\tilde{\gamma}/2)]^2\}/8\mu^2 q_0^4 \\ f^8(\tilde{\gamma}/2)f^8(-\tilde{\gamma}/2), \tag{31}$$

$$P_0 = \frac{z(\psi_1+\psi_2)}{r}\int_1^\infty \exp\left[-\frac{\hat{m}\kappa}{\sqrt{2\pi}}\exp\left(-\frac{\kappa^2}{2}\right)\right] \\ \left\{\frac{\psi_1}{\psi_1+\psi_2}\exp\left[\frac{\psi_1^2 z^2}{2}+\psi_1 z\left(z-\frac{\kappa}{r}\right)\right]\right\}\times \\ \times\Phi\left[\frac{\kappa}{r}-z(\psi_1+1)\right]+\frac{\psi_2}{\psi_1+\psi_2}\exp\left[\frac{\psi_2^2 z^2}{2}+ \\ +\psi_2 z\left(z-\frac{\kappa}{r}\right)\right]\Phi\left[\frac{\kappa}{r}-z(\psi_2+1)\right]- \\ -\exp\left[\frac{z^2(\psi_1+\psi_2)^2}{2}+z(\psi_1+\psi_2)\left(z-\frac{\kappa}{r}\right)\right]\Phi\times \\ \times\left[\frac{\kappa}{r}-z(\psi_1+\psi_2+1)\right]\Big\}d\kappa,$$

where $\hat{m} = m[g_{42}(1/2)+g_{42}(-1/2)]/2G_{42}(1/2)$ is reduced length [6] of the prior limit of signal (1) appearance time, $\psi_1 = 2g_{41}(1/2)G_{40}(1/2)/G_{41}(1/2)[g_{40}(1/2)+g_{42}(-1/2)]$, $\psi_2 = 2g_{41}(-1/2)G_{40}(1/2)/G_{41}(1/2)[g_{40}(-1/2)+g_{42}(-1/2)]$, $r = \sqrt{G_{40}(1/2)/G_{42}(1/2)}$. Accuracy of formulas (31) increases with μ (23), z (29) and m (27).

If $f(t) \equiv 1$, then from Eqs. (31) we receive known expressions for conditional bias, conditional variance and probability of a reliable estimate for appearance time MLE λ_m of a HF random pulse (1), (14) with rectangular envelope [3].

5. Detection of the random Gaussian pulse with unknown appearance time

Now let us consider a detection problem of the HF random pulse (1), (14) with unknown appearance time λ_0. As it is well known from [6], MLR makes a decision about the presence of a useful signal in terms of the comparison of the absolute (greatest) maximum value of the logarithm of FLR (21), with a threshold c which is chosen according to the set optimality criterion of detection. Therefore, the magnitude

$$L = \sup_{\lambda\in[\Lambda_1,\Lambda_2]} L(\lambda) = \sup_{\lambda\in[\Lambda_1,\Lambda_2]} M(\lambda) \tag{32}$$

should be compared with a threshold c. Here $M(\lambda)$ is determined from Eq. (22).

The block diagram of the detection algorithm (32) of the random pulse can be obviously received through the block diagram presented in Fig. 1 by substituting extremator 5 for solving device, which analyzes input realization $M(\lambda)$ (22) within the interval $\lambda \in [\Lambda_1, \Lambda_2]$ and makes a decision about presence or absence of a signal (1), (14), comparing an absolute maximum of realization $M(\lambda)$ with a threshold c.

Let us find characteristics of random pulse detector (32). As such characteristics we will use type I (false-alarm) and II (signal missing) error probabilities [1, 2, 4, 6, etc.]. The starting point is that the useful signal is absent. Then the false-alarm probability α can be determined as follows

$$\alpha = P\left[\sup_{\lambda\in[\Lambda_1,\Lambda_2]} M(\lambda) > c \,\middle|\, x(t) = n(t)\right] = \\ = P\left[\sup_{l\in[\tilde{\Lambda}_1,\tilde{\Lambda}_2]} \mathring{M}(l) > u \,\middle|\, x(t) = n(t)\right]. \tag{33}$$

Here, $\mathring{M}(l)[M(l)-S_N]/\sigma_N$, $\sigma_N = N_0\sqrt{\mu G_{42}(1/2)}$, and $u = (c-S_N)/\sigma_N$ is normalized threshold.

As follows from [4], (25), the functional $\mathring{M}(l)$ is asymptotically Gaussian (under $\mu \to \infty$) with zero mathematical expectation and unit dispersion. According to [11 and 12], while increasing the threshold c, the distribution of number of outliers over level c by stationary centered Gaussian random process converges to the Poisson's law with threshold c growth. On the basis of results [4 and 9] it allows to write down asymptotically (under $m \to \infty, c \to \infty$) exact expression for false-alarm probability (33) as

$$\alpha = \begin{cases} 1-\exp\left[-\dfrac{\hat{m}u}{\sqrt{2\pi}}\exp(-u^2/2)\right], & u \ge 1, \\ 1, & u < 1. \end{cases} \tag{34}$$

Let suppose now that the signal (1), (14) is present on the detector input. Then the missing probability β will be defined as [1, 2, 4, 6, etc]

$$\beta = P\left[\sup_{\lambda\in[\Lambda_1,\Lambda_2]} M(\lambda) < c \,\middle|\, x(t) = s(t)+n(t)\right] = \\ = P\left[\sup_{l\in[\Lambda_1,\Lambda_2]} M(l) < c \,\middle|\, x(t) = s(t)+n(t)\right]. \tag{35}$$

Using Eqs. (23)-(25) it is easy to show that if condition (27) is satisfied then values of the absolute maxima of functional $M(l)$ are approximately statistically independent in subareas Γ_S and Γ_N. The specified property allows similarly [4 and 9] to present Eq. (35) in a kind of

$$\beta = F_N(u)F_S(u/r), \tag{36}$$

Here, $F_S(u) = P\left\{\sup_{l\in\Gamma_S} \mathring{M}(l)/\sigma_S < u\right\}$,

$F_N(u) = P\left\{\sup_{l\in\Gamma_N} \mathring{M}(l)/\sigma_N < u\right\}$ are distribution functions of the normalized absolute maxima of centered functional $\mathring{M}(l) = M(l) - S_N$ within intervals Γ_S and Γ_N correspondingly, $\sigma_S = N_0\sqrt{\mu G_{40}(1/2)}$, $r = \sigma_S/\sigma_N = \sqrt{G_{40}(1/2)/G_{42}(1/2)}$.

When condition (27) holds

$$P\left\{\sup_{l\in\Gamma_N} \mathring{M}(l)/\sigma_N < u\right\} \approx P\left\{\sup_{l\in\Gamma} \mathring{M}(l)/\sigma_N < u \,\middle|\, x(t) = n(t)\right\},$$

and approximation

$$F_N(u) = 1 - \alpha = \begin{cases} \exp\left[-\frac{\hat{m}u}{\sqrt{2\pi}}\exp\left(-\frac{u^2}{2}\right)\right], u \geq 1, \\ 0, \quad u < 1. \end{cases} \qquad (37)$$

can be used for function $F_N(u)$.

For probability $F_S(u)$, using results [4 and 9] and taking into account Eqs. (23), we find

$$\begin{aligned} F_S(u) &= \Phi(u-z) - \exp[\psi_1^2 z^2/2 + \psi_1 z(z-u)]\times \\ &\times\Phi[u - z(\psi_1+1)] - \exp[\psi_2^2 z^2/2 + \psi_2 z(z-u)]\times \\ &\times\Phi[u - z(\psi_2+1)] + \exp[z^2(\psi_1+\psi_2)^2/2 + \\ &+ z(\psi_1+\psi_2)(z-u)]\Phi[\kappa - z(\psi_1+\psi_2+1)]. \end{aligned} \qquad (38)$$

Now, applying the approximations (37), (38) to the Eq. (36) we have finally

$$\begin{aligned} \beta &= \exp\left[-\frac{\hat{m}u}{\sqrt{2\pi}}\exp\left(-\frac{u^2}{2}\right)\right]\left\{\Phi\left(\frac{u}{r} - z\right) - \right. \\ &- \exp\left[\frac{\psi_1^2 z^2}{2} + \psi_1 z\left(z - \frac{u}{r}\right)\right]\times\Phi\left[\frac{u}{r} - z(\psi_1+1)\right] - \\ &- \exp\left[\frac{\psi_2^2 z^2}{2} + \psi 2 z\left(z - \frac{u}{r}\right)\right]\Phi\left[\frac{u}{r} - z(\psi 2+1)\right] + \\ &+ \exp\left[\frac{z^2(\psi_1+\psi_2)^2}{2} + z(\psi_1+\psi_2)\left(z - \frac{u}{r}\right)\right]\times \\ &\left.\times\Phi\left[\frac{u}{r} - z(\psi_1+\psi_2+1)\right]\right\}, \end{aligned} \qquad (39)$$

if $u \geq 1$, and $\beta \approx 0$ if $u < 1$. The accuracy of the formula (39) increases with u, m, μ, z.

Supposing in Eqs. (34), (39) $f(t) \equiv 1$, we receive expressions for false-alarm and missing probabilities at the reception of a HF random pulse (1), (14) with rectangular envelope and unknown appearance time [4 and 9].

6. Results of statistical modeling

For the purpose of an establishment of the applicability borders of the asymptotically exact formulas for the detection and estimation characteristics, we applied the MLR statistical computer modeling.

In the process of modeling, we followed the technique, introduced in [9], and formed the samples of the normalized functional $\tilde{M}(l) = M(\lambda)/N_0$ (22) within an interval $[\tilde{\Lambda}_1, \tilde{\Lambda}_2]$ with a step $\Delta l = 0.01$, both in the presence and in the absence of the signal (1), (14). And thus the relative mean square error of step approximations of continuous realizations of process $\tilde{M}(l)$ in terms of the generated discrete samples did not exceed 10%. For each realization of $\tilde{M}(l)$ we compared the value of the greatest maximum sample of the functional (22) with the normalized threshold c/N_0 and found the false-alarm and missing probabilities. Besides, according to (26), we determined the estimate l_m and its variance.

Some results of statistical modeling for $l_0 = (\tilde{\Lambda}_2 + \tilde{\Lambda}_1)/2$, $\tilde{\Lambda}_1 = 1/2$, $\tilde{\Lambda}2 = m + 1/2$ and $f(\tilde{t}) = \exp(-\tilde{\gamma}^2\tilde{t}^2)$, $\tilde{\gamma} = 1$ are shown in Figs. 2a - 4a, while for $f(\tilde{t}) = 1 - \tilde{\gamma}|\tilde{t}|$, $\tilde{\gamma} = 1/4$ - in Figs. 2b - 4b. Each experimental value in Figs. 2 - 4 was obtained as a result of the processing of no less than 10^4 realizations of the solving statistics $\tilde{M}(1)$. In this case, with probability of 0.9 confidence intervals boundaries deviate from experimental values no more than for 5...10%.

In Figs. 2 the theoretical dependences of the normalized conditional variance $V_1(q_0) = 12V(l_m|l_0)/m^2$ (28) of MLE l_m, calculated in view of m=20 and with the allowance for anomalous errors, are drawn as solid lines. The dashed lines in Figs. 2 show the analogous dependences of the normalized conditional variance $V_1(q_0) = 12V(l_m|l_0)/m^2$ (31) of reliable MLE l_m. Curves 1 correspond to $\mu = 50$, curves 2 to $\mu = 100$, curves 3 to $\mu = 200$. In Figs. 2 the experimental values for $\mu = 50$, 100 and 200 are denoted by rectangles, crosses, and rhombuses (for variance V_l of MLE l_m with the allowance for anomalous errors), respectively, as well as by plus signs, circles and triangles (for variance V_{0l} of reliable MLE l_m).

In Figs. 3 the theoretical dependences (34) of false-alarm probability $\alpha(u)$ (33) are plotted. The curve 1 corresponds to q=0.1 and curve 2 to q=4. Parameter quantity m assumed equal 20. Experimental values of false-alarm probability (33) for m=20 are shown in Figs. 3 by rectangles and crosses (for q=0.1 and $\mu = 50$ or $\mu = 200$), respectively, as well as rhombuses and circles (for q=4 and $\mu = 50$ or $\mu = 200$).

At last, in Figs. 4 for m=20 the theoretical dependences of missing probability $\beta(q_0)$ (35) are represented. The curve 1 is calculated with the formula (39) for $\mu = 50$, curve 2 for $\mu = 100$ and curve 3 for $\mu = 200$. The threshold quantity u was determined from Eq. (34) by Neumann-Pirson criterion, according to the preselected level of false-alarm probability equal to 0.01. Experimental values of the missing probability (35) for $\mu = 50$, 100 and 200 are designated in Figs. 4 by rectangles, crosses, and rhombuses respectively.

In terms of the received results, we can draw the following conclusions.

As is evident from Figs. 2 - 4, the theoretical dependences both of the detection and of the appearance time estimation of the random pulse (1), (14), with the allowance for the anomalous errors, approximate the experimental results in a satisfactory manner, at least, for m≥20, $\mu \geq 50$, z≥1.5...2,

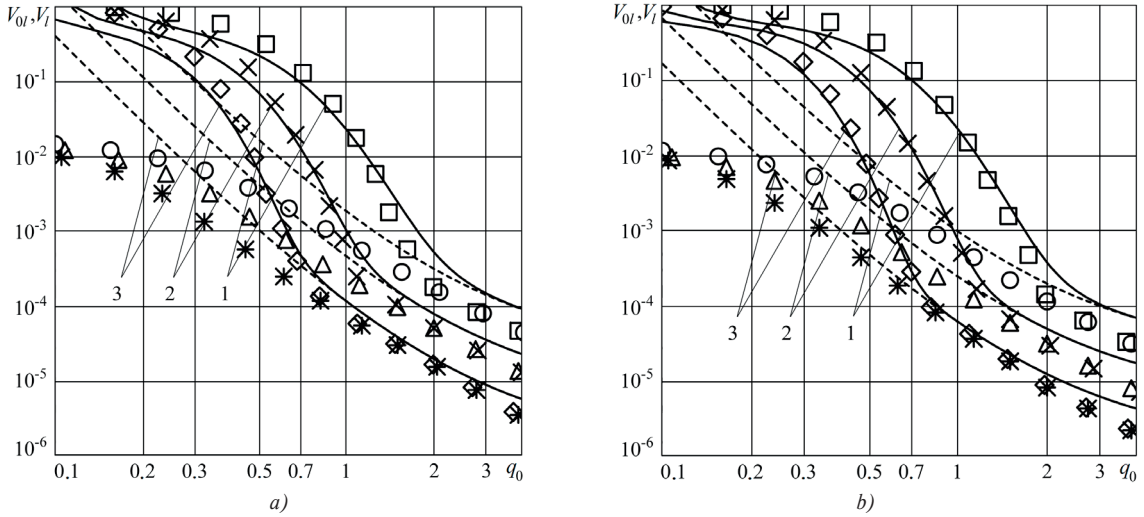

Fig. 2 The theoretical and experimental dependences of normalized variance of appearance time estimate

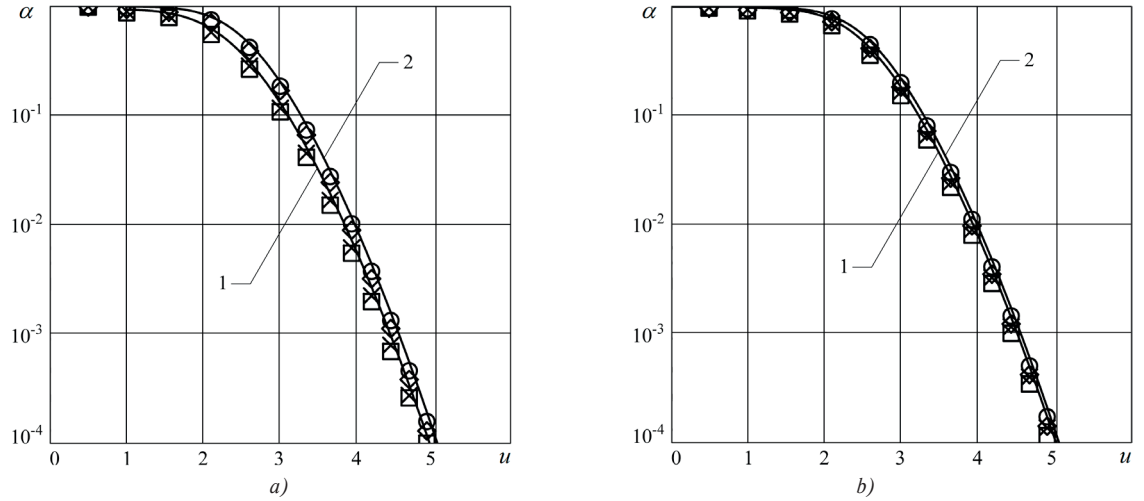

Fig. 3 The theoretical and experimental dependences of false-alarm probability

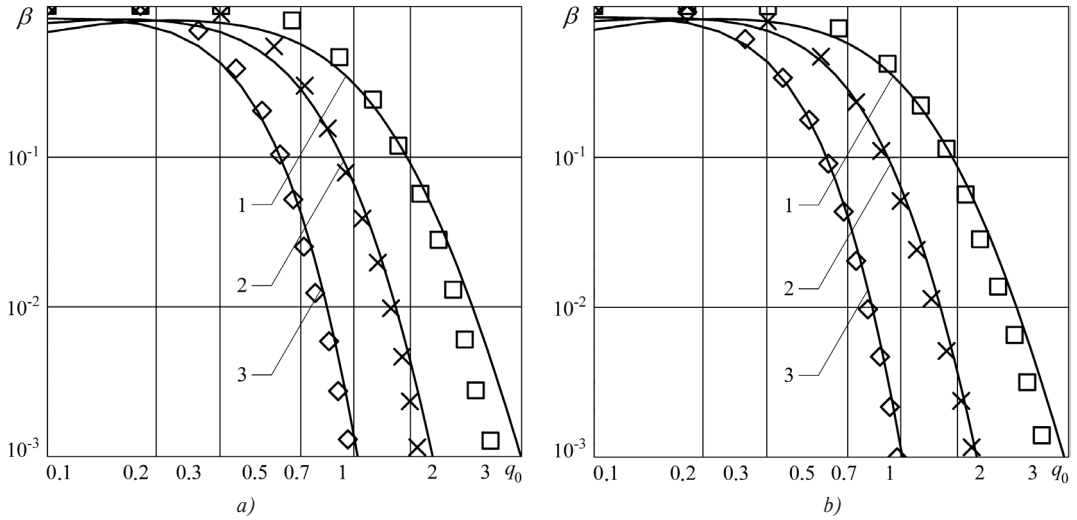

Fig. 4 The theoretical and experimental dependences of missing probability

$(f_{max} - f_{min})/\mu < 4 \cdot 10^{-3}$. Here, $f_{min} = \min f(t)$ and $f_{max} = 1$ are minimum and maximum values of the function $f(t)$.

As q_0 decreases when the SNR $z \leq 5...6$, the probability $P_a = 1 - P_0$ of the anomalous errors increases significantly and approaches 1. This leads to a jump-like (compared with the case of reliable estimate) increase in the variance of the appearance time estimate (so-called threshold effects occur). As q_0 increases, when $z > 5...6$, the variance V_l converges to the variance V_{0l}, and the estimate l_m (26) becomes reliable with the probability close to 1. From Eqs. (28), (31) and Figs. 2 follows that the minimum (threshold) value of the parameter q_0, at which the influence of the anomalous errors on the accuracy of MLE of the signal (1), (14) appearance time can be still neglected, decreases with μ and increases with m.

For $z < 2...3$ the theoretical dependences of variance V_{0l} of the reliable MLE (26) deviate from experimental ones substantially, as are found without finite length of the interval Γ_S of the reliable MLE like values. Departing of theoretical dependences $V_0(l_m | l_0)$ (31), $V(l_m | l_0)$ (28) from experimental data is observed under high SNR when $q > 2...3$ too. This is due to the fact that Eq. (31) for the variance $V_0(l_m | l_0)$ of the reliable estimate of the appearance time is obtained ignoring the errors in estimating the order of correlation time of the random substructure of the pulsed signal (1), (14). Consequently, the error of Eqs. (28), (31) becomes significant, as the relative variance of the MLE decreases to a magnitude of order μ^{-2}.

7. Conclusion

For the synthesis of the algorithms of the statistical analysis of random pulsed signals with the arbitrary-function envelope, the approach neglecting the values of an order of correlation time of a pulse random substructure is effective. The given approach makes it possible to receive detectors and measurers of the random pulses with the unknown parameters sufficiently simply realized in practice.

Quality of the synthesized processing algorithms of the pulsed signals with the unknown discontinuous parameters can be theoretically estimated by means of the local Markov approximation method based on the representation of the solving statistics increments by the Markov random process of diffusion type in a small neighborhood of the point of the true value of the unknown parameter [9]. As a result, it is possible to write down the closed analytical expressions for detection and estimation characteristics having acceptable accuracy for SNR being more than 1...2, and that was proved by the results of the statistical modeling.

The results of the study are of a general importance. They can be used in radio physical measurements while processing the random pulses of optical, acoustic, electromagnetic and other origins, in the systems information transmission and processing and in the systems of the technological processes monitoring and control, and also in other fields of science and technology, dealing with registration and measurement of random processes.

Acknowledgement

The reported study was supported by the Russian Science Foundation (research project No. 14-49-00079).

References

[1] VAN TREES, H. L.: *Detection, Estimation, and Modulation Theory, Part III*, Wiley: New York, 1971.

[2] Problems of the Statistical Radiolocation Theory [in Russian], Edited by G. P. Tartakovsky, *Sovetskoe Radio*, Moscow, 1963.

[3] TRIFONOV, A. P., ZAKHAROV, A. V.: Reception of Signals with Unknown Delay in the Presence of Modulating Noise, *Radioelectronics and Communications Systems*, vol. 29, No. 4, 1986, pp. 32-36.

[4] TRIFONOV, A. P., NECHAEV, E. P., PARFENOV, V. I.: Detection of Stochastic Signals with Unknown Parameters [in Russian], *Voronezh State University*, Voronezh, 1991.

[5] TRIFONOV, A. P., PARFENOV, V. I.: Theoretical and Experimental Investigations of a Maximum-Likelihood Receiver of a Random Pulse with an Unknown Arrival Time, *J. of Communications Technology and Electronics*, vol. 43, No 7, 1998, pp. 769-775.

[6] TRIFONOV, A. P., SHINAKOV, Yu. S.: Joint Discrimination of Signals and Estimation of their Parameters against Background [in Russian], *Radio i Svyaz'*, Moscow, 1986.

[7] CHERNOYAROV, O. V., BREZNAN, M., TEREKHOV A. V.: Restoration of Deterministic and Interference Distorted Signals and Images with Use of the Generalized Spectra in Bases of Orthogonal Polynomials and Functions, *Communications - Scientific Letters of the University of Zilina*, vol. 15, No. 2A, 2013, pp. 71-77.

[8] TARTAKOVSKY, G. P.: Synthesis of a Heterodyne Light Signal Receiver [in Russian], *Problemy Peredachi Informatsii*, vol. 1, No. 3, 1965, pp. 56-70.

[9] CHERNOYAROV, O. V., SAI SI THU MIN, SALNIKOVA, A.V., SHAKHTARIN, B. I., ARTEMENKO, A. A.: Application of the Local Markov Approximation Method for the Analysis of Information Processes Processing Algorithms with Unknown Discontinuous Parameters, *Applied Mathematical Sciences*, vol. 8, No 90, 2014, pp. 4469-4496.

[10] CHERNOYAROV, O. V., SALNIKOVA, A. V., ROZANOV, A. E., MARCOKOVA, M.: Statistical Characteristics of the Magnitude and Location of the Greatest Maximum of Markov Random Process with Piecewise Constant Drift and Diffusion Coefficients, *Applied Mathematical Sciences*, vol. 8, No 147, 2014, pp. 7341-7357.

[11] PICKANDS, J.: Upcrossing Probabilities for Stationary Gaussian Process, *Trans. Amer. Math. Soc.*, vol. 145, No. 11, 1969, p. 51-73.

[12] QUALLS, C., WATANABE, H.: Asymptotic Properties of Gaussian Processes, *Ann. on Math. Statist.*, vol. 3, No. 2, 1972, p. 580-596.

Elena Zaitseva - Miroslav Kvassay - Vitaly Levashenko - Jozef Kostolny *

RELIABILITY ANALYSIS OF LOGIC NETWORK WITH MULTIPLE OUTPUTS

Reliability analysis of a logic network with multiple outputs is considered in this paper. One of the principal tasks of reliability engineering is identification of those system components that have the most influence on the system activity. There exist several measures that are used for this purpose. One of them is Structural Importance Measure (SIM) which focuses on topological importance of individual system components. This measure is calculated from the system structure function, i.e. function that defines dependency between system activity and activity of its components, using logical differential calculus. In this paper, we present a method that can be used to identify the structure function of a logic network with multiple outputs and, based on logical differential calculus, we propose several definitions of the SIM for this type of systems. As a case study, the topological analysis of a one-bit full adder is considered in the last part of this paper. This study demonstrates usefulness of our approach in reliability analysis of logic networks and indicates that its further development and practical implementation could be beneficial.

Keywords: *Logic network, structure function, availability, logical differential calculus, structural importance measure.*

1. Introduction

Reliability has been considered as an important design measure in many technical systems [1 - 6]. A logic network is one of them [1, 4 - 6]. One of principal problems in reliability analysis of a logic network is investigation of influence of breakdown of each gate upon the network failure [1, 5 and 6]. The system reliability modeling and calculation of reliability indices and measures are principal steps in such analysis.

A real system contains a lot of components. From reliability point of view, the system and all its components can be in one of two possible states: functional (presented as 1) and failed (presented as 0). The dependency between system state and states of its components is defined by the structure function [7 and 8]:

$$\phi(x_1,x_2,...,x_n) = \phi(\boldsymbol{x}): \{0,1\}^n \rightarrow \{0,1\}, \quad (1)$$

where n is the number of system components, x_i is the state of component i, for $i = 1,2,...,n$, and $\boldsymbol{x} = (x_1, x_2,..., x_n)$ is a vector of components states (state vector).

The structure function of many systems is monotonic. This means that there exists no situation in which the failure of some components causes the system repair. This type of systems is known as coherent. Coherency is a typical property of many systems in reliability analysis. However, there exist some systems that are noncoherent [9] - [12]. Their structure function is non-monotonic, which means that there exist situations in which the failure of some component results in system repair. The logic networks are typical example of such systems and, therefore, classical approaches of reliability engineering cannot be used in their analysis [12].

The structure function does not take the availabilities of individual system components into account and, therefore, it allows analyzing only topological characteristics of the system. When other aspects of system availability have to be studied, then the probabilities of working/non-working state of every component should be known:

$$p_i = \Pr\{x_i = 1\}, \quad q_i = \Pr\{x_i = 0\}, \quad p_i + q_i = 1. \quad (2)$$

Probabilities p_i and q_i are known as the availability and unavailability of component i.

When the system structure function and availabilities of all system components are known, then system availability and unavailability can be computed as follows [7 and 8]:

$$A = \Pr\{\phi(\boldsymbol{x}) = 1\}, \quad U = \Pr\{\phi(\boldsymbol{x}) = 0\}, \quad A + U = 1. \quad (3)$$

The availability is one of the most important characteristics of any system because it defines the proportion of time in which the steady-state system will be working. It can also be used to compute other reliability characteristics, e.g. mean time to failure, mean time to repair, some types of importance measures, etc. [7].

* **Elena Zaitseva, Miroslav Kvassay, Vitaly Levashenko, Jozef Kostolny**
Department of Informatics, Faculty of Management Science and Informatics, University of Zilina, Slovakia
E-mail: elena.zaitseva@fri.uniza.sk

2. Logic Network with Multiple Outputs

In reliability analysis of logic networks, the studied system is a logic network of k logic inputs and n logic gates, which realizes a logic function:

$$F(y_1, y_2,..., y_k) = F(\boldsymbol{y}): \{0, 1\}^k \rightarrow \{0, 1\}, \quad (4)$$

where k is a number of input signals, y_l is the l-th variable of the logic function and it corresponds to the l-th input of the logic network, for $l = 1, 2,...,k$, and $\boldsymbol{y} = (y_1, y_2,..., y_k)$ is a vector of input signals (input vector).

A lot of logic networks have more than one output and realize a set of logic functions. Therefore, the general logic network is a realization of m-dimensional vector logic function:

$$\boldsymbol{F}(y_1, y_2,..., y_k) = \boldsymbol{F}(\boldsymbol{y}): \{0, 1\}^k \rightarrow \{0, 1\}^m, \quad (5)$$

where k is a number of input signals and m is a number of output signals.

With relation to reliability analysis, a logic network has two different types of components:

- n logic gates – they can be working or failed;
- k inputs – they can be correct or incorrect.

In paper [12], there has been considered assumption that the input signals are always correct and, therefore, only logic gates are relevant system components. Using this assumption, the structure function of a logic network and the *Structural Importance Measure* (SIMs) of individual logic gates have been defined. However, they have been proposed for networks with only one output. Now, we concentrate on a logic network with m outputs.

3. Reliability Analysis of Logic Network with Multiple Outputs

A. Structure Function

The output of a real logic network is determined not only by values of inputs but also by proper work of individual logic gates. Therefore, the real output of a logic network has to be defined by logic function $\boldsymbol{F}_o(\boldsymbol{y}; \boldsymbol{x})$ which takes into account not only the values of the input signals (input vector $\boldsymbol{y}$) but also the states of logic gates of the network (state vector $\boldsymbol{x}$) [5]:

$$\boldsymbol{F}_o(\boldsymbol{y}; \boldsymbol{x}): \{0, 1\}^{k+n} \rightarrow \{0, 1\}^m, \quad (6)$$

where k is a number of input signals, m is a number of output signals, and n is a count of logic gates that are used in the logic network.

When the expected output $\boldsymbol{F}(\boldsymbol{y})$ and real output $\boldsymbol{F}_o(\boldsymbol{y}; \boldsymbol{x})$ of a logic network are known, then its availability can be defined as probability that these two output signals have the same values [5]:

$$A = \Pr\{\boldsymbol{F}_o(\boldsymbol{y}; \boldsymbol{x}) = \boldsymbol{F}(\boldsymbol{y})\}. \quad (7)$$

Using relation between the system structure function and its availability (3), the structure function of a logic network with m outputs can be defined in the following way:

$$\phi(\boldsymbol{x}; \boldsymbol{y}) = \boldsymbol{F}_o(\boldsymbol{y}; \boldsymbol{x}) \leftrightarrow \boldsymbol{F}(\boldsymbol{y}), \quad (8)$$

where $\leftrightarrow$ is the symbol of logical biconditional and it can be interpreted in terms of vector logic functions as follows:

$$\boldsymbol{F}_o(\boldsymbol{y}; \boldsymbol{x}) \leftrightarrow \boldsymbol{F}(\boldsymbol{y}) = \{F_{1,o}(\boldsymbol{y}; \boldsymbol{x}) \leftrightarrow F_1(\boldsymbol{y})\} \wedge \{F_{2,o}(\boldsymbol{y}; \boldsymbol{x}) \leftrightarrow F_2(\boldsymbol{y})\} \wedge ... \wedge \{F_{m,o}(\boldsymbol{y}; \boldsymbol{x}) \leftrightarrow F_m(\boldsymbol{y})\}, \quad (9)$$

where $F_t(\boldsymbol{y})$ is the t-th element of the vector logic function $\boldsymbol{F}(\boldsymbol{y})$, i.e. $F_t(\boldsymbol{y})$ represents the expected value of the t-th output signal, and $F_{t,o}(\boldsymbol{y}; \boldsymbol{x})$ is the t-th element of the vector logic function $\boldsymbol{F}_o(\boldsymbol{y}; \boldsymbol{x})$ that defines the real value of the t-th output signal ($t = 1,2,...,m$).

B. Substructure Functions of Logic Network with Multiple Outputs

The structure function (8) and (9) allows analyzing the correlation between values of input signals and the correct work of the network (i.e. correct work of all outputs) on one side and correlation between activity of logic gates and the correct work of all outputs on the other side. However, it can also be useful to analyze these correlations with respect to only one output. Therefore, using notation (9), we can define m substructure functions:

$$\phi_t(\boldsymbol{x}; \boldsymbol{y}) = \{F_{t,o}(\boldsymbol{y}; \boldsymbol{x}) \leftrightarrow F_t(\boldsymbol{y})\}, \text{ for } t = 1,2,...,m, \quad (10)$$

that describe the relation between the correct work of the t-th output and values of input signals and operability of individual logic gates.

Clearly, according to the previous paragraphs, the structure function of a general logic network can also be defined in the following way:

$$\phi(\boldsymbol{x}; \boldsymbol{y}) = \phi_1(\boldsymbol{x}; \boldsymbol{y}) \wedge \phi_2(\boldsymbol{x}; \boldsymbol{y}) \wedge ... \wedge \phi_m(\boldsymbol{x}; \boldsymbol{y}). \quad (11)$$

According to the previous formula, the structure function of a logic network with multiple outputs can be simply derived from substructure functions of individual outputs.

C. Unreliable Logic Gates

Every logic gate realizes some logic function (e.g. AND, OR, etc.). However, this is true if the gate is functional. Now, assume that the failed gate in mathematical interpretation generates signals that can also be interpreted as values 0 or 1. This assumption implies that the broken gate realizes a logic function too, but it is different from the original one. Therefore, the failure

of a logic gate can be modeled as a change of function realized by the gate [6 and 12].

Consider a logic network of n logic gates. The i-th gate of the network realizes two different functions depending on the state (functional/failed) of the gate: (i) when the gate is functional, then it implements function $f_i(\boldsymbol{y})$, (ii) when it is broken, then it realizes function $f_{i,u}(\boldsymbol{y})$. Therefore, the unreliable logic gate is a realization of function $f_{i,o}(\boldsymbol{y}; x_i)$ [12]:

$$f_{i,o}(\boldsymbol{y};x_1) = x_i f_i(\boldsymbol{y}) \vee \overline{x}_i f_{i,u}(\boldsymbol{y}). \quad (12)$$

When functions $f_{i,u}(\boldsymbol{y})$ are known for all logic gates of the network, function $F_{t,o}(\boldsymbol{y}; \boldsymbol{x})$, which defines the real value of the t-th output of the network, can be obtained simply by replacement of every logic gate in the scheme of the network by functions $f_{i,o}(\boldsymbol{y})$ of individual gates and then the substructure functions (10) and the structure function (11) can be identified.

D. Direct Partial Logic Derivatives

Direct Partial Logic Derivatives (DPLDs) are part of logical differential calculus that has been developed to analyze dynamic properties of Boolean functions [13]. The structure function can also be interpreted as a Boolean function and, therefore, DPLDs can be used in reliability analysis [8].

In paper [12], two types of DPLDs of the structure function have been considered in the analysis of a logic network. The first one is defined as follows:

$$\frac{\partial \phi(j \to \overline{j})}{\partial x_i(a \to \bar{a})} = \{\phi(a_i, \boldsymbol{x}; \boldsymbol{y}) \leftrightarrow j\} \wedge \{\phi(\overline{a}_i, \boldsymbol{x}; \boldsymbol{y}) \leftrightarrow \overline{j}\}, \quad (13)$$

where $\phi(a_i, \boldsymbol{x}; \boldsymbol{y}) = \phi(x_1, x_2, ..., x_{i-1}, a, x_{i+1}, ..., x_n; \boldsymbol{y})$, $a, j \in \{0, 1\}$.

DPLD (13) identifies situations when the failure/repair of given component results system failure/repair [8, 11 and 12]. However, the structure function of a logic network depends not only on states of individual components (logic gates) but also on the values of individual input signals. Therefore, we can define another logic derivative that analyzes situations in which the change of given input results the failure/repair of the logic network:

$$\frac{\partial \phi(j \to \overline{j})}{\partial y_l(a \to \bar{a})} = \{\phi(\boldsymbol{x}, a_l; \boldsymbol{y}) \leftrightarrow j\} \wedge \{\phi(\boldsymbol{x}, \overline{a}_l; \boldsymbol{y}) \leftrightarrow \overline{j}\}, \quad (14)$$

where $\phi(\boldsymbol{x}; a_l, \boldsymbol{y}) = \phi(\boldsymbol{y}; y_1, y_2, ..., y_{l-1}, a, y_{l+1}, ..., y_n)$, $a, j \in \{0, 1\}$.

These two DPLDs can also be defined for individual substructure functions of the system. In this case, DPLD (13) has the following form:

$$\frac{\partial \phi_t(j \to \overline{j})}{\partial x_i(a \to \bar{a})} = \{\phi(a_i, \boldsymbol{x}; \boldsymbol{y}) \leftrightarrow j\} \wedge \{\phi(\overline{a}_i, \boldsymbol{x}; \boldsymbol{y}) \leftrightarrow \overline{j}\}, \quad (15)$$

and it can be used to detect situations in which the failure/repair of given logic gate results in the failure of the t-th output, i.e. situations when the real value of the t-th output is different from the expected one.

Similarly, DPLD (14) can be defined for system substructure function as follows:

$$\frac{\partial \phi_t(j \to \overline{j})}{\partial y_l(a \to \bar{a})} = \{\phi_t(\boldsymbol{x}, a_l; \boldsymbol{y}) \leftrightarrow j\} \wedge \{\phi(\boldsymbol{x}, \overline{a}_l; \boldsymbol{y}) \leftrightarrow \overline{j}\}. \quad (16)$$

Derivatives (13) – (16) are very similar, but there is a principal difference in their meaning and use. DPLDs (13) and (15) analyze the impact of the failure/repair of given component and, therefore, they can be used in importance analysis to find components with the most influence on the system proper work. On the other hand, DPLDs (14) and (16) are useful in the creation of test cases for detection of failed logic gates, because, when some gates are failed, then these DPLDs reveal situations in which the change of given input signal causes the change of the value of the structure function [12 and 14].

E. Structural Importance Measure

System availability (3) is very important measure that defines the probability that the system is working. However, it does not allow us to find the influence of individual system components on the system activity, i.e. to identify which components are the most important for proper work of the system. For this purpose, there exist other measures that are known as *Importance Measures* (IMs) [15].

One of the basic IMs is *Structural Importance Measure* (SIM) that estimates the topological influence of given component on the system work. For noncoherent systems, it is defined as the relative number of situations in which the change of system component state (component failure/repair) results in the system failure [11].

In paper [12], two types of the SIM for logic network with one output have been considered. The first one estimates the topological importance of given component when the exact values of input signals are known. This SIM is defined for given logic gate and given vector $\boldsymbol{s}$ of input signals as follows:

$$SIM_{i,y=s} = \frac{\rho(\partial \phi_{y=s}(1 \to 0) / \partial x_i(1 \to 0))}{2^{n-1}} + \\ + \frac{\rho(\partial \phi_{y=s}(1 \to 0) / \partial x_i(1 \to 0))}{2^{n-1}}, \quad (17)$$

where $\phi_{y=s}(\boldsymbol{x}) = \phi(\boldsymbol{x}; \boldsymbol{y} = \boldsymbol{s}) = \phi(\boldsymbol{x}; s_1, s_2, ..., s_k)$ and $\rho(.)$ is the function that returns the number of state vectors for which the argument has nonzero, i.e. true value. For example $\rho(x_1 \vee x_2) = 3$, because the logic function $x_1 \vee x_2$ is true for 3 state vectors, i.e. (0,1), (1,0) and (1,1); $\rho(x_1 x_2) = 1$, because the logic function $x_1 x_2$ has true value only for state vector (1,1).

The SIM (17) permits to identify which gates are the most important for given values of input signals, but, it does not allow analyzing the overall influence of given gate on the proper work of the network. For this purpose, another type of the SIM has been defined in paper [12]. Using the SIM (17), this IM is defined in the following way:

$$SIM_i = \sum_{s\in\{0,1\}^k} \Pr\{y = s\} SIM_{i,y=s}, \tag{18}$$

where $[0, 1]^k$ is the space of all possible input signals.

In the case of a logic network with multiple outputs, definitions (17) and (18) can be used in two ways. Firstly, they can be used with the structure function (8) of the network. In this case, they have the same meaning as those proposed in paper [12] because they analyze the influence of given gate on the whole logic network. On the other hand, the structure function $\phi_{y=s}(\boldsymbol{x})$ in (17) can be replaced by the substructure function $\phi_{t,y=s}(\boldsymbol{x}) = \phi_t(\boldsymbol{x}; \boldsymbol{y} = \boldsymbol{s}) = \phi_t(\boldsymbol{x}; s_1, s_2, ..., s_k)$. In this case, SIM (17) will identify the influence of gate i on the correct value of the t-th output when individual input signals have values $s_1, s_2, ..., s_k$ and SIM (18) will estimate the total topological influence of component i on the correct value of the t-th output.

4. Case Study: One-bit Full Adder

F. Structure and Substructure Functions

Consider a one-bit full adder that is implemented according to the scheme depicted in Fig. 1. It has three input signals where y_1 and y_2 represent bit operands and y_3 represents a bit carried from the previous less significant stage, and 2 outputs whose behavior is defined by functions $F_1(\boldsymbol{y})$ (an output bit) and $F_2(\boldsymbol{y})$ (a carry out bit).

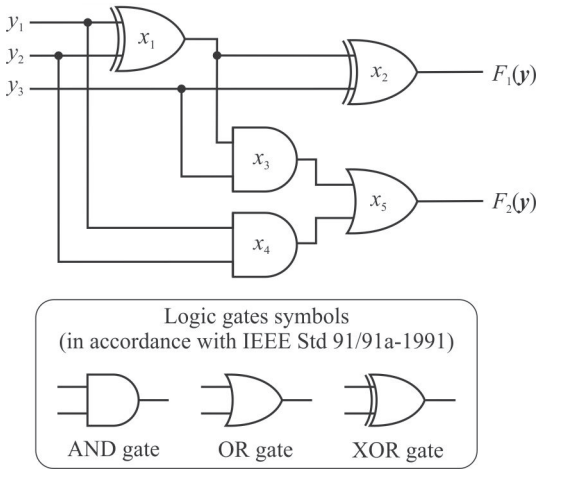

Fig. 1. A one-bit full adder

According to the scheme in Fig. 1, the outputs of the adder are realized as follows:

$$\begin{aligned} F_1(\boldsymbol{y}) &= \mathrm{XOR}(\mathrm{XOR}(y_1, y_2), y_3) = (y_1 \oplus y_2) \oplus y_3, \\ F_2(\boldsymbol{y}) &= \mathrm{OR}(\mathrm{AND}(\mathrm{XOR}(y_1, y_2), y_3), \\ AND &= (y_1, y_2)) = (y_1 \oplus y_2) y_3 \vee y_1 y_2, \end{aligned} \tag{19}$$

where symbol $\oplus$ denotes exclusive or (XOR).

Equations (19) define the expected values of the output signals. Now, we need to find their real values. This can be done simply by replacement of every logical operator using (12). So, we get the next formula for the first output:

$$\begin{aligned} F_{1,o}(\boldsymbol{y};\boldsymbol{x}) &= x_2 \mathrm{XOR}(x_1 \mathrm{XOR}(y_1, y_2) \vee \overline{x_1} f_{1,u}(y_1, y_2) y_3) \\ &\vee \overline{x_2} f_{2,u}(x_1 \mathrm{XOR}(y_1, y_2) \vee \overline{x_1} f_{1,u}(y_1, y_2) y_3), \end{aligned} \tag{20}$$

where $f_{1,u}(\boldsymbol{y})$ represents the logic function that is realized by the 1-st logic gate when it is failed and $f_{2,u}(\boldsymbol{y})$ represents the logic function realized by the failed 2-nd gate. Similarly, we can identify the real value of the second output.

There are different types of failures in logic networks [5 and 16]. For the simplicity, assume that the failure of the XOR gates results that they will generate only value 1 regardless of the values of input signals while the failure of the AND and OR gates causes that they will generate only 0-signal on the output. Using this assumption, the real outputs of the adder are:

$$\begin{aligned} F_{1,o}(\boldsymbol{y};\boldsymbol{x}) &= x_2((x_1(y_1 \oplus y_2) \vee \overline{x_1}) \oplus y_3) \vee \overline{x_2}, \\ F_{2,o}(\boldsymbol{y};\boldsymbol{x}) &= x_5(x_3(x_1(y_1 \oplus y_2) \vee \overline{x_1}) y_3 \vee x_4 y_1 y_2). \end{aligned} \tag{21}$$

In the next step, the substructure functions $\phi_1(\boldsymbol{x}; \boldsymbol{y})$ and $\phi_2(\boldsymbol{x}; \boldsymbol{y})$ can be identified by comparing functions $F_{1,o}(\boldsymbol{y}; \boldsymbol{x})$ and $F_{2,o}(\boldsymbol{y}; \boldsymbol{x})$ from (21) with functions $F_1(\boldsymbol{y})$ and $F_2(\boldsymbol{y})$ from (19) according to definition (10) of the substructure function. After using some rules of Boolean algebra, the following equations can be obtained:

$$\begin{aligned} \phi_1(\boldsymbol{x};\boldsymbol{y}) &= x_1 x_2 \vee x_2 y_1 \overline{y_2} \vee x_2 \overline{y_1} y_2 \vee \overline{x_2} y_1 y_2 y_3 \vee \\ &\overline{x_2}\,\overline{y_1}\,\overline{y_2} y_3 \vee y_1 \overline{y_2}\,\overline{y_3} \vee \overline{y_1} y_2 \overline{y_3}, \\ \phi_1(\boldsymbol{x};\boldsymbol{y}) &= x_1 x_3 x_5 \overline{y_1} \vee \overline{x_1} x_3 x_5 y_2 y_3 \vee x_3 x_5 y_1 \overline{y_2} \vee \\ &\overline{x_3}\,\overline{y_1}\,\overline{y_2} \vee x_4 x_5 y_1 y_2 \vee \overline{x_5}\,\overline{y_1}\,\overline{y_2} \vee \overline{y_1}\,\overline{y_3} \vee \overline{y_2}\,\overline{y_3}. \end{aligned} \tag{22}$$

The first (second) equation identifies all conditions that ensure that the first (second) output will generate the correct value. For example, according to the first equation, the first output is correct when both XOR gates are working $(x_1 x_2)$, or the second XOR gate is working and values of the 1-st and 2-nd input are 1 and 0 respectively $(x_2 y_1 \overline{y_2})$, or the second XOR gate is working and values of the 1-st and 2-nd input are 0 and 1 respectively $(x_2 \overline{y_1} y_2)$, or the second XOR gate is failed and all input signals have value 1 $(\overline{x_2} y_1 y_2 y)$, etc.

The previous equations define the relations between states of individual logic gates, values of input signals and correctness of individual outputs and, therefore, they are useful for analysis of this kind of dependencies. However, they do not allow us to evaluate the reliability of the network as a whole. For this purpose, the structure function has to be found. This can be done using definition (11) of the structure function:

$$\phi(\boldsymbol{x};\boldsymbol{y}) = x_1x_2x_3x_5\overline{y_1} \vee x_1x_2x_3x_5y_1\overline{y_2} \vee x_1x_2\overline{x_3}\,\overline{y_1}\,\overline{y_2} \vee x_1x_2x_4x_5y_1y_2 \vee x_1x_2\overline{x_5}\,\overline{y_1}\,\overline{y_2} \vee x_1x_2\overline{y_1}\,\overline{y_3} \vee x_1x_2\overline{y_2}\,\overline{y_3} \vee x_2x_3x_5y_1\overline{y_2} \vee \overline{x_1}x_2x_3x_5\overline{y_1}y_2y_3 \vee \overline{x_1}\,\overline{x_2}x_3x_5y_1y_2y_3 \vee \overline{x_2}x_4x_5y_1y_2y_3 \vee x_1\overline{x_2}x_3x_5\overline{y_1}y_2y_3 \vee \overline{x_2}\,\overline{x_3}\,\overline{y_1}y_2y_3 \vee \overline{x_2}x_5\overline{y_1}y_2y_3 \vee y_1\overline{y_2}\,\overline{y_3} \vee \overline{y_1}y_2\overline{y_3} \quad (23)$$

According to definition (3), the overall network availability, i.e. the probability that both outputs are correct, can be computed from formula (23) if the availabilities of individual logic gates and probabilities of individual values of input signals are known.

G. Topological Analysis of the One-bit Full Adder

Consider the one-bit full adder in Fig. 1. Using equations (17) and (18), the topological importance of every gate can be computed if the probabilities of values of input signals are known. For this purpose assume that the input signals have probabilities defined in Table 1.

When we want to analyze the topological importance of individual logic gates, the values of SIMs (17) have to be computed for every combination of input signals for every component. This implies that DPLDs (13) should be computed and, then, numbers of state vectors, for which the DPLDs are true, have to be identified. For illustration, these numbers are presented in Table 2 for the first 3 components.

The Probabilities of Individual Values of Input Signals of the One bit-Adder — Table 1

Input signal	Probability of value 0	Probability of value 1
y_1	0.5	0.5
y_2	0.5	0.5
y_3	0.75	0.25

When the DPLDs and numbers of their nonzero elements are computed, then we can calculate the SIMs (17) for individual logic gates (Table 3).

Finally, using the probabilities in Table 1 and the SIMs in Table 3, the overall SIMs (18) of individual logic gates can be computed. These values are computed in Table 4.

SIMs of Logic Gates for Individual Input Signals — Table 3

Vectors of Input Signals	$SIM_{1,y=s}$	$SIM_{2,y=s}$	$SIM_{3,y=s}$	$SIM_{4,y=s}$	$SIM_{5,y=s}$
(0,0,0)	0.5	0.5	0	0	0
(0,0,1)	0.625	0.375	0.125	0	0.125
(0,1,0)	0	0	0	0	0
(0,1,1)	0	0.25	0.25	0	0.25
(1,0,0)	0	0	0	0	0
(1,0,1)	0	0.25	0.25	0	0.25
(1,1,0)	0.125	0.125	0	0.125	0.125
(1,1,1)	0.1875	0.1875	0.0625	0.3125	0.4375

The Overall SIMs of Logic Gates in the One-bit Adder — Table 4

Logic Gate	SIM_i
x_1	0.167969
x_2	0.183594
x_3	0.042969
x_4	0.042969
x_5	0.089844

According to Table 4 the most important components of the one-bit full adder are the first and second XOR gate, i.e. gates 1 and 2, while gates 3 and 4 (AND gates) have the smallest

Numbers of Nonzero Elements of Individual DPLDs — Table 2

Vectors of Input Signals	$\rho\left(\frac{\partial\phi_{y=s}(1\to 0)}{\partial x_1(1\to 0)}\right)$	$\rho\left(\frac{\partial\phi_{y=s}(1\to 0)}{\partial x_1(1\to 0)}\right)$	$\rho\left(\frac{\partial\phi_{y=s}(1\to 0)}{\partial x_2(1\to 0)}\right)$	$\rho\left(\frac{\partial\phi_{y=s}(1\to 0)}{\partial x_2(1\to 0)}\right)$	$\rho\left(\frac{\partial\phi_{y=s}(1\to 0)}{\partial x_3(1\to 0)}\right)$	$\rho\left(\frac{\partial\phi_{y=s}(1\to 0)}{\partial x_3(1\to 0)}\right)$
(0,0,0)	8	0	8	0	0	0
(0,0,1)	10	0	0	6	0	2
(0,1,0)	0	0	0	0	0	0
(0,1,1)	0	0	4	0	4	0
(1,0,0)	0	0	0	0	0	0
(1,0,1)	0	0	4	0	4	0
(1,1,0)	2	0	2	0	0	0
(1,1,1)	2	1	0	3	1	0

influence. Therefore, we should focus on the XOR gates in other phases of reliability analysis.

5. Conclusion

Logic networks are special type of systems from reliability point of view because their structure function depends not only on states of their components (logic gates) but also on other characteristics that can be identified as the environment influence. This influence is included in input signals whose values do not depend on the network properties but on the environment in which the network is situated.

Most techniques of reliability engineering assume that the studied system is coherent. However, this assumption is not valid for logic networks because there can exist situations when the failure of some logic gate results that the network begin generate the correct output signal, while, before the failure, the output signal has been incorrect [12]. Therefore, the reliability analysis of logic networks is more complicated than analysis of other types of systems.

One of the principal steps of reliability analysis is identification of the system structure function. In paper [12], there has been proposed a method for this task when the analyzed system is a logic network with one output. That method is based on the assumption that a real logic gate is unreliable and, therefore, its output depends on whether it is working or failed. In this paper, we generalized this concept on logic networks with multiple outputs.

Two types of structure functions can be identified in a logic network with multiple outputs. The first one is the structure function of the whole network that characterizes the network as a whole because it defines the dependency between proper work of logic gates and the correct values of all outputs. This structure function can be used to estimate network availability or to analyze the importance of individual logic gates for the proper work of the network.

The second ones are the substructure functions of individual network outputs. They define the correlation between the proper work of individual logic gates and the correct value of one output signal. These functions can be used to evaluate the influence of logic gates on the value of studied output signal and, therefore, they can be used in importance analysis or in creating scenarios for identification of failed logic gates.

In the last part of this paper, we focused on the use of the structure and substructure functions in importance analysis. We proposed the definitions of the SIM for logic networks with multiple outputs. Our definitions are based on logical differential calculus and they allow identify which components have the most influence on the proper work of the whole network or on the correct value of one concrete output signal from topological point of view. Although results of this paper have more theoretical significance, a case study considered at the end of this paper indicates that our approach is useful and its further development and practical implementation could be beneficial for reliability analysis of logic networks.

Acknowledgment

This work was partially supported by the research grants of Slovak Research and Development Agency SK-PL-0023-12 and VEGA 1/0498/14.

References

[1] SHOOMAN, M. L.: *Reliability of Computer Systems and Networks: Fault Tolerance, Analysis, and Design*. New York, : John Wiley & Sons, 2002.

[2] RADOS, I., SCHWARTZ, L.: The Worst Availability as a Parameter for Designing and Reporting on the Network Performances, *Communications - Scientific Letters of the University of Zilina*, vol. 13, No. 1, pp. 60-66, 2011.

[3] BRIS, R.: Assessment of the Availability of an Offshore Installation by Stochastic Petri Net Modeling, *Communications - Scientific Letters of the University of Zilina*, vol. 16, No. 1, pp. 90-96, 2014.

[4] TAYLOR, E., FORTES, J.: *Faults, Error Bounds and Reliability of Nanoelectronic Circuits,* 2005 IEEE Int. Conf. Appl. Syst. Archit. Process., pp. 247-253, Jul. 2005.

[5] FRANCO, D. T., VASCONCELOS, M. C., NAVINER, L., NAVINER, J.-F.: Signal Probability for Reliability Evaluation of Logic Circuits, *Microelectron. Reliab.*, vol. 48, No. 8-9, pp. 1586-1591, Aug. 2008.

[6] HAN, J., CHEN, H., BOYKIN, E., FORTES, J.: Reliability Evaluation of Logic Circuits Using Probabilistic Gate Models, *Microelectron. Reliab.*, vol. 51, No. 2, pp. 468-476, Feb. 2011.

[7] RAUSAND, M., HØYLAND, A.: *System Reliability Theory: Models, Statistical Methods, and Applications*. Haboken, : John Wiley & Sons, Inc., 2004.

[8] ZAITSEVA, E. N., LEVASHENKO, V. G.: Importance Analysis by Logical Differential Calculus, *Autom. Remote Control*, vol. 74, No. 2, pp. 171-182, Feb. 2013.

[9] ANDREWS, J. D., BEESON, S.: Birnbaum's Measure of Component Importance for Noncoherent Systems, *IEEE Trans. Reliab.*, vol. 52, No. 2, pp. 213-219, Jun. 2003.

[10] BEESON, S., ANDREWS, J. D.: Importance Measures for Non-coherent-system Analysis, *Reliab. IEEE Trans.*, vol. 52, No. 3, pp. 301-310, Sep. 2003.

[11] KOSTOLNY, J., KVASSAY M., KOVALIK, S.: Reliability Analysis of Noncoherent Systems by Logical Differential Calculus and Binary Decision Diagrams, *Communications - Scientific Letters of the University of Zilina*, vol.16, No. 1, pp. 114-120, Feb. 2014.

[12] ZAITSEVA, E., KVASSAY, M., LEVASHENKO, V., KOSTOLNY, J.: Reliability Analysis of Logic Network by Logical Differential Calculus, *ELEKTRO, 2014*, May 2014, pp. 245-250.

[13] YANUSHKEVICH, S. N., MILLER, D. M., SHMERKO, V. P., STANKOVIC, R. S.: *Decision Diagram Techniques for Micro- and Nanoelectronic Design. Handbook*. Boca Raton, FL: CRC Press, 2006.

[14] CHANGQIAN, W., CHENGHUA, W.: *A Method for Logic Circuit Test Generation Based on Boolean Partial Derivative and BDD,* World Congress on Computer Science and Information Engineering, pp. 499-504, Mar. – Apr. 2009.

[15] KUO, W., ZHU, X.: *Importance Measures in Reliability, Risk, and Optimization: Principles and Applications*. Chichester,: John Wiley & Sons, Ltd., 2012.

[16] LEVASHENKO, V., MORAGA, C., SHMERKO, V., KHOLOVINSKI, G., YANUSHKEVICH, S.: Test Algorithm for MVL Combinational Circuits, *Autom. Remote Control*, vol. 61, No. 5, pp. 844-857, May 2000.

Roman Radil - Jan Barabas - Patrik Kamencay *

NEW APPROACH TO METAL BIOMARKER DETECTION USING NONIONIZING ELECTROMAGNETIC FIELD

Medical detection techniques used for preoperative scanning of certain marked areas are mostly based on ionizing radiation as it is in case of CT. This paper provides an unusual approach to detection of metal biomarkers implanted into the human body, based on nonionizing radiation and discusses problems and complications connected with chosen technique.

Keywords: *Non-destructive evaluation; eddy current testing, metal biomarker detection, modeling and numerical simulation.*

1. Introduction

The development in medicine and material engineering produced a group of materials called biomarkers which are used to highlight a specific part of biological object, mainly during diagnostic processes. This group consists of materials such as special dyes, plastics or metals. One could manage to write a book which would deal with the whole group of biomarkers, but the aim of this work is only the group of small metal biomarkers and their detection.

Metal biomarkers with a size of a few mm are often implanted into soft tissue of oncological patients to indicate the treated area of a tumor during the radiotherapy, and to observe further development of the disease in this area, as it is mentioned in [1]. That's why their correct detection is very important.

These biomarkers could be easily detected via commonly used medical detection techniques such as computer tomography (CT) or X-ray imaging, as it was published in [1, 2 and 3]. The only disadvantage of these methods is that they are based on ionizing radiation and thus are harmful for human organism. An alternative for the detection could be provided by ultrasound. But the ultrasound probes are principally designed to focus on soft tissues, and need not resolve problems with detection of biomarker implanted into the bone. That's the reason for investigation of alternative detection methods.

2. Materials and methods

The aim of this work is to present some innovative ideas for the detection of small metal biomarkers. The first step of this investigation is selection of proper detection method which should not be anyway invasive or potentially harmful. According to research currently being pursued at the Department of electromagnetic and biomedical engineering at the University of Zilina, the most likely method to begin with is eddy current testing (ECT). This technique is not common in medical environment, but under certain conditions, it could principally help to solve some of the medical problems.

a. Eddy current testing principle

Non-destructive evaluation (NDE) is recently a very progressive industrial method used for determination of surface and subsurface defects, leaks, discontinuities, thermal anomalies, etc. ECT represents one branch of NDE. Eddy current testing is widely used for quality assurance of structural components made of conducting materials [4]. Its principle comes out from the electromagnetic induction phenomena. When a probe is electromagnetically linked with a part under inspection, the alternating magnetic field created by the probe driven with alternating current induces eddy currents in the test part [5]. Discontinuities or property variations in the test part change the flow pattern of the eddy currents and this change can be detected by the probe. The simple scheme of the ECT method principle is shown in Fig. 1.

* [1]**Roman Radil, [1]Jan Barabas, [2]Patrik Kamencay**
[1]Department of Electromagnetic and Biomedical Engineering, Faculty of Electrical Engineering, University of Zilina, Slovakia
[2]Department of Telecommunications and Multimedia, Faculty of Electrical Engineering, University of Zilina, Slovakia
E-mail: roman.radil@fel.uniza.sk

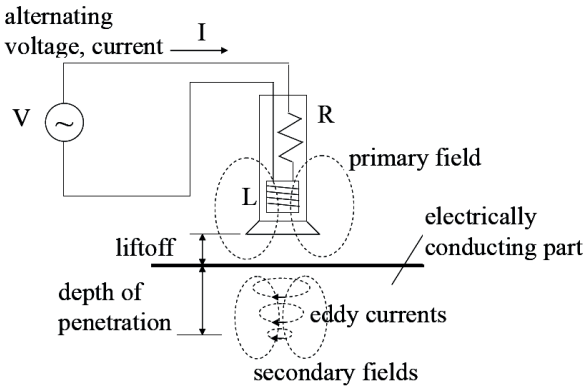

Fig.1 Eddy current testing principle [2]

b. Biomarker selection

It is well known that all implantable materials, not only biomarkers, must fulfill certain specific conditions of biocompatibility, which means that not all of the metal materials could be used as biomarkers. A very frequent solution to this problem in medicine is utilization of noble metals, especially gold. For this reason a gold biomarker shown in Fig. 2, called BiomarC, produced by the Aptum company, was selected.

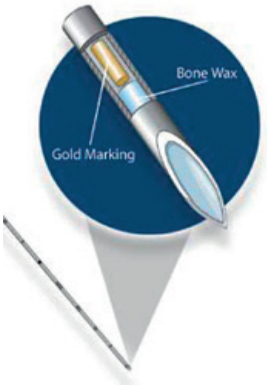

Fig. 2 BiomarC – gold biomarker at a size of 1.2 x 3 mm located in the needle tip

Since gold represents a perfect conductive material, in comparison with human bone, the principle of ECT detection method could produce significant results. To verify the application of ECT method, the means of numerical simulations were used.

3. Biological tissue modeling

Biological environment, in which the biomarker should be detected, is a multilayer environment which could be generally divided into four layers - tissues: skin, fat, muscle and bone. Each of these tissues is characterized by its own dielectric properties which are frequency dependent. The frequency dependence of biological tissues in correlation with applied electromagnetic field (EMF) has been proven by many research works, some of which could be found in [6]. Tissue dielectric properties could be in general characterized by their relative permittivity:

$$\varepsilon_{rel} = \varepsilon' - i\varepsilon'', \tag{1}$$

where ε' is relative permittivity of material, and ε'' is the out-phase factor which can be computed as:

$$\varepsilon'' = \frac{\kappa}{\varepsilon_0 \omega'} \tag{2}$$

where κ is the total conductivity of material which also may contain a frequency-independent ionic contribution, ε_0 is vacuum permittivity and ω is angular velocity.

With respect to the tissue dielectric properties in a wide frequency range, a high resolution model of human body has been created by authors in several research works [7, 8 and 9].

From the aforementioned, it is clear that the biological modeling should reflect the environment inhomogeneity and variability of the dielectric properties. According to this, two modeling phantoms could be basically defined:

- tomographic phantom,
- stylized phantom.

"*Tomographic phantoms are obtained from modern medical imaging techniquesas the Magnetic Resonance Imaging (MRI), or the CT and represent the body by sampled volume pixels, the so-called voxels.*

Stylized phantoms describe the human anatomy by using simple mathematical equations of analytic geometry" [6].

4. Experimental section

As the primary problem of this work is the biomarker detection, the problem with the modeling of biological tissues was simplified, thus the stylized phantom approach was deemed as sufficient. Furthermore, the region of the gold biomarker insertion was consulted with medical experts, and the area of pelvis where the thickness of tissue is only few mm, was chosen.

a. Modeling and numerical simulations

The decisions reduce the number of modeled layers to three – skin, subcutaneous fat and bone. So the model of biological environment could be created as shown in Fig. 3.

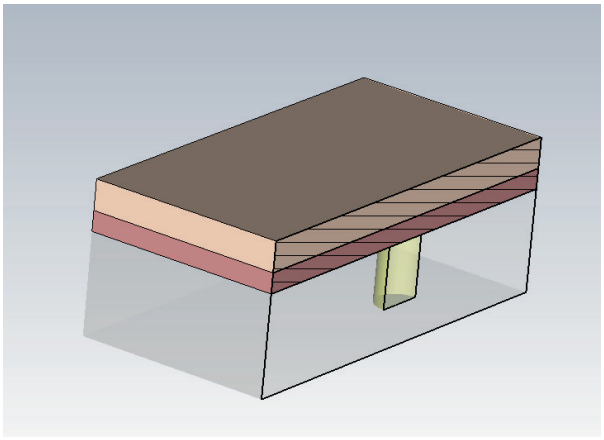

Fig. 3 Model of biological tissues with implanted gold biomarker - crossection

The dielectric properties of modeled tissues were changed according to the frequency of intended EMF application. An example of the fat tissue dielectric properties at a chosen frequency range is presented in Table 1.

Fat tissue dielectric properties [7, 8 and 9] Table 1

Frequency [kHz]	Conductivity [S/m]	Relative permittivity	Penetration depth [m]
5	0.023589	2816.5	47.118
9.5	0.023815	1161.4	33.894
14	0.023926	705.36	27.817
18.5	0.023999	502.77	24.144
23	0.024055	390.51	21.62
27.5	0.0241	319.83	19.749
32	0.024137	271.47	18.291
36.5	0.024169	236.41	17.114
41	0.024198	209.87	16.137
45.5	0.024223	189.1	15.31
50	0.024246	172.42	14.598

The data in Table 1 are computed using an application based on the parametric model for the calculation of the dielectric properties of body tissues developed by C. Gabriel et al. [7, 8 and 9]. The given frequency range was selected to be possibly verified via real measurements using the Rohmann GmbH ELOTEST B300 – a commercial device for ECT which works at 10 Hz - 10 MHz frequency range.

Before starting with the simulation an ECT probe has to be modeled. The probe was designed as a small copper wire coil, driven by 0.1 ampere sinusoidal current, wound around a ferrite core. To avoid noise produced by surrounding appliances, an iron casing was designed. The simplified scheme of the model is displayed in Fig. 4 together with the probe proportions.

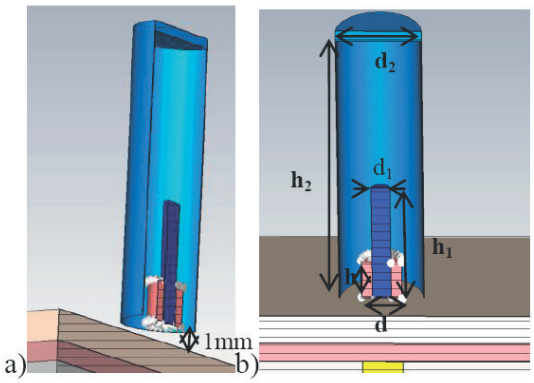

Fig. 4 Cross-section of probe modeling: a) location above the skin, b) probe parameters: external coil diameter d=2.2mm, winding height h= 2mm, core diameter d_1= 1.1mm, core height h_1= 6mm, diameter of the cover d_2=5mm, cover height h_2= 14.5mm

Once the model design is completed, the numerical simulations take place. Since the metal biomarker could be considered as an electrically small structure, the low frequency domain solver was chosen to conduct the computations. The solver is based on finite integration technique (FIT), which represents the discretization of each Maxwell equation. An example of grid creation using FIT is shown on Fig.5.

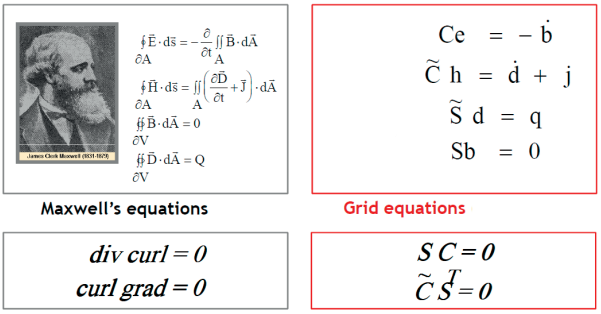

Fig. 5 Discretizing Maxwell's equations to create a grid

The choice of hexahedral mesh was essential to achieve the best geometry approximation available. Four simulation frequencies from the given frequency range were chosen to be calculated with. The said frequencies are 5, 10, 25 and 50 kHz. Results of the experiments with the gold biomarker detection using simulations can be seen as 3-D capture of electrical intensity field (E-field) in Fig. 6 where results of chosen calculation frequencies are compared.

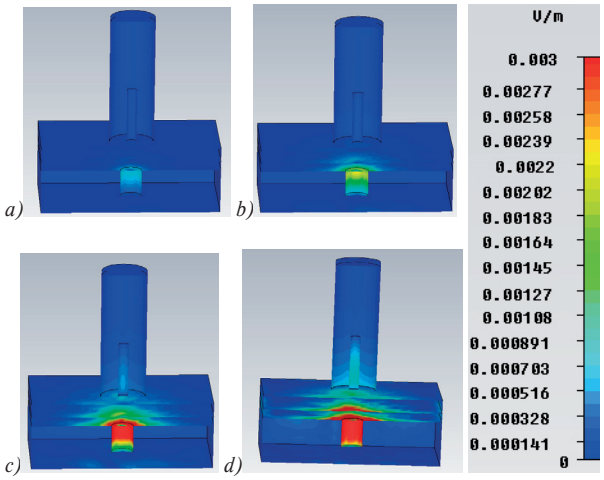

Fig. 6 Magnetoquasistatic simulation results – E-field at frequency: a) 5 kHz, b) 10 kHz, c) 25 kHz d) 50 kHz.

As can be seen from the color map of results, the higher the applied frequency is, the better the detection of the biomarker should be. But, on the other hand, the capture of E-field distribution should be considered in accordance with the absorption law theory and standards presented in [10]. This means the energy losses in soft tissues (especially skin) should be expected at higher frequencies, and for this reason it seems that the smaller frequency values up to 25 kHz could be optimal for the detection process.

b. Experimental verification of numerical simulations

Obtained simulation results showed a possibility of the biomarker detection using the ECT method. To verify the results, experiments with real measurements on 3D phantom model of human pelvis presented in Fig. 7, were collected.

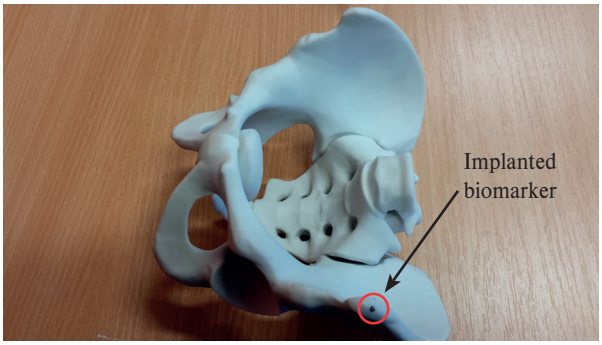

Fig. 7 3D phantom model of human pelvis with implanted biomarker

The ECT device ELOTEST B300, mentioned before in this article was chosen to be used for the real measurements. Also a special probe, proportionally comparable with the one modeled during the simulations, was used for eddy current excitation and detection. Both devices are depicted in Fig. 8.

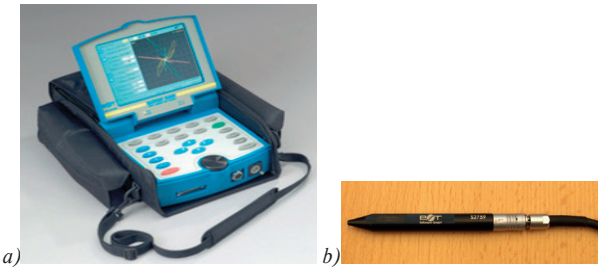

Fig. 8 ECT devices: a)Rohmann GmbH ELOTEST B300, b) ECT probe

Since there was no other material available to simulate at least a skin tissue, it was opted to measure each of the simulation frequencies at various distances from the pelvis surface to verify whether or not such a small gold particle could be detected. The detection process results show interesting contrast between numerical simulations and real measurements, which is documented by Table 2. The successful detections are marked as "1", undetected cases are marked as "-".

Results of measurements Table 2

Distance from surface [mm]	Frequency			
	1 kHz	10 kHz	25 kHz	50 kHz
0.5	-	1	1	1
1	-	-	1	1
3	-	-	-	1
5	-	-	-	-

To enhance the experimental verification of the numerical simulations, two more configurations were tested for the biomarker detection. The first one was the probe using a giant magneto-resistive (GMR) sensor as a detector while the second one uses an anisotropic magneto-resistive sensor (AMR) for detection. The function of both the GMR and AMR sensors is principally described in [11]. In our measurements two excitation coils were used to create the magnetic field which should change due to the presence of the biomarker, and these changes should be detected by the sensor. The whole probe composition is shown in Fig. 9, and results for each sensor are presented in Table 3.

The failure of the detection process led to only one conclusion – magneto-resistive sensors couldn't be used as detectors of the gold biomarkers. Furthermore, from the presented results it is clear that real life measurements uncovered new problems. On the one hand, it was confirmed to use the highest possible frequency (in case of ELOTEST), but, on the other hand, it was shown that the distance between the probe and detected biomarker should be very small as the last detected case was at frequency of 50 kHz in the distance of 2.5 mm. The detection distance is quite a big problem, especially when the influence of other biological tissues wasn't considered during the experiments. Another problem is supposed to be with the material magnetic properties of the used

Results conducted on two types of detection sensors Table 3

Distance from surface [mm]	Frequency AMR				Frequency GMR			
	1 kHz	10 kHz	25 kHz	50 kHz	1 kHz	10kHz	25 kHz	50 kHz
0.5	-	-	-	1	-	-	-	-
1	-	-	-	-	-	-	-	-
3	-	-	-	-	-	-	-	-
5	-	-	-	-	-	-	-	-

biomarker and its small dimensions. All mentioned problems could be considered as reasons for detection failure.

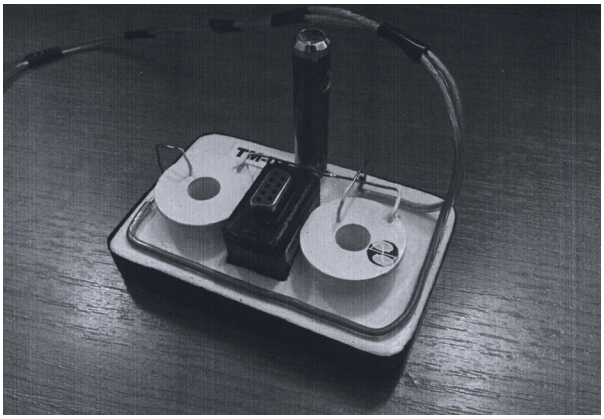

a)

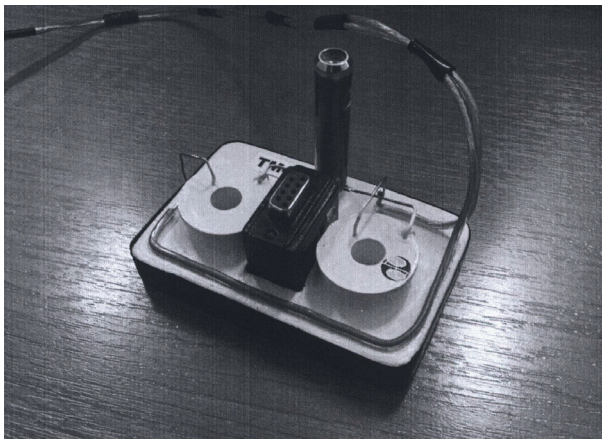

b)

Fig. 9 Composition of the detection probe using: a) AMR sensor b) GMR sensor

A. Research focused on problem solving

To address the observed problems further experiments were conducted regarding the ECT method. First of all, a new probe model was created. The probe was designed as a 3x3 matrix of previously created single coil sensors. The value of the driving current remains the same, with the exception of central coil which was designed as a detection coil to measure the changes caused by the presence of the biomarker in the tissue. The whole configuration as well as results of numerical simulations is illustrated in Fig. 10.

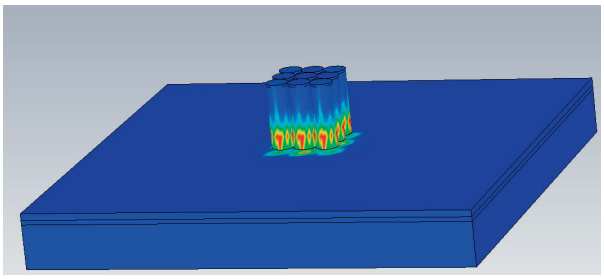

a)

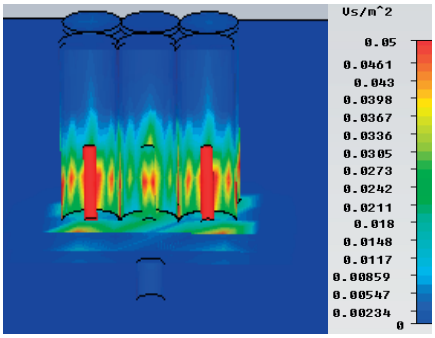

b)

Fig. 10 Simulation results: a) Matrix configuration of sensors, b) cross-section with induction changes on central detector

To verify this possibility of detection a matrix of GMR sensors, shown in Fig. 11 was used for measurements.

But as it is clear from the table, attached to the capture in Fig. 11, the only detected case was at the frequency of 100 kHz, so no progress was achieved.

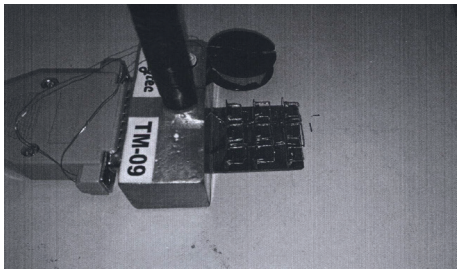

	1 kHz	5 kHz	10 kHz	50 kHz	100 kHz
0.5mm	0	0	0	0	1
1mm	0	0	0	0	0
3mm	0	0	0	0	0
5mm	0	0	0	0	0

Fig. 11 3x3 matrix of GMR sensors with detection results

5. Conclusion

According to the aim of presented work, an innovative approach to small metal biomarker detection using the ECT method was presented. Numerical simulation results uncover potential of the proposed method. Its main advantages include fast examination rate, non-invasiveness and cheapness.

But experiments with real measurements depict another picture and showed limits of the detection method. Probably the most important limitations identified as the main reasons of detection failure are: the distance between probe and biomarker, the biomarker dimensions and biomarker material.

As the biomarker dimensions must stay as low as possible, to solve the mentioned problems the biomarker material could be changed from gold to iron and thus better magnetic properties to strengthen the detection process can be obtained and obviously the detection distance can be enlarged. Of course, it cannot be forgotten that the biocompatibility must be assured in order of iron biomarker implementation.

The mentioned solution proposal together with other detection possibilities are currently investigated and results of this research will be published soon.

Acknowledgement

This work has been supported by the European Regional Development Fund and the Ministry of Education of the Slovak Republic, ITMS 26220220153 – Centre of competence for research and development in the area of diagnostics and therapy of oncological diseases.

References

[1] DEHNAD, H., NEDERVEEN, A.J., VAN DER HEIDE, U.A., VAN MORSELAAR, R.J.A., HOFMAN, P., LAGENDIJK, J.J.W.: Clinical Feasibility Study for the Use of Implanted Gold Seeds in the Prostate as Reliable Positioning Markers During Megavoltage Irradiation, *Radiotherapy and Oncology,* vol. 55, 2003, pp. 295-302

[2] KITAMURA, K., SHIRATO, H., SHIMIZU, S., SHINOHARA,N., HARABAYASHI, T., SHIMIZU, T., KODAMA, Y., ENDO, H., ONIMARU, R., NISHIOKA, S., AOYAMA, H., TSUCHIYA, K., MIYASAKA, K.: Registration Accuracy and Possible Migration of Internal Fiducial Gold Marker Implanted in Prostate and Liver Treated with Real-time Tumor-tracking Radiation Therapy (RTRT), *Radiotherapy and Oncology,* vol. 62, 2002, pp. 275-281

[3] KOTTE, A.N.T.J., HOFMAN,P., LAGENDIJK, J.J.W., VAN VULPEN, M., VAN DER HEIDE, U.A.: Intrafraction Motion of the Prostate During External-beam Radiation Therapy: Analysis of 427 patients with implanted fiducial markers, *Int. J. Radiation Oncology Biol. Phys.,* vol. 69, No. 2, 2007, pp. 419 - 425

[4] JANOUSEK, L., CAPOVA, K., GOMBARSKA, D., SMETANA, M.: Progress in Eddy-current Non-destructive Evaluation of Conductive Materials, *Acta Technica CSAV*, vol. 55, No. 1, 2010, pp. 13-28.

[5] STRAPACOVA, T., SMETANA, M., CAPOVA, K.: Non-destructive Investigation of the Artificial Heart Valves Using Eddy Current Testing – an Inovative Approach, *Lecture Notes in Computer Science*, vol. 7339, 2012, pp. 331-340.

[6] BARCHANSKI, A.: *Simulations of Low-Frequency Electromagnetic Fields in the Human Body*, Dissertation thesis. Darmstadt: Technische Universitat, 2007, pp.1-111

[7] GABRIEL, S., CORTHOUT, E., GABRIEL, C.: The Dielectric Properties of Biological Tissues: I. Literature Survey. *Physics in Medicine and Biology*, vol. 41, No. 11, 1996, pp. 2231-2249. ISSN: 1361-6560

[8] GABRIEL, S., LAU, R. W., GABRIEL, C.: The Dielectric Properties of Biological Tissues: II. Measurements in the Frequency Range 10 Hz to 20 GHz, *Physics in Medicine and Biology*, vol. 41, No.11, 1996, pp. 2251-2269, ISSN: 1361-6560

[9] GABRIEL, S., LAU, R. W., GABRIEL, C.: The Dielectric Properties of Biological Tissues: III. Parametric Models for the Dielectric Spectrum of Tissues, *Physics in Medicine and Biology*, vol. 41, No. 11,1996, pp. 2271-2293. ISSN: 1361-6560

[10] MICHAELSON, S. M.: *Human Exposure to Nonionizing Radiant Energy-Potential Hazards and Safety Standards*, Proc. of the IEEE, vol. 60, No. 4, 1972, pp. 389-421. ISSN: 0018-9219G.

[11] JANOUSEK, L., REBICAN, M. I., SMETANA, M., STRAPACOVA, T., DUCA, A., PERNISOVA, V.: Recent Innovative Solutions in Eddy Current Non-destructive Diagnosis, *Communications - Scientific Letters of the University of Zilina*, vol. 15, No. 2, 2013, pp. 102-108. ISSN 1335-4205.

Vasilios Zarikas - Theofilos Chrysikos - Konstantinos E. Anagnostou - Stavros Kotsopoulos
Panagiotis Avlakiotis - Charalambos Liolios - Theodoros Latsos - Georgios Perantzakis
Athanasios Lygdis - Dimitirios Antoniou - Asimakis Lykourgiotis *

WIRELESS TELEMETRY: CHANNEL CHARACTERIZATION AND STATISTICAL IMPUTATION OF MISSING VALUES

An implemented communication wireless telemetric system is presented. It has been built to serve as a measuring station at Thermopiles hot springs. The present work analyzes the method applying several models for adjusting and optimizing the functions of the system. The system also includes a unit that receives and stores data in an appropriate form, ready to be used for statistics. Data of critical physicochemical parameters are continuously measured, processed and transmitted over a wireless link. Path loss is investigated in order to ensure reliable signal reception. In the examined case study of low SNR region with the integrated in the open field sensors, missing data can be a common occurrence. The development of a mathematical technique, based on best prediction, for mitigating the missing values problem is of great significance in establishing a reliable system of wireless telemetry. A novel technique for handling missing values is proposed. An algorithm that evaluates missing values for imputation has been developed, based on a new general linear model analysis for prediction. The full detailed code, is explained and applied on the data that have been captured by the measuring station.

Keywords: *Telemetric communication system, path loss, measuring station, hydrogeology engineering, seismic activity, modeling/statistics.*

1. Introduction

In general, a wireless network with sensors is a system consisting of spatially distributed autonomous devices using sensors to cooperatively monitor a variety of context conditions, such as temperature, vibration/frequencies, acceleration/pressures, fields, pollutants, at different locations. Critical characteristics of a wireless network with sensors are: the size scale of sensor nodes, harsh context conditions, mobility/portability, network topology, communication failures, adjustability of dynamic operationand large scale of deployment. Such systems with sensors can be used in a variety of contexts of use; environmental monitoring, medical monitoring, acoustic/fields detection, military surveillance, or process monitoring.

In large surveys that carry on for extended time periods, it is very common to encounter the missing values problem. Measuring stations like the one under discussion, almost always comprise missing measurements. There is a variety of reasons that cause this problem, including extreme weather conditions, information system failures, power shutdowns, rare and unpredictable events, malicious acts, sensor blockages etc. Most of these events appear randomly contrary to machine failures that appear more often at the early stages of the measurements.

The proper treatment of missing values helps to address several concerns resulted by incomplete data. If there are cases with missing values which are systematically different from cases without missing values, the statistical inferences can be misleading. Moreover, missing data often decrease the precision of calculated statistical outputs since there is less information than originally designed. One more worry is that the assumptions behind many statistical procedures are based on complete cases, and missing values can complicate the theory required.

2. State of the art

In this work a measuring station is described comprising sensors for different physicochemical parameters of thermal waters (for a review of similar measuring stations see [1]). The station has been implemented for a particular hot spring located in Thermopiles, Greece. The factors that are continuously measured, using the constructed wireless network with sensors, are the concentration levels of radon in water, the water temperature to capture the flow rate and depth variations, PH to investigate the acidity variations, Redox potential to study the biologic load variations, and electrical conductivity as a measure of the salinity variations.

* [1]Vasilios Zarikas, [2]Theofilos Chrysikos, [1]Konstantinos E. Anagnostou, [2]Stavros Kotsopoulos, [1]Panagiotis Avlakiotis, [1]Charalambos Liolios
[1]Theodoros Latsos, [1]Georgios Perantzakis, [1]Athanasios Lygdis, [1]Dimitirios Antoniou, [2]Asimakis Lykourgiotis
[1]ATEI of Central Greece, Department of Electrical Engineering, Lamia, Greece
[2]University of Patras, Department of Electrical & Computer Engineering, Patras, Greece
E-mail: vzarikas@teilam.gr; kotsop@ece.upatras.gr

This study reports a) the models that have been used in order to tune and optimize the telemetric module of the measuring station, b) a novel statistical technique for handling missing values of the transmitted data, based on a new best for prediction general linear model technique and c) a detailed algorithm that realizes this mathematical method. In Appendix A the algorithm is described in pseudocode. .

The measuring station has been designed and implemented under the framework of a research project; it is a major research program that has received so far two national and EU research grants. The whole project has as a main scope to design, develop, test and optimize a novel system that integrates hardware and software modules capable to perform the required environmental measurements. It is also able to collect, maintain, transmit receive and store data. A second objective is to perform a modern statistical analysis of the data in order to understand their structure and capture the encoded information. Towards this scope we have developed, for the first time, an algorithm which is able to calculate the missing values for imputation based on a new best fitting polynomial designed to be the best as far as prediction is concerned.

A quite general architecture has been designed for the implemented platform. This platform includes also an independent source of energy via photovoltaic elements and a power management electronic module, see Fig. 1.

Fig. 1. The telemetric measuring station

In all telemetric measuring stations a crucial concern is how to minimize and consequently how to care missing values. The presented measuring station is an integrated system that was designed and adjusted after three evaluations in a way to minimize missing values for all the measuring factors from the sensors. However, it is always unavoidable such lost measurements to occur. Thus, it is important to fill in missing values. Common techniques that help impute missing values with estimated values are regression models or EM methods. The EM method assumes a distribution for the partially missing data and extract inferences on the likelihood under that distribution. Each iteration consists of an “E” step and an “M” step. The “E” step calculates the conditional expectation of the complete-data log likelihood given the observed data and the parameter estimates. In the “M” step, maximum likelihood estimates of the parameters are computed as though the missing data had been filled in. However note that the missing values are not being directly imputed. Instead, their functions are used in the log-likelihood.

The regression method instead computes multiple linear regression estimates. For every predicted case, the algorithms can even add a residual from a randomly selected complete case, a random normal deviate, or a random deviate from the t distribution. However this method and all its versions adopt the usual statistical criteria in model selection [2] which are designed to the target: find the model, wh ich “best”, under some distance criteria, fits the data. Since these criteria are, in principle, functions of the residual sum of squares [3] they can not address the need for the best prediction of the missing value. Nevertheless, these best fitting models are applied for prediction too, although these “distance” criteria were not designed for this purpose.

3. Telemetric system and Outdoor Path Loss Models

The data collection measuring station transmits the digital data through a wireless radio network (using the radio modem). The receiver main unit for data processing was placed in the campus of Technological Educational Institute (ATEI) of Central Greece, Lamia, Greece.

The wireless link between transmitter and receiver is considered to be Line of Sight (LOS). We assume that the transmitter collects all sensor data from a local wireless sensor network protocol (ZigBee) and then proceeds to transmit all data to the main receiver at the campus of ATEI in Lamia.

The status of the wireless channel characterization was studied on theoretical basis and the theoretical reliability was tested by performing a scenario of outdoor measurements using the portable broadband measuring device Narda Selective Radiation Meter - SRM 3006. The measurement experimental scenario followed the guidelines of the recommendation ΕΛΟΤ EN 61566, IEC 61566 [26-02-1999]. Based on this analysis, the main technical characteristics of the transmitter output, receiver input and antennae electrical & electromagnetic characteristics were estimated.

In order to estimate the average level of local mean strength at the receiver, we employed two different path loss models [4] - [6]. Antenna heights are considered to be sufficient to provide LOS and avoid blockage of local foliage. The terrain irregularities need to be accounted for, however, and these losses will be incorporated in a zero-mean Gaussian variable (in dB) for the large-scale variations of the local mean value of the received

power. For our calculations, the receiving antenna gain was not taken into consideration since we are interested in isolating the propagation phenomena from any possible variation of gains depending on whether an omni-directional antenna of low gain (2 dBi) or a high-gain directional antenna (9 dBi) will be employed [7] - [12].

We calculated as a sum of two independent processes: the distance-dependent path loss which is a deterministic loss due to free space propagation (provided by the idealistic Friis equation) [9], and the 'excess path loss', defined by Jakes as "the difference (in decibels) between the computed value of the received signal strength in free space and the actual measured value of the local mean received signal" [10].

The Free Space Model accounts only for the distance-dependent losses whereas the Log-Distance model incorporates the excess path loss as well, which, in this scenario, since LOS is considered, stands for the losses due to terrain and other geographical irregularities.

The average path loss (in dB) is provided by the following formula [13] for the Free Space Model:

$$P_L = 32.45 + 20\log_{10} f(MHz) + 20\log_{10} d(km) \quad (1)$$

The mathematical expression of the Log-Distance path loss model is given by [3]:

$$L_{total} = PL(d_0) + N\log_{10}\left(\frac{d}{d_0}\right) + X_\sigma \quad (2)$$

Where $PL(d_0)$ is the path loss at the reference distance, usually taken as (theoretical) free-space loss at 100 m, for outdoor propagation scenarios, N is the path loss distance exponent and Xs is a Gaussian random variable with zero mean and standard deviation of σ dB. N and σ are derived from experimental data. During our work a coverage probability of 95% was assumed and thus:

$$X_\sigma = z \times \sigma(dB) = 1.645 \times \sigma(dB) \quad (3)$$

Both models are suitable [1] for open areas unlike other models which are more practical for urban areas, such as the Hata and Okumura model [14] - [15].

In the case examined in this work, the path loss exponent assumes a value of 2 so as to express the free-space distance-dependent attenuation phenomena without incorporating any other losses. The zero-mean Gaussian variable is employed to express the 'excess path loss' and is set, in this paper, to a value of 6 dB so as to reflect losses due to terrain irregularities.

The distance required for signal propagation (T-R separation is approximately 38 km) calls for the employment of specific wireless technologies such as WiMax or LTE. Since in Greece LTE is provided in band 3 (1800 MHz), our calculations will focus on that frequency band. A bandwidth of 20 MHz is assumed and a medium-range LTE Base Station (BS) is assumed, with a maximum transmit power of 38 dBm. Since the LTE receiver sensitivity level for band 3 is -91 dBm, our main interest is to investigate the boundaries of reliable signal reception for distances close to, and beyond, the estimated T-R separation. Free Space model is more idealistic whereas the Log-Distance model may be more pessimistic but provides a "worst-case assumption" which is important when planning such long-distance links.

In our calculations, the antenna gain of the receiver unit was not included. The reason is that we want to provide estimations of the local mean value of the received signal at the "close proximity" of the receiver so as to provide numerical estimations without becoming dependent on the gain and directivity of receiver antennae. Results are depicted in Fig. 2 for both models.

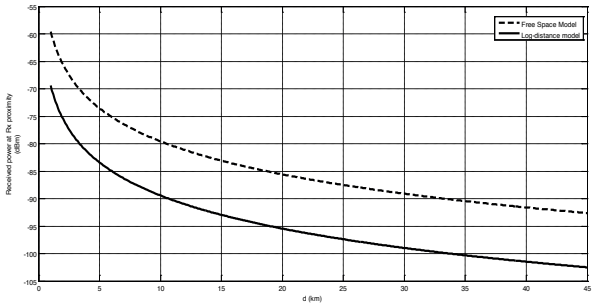

Fig. 2. Local mean value of received power as a function of distance

Figure 2 confirms that a dominant LOS component is essential for signal reception near the threshold. In the case of LOS propagation, where clearance of th 1st Fresnel zone is guaranteed, signal reception above receiver sensitivity level can be accomplished, thus allowing for a significant signal enhancement if a directional antenna is employed at the receiving end of the link. It should be reminded that in Fig. 2 results do not include antenna gain since the detection of signal levels above the sensitivity level in the proximity of the receiving antenna is investigated. Log-normal excess path loss can be discarded in a LOS-dominant propagation topology where the Free Space Model can provide reliable prediction of the local mean value of the received power (as a function of distance).

If scattering losses or any other excess path loss that does not comply with the distance-dependent free space attenuation assumption need to be considered, then signal reception drops below sensitivity level for LTE (-91 dBm) and outage occurs. In this case, the BS needs to be wide-area instead of medium-range.

In the case of low SNR region as the one examined in our case study, missing data can be a common occurrence. The development of a robust mathematical method for mitigating the missing values problem is of great significance in establishing a reliable system of wireless telemetry.

4. Imputation of missing data

In this study we propose a novel approach to the problem of missing values. Instead of applying the conventional linear regression models a new method which selects the best for prediction fitting model is followed [16], [17], [18] and [19]. The derived models used for imputing the missing values are therefore models optimized for prediction. They can best predict on the average the value which lies on a certain interval with some probability. This is achieved with the help of a mathematical quantity named beta expected tolerance regions. While the ordinary regression works with an extrapolation or interpolation of the best model fitting the data, the proposed technique lies on a probabilistic concept and suggests that model which best predicts a missing value within experimental region.

There are three distinct intervals in statistical analysis of data. For the problem of determining a missing value fitting a parameter to a model, the accuracy or precision may be described as a confidence interval, a prediction interval or a tolerance interval which are quite distinct.

Confidence intervals suggest how well the best-fit parameter determined by regression has been estimated. The crucial property is that confidence intervals provide information regarding the likely location of the true population parameter. On the other hand prediction intervals are different. They inform where next value sampled is expected to be found. The important point is that the prediction interval concerns the distribution of values, not the uncertainty in determining the population parameter.

The more demanding interval is the tolerance interval. It is defined on the basis of two percentages. The first percentage expresses "how sure" it is required the value to be and the second one represents what fraction of the values the interval will contain.

In our case a general linear model (GLM) can be expressed as $Y = T\beta + \sigma\varepsilon$ where $Y \in M_{n\times 1}$ is the observed vector of responses, $T \in M_{n\times(m+1)}$ is a matrix of known constant time intervals based on the m input variables and $\beta \in M_{(m+1)\times 1}$ with β being a vector of unknown parameters. Moreover $\varepsilon \in M_{n\times 1}$ is an unobserved random vector of errors and $\sigma^2 > 0$ unknown. Note that $M_{a\times b}$ is the set of $a \times b$ matrices. The unobserved random vector of errors ε satisfies $E(\varepsilon) = 0$, $E(\varepsilon\varepsilon') = I_n$ with $0 \in M_{n\times 1}$ a vector of zeros and $(I_n)_{ij} = \delta_{ij}$ is the unit matrix. In the contexts under discussion it is a safe assumption that errors follow a normal distribution with mean zero and variance 1. The coefficients β that have been modeled as a vector are determined by the least squared method. This is allowed due to the Gauss – Markov theorem. The least squared estimators will be determined from

$$\hat{\beta} = (T'T)^{-1}T'Y \tag{4}$$

where from now on, Y denotes a given realization of Y. The proposed algorithm is based on two strong and rich in content theorems that follow. The first theorem [20] allows us to evaluate the β-expectation structural tolerance region. Instead of using the concept of tolerance region it is better to use its improvement, the so called β-expectation structural tolerance region. For central 100β% of normal distributions being sampled it is given by the interval

$$\left[T'_{o,p}\hat{\beta}' - C(p)(S^{-1}_{1,p})^{-1/2}, T'_{o,p}\hat{\beta} + C(p)(S^{-1}_{1,p})^{-1/2}\right] \tag{5}$$

with

$$T'_{o,p} = (1, t, t^2, ..., t^p) \tag{6}$$

$$S^{-1}_{1,p} = I - T'_{o,p}(T'T + T_{o,p}{}'T_{o,p})^{-1}T_{o,p} \tag{7}$$

$$C(p) = t_{n-p}(\beta/2)(n-p)^{-1/2}(RSS_p)^{1/2} \tag{8}$$

Here, t_{n-p} denotes the student distribution with n-p degrees of freedom, and finally

$$\mathrm{RSS} = \left(\mathrm{Y} - \mathrm{T}\,\hat{\beta}\right)'\left(\mathrm{Y} - \mathrm{T}\,\hat{\beta}\right) \tag{9}$$

The prediction distribution can be evaluated as well with the help of the same theorem.

A second important theorem [17] that is going to be used, provides for the linear model the β-expectation tolerance region *Q(T, Y)*,

$$Q(T,Y) = \{\mathrm{w} \in M_m : \left(\mathrm{w} \simeq T^*\,\hat{\beta}\right)'S(T)\left(\mathrm{w} \simeq T^*\,\hat{\beta}\right) \le \frac{m}{n-p}F_{m,n-p1,\tilde{\beta}}\} \tag{10}$$

and

$$S(T) = \mathrm{I_m} + T^*(T'T)^{-1}T^{*\prime} \tag{11}$$

with $F_{\mathrm{m,n-p1},\tilde{\beta}}$ the $\tilde{\beta}$ quantile of the F distribution with m and n-p degrees of freedom. Note that the matrix T* corresponds to the matrix of the input observations of the missing values.

The novel algorithm for the missing value problem we are a going to present is written in pseudocode. It is a modification of the algorithm described in [19]. It consists of five steps.

The first step is to define matrix Y. Y in our case comprises PH, Radon, Redox, temperature and conductivity. All missing values Y* have to be determined, as well as their corresponding time values. In the presented code in Appendix A, we place each of the five factors that are components of Y in one dimensional matrices. If there are some missing values we have just to omit them and continue consecutively keeping the time ordering. The values of time at which measurements were taken comprise matrix T. They have to be placed in a list too. The time at which a measurement was lost, is omitted. In addition, the code

normalizes data T in the interval [-1,1] and the transformed data are placed in the list named "T'TRN".

The second step comprises the evaluation of the vector θ with the estimators of GLM model of *p-th* order polynomial. For every *p=0* to *k* we should evaluate from Eq. (4), estimators $\hat{\beta}$.

The third step is about the determination of the largest volume of the β-expectation tolerance region since this is the worst case of the input variables set, as far as prediction concerns. Then, in the fourth step we find the minimum β-expectation tolerance region among the worst models. This model with min β-expectation tolerance region is also the best one.

Therefore, in the third step we have for all p=0 up to k, to define matrices $T_{o,p}$ from Eq. (6). In the presented realization of the algorithm we have set k=10. Furthermore, it is essential to evaluate the length L_p at the point t_o. Following (5), (10) and working for the one variable degree polynomial the length of the tolerance region can be derived equal to

$$\mathrm{L_p(t_o)} = 2\mathrm{t_{n\text{-}p;1-\beta/2}}(\mathrm{n-p})^{-1/2}\mathrm{RSS}^{1/2} \left\{\left(\mathrm{I-T'_{op}\left(T'T+T'_{op}}T_{op}\right)^{-1}T_{op}\right)^{-1}\right\}^{1/2} \quad (12)$$

with the point t_0 being the point that gives maximum value as follows

$$\mathrm{Max}\left[\mathrm{T'_{o,p}\left(T'T\right)^{-1}T_{o,p}}\right] \text{ with } -1 \le t \le 1 \quad (13)$$

The pseudocode names as "LTR" the length of the tolerance region Eq. (12) while expression named "quantity" is the one that has to be maximized at time t_o.

The fourth step is realized with a loop that runs from p=0 to as much as 10 in the function named "ORDER". This function chooses the minimum of the stored maximum "lengths" and finds the corresponding *p* value which is the degree of the response function for the best predictive model. It also compares the best predictive model with the ordinary best fitting model finally, evaluating $\mathrm{RMS} = \mathrm{RSS}/\sqrt{\mathrm{n-p-1}}$. The best fit model according to the conventional method is the one with the minimum RMS.

The fifth and final step refers to the evaluation of all the missing values based on the best predictive model. This becomes possible with the help of the code calling the function named "MISSINGVALUES".

For all measured quantities the proposed method was applied for evaluating the missing values according to the best for prediction polynomial. This was done for several different time durations. Results reveal that for many datasets the best fitting for prediction polynomial is different from the one suggested from ordinary methods with distance criteria like RMS, and therefore, the imputation of missing values is different as well. If the designer of an experiment is interested in correct predictions then the discussed method gives distinctive and correct results.

The applied algorithm differs nontrivially from all other methods that impute missing data with a distance criterion. Furthermore, it was tested that it suggests in many cases different values than those derived with the ordinary methods. The numerical study of this methodology proved that the algorithm, which chooses a polynomial model according to the best prediction criterion, does not have the disadvantage to select the largest order polynomial, as the best model. This is a well known problem associated with methods using distance criteria. Finally, data analysis with respect to the proposed method showed that for data with large dispersion, the estimated missing data are different from the values suggested by an RMS criterion.

5. Discussion

For the LOS wireless system a study was performed in order to find out the link budget parameterization. Local mean values of the received signal at the "close proximity" of the receiver (without considering any specific antenna gain for the receiver unit) is found to be approximately equal to the receiver sensitivity level of -91 dBm, if free space (distance-dependent) losses are considered. If terrain and/or foliage irregularities are taken into considered in a generic assumption of a 6 dB shadow depth, then the local mean value of the received signal suffers an additional attenuation of approximately 10 dB, resulting in a value below -100 dBm. Since we have already assumed a worst-case path loss of 150 dB [21], all possible attenuation scenarios have been accounted for.

Site-specific measurements and a more thorough investigation of plantation, foliage, and their effect on signal propagation with regard to variable antenna heights will validate the robustness of each assumption. Furthermore, the use of a high-gain directional antenna at the receiver unit will provide the necessary signal enhancement (in the order of 9 dB) so that the signal will be well above the sensitivity levels. Finally, it should be noted that the maximum transmit power of 38 dBm concerns a medium-range LTE BS that applies for micro-cell scenarios. LTE specifications explicitly provide a macro-cell (suburban-open areas) option of a wide-area BS where no upper bound in maximum transmit power was considered (and will be subsequently provided by local and/or regional band regulations by respective authorities). Therefore, our calculations simply provide scenarios that range from sub-optimal to worst-case in order to test the robustness of signal propagation under specific conditions, leaving room for improvement on both transmitter and receiver side, as well as addressing issues for future work in the channel characteristics, as heralded by other published works [22] - [24].

6. Results

The testing of the proposed algorithm with the measured data reveals an affirmative conclusion for using the proposed method. There is a strong theoretical background [16], [17], [18] and [19] that ensures the success of the method to any applied field. It was found that for several datasets the proposed novel method for missing data imputation differs non trivially from the other existing methods. In the present study a three cycles evaluation scheme was selected for the adjustment of the whole measuring station including the sensors, the control unit as well the transmission and the data recorder. The first and second evaluation periods lasted 25 days each. The third evaluation period lasted 30 days. These three time periods were consecutive started on March 2014. During the first period we had 2.3%, 2.5% , 3.4%, 0.5% and 2.8% of missing values for PH, Radon, Redox, temperature and conductivity respectively. In this first period there was a two days out of operation time duration that was excluded. In the second period we had 2.1% , 2.9%, 2.3%, 0.3% and 3.8% of missing values for PH, Radon, Redox, temperature and conductivity respectively while in the third period we got 2%, 1.9%, 2.4%, 0.3% and 1.9% missing values. Utilizing the developed algorithm we managed to impute the missing values in all the fifteen time series referring to the measured five factors of these three evaluation periods. The derived best for prediction polynomials each for every one of the five factors were then used to model the time evolution and calibrate the measuring station for best performance. The reliability of the measurement of each factor and the reliability of the whole measurement process were evaluated. The reliability (intraclass correlation coefficient, average measures at 95% CL) of the third period of evaluation reached 0.83, 0.77, 0.84, 0.95 and 0.75 for PH, Radon, Redox, temperature and conductivity respectively. In addition, using the derived best fitting polynomials we were able to calculate various statistical inferences regarding trends, and correlations which will be part of a larger statistical analysis of the measurements.

For research programs under the scope to utilize data for making safe and scientifically concrete predictions, it is not considered reasonable and appropriate to build models based on curve fitting as closely as possible to the data. Instead, it is desirable for the model to be determined by a curve that fits data with the help of a best fit polynomial for the prediction of the Y value for a certain X (within the experimental region), establishing a specific degree of high probability.

It would also be interesting as a future research to generalize the proposed method for problems with multiple independent variables or for cases like [25] and [26]. Another interesting investigation is to develop an algorithm capable to handle both time series analysis and missing data imputation.

Appendix A

The present section, presents the pseudo-code that realizes the algorithm.

(*Here we set data for matrix T. The time intervals that correspond to the missing data should be omitted, for example {1,2,3,4,6,7,8} for a missing value at t=5*)

1. Set an one dimensional matrix TIME`INTERVALS with elements consecutive integers that represent the time intervals at which measurements were performed
   (*Here we set all data for matrix Y which in our example concerns radon, PH, conductivity or OPR. *)
2. Set an one dimensional matrixY that consists of all time ordered measurements of factor Y omitting the missing values
3. Define the function/routine that estimates the t student distribution probability density function for the relevant tolerance region
   tst[n_] := Sqrt[-n + (1/n*(0.05*(Sqrt[n]*Beta[n/2, 1/2]))^(2/(1 + n)))^(-1)];
   (*Here we transform adequately the data*)
4. Set to variable T`TRN a normalized value in the interval (-1,1) i.e.
   T`TRN := (TIME`INTERVALS - A)/B;
5. Set variable “n” as the number of all time intervals
6. Calculate in variable A and B the quantities A := 1/2 (UU + DD);
   B := UU - A;
7. Estimate the minimum and maximum values of time intervals and set them in variables DD and UU respectively
   DD = Min[TIME`INTERVALS];UU = Max[TIME`INTERVALS];
8. Set a 2 X N “TRNdata” matrix with first column the transformed time intervals and second column the relevant Y factor. N is the number of all time intervals.
   (* the main code*)
9. Define the coefficients T[0],T[1],...T[10] of the ten polynomials which will be tested with both criteria
   T[0] := {1}
   T[1] := {1, T`TRN
   T[2] := {1, T`TRN, T`TRN^2}
   ...
   Set each of the 10 polynomials of order “i” Top[i]=1+t+t^2+...t^i
10. Set the quantity that should be maximized, see Eq.(13)
    quantity := $Top^T. (T^T.T)^{-1}.Top$;
11. Define a subroutine function “Maximize” which finds the value of t inside the normalized region[-1,1] that maximizes distance “quantity”
12. Define the useful expression EXPR, see equation (7), which is used in the definition of the “probabilistic length” Lp
    EXPR := $[1 - Top^T. [T^T.T + Top.Top^T]^{-1}. Top]^{-1}$;
13. Define the useful quantity “bi” that is used in the definition of the criterion RMS
    bi := $[T^T. T]^{-1}.(T^T.Y)$;

14. Define the quantity RSS (see equation (9)) used in the definition of the criterion RMS
    RSSp := [Y - T. bi]^T . (Y - T. bi);
15. Define the quantity"LTR" which is the length of the tolerance region and it is evaluated for the t that maximizes "quantity". This is the prediction criterion
    LTR := 2*tst[n- i] *(n - i - 1)^(-1/2)
    ((EXPR)^(1/2))(RSSp)^(1/2);
16. Define the expression that gives the conventional RMS criterion for best fitting model
    RMS := RSSp/(n - i - 1);
17. Define a subroutine/function returning a report order by order which provides justification about the best fitting polynomial. The user must set as an argument for this function the largest order of the polynomial to be tested. The maximum possible order that can be selected is 10. The prediction criterion LP and the conventional criterion RMS are estimated for each order of the polynomial. In addition the function returns for each order of the polynomial the plot of the data together with the best fitting polynomial for prediction.
    START LOOP
    For i=0 to n Maximize[quantity, -1 <= t <= 1}, t]];
    g1 = ListPlot[TRNdata];
    g2 = Plot[Top^T.bi, in the interval {t, -1, 1}];
    Print[Top^T.bi];
    Find the value t and name it "maxquant" that maximizes "quantity"
    maxquant := NMaximize[quantity, [respecting the constraint -1 <= t <= 1}] ;
    Print["RMS=", RMS];
    Set t = maxquant;
    Print["LP=", LTR];
    Print[Show[g1, g2, PlotRange -> All]]
    END LOOP
18. Define the subroutine/function that returns the missing value, the order of the best fitting polynomial used for estimating the missing value and the minimum tolerance length. The user sets as first argument the time that corresponds to the missing value and the largest order of the polynomial to be tested
    Set the time of missing value in the variable "timeofevent"
    Calculate tt = (timeofevent - A)/B;
    Set the maximum order of the polynomials to "nn"
    START LOOP
    For i=0 to nn
    Find the value t and name it "maxquant" that maximizes "quantity"
    maxquant := Maximize[quantity, {respecting constraint -1 <= t <= 1}] ;
    t = maxquant; LTRmin := LTRR[0]
    order := i ;
    IF LTRR[i] <= LTRmin; THEN LTRmin := LTRR[i]
    t = tt;
    MISSINGVALUE = Top[order]^T.bi;
    Print["MISSING VALUE=", N[MISSINGVALUE],
    " order of best polynomial=", order, " minimum LP=", LTRmin]
    END LOOP

Acknowledgment

Authors acknowledge that this work has been financially supported by the research program, entitled: "Measurement of Environment Physical-Chemical Parameters by Development Autonomous Data Collection Processing Transmission Systems with use of green Power and most optimal management", MIS 380360, within the research activity "Archimedes III", funded by the NSRF 2007-2013.

References

[1] GLASGOW, H. B, BURKHOLDER J. M., REED R. E., LEWITUS, A. J, KLEINMAN, J. E.: *Real-time remote monitoring of water quality: a review of current applications, and advancements in sensor, telemetry, and computing technologies*, Journal of Experimental Marine Biology and Ecology, Volume 300, Issues 1–2, pp. 409-448, 31 March 2004.
[2] MADDALA, G.: Introduction to Econometrics, 2nd Edn. Macmillan : New York, pp.: 663,1992
[3] STIGLER, S. M.: *Gauss and the Invention of Least Squares*. The Annals of Statistics, vol. 9, No. 3, 465-474, 1981.
[4] GOLDSMITH, A.: Wireless Communications. Cambridge : Cambridge University Press, 2005.
[5] PARSONS, J. D.: The Mobile Radio Propagation Channel. Hoboken : NJ : Wiley Interscience, 2000.
[6] RAPPAPORT, T.: Wireless Communications: Principles & Practice. *Upper Saddle River*, NJ: Prentice Hall, 1999.
[7] CHRYSANTHOU, C. , BERTONI, H. L.: Variability of Sector Averaged Signals for UHF Propagation in Cities, *IEEE Transactions on Vehicular Technology*, vol. 39, No. 4, pp. 352-358, November 1990.
[8] ERCEG, V. , GREENSTEIN, L. J. , TJANDRA, S. Y. , PARKOFF, S. R. , GUPTA, A. , KULIC, B. , JULIUS, A. A., BIANCHI, R.: An Empirically Based Path Loss Model for Wireless Channels in Suburban Environments, IEEE *J. on Selected Areas in Communications*, vol. 17, No. 7, July 1999.

[8] ODA, Y., TSUCHIHASHI, R., TSUNEKAWA, K., HATA, M.: *Measured Path Loss and Multipath Propagation Characteristics in UHF and Microwave Frequency Bands for Urban Mobile Communications,* Vehicular Technology Conference, 2001. VTC 2001 Spring. IEEE VTS 53rd, vol. 1, 6-9 May 2001 pp. 337-341 vol.1.

[10] SALO, J., VUOKKO, L., EL-SALLABI, H. M., VAINIKAINEN, P.: An Additive Model as a Physical Basis for Shadow Dading, *IEEE Transactions on Vehicular Technology*, vol. 56, No. 1, pp. 13-26, January 2007.

[11] CHRYSIKOS T., KOTSOPOULOS, S.: *Site-specific Validation of the Path Loss Models and Large-scale Fading Characterization of Large-scale Fading for a Complex Urban Propagation Topology at 2.4 GHz*. The 2013 IAENG Intern. Conference on Communication Systems and Applications (IMECS 2013), March 13-15, 2013, Hong Kong.

[12] SEYBOLD, J.: Introduction to RF Propagation. Hoboken, NJ : Wiley Interscience, 2005.

[13] JAKES, W. C. (Ed.): Microwave Mobile Communications. New York : Wiley Interscience, 1974.

[14] HATA, M. : Empirical Formula for Propagation Loss in Land Mobile Radio Services, IEEE Transactions on Vehicular Technology, vol. 29, No. 3, pp. 317-325, August 1980.

[15] OKUMURA, Y., OHMORI, E., KAWANO, T., FUKUDA, K. : Field Strength and its Variability in VHF and UHF Land-Mobile Radio Service, *Review of the Electrical Communication Laboratory,* vol. 16, No. 9-10, pp. 825-873, September-October 1968.

[16] KITSOS, C. P.: An Algorithm for Construct the Best Predictive Model. Softstat' 93: Advances in Statistical Software, Faulbaum, F. (Eds.). Stuttgart : New York, pp. 535-539, 1994.

[17] ELLERTON, R. R. W., KITSOS, C. P., RINCO, S.: Choosing the Optimal Order of a Response Polynomical-structural Approach with Minimax Criterion. *Commun. Stat. Theory Meth.*, 15: 129-136, 1986.

[18] MULLER, C. H., KITSOS, C. P.: Optimal Design Criteria Based on Tolerance Regions. mODa 7-Advances in Model-Oriented Design and Analysis, Bucchianico, A., H. Lauter and H. P. Wynn (Eds.). Physica-Verlag, pp. 107-115, 2004.

[19] Kitsos, C. P., V. Zarikas, "On the Best Predictive General Linear Model for Data Analysis: A Tolerance Region Algorithm for Prediction", Journal of Applied Sciences 01/2013; 13(4):513-524. DOI:10.3923/jas.2013.513.524, 2012

[20] HAQ, M. S., RINCO, S.: β-Expectation Tolerance Rfor a Generalized Multivariate model with Normal Error Variables, *J. of Multivariate Analysis*, 6 (3), pp. 414-421, 1976

[21] ZARIKAS, V., CHRYSIKOS, T., ANAGNOSTOU, K., KOTSOPOULOS, S., AVLAKIOTIS, P., LIOLIOS, G.T. LATSOS, C. PERATZAKIS, LYGDIS, A., LYKOYRGIOTIS, A. A.: *Telemetry, Analysis and Wireless Data Communications for a Measuring Station*, Elektro 2014 10th Intern. Conference, May 2014, Rajecké Teplice

[22] MICEK, J., KARPIS, O.: Wireless Sensor Networks for Road Traffic Monitoring. *Communications - Scientific Letters of the University of Zilina*, vol. 12, pp. 80-85, 2010, ISSN 1335-4205.

[23] HODON, M., PUCHYOVA, J., KOCHLAN, M.: Smartphone-Based Body Area Network for Stress Monitoring: Radio Interference Investigation. *Communications - Scientific letters of the University of Zilina*, ISSN 1335-4205.

[24] BRIDA, P., MATULA, M., DUHA, J.: Using Proximity Technology for Localization in Wireless Sensor Networks. *Communications - Scientific Letters of the University of Zilina*, ISSN 1335-4205, vol. 9, No. 4, pp. 50-54, 2007.

[25] GIKAS, V., STRATAKOS, J.: A Novel Geodetic Emethod for Accurate and Automated Road/railway Centerline Geometry Extraction Based on the Bearing Diagram and Fractal Behavior, *IEEE Trans. Intell. Transp. Syst*., 13: 115-126, 2012.

[26] ZARIKAS, V., GIKAS, V., KITSOS, C. P.: Evaluation of the Optimal Design "Cosinor Model" for Enhancing the Pof Robotic Theodolite Kinematic Observations, *Measurement*, vol. 43, No. 10, December 2010, pp. 1416-1424.

Stefan Borik - Ivo Cap - Branko Babusiak *

RESONANT FREQUENCIES OF SMALL ARTERIAL SEGMENTS AS DETERMINING FACTORS FOR ESTIMATION OF TERMINAL SEGMENTS IN ELECTROMECHANICAL ARTERIAL TREE MODEL

A model of the nonsymmetrical arterial tree was analyzed. The arterial branching model was based on the principle of the electromechanical analogy. The nonsymmetrical arterial tree was divided to 7 arterial generations, starting from larger arteries towards small arteries and arterioles. For each generation the resonant frequency and the transfer function were calculated and there are presented the pressure simulation results for each arterial generation. Terminal segments were determined regarding to calculation of the resonant frequencies and the transfer functions and simulation results.

Keywords: *Arterial system, electromechanical analogy, outflow condition, resonant frequency, transfer function.*

1. Introduction

The arteries deliver a blood containing oxygen to the tissues of whole human body. Blood delivery starts at heart output connected to aortic arterial segments and continues towards the periphery. On the peripheral side of the arterial system small arteries play more than one role such as blood delivering pipelines. They serve for regulation of systemic vascular resistance by changing their radii which are modulated by innervated smooth muscles [1].

2. Material and methods

1.1 Arterial Branching

In this contribution we adopted the results of works which deal with arterial branching questions [2 - 6]. In most cases, the arterial branching consists of mother vessel which bifurcates into two daughter vessels. We can define the daughter vessel radii by Eq. (1) and Eq. (2):

$$r_{d_1} = \alpha r_p \qquad (1)$$

$$r_{d_2} = \beta r_p \qquad (2)$$

where r_{d_1} are daughter vessel radii, r_p is radius of the mother vessel and α, β are the coefficients modulating the daughter vessel radii [2] and [3].

More information about derivation of the concrete values of the α and β coefficients can be found in the [3] where author defines asymmetry and area ratio of the mother and daughter vessels. Olufsen in [6] combines generalized "Murray's law" [4] and [5] with Zamir's [3] definitions of bifurcating vessel ratios.

Based on these assumptions, we used for our analysis and simulation the following adopted values of parameters [3 - 6]: $\gamma = 0.41$, $\eta = 1.16$, $\xi = 2.76$, $\alpha = 0.91$ and $\beta = 0.58$.

1.2 Model of Arterial System Based on Electromechanical Analogy

The properties of the arterial system can be transformed by using appropriate electromechanical analogies to system consisting of discrete electrical elements such as resistor, inductor or capacitor [7 - 10]. A blood pressure is equivalent to electrical voltage and a blood flow can be modeled as electrical current. These equivalences can be used in the case when we divide the modeled arterial tree to the discrete arterial segments with defined length. We used for our simulation of arterial system behavior the model consisting of interconnection of single vessel segments (see Fig. 1).

* **Stefan Borik, Ivo Cap, Branko Babusiak**
Department of Electromagnetic and Biomedical Engineering, Faculty of Electrical Engineering, University of Zilina, Slovakia
E-mail: stefan.borik@fel.uniza.sk

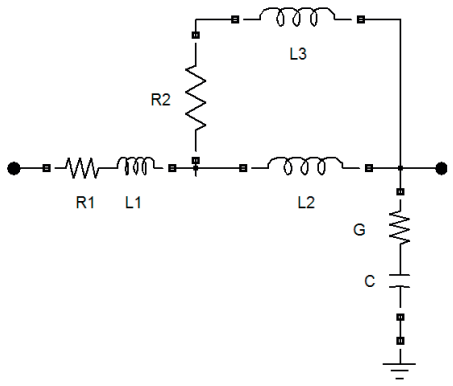

Fig. 1 Vessel segment model

The single element values can be determined [7] and [8]:

$$R_n = 2nR_0,\ L_n = \frac{1}{2n-1}L_0,\ n = 1,2,3,... \tag{3}$$

$$R_0 = \frac{4\eta}{\pi r_0^4},\ L_0 = \frac{\rho}{\pi r_0^2} \tag{4}$$

$$C = \frac{2\pi r_0^2}{k_w E_{stat}},\ G = \frac{2\pi r_0^2}{k_w \eta},\ k_w = \frac{2h(2r_0+h)}{3(r_0+h)^2} \tag{5}$$

The meaning of the elements, which are described by (3), (4) and (5), is listed in Table 1 [7] and [8].

Elements and parameters of the vessel segments — Table 1

Element/ Parameter	Description	Unit
R_n	Specific resistance of the appropriate vessel segment	[Ω·m^{-1}]
L_n	Specific inductance of the appropriate vessel segment	[H·m^{-1}]
C	Specific capacitance of the appropriate vessel segment	[F·m^{-1}]
G	Specific conductance of the appropriate vessel segment	[S·m^{-1}]
r_0	Radius of the appropriate vessel segment	[mm]
η	Blood viscosity	[mPa·s]
ρ	Blood density	[kg·m^{-3}]
k_w	Geometrical factor	[-]
E_{stat}	Static elastic modulus	[MPa]
h	Vessel wall thickness	[mm]

1.3 Small arteries branching implementation

Before implementation of small artery models to existing model of arterial system involving the large arteries, it is needed to determine a finishing radius of last arterial generation. Radii of arterioles vary from 5 to 30 μm [1]. Therefore the new generation of small arteries should be finished when their radii are approximately equal to arteriole radii. We attempted to solve this problem in another way.

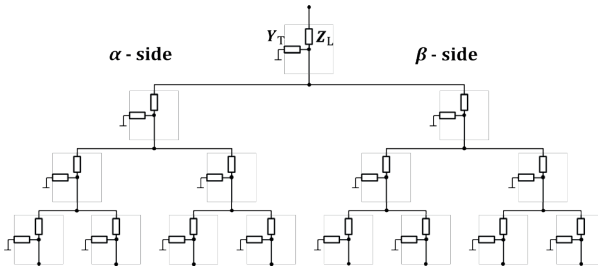

Fig. 2 Small arteries branching schematic

1.4 Transfer Function of Single Arterial Segments

At first, we made an analysis of transfer function of arterial segments placed in the single generations (see Fig. 2). Pressure or voltage transfer function of the single segments is defined by:

$$H_U(\omega) = \frac{\dot{U}_2}{\dot{U}_1} \tag{6}$$

where $\dot{U}_2$ is output harmonic voltage of the simplified arterial segment (see Fig. 3) and $\dot{U}_1$ is input harmonic voltage of this segment. According to the theory of electromechanical analogy the voltage is interconnected with the pressure in physiological segment described by its mechanical properties.

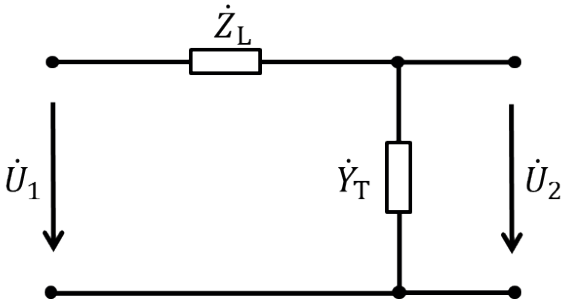

Fig. 3 Simplified arterial segment

Then we can express the voltage $\dot{U}_2$ by using relation for voltage divider and we get the equation for the voltage transfer function $\dot{H}_U(\omega)$ in the following form:

$$\dot{H}_U(\omega) = \frac{1}{1+\dot{Z}_L\dot{Y}_T} \tag{7}$$

where $\dot{Z}_L$ is longitudinal impedance of arterial segment in Fig. 1 and $\dot{Y}_T$ is transversal admittance of this segment.

Both parts of this basic arterial segment model can be expressed by (8) and (9):

$$\dot{Z}_L = R_1 + j\omega L_1 + \frac{j\omega L_2(R_2 + j\omega L_2)}{j\omega L_2 + R_2 + j\omega L_3} \tag{8}$$

$$\dot{Y}_T = \frac{j\omega GC}{G + j\omega C} \tag{9}$$

The meaning of the elements used in (8), (9) is listed in Table 1.

From the point of view of the electrical circuit theory, we can express impedance of the unloaded segment such as the serial connection of its longitudinal impedance (8) and reciprocal of its transversal admittance (9):

$$\dot{Z} = \dot{Z}_L + \frac{1}{\dot{Y}_T} \tag{10}$$

The total impedance will be helpful at analysis of transfer characteristics of the single arterial segments placed in different generations. Concretely, there are resonant frequencies which are indicators of the arterial segment properties regarding to inductive and capacitive properties of the equivalent electrical circuit (Figs 1 - 3). The resonant frequency of the corresponding segment (see two-port circuit in Fig. 3) is determined by equaling of the imaginary part of the total impedance to zero:

$$\mathrm{Im}\{\dot{Z}\} = 0 \tag{11}$$

Having expressed the single elements and edited the Eq. (6), we get a biquadratic equation:

$$\mathrm{Im}\{\dot{Z}\} = \omega L_1 + \frac{\omega^3\left(L_2^2 L_3 + L_2 L_3^2\right) + \omega L_2 R_2^2}{\left(\omega L_2 + \omega L_3\right)^2 + R_2^2} - \\ - \frac{1}{\omega C} = 0 \tag{12}$$

which has 4 roots but only one of them is positive. Then for resonant frequency, we obtain the following relation:

$$\omega_r = \sqrt{\frac{\left[\sqrt{\begin{pmatrix} C^2L_1^2R_2^4 + 2C^2L_1L_2R_2^4 + C^2L_2^2R_2^4 + \\ +2CL_1L_2^2R_2^2 + 4CL_1L_2L_3R_2^2 + 2CL_1L_3^2R_2^2 - \\ -2CL_2^3R_2^2 + 2CL_2L_3^2R_2^2 + L_2^4 + \\ +4L_2^3L_3 + 6L_2^2L_3^2 + 4L_2L_3^3 + L_3^4 \end{pmatrix}} + \right.}{\left. +L_2^2 + L_3^2 + 2L_2L_3 - CL_1R_2^2 - CL_2R_2^2\right]} \\ \left(2CL_2^2L_3 + 2CL_1L_2^2 + 2CL_2L_3^2 + 4CL_1L_2L_3 + 2CL_1L_3^2\right)} \tag{13}$$

The values of the resonant frequencies of the arterial segments placed in the different generation are listed in Table 2.

Resonant frequencies of the arterial segments placed in the different generations Table 2

	α-side		β-side	
Generation	ω_r [rad·s^{-1}]	f_r [Hz]	ω_r [rad·s^{-1}]	f_r [Hz]
Mother vessel	97.12	15.46	97.12	15.46
1.	111.98	17.82	221.94	35.326
2.	129.15	20.55	508.25	808.90
3.	149.01	23.72	1147.91	1826.96
4.	171.98	27.37	2526.53	4021.10
5.	198.53	31.60	5406.21	8604.25
6.	229.21	36.48	11319.73	18015.91
7.	264.64	42.12	23402.74	37246.62

3. Results

3.1 Determination of outflow condition

As written in the text above, we used the calculation of the transfer functions for assessment of the properties of the single arterial segments. They can be used for determination of outflow conditions of the segments placed in the last generation of small arteries, concretely in our case in the 7th generation. We can list several approaches how to determine an element which finishes arterial tree. We can start with "windkessel" models and continue with simple resistive elements which represent resistive nature of capillary bed [11] and [12].

In our contribution we focus on determining outflow condition in the following way: in the real world the arterial tree consists of approximately 20 generations. It follows from that there are 2^{20} elements needed for modeling the last generation [2] and [11]. By using the calculation of the transfer functions we can estimate "cut-off" generation which means that we can determine when we can stop the generating of new elements and by that way it is possible to minimize computing costs of computer simulation. In our work we set the threshold for stopping generating of the new segments by observing the resonant properties of the single segments on the alpha and beta sides of the particular arterial generations.

As defined by (1) and (2) the radius of the new segment descends much slower on the alpha side than on the beta side of the modeled arterial tree. It follows from Fig. 4 which characterizes transfer functions of arterial tree segments (see Fig. 2) on the alpha side. The change in resonant frequency is much evident in single generations on the beta side of arterial bed (Fig. 5).

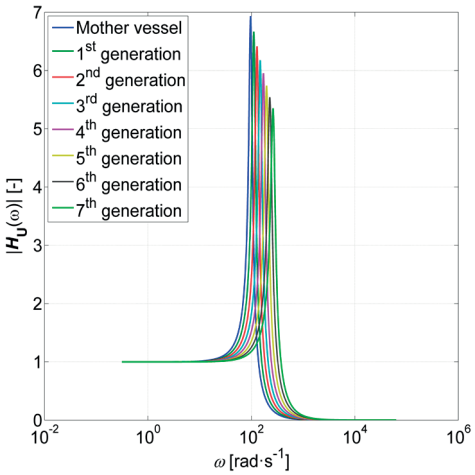

Fig. 4 Transfer function of single generations – α-side

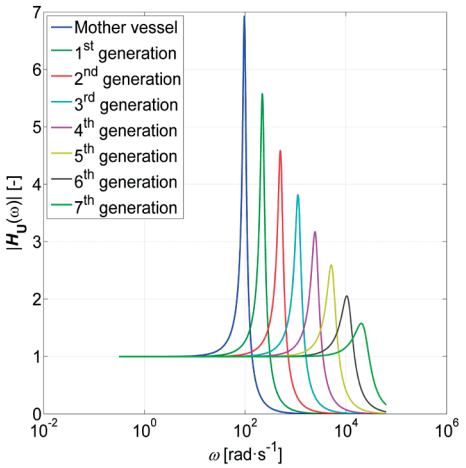

Fig. 5 Transfer function of single generations – β-side

We performed the simulations of the model of arterial tree consisting of small arteries towards arterioles. This model was implemented to the existing model of arterial system based on electromechanical analogy. Comparing to the previous arterial tree model [7 - 10], where the arterial peripheral segments were ended by terminal segments at the level of large arteries, the arterial branching continues to the seventh arterial generation in our implementation. Input signal of this branching extension corresponds to the mother vessel curve (blue line – see Fig. 6). The radii of the segments placed on the left side of the modeled arterial tree are around 45 μm (see Fig. 7) which is value close to arteriolar tree border (arterioles have resistive character and serve for peripheral vascular resistance regulation [1]). The simulated pressure values (see Fig. 6) in the seventh generation correspond to pressure values measured in arteriolar tree [1].

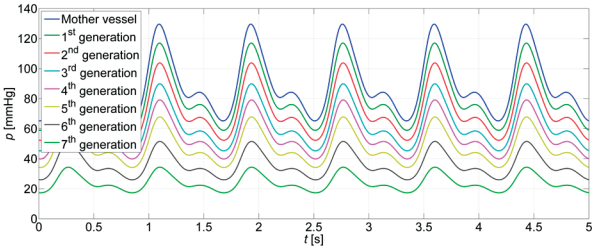

Fig. 6 Simulation results – blood pressure in particular vessel generations

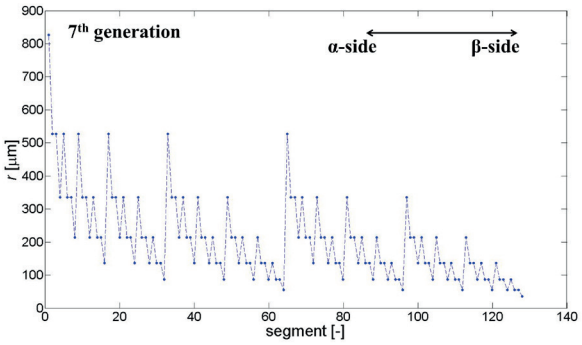

Fig. 7 The arterial radii in dependence on their position within the model of the small arteries

4. Conclusion

We estimated the criteria for stopping of creation of the new elements in the next generation by evaluating the resonant peaks in single transfer functions. The segment placed on the beta side of modeled arterial tree has resonant frequency approximately equal to 10^4 rad·s^{-1}. It is negligible from the point of view of possible heart rate frequencies which can exist in arterial system. Therefore, we can assume that the segments placed in the seventh generation have resistive character in the range of the possible heart rate frequencies and with them connected upper harmonic components which form the basic pulse wave propagating through arteries and they can be finished by simple resistive elements – resistors with values comparable to total resistance of the previous segment.

The modeling of the vascular system by using the electromechanical analogies can lead to better understanding of processes which occur in arteries. Also it could be possible to evaluate the degree of pathological changes in arterial system by using appropriate measurement methods (e.g. photoplethysmography) [13] and by reverse comparing of measured and simulated data. In this way the malformation such as arterial stenosis or aneurysm could be deeply studied.

References

[1] JAVORKA, K., BEDER, I.: *Medical Physiology (in Slovak)*. Osveta, Martin, 2001.

[2] OLUFSEN, M. S., PESKIN, C. S., KIM, W. Y., PEDERSEN, E. M., NADIM, A., LARSEN, J.: Numerical Simulation and Experimental Validation of Blood Flow in Arteries with Structured-tree Outflow Conditions. *Annals of Biomedical Engineering,* 28(11), 2000, pp. 1281-1299.

[3] ZAMIR, M.: Nonsymmetrical Bifurcations in Arterial Branching. *J. of General Physiology,* 72(6), 1978, pp. 837-845.

[4] MURRAY, C. D.: *The Physiological Principle of Minimum Work: I. The Vascular System and the Cost of Blood Volume*. Proc. of the National Academy of Sciences of the United States of America, 1926, 12.3: 207.

[5] UYLINGS, H. B. M.: Optimization of Diameters and Bifurcation Angles in Lung and Vascular Tree Structures. *Bulletin of Mathematical Biology,* 39(5), 1977, pp. 509-520.

[6] OLUFSEN, M. S.: Structured Tree Outflow Condition for Blood Flow in Larger Systemic Arteries. *American J. of Physiology - Heart and Circulatory Physiology,* 276(1 45-1), 1999, pp. H257-H268.

[7] CAP, I., CZIPPELOVA, B.: Electromechanical Model of Blood Flow in Vessels. *Advances in Electrical and Electronic Engineering*, 7(1-2), 2011, pp. 338-341.

[8] GOMBARSKA, D., CZIPPELOVA, B.: Computer Simulation of Human Cardiovascular System. *Acta Technica CSAV*, 57(4), pp. 407-420, 2012.

[9] CZIPPELOVA, B., GOMBARSKA, D.: Modelling of Arterial Bifurcation by Means of Electromechanical Model with Distributed Parameters, *Communications - Scientific Letters of the University of Zilina,* 13(1), 2011, pp. 22-26.

[10] GOMBARSKA, D., CZIPPELOVA, B., CAP, I.: The Investigation of Terminal Segment Effect on Blood Pressure Propagation Patterns in Cardiovascular System Models, *Communications - Scientific Letters of the University of Zilina,* 13(2A), 2011, pp. 38-43.

[11] OLUFSEN, M. S., NADIM, A.: On Deriving Lumped Models for Blood Flow and Pressure in the Systemic Arteries. *Math Biosci Eng*, 1(1), 2004, pp. 61-80.

[12] STERGIOPULOS, N., WESTERHOF, B. E., WESTERHOF, N.: Total Arterial Inertance as the Fourth Element of the Windkessel Model. *American J. of Physiology - Heart and Circulatory Physiology,* 276(1 45-1), 1999, pp. H81-H88.

[13] BLAZEK, V.: Biomedical Technology - 2011 and beyond. *Communications - Scientific Letters of the University of Zilina,* 13(1), 2011, pp. 5-12.

Stanislav Misak - Lukas Prokop - Petr Bilik - Petr Krejci *

EVALUATION OF POWER QUALITY IN OFF-GRID POWER SYSTEM

The energy independence, reliability and safety of energy distribution system operation as well as use of renewable resources have been hot research topics in recent years. This research leads to the development of active distribution grids with specific requirements. The Power Quality problems can arise when using renewable sources in active distribution grids. Problems are caused by decreased short-circuit power of local renewable sources, stochastic supply of electric energy from renewable sources and operating the active distribution grid in off-grid regime without connection to the external distribution system. In case of these conditions, the mutual interference between sources and loads is relevant and parameters of quality of electric energy can be exceeded. The results from analysis of quality of electric energy in the particular active distribution grid (off-grid power system) are introduced in this paper.

Keywords: *Wind power generation, photovoltaic systems, power quality, hybrid power system.*

1. Introduction

This paper introduces the initial evaluation of power quality (PQ) of an off-grid power system which was built as a research platform for renewable energy sources (RES) testing. The off-grid system was sized as a model for usual residential house supply [1].

The main idea of this concept is to find links or relations between environmental (solar irradiation and wind speed) and PQ variables associated with solar and wind energy. Based on these links the prediction of PQ for the off-grid power system will be introduced to optimize PQ level within the off-grid power system.

In particular, this contribution concentrates on the relationships between environmental (solar irradiance and wind speed) and power quality (PQ) quantities.

The paper is organized in four main sections. Section 2 provides a brief introduction to issues of power quality in general and problems specific to RES power quality. It also brings an overview of relevant technical standards. Section 3 provides a review of work on PQ prediction related to off-grid power systems. Section 4 describes an overall structure of the off-grid power system and also describes its individual components. Section 5 describes weather (solar irradiance and wind speed) data which are analyzed and some of the partial results are introduced from this data. Conclusions are presented in Section 6.

2. Background

Power quality can be explained as the fitness of consumed electric power to user appliances and devices. Good power quality allows electric systems to function in their intended manner without significant loss of performance or life. Without the proper power quality, an appliance (or load) may result in appliance damage or complete operation stoppage. There are many ways in which electric power can be of poor quality. And there are also many more causes of such poor quality power.

With the RES installation for off-grid power system supply, their impact on the power quality should be significant. One of the most important issues is voltage fluctuation in connection with the variability of photovoltaic (PV) and wind power generation. The other significant problem is harmonic distortion since both types of generation plants are usually connected to the power system through inverters. A wiring diagram of the described off-grid power system together with individual system components can be found in section 4. A more detailed characterization and overall off-grid power system description is fully introduced in [1] and [2].

A. Power Quality

It is not necessary to reach power quality levels defined by several international standards in off-grid power systems, but

* **Stanislav Misak, Lukas Prokop, Petr Bilik, Petr Krejci**
Faculty of Electrical Engineering and Computer Science VSB – Technical University of Ostrava, Ostrava, Czech Republic
E-mail: stanislav.misak@vsb.cz

only good power quality allows electric devices to operate in their given manner without loss of performance or possible damage.

B. Standards and Rules for PQ

PQ levels in a grid connected power system are usually defined and maintained by several international technical standard organizations. The well-known are as follows: IEC (Int. Electrotechnical Commission) and the IEEE (Institute of Electrical and Electronics Engineers). In off-grid applications where PQ limits are not defined by common standards we can use for PQ evaluation limits defined for grid connected power systems.

1) European Standards

IEC61000-4-30 (2008) "Testing and measurement techniques – Power quality measurement methods" is part of series IEC61000 "Electromagnetic compatibility". It defines the methods of measurement and interpretation of results for power quality parameters in 50/60Hz AC power supply systems. The measurement methods describe, for each type of parameter, how to obtain reliable, repeatable and comparable results regardless of the compliant instrument used for measurement and its environmental conditions. The standard defines three measurement classes A, S, B. Class A is used where precise measurements are necessary, e.g. for contractual applications to resolve disputes. The processing requirements and instrument prices for class S are lower. Class B is obsolete. It has the weakest requirements and it is not recommended for new designs. The standard also contains links to two other standards: IEC61000-4-7 for measurement of voltage harmonics and IEC61000-4-15 for measurement of flicker.

PQ analyzers with functionality defined in IEC61000-4-30 provide periodical data which has to be statistically processed. European standard EN 50160 describes how the measured data should be processed. It describes how to determine the main voltage characteristics of electricity supplied by public networks. It defines the "electric product" for high, medium and low voltage systems in terms of the characteristics at the supply terminals.

2) IEEE Standards

IEEE Std 1159 (2009) "Recommended Practice for Monitoring Electric Power Quality" is maintained by the Working Group for Power Quality Monitoring which was formed in response to the need for standardizing the rapidly expanding power quality monitoring manufacturing industry and the field use of their products by utilities and end-users. The standard introduces consistent terminology and definitions, and discusses power quality monitoring devices, application techniques, and the interpretation of monitoring results. It includes descriptions of conducted electromagnetic phenomena occurring in single- and poly-phase AC power systems, and encompasses the monitoring of electric characteristics of these systems. The standard describes nominal conditions and deviations from these conditions that may originate within the source of supply, load equipment, or from the interactions between the source and the load.

3) Enforcement of Standards

Both the IEEE1159 and IEC61000 series of standards cover issues of power quality. They agree on compatibility, the basic concepts and terminology. However, IEEE 1599 is not enforced; it is an informative and instructive tutorial developed by volunteers and approved by consensus. Conversely, the IEC 61000 series of standards has been developed by a group of assigned national experts through careful drafting before being approved by national voting. It is enforced at the national level by many countries.

3. Related work

Guidelines for the measurement and assessment of power quality characteristics for photovoltaic system are described in [3]. Harmonics, flicker, unbalance and slow voltage variations were included in these guidelines [3]. Power quality analyses for grid connected photovoltaic plants and converters were introduced in various papers; also general PQ issues associated with grid connected PV systems are discussed, for example, in [3], [4], [5] and [6].

Power quality analyses for off-grid connected power system were discussed only in a few papers. In [7] there were analyzed main factors of the impact of fluctuations of wind power from the off-grid wind power systems and energy storage technology to mitigate the off-grid wind turbine power fluctuations. Smart control systems for standalone and grid connected PV systems were introduced in [8]. Also fluctuation of total harmonics distortion (THD) in islanding mode was shortly evaluated. The THD during islanding mode of operation was around 6% [8].

However, none of these papers provides an overall PQ analysis of the whole hybrid power system with RES. In this paper we try to find relationship between environmental, electric and PQ variables [9]. The main goal is to find interconnections between environmental variables like solar irradiance or wind speed and PQ variables and arrange the basis for the PQ variables prediction for off-grid power systems.

4. System configuration

The developed off-grid power system was designed according to requirements for usual consumption of a single family home whereas the mentioned system has to satisfy features of a smart grid system.

Basic features of the developed smart grid system are as follows:

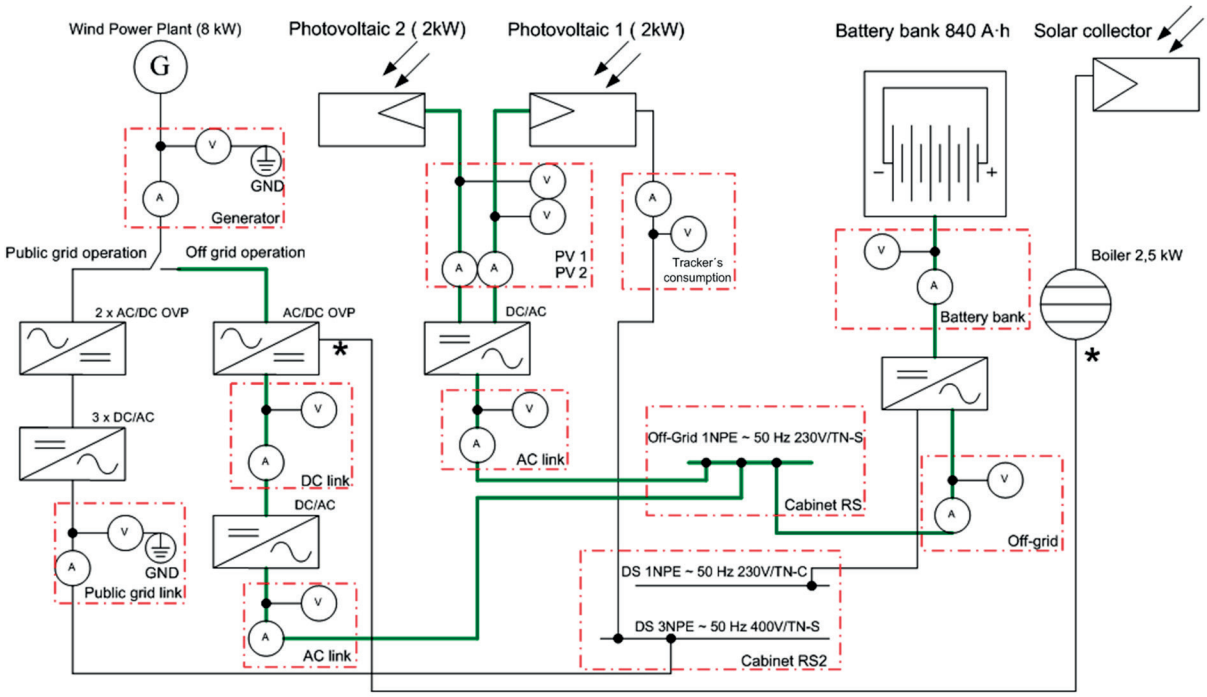

Fig. 1 The block scheme of off-grid power system

- independence on the delivering of energy from external power grids,
- operation of grid system with well-balanced production and consumption of electric energy,
- energy storage possibility,
- using mainly renewable sources of electric energy,
- nontraditional character of load,
- new conception of protection with bi-directional power flow and
- active energy management system supported by methods of artificial intelligence (main principles are illustrated in [7].)

The off-grid power system consists of three basic parts. The first part, part of sources, contains two types of renewable sources, namely a wind power plant and photovoltaic system. These types of renewable sources were selected purposefully because mutual combination of their running ensures energy supply during all year. It is given by character of individual sources where the electric energy is mainly supplied by a wind power plant for the seasons of spring and winter and by a photovoltaic system for the seasons of summer and autumn. If only one of these sources is used, it is not capable to provide enough power for the off-grid system due to the insufficient weather conditions in the Czech Republic where the system is installed. The block scheme of off-grid power system is introduced in Fig. 1.

The first source of electric energy is formed by the wind power plant (WPP) equipped with a synchronous generator with permanent magnets and the total installed capacity of 12 kVA. The synchronous generator is connected through a protection box with controlled (AC/DC) converter and frequency converter (DC/AC) with a recuperative unit to a 1phase AC busbar with 230 V level and 50 Hz frequency. The photovoltaic system (PV1) based on monocrystalline technology is placed on the tracker for its better utilization and higher efficiency of energy conversion. PV1 has installed power similar to PV2. The photovoltaic power plant (PV2) with polycrystalline technology and the total installed output of 2 kWp is used as another renewable electric power source. The electric output from photovoltaic system is connected also through a frequency converter (DC/AC) to the common 1phase AC busbar as a part of transmission. The PV2 with polycrystalline technology is placed on the stabile construction.

Individual appliances are supplied from the busbar and their individual connections are controlled according to the condition of the actual state of a storage device, connection priorities, character of current surge of load and the predicted value of available power from the wind and photovoltaic power plants.

Connecting of the loads according to the requirements mentioned above is done using the smart control system which also controls charging of the storage device with the total capacity of 840 A·h and voltage 48 V DC (third part of the off-grid power system). This storage device with lead batteries balances the power and thus accumulates electric power in the case of surplus of electric power from the photovoltaic and wind power plants. This storage device works as a backup source for supply of individual power components in the case of lack of energy from power sources. The weather station is part of the off-grid

power system conception for definition of relations between meteorological, electric and mechanical values. The weather station measures wind velocity, wind direction, temperature, relative humidity, pressure, UV radiation. The power flow between individual components, actual values of required parameters and total efficiency of the off-grid power system are monitored by the monitoring system in specific measuring points.

5. Initial evaluation of the off-grid pq data

Initial PQ evaluation was processed in compliance with European standard EN 50160 and a database of monitored variables (meteorological and electric) was used. The following marks "-" for power production and "+" for power consumption are used in this initial evaluation.

Two weekly periods (from January 24 to January 30, 2014 and from May 1 to May 7, 2014) were chosen from long-term power quality measurements. The first week (January) represents the evaluation of the system in the on-grid mode with the operating photovoltaic power plant and wind power plant. The second week (May) represents the evaluation of the system in the off-grid mode with the operating photovoltaic power plant only. So far the results are not available for the off-grid mode with both sources operating.

Values of flicker, harmonic voltages and THDu are shown in Table 1. The short-term flicker severity (Pst) was chosen for the figure instead of long-term flicker severity (Plt) due to better information.

Values of flicker, harmonics voltages and THDu Table 1

	on-grid WPP+PV	off-grid PV
Pst_1	0.93	4.81
Plt_1	1.06	4.77
Uharm[%]3_1	5.37	6.73
Uharm[%]5_1	2.95	1.90
Uharm[%]7_1	0.59	0.69
Uharm[%]9_1	0.28	0.31
Uharm[%]11_1	0.31	0.31
Uharm[%]13_1	0.33	0.23
Uharm[%]15_1	0.16	0.10
Uharm[%]17_1	0.22	0.06
Uharm[%]19_1	0.15	0.04
Uharm[%]21_1	0.08	0.04
Uharm[%]23_1	0.23	0.04
Uharm[%]25_1	0.14	0.03
THDu[%]_1	6.59	7.05

Table 1 shows 95% of the values of selected quality parameters (95% interval is used according to EN 50160, 5 % of the worst values are removed from analysis). These values imply that the connected photovoltaic power plants significantly affect flicker besides the frequency. The value of flicker achieves 1 (95% of the value Pst and Plt) in the on-grid mode. The value of flicker achieves almost 5 in the off-grid mode in this particular case. This very high value of flicker is caused by "soft" network.

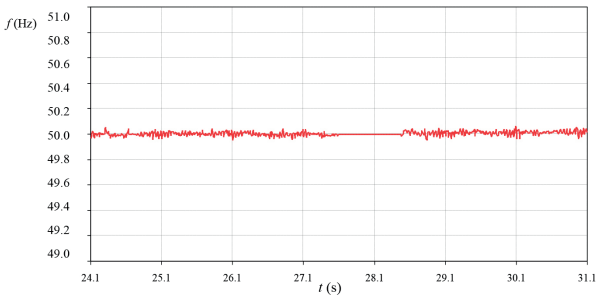

Fig. 2 Frequency of power system in the on-grid mode

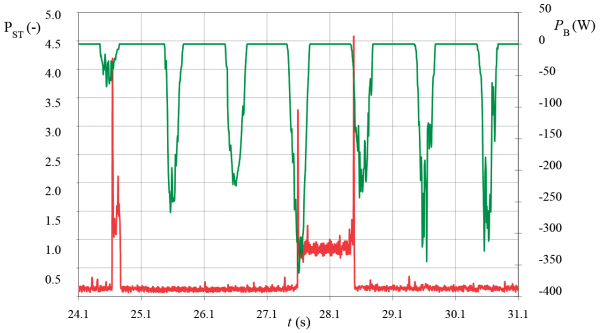

Fig. 3 Flicker and photovoltaic power in the on-grid mode

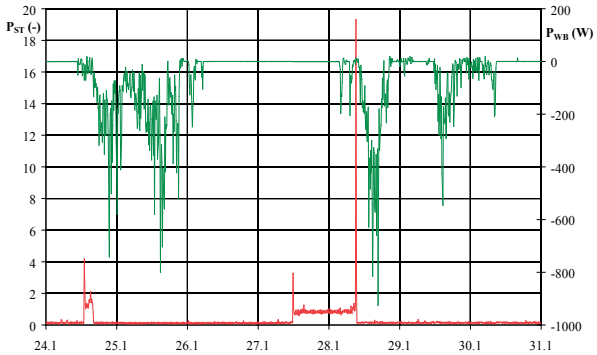

Fig. 4 Flicker and wind power in the on-grid mode (January)

In Figures 2 - 4 there are waveforms of frequency, flicker and powers of photovoltaic and wind power plants in the on-grid mode (January). From curves we can see that the frequency is given by the frequency of 50 Hz and waveform of flicker is not

affected by the power of connected photovoltaic and wind power plants. Higher values of flicker may have originated either in the background of network or in changes of load at the point of measurement.

Figures 5 - 6 show waveforms of frequency, flicker and power of photovoltaic power plant in the off-grid mode (May). We can see that during the supply of power from the photovoltaic power plant, the frequency increased to about 52 Hz, and also the value of the short-time flicker severity significantly increased to 6.

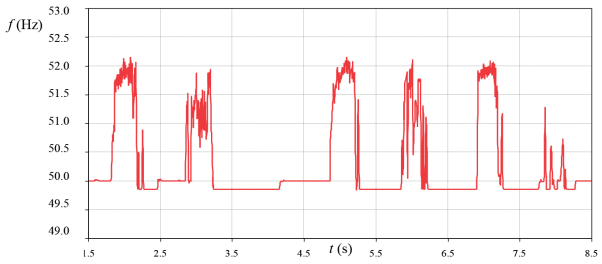

Fig. 5 Frequency in the off-grid mode (May)

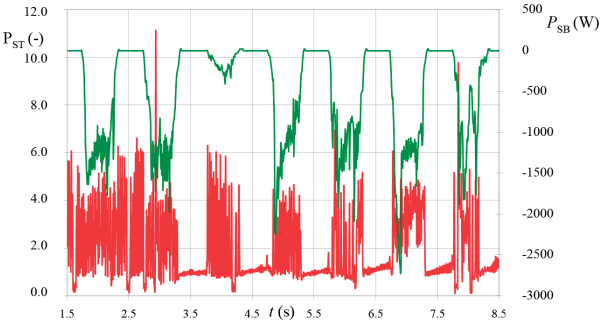

Fig. 6 Flicker and photovoltaic power in the off-grid mode (May)

6. Conclusions and future work

Utilization of solar and wind power in off-grid power systems for residential house supply is in contradiction with the increasing PQ sensitivity of equipment and devices being connected to the off-grid power system. Defined links and relations between the solar radiation and wind speed and direction allow reduction of the negative effects of solar and wind power and of course defined links and relations help to keep acceptable level of PQ.

This paper introduces initial evaluation of power quality in the hybrid power system where both on-grid and off-grid operation modes are possible.

Acknowledgement

This work was supported within the framework of the IT4Innovations Centre of Excellence project, reg. no. CZ.1.05/1.1.00/02.0070 supported by Operational Programme 'Research and Development for Innovations' funded by the Structural Funds of the European Union and state budget of the Czech Republic, Additionally, this article has been elaborated in the framework of the project New creative teams in priorities of scientific research, reg. no. CZ.1.07/2.3.00/30.0055, supported by the Operational Program Education for Competitiveness and co-financed by the European Social Fund and the state budget of the Czech Republic, project ENET – Energy Units for Utilization of non-Traditional Energy Sources CZ.1.05/2.1.00/03.0069, Students Grant Competition project reg. no. SP2015/178, project LE13011 Creation of a PROGRES 3 Consortium Office to Support Cross-Border Cooperation and project InterEnergy (CZ.1.07/2.3.00/20.0075).

References

[1] MISAK, S., PROKOP, L.: *Technical-Economic Analysis of Hybrid Off-Grid Power System*, Prof. of 11th intern. Scientific conference Electric power engineering 2010, (Drapela, J. Machacek, J, ed.), pp. 295-300, Brno: Univ Technol, May 2010.

[2] MISAK, S., PROKOP, L.: *Off-Grid Power Systems. Intern.* Conference on Environment and Electrical Engineering 2010. ISBN 978-1-4244-5370-2, pp. 23-26.

[3] ORTEGA, M. J., HERNANDEZ, J. C., GARCIA, O. G.: Measurement and Assessment of Power Quality Characteristics for Photovoltaic Systems: Harmonics, Flicker, Unbalance, and Slow Voltage Variations, *Electric Power Systems Research*, vol. 96, March 2013, pp. 23-35, ISSN 0378-7796, 10.1016/j.epsr.2012.11.003.

[4] AL-HADDAD, K.: *Power Quality Issues under Constant Penetration Rate of Renewable Energy into the Electric Network*, 14th intern. Power Electronics and Motion Control Conference (EPE/PEMC), 2010, pp.S11-39, S11-49, Sept. 2010.

[5] DRABEK, P., KUS, V.: EMC Issues of Low Frequency Interference of Power Electronic Converters. *Applied Mechanics and Materials,* vols. 284-287, 2013, pp. 2516-2520, ISSN 1662-7482, doi: 10.4028/www.scientific.net/AMM.284-287.2516.

[6] OTCENASOVA, A., ALTUS, J., HECKO, P., ROCH, M.: Measurement Characteristics of Voltage in Practice and Possibilities for Improvement of Voltage, *Przeglad elektrotechnniczny - Electrical Review*, Varsava, 2012, R. 88 NR 9a/2012, pp. 103-106, ISSN 0033-2097, WOS:000308318000021

[7] MOSTAFA, H. A., SHATSHAT, R. E., SALAMA, M. M. A.: *Smart Control System for Standalone and Grid Connected PV Systems*, Power and Energy Society General Meeting, 2012 IEEE , pp. 1-6, July 2012.

[8] HOGER, M., BRACINIK, P., ROCH, M.: Simulation of a Power Substation's Control System Operation, *Communications - Scientific Letters of the University of Zilina*, 13(2A), 2011, pp. 44-48.

[9] FARHOODNEA, M., MOHAMED, A., SHAREEF, H., ZAYANDEHROODI, H.: Power Quality Analysis of Grid-Connected Photovoltaic Systems in Distribution Networks, *Przeglad Elektrotechniczny - Electrical Review*, 2013, vol. 89, No. 2A, pp. 208-213.

Vladimir Kindl - Tomas Kavalir - Roman Pechanek *

CONSTRUCTION ASPECTS OF SYSTEM FOR WIRELESS LOW POWER TRANSFER ON MOVING PARTS OF ELECTRIC MACHINERY

The paper discuses important construction aspects of resonant wireless power transfer (WPT) system for moving parts of electric machinery. It focuses mainly on key electrical parameters of the systems resonant linkage and its simple and durable construction shape. All presented theoretical presumptions are consequently verified by detailed measurement.

Keywords: *Wireless, power, transfer, resonant, coupling, efficiency.*

1. Introduction

In the last few years there has been a growing interest in wireless power transfer systems. Considerable attention has been paid mainly to the possibilities in construction [1], [2] and [3] and the design of various systems structures. The mathematical description of operating characteristics and properties has been closely studied [4], [5], [6] and [7] by many researchers and it is therefore possible to qualitatively compare several variations of arrangement of relevant systems coils.

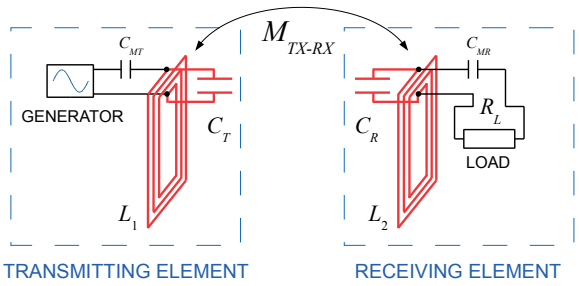

Fig. 1 The schematic diagram of system's construction

In this paper the two rectangular coils construction [4], [5] and [6] (see Fig. 1) of WPT system is studied. The operating frequency 13.56 MHz is permitted by the scientific and industrial (ISM) band [7]. Based on the approach presented in [4], [5] and [6], the purpose of this paper is to study the impact on the efficiency of WPT within changing relations between chosen key elements of the structure. The analyzed modifications lie in various inductances of coils L_1 and L_2. Parameter $M_{TX\text{-}RX}$ represents the mutual inductance between respective coils. The capacitors C_{MT} and C_{MR} work as components of capacitive coupling matching the impedance of the system. This causes less decrease in value of the operational quality factor Q of resonators L_1 and L_2 and prevents reflecting the power back to the source. Capacities C_T and C_R adjust the system's resonance frequency. As referred to [6], the efficiency can be easily derived from the equation (1).

$$\eta_{12} = \frac{k_{TR}^2 Q_1 Q_{2L}}{1 + k_{TR}^2 Q_1 Q_{2L}} \frac{Q_{2L}}{Q_L} \tag{1}$$

The parameter k_{TR} represents the mutual magnetic coupling coefficient between both coils.

$$k_{TR} = \frac{M_{TX-RX}}{\sqrt{L_1 L_2}} \tag{2}$$

While the theoretical (standalone) quality factors Q_1, Q_2 are both given by

$$Q_{1,2} = \frac{\omega L_{1,2}}{R_{1,2}} \tag{3}$$

in the real structure there is a significant influence of the mutual inductance between neighboring coils which measurably complicates its calculation [8] and [9]. The suitable computing method is described in the subsequent section. The parameter

$$Q_L = \frac{R_L}{\omega L_2} \tag{4}$$

from the equation (1) is often referred to as the load quality factor which in interaction with the Q_2 defines operational quality factor

* **Vladimir Kindl, Tomas Kavalir, Roman Pechanek**
Faculty of Electrical Engineering, University of West Bohemia, Plzen, Czech Republic
E-mail: vkindl@kev.zcu.cz

of the last systems coil connected to the loading resistor R_L. The parameter

$$Q_{2L} = \frac{Q_2 Q_L}{Q_2 + Q_L} \tag{5}$$

is the quality factor of the receiving circuit with load. From the foregoing thoughts it is clear that the large $Q_{1,2}$ and k_{TR} positively affect (increase) the efficiency of the power transmission through the resonant magnetic coupling system.

2. Key electrical parameters

A. *Standalone Quality Factor*

The equation (3) describing the parameter was mentioned above. The angular frequency ω is set according to ISM band and therefore cannot be changed. The resistance and inductance are both strongly defined by the chosen geometry. While the planar square-shaped coil brings very high inductance and many construction advantages, it also exhibits considerable lateral parasitic capacity degrading the Q. This effect may be reduced by equidistantly wound coil turns, but on the other hand, it contrarily decreases back the inductance. With regard to previous statements the optimal shape of coils comes from all technical and geometrical requirements to be met. The exact value of self-inductance may be given either by FEA or from Grover's formula [10], [11] and [12] using the elliptical integrals.

B. *Operating Quality Factor*

If another coil appears within reach, the mutual inductance notably changes the numerator of (3). Moreover, there are several additional embedded resistances (see Fig. 2) having a significant reducing effect on the operational quality factor, especially the internal resistance of the power source R_G and the load resistance R_L of receiving resonant element. The situation may be easily explained by using the analogy of parallel resonant circuit. Both resonators L_1-R_1-C_T and L_3-R_3-C_R can be substitutely expressed by the parallel connection with permuted internal resistances of coils (see Fig. 3)

$$R_{1P} = \frac{L_1}{C_T R_1} \text{ and } R_{2P} = \frac{L_2}{C_R R_2}. \tag{6}$$

This new resonant circuit is further loaded with mentioned R_G or R_L linked in via matching capacitors (Fig. 2).

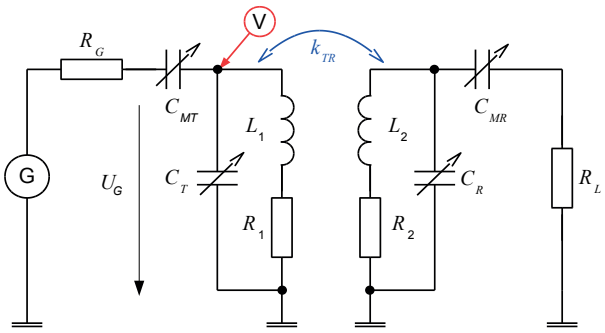

Fig. 2 The PSpice model of system's construction

As the loading impedance is connected in parallel to the resonator, we get the operating quality factor in following form

$$Q_{pT} = \omega C_T \frac{R_{1P} R_G}{R_{1P} + R_G} \tag{7}$$

and

$$Q_{pR} = \omega C_R \frac{R_{2P} R_L}{R_{2P} + R_L} \tag{8}$$

The substitutive parallel circuit is depicted in Fig. 3.

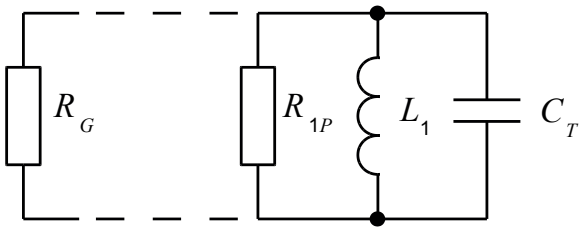

Fig. 3 The substitutive parallel resonant circuit-transceiver part

This budget of interlaced influences cannot be easily covered by simple analytical equation and must be therefore considered in another way [8] and [9]. To calculate the operational Q correctly, we can assemble a simple PSpice model (see Fig. 2). The model performs an AC sweep analysis in which computes all necessary electrical quantities as they depend on the set frequency range. The quality factor can be further derived from the voltage curve measured on the resonator (see example in Fig. 4).

$$Q_{RES} = \frac{f_0}{B} = \frac{f_0}{f_2 - f_1} \tag{9}$$

The frequency f_0 matches the resonant frequency found in the extremum of the function from Fig. 3. The f_2-f_1 is the half-power bandwidth, i.e., the bandwidth over which the voltage is greater than -3 dB of the voltage at the resonant frequency.

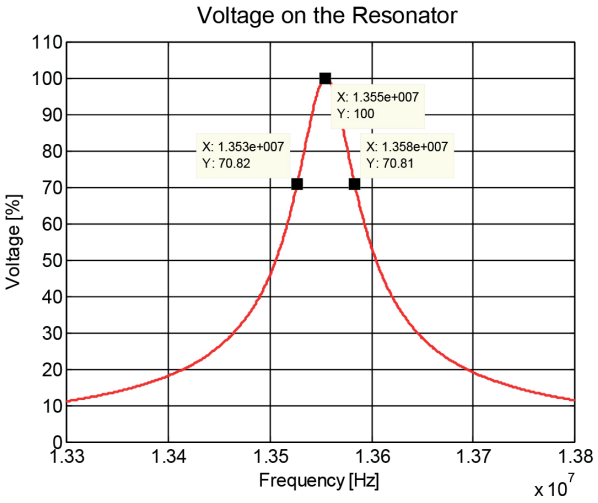

Fig. 4 Example for Q calculation

Since the calculation combines influences of all components in the circuit, the following key parameters must be properly set into (1).

$$Q_1 = Q_2 = Q_{RES} \tag{10}$$

C. Structural Variations

Discussed system is tested in three various structures composed of a combination of two types of planar coils (see Figs. 5 and 6).

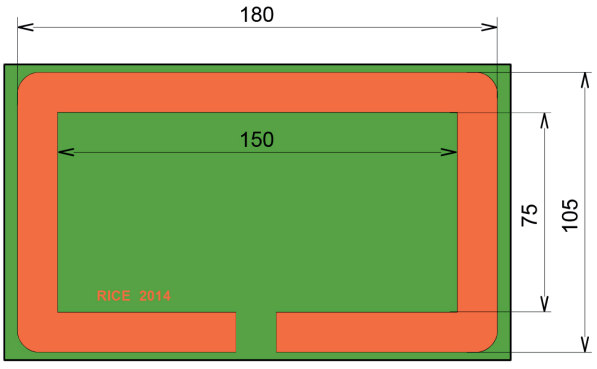

Fig. 5 The chart of planar coil - "version A"

While the coils are made as a pattern (PCB) on composite board FR4 or better [13], their manufacturing is very cheap, easy and quick. On the other hand, the lack of available space forbids linking the input power to the coil using magnetic coupling (capacitive coupling utilized). This negatively affects the ability to reach very high efficiency of power transmission. As compared with the coil "version B" (Fig. 6), the coil "version A" (Fig. 5) has higher effective area with only one turn to achieve higher quality factor with less sensitivity on near vicinity subjects.

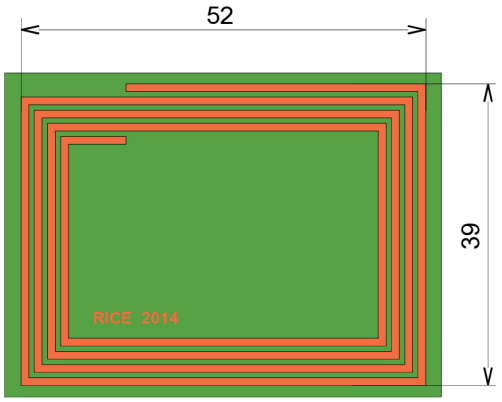

Fig. 6 The chart of planar coil - "version B"

The coil "version B" is made as a four-turn pattern of one millimeter thickness. The distance between each turn is 0.7 mm. Since the coil is smaller and has lower quality factor, it finds some advantages in wider feasibility of mounting on moving parts. All important electrical parameters are listed in Table 1.

Important Electrical Parameters Table 1

	Parameter	Values	Units
	$U_G/R_G/R_L$	10/50/50	[V]/[Ω]/[Ω]
"version A"	L_1	$278e^{-9}$	[H]
"version A"	C_{MT}/C_T	$23e^{-12}/453e^{-12}$	[F]/[F]
"version B"	L_2	$1.3e^{-6}$	[H]
"version B"	C_{MR}/C_R	$13e^{-12}/92e^{-12}$	[F]/[F]

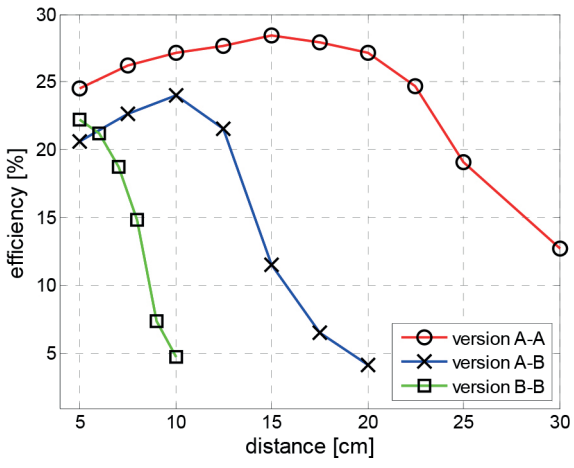

Fig. 7 The efficiency of WPT - all construction versions

The first investigated framework utilizes two coils of "version A" for transmitting and receiving the power. Due to the same dimensions of both coils and their coaxial position during the measurement they exhibit relatively good efficiency even at very high distance. The resulting plot (red curve) for fixed frequency can be seen in Fig. 7.

The second tested configuration comprises the coil "version A" working as a transmitter and coil "version B" working as a receiver. Their unmatched dimensions decrease the maximum of reachable efficiency and short effective distance range. The resulting efficiency is depicted by a blue curve seen in Fig. 7.

The third analyzed configuration consists only of the coils "version B". While the smaller coil features considerably lower quality factor than exhibited by the bigger one, the resulting efficiency and distance range must be according to (1) measurably lower. The resulting efficiency (green curve) is plotted in Fig. 7.

As it is clear from Fig. 7, the system exhibits at least one optimal distance at which the efficiency is maximal. This distance varies with the coils configuration whereas the higher Q extends it. The starting low efficiency (small distance) is caused by increase of mutual inductance which consequently re-tunes the resonant frequency. This may be avoided either by using frequency tracking or tuning the resonant capacitors. Unfortunately, both countermeasures are either much expensive for real application, or may be implemented only with notable difficulties. The decrease in efficiency at large distances is mainly caused by the native character of near magnetic field (evanescent wave). According to (7) the lower impedance of source/load causes considerable decrease in the operating quality factor which makes the systems efficiency fall. Another important component of the system is the resonant capacitor itself. The quality of dielectric has strong impact on its internal resistance which is obviously parallel to the resonator and has therefore similar influence on the quality factor as well as the resistances from (6). For the practical application it is useful to pay attention even to the type dielectric of capacitors (low loss and low ESR).

The proposed system should be used to supply any measuring device for monitoring motor shaft parameters. As obvious, the smaller coil "version B" is more suitable for mounting on the shaft than the bigger coil "version A" and may be easily assembled in bond of many parallel coils connected to mutual DC bus (see Fig. 8).

If flexible PCB used, it is easy to cut this resulting elastic belt onto certain length and wound it on the shaft very quickly. The belt should be glued on strip of soft material (foam rubber) to get some distance from the shaft and to smooth its asperity. On the other hand, the smaller coil delivers the energy to the load with lower efficiency which produces stronger leakage flux having no negative impact on biological structures [14] in case of transferring low level energy. As a transmitter it is better to use the coil "version A" because of its less sensitivity on near objects and higher quality factor. The situation can be seen in Fig. 9.

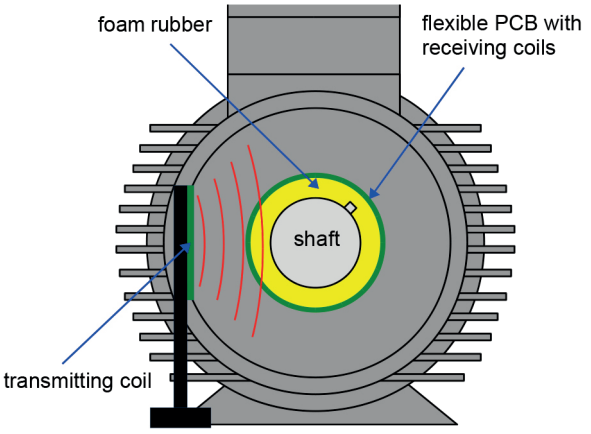

Fig. 9 System for WPT on the shaft

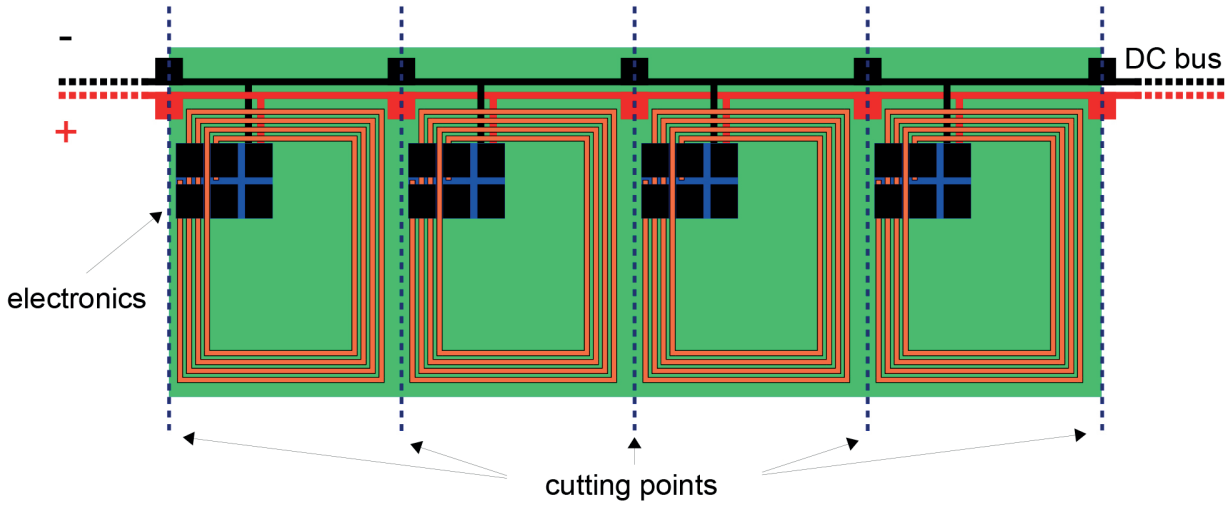

Fig. 8 Flexible PCB to be mounted on the shaft

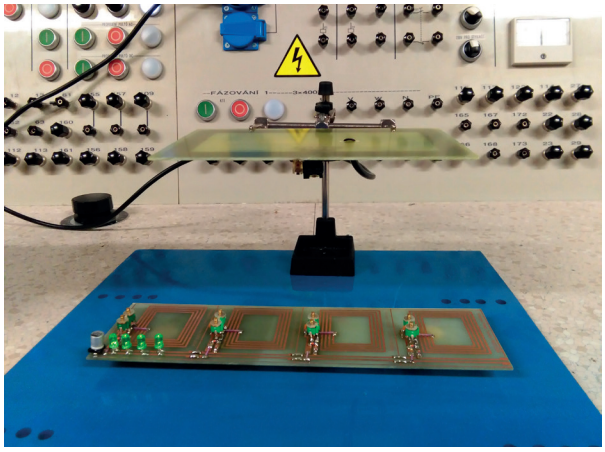

Fig. 10 The real shape of tested arrangement - demonstration

The real shape of tested (demonstrating) system is shown in Fig. 10. The receiving coils are placed on metal plate with 10 mm distance.

3. Laboratory arrangement for measuring

The measuring arrangement can be seen in Fig. 11. Here the radio transceiver FT-857D is used as a source of transmitting energy. The operational frequency is 13.56 MHz, which is permitted by the ISM band. The input/output power is measured by the Watt-meter CN-801 (type H) of 200 MHz bandwidth and relatively large power range (20/200/2000 W). The impedance was matched by linking capacitors C_{MT} and C_{MR}.

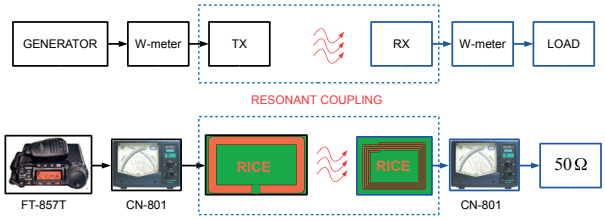

Fig. 11 The measuring arrangement

4. Conclusions

The experimental results indicate relatively high sensitivity on making alternations to the system arrangement. From the outcome of our investigation it is possible to give several conclusions.

The first, the system exhibits at least one optimal coils' distance in which the efficiency is maximal. This is true only for the constant supplying frequency and it is therefore possible to partially improve the short-distance efficiency. The improvement may be done either by using frequency tracking or tuning the resonant capacitors. The decrease in efficiency at large distances is mainly caused by the native character of near magnetic field (evanescent wave). The magnetic field range can be effectively extended by increasing in coils' quality factor.

The second, the full-range efficiency of the system is also strongly influenced by the internal impedance of the power source and the load itself. Another key parameter is the quality of dielectric of the resonant capacitor. It has strong impact on its internal resistance which is obviously parallel to the resonator and has therefore the similar influence on the quality factor as exhibited by source/load resistance. The findings suggest that despite of the higher cost it is better to choose the low loss and low ESR capacitors making the system efficient even at large distances.

The proposed receiving coil "version B" is small enough to be easily assembled in bond of many repeating parallel coils having the belt-shape. All coils may be connected to mutual DC bus which together with flexible PCB makes possibility to cut the structure at any required length and mount it on the shaft very quickly. The foam rubber strip glued on the bottom side of the belt makes some distance between the shaft and mounted coils and smoothes any asperity of the surface. While the dimensions of transmitting coil are not so limited, it is better to use the (larger) coil with higher Q to achieve less sensitivity on precise mutual position and near disturbing objects.

Acknowledgements

This research has been supported by the European Regional Development Fund and the Ministry of Education, Youth and Sports of the Czech Republic under the Regional Innovation Centre for Electrical Engineering (RICE), project No. CZ.1.05/2.1.00/03.0094, TACR project No. TA02000103 CIDAM and funding program SGS-2015-038.

References

[1] SANGCHEOL, M., BONG-CHUL, K., SHIN-YOUNG, CH., GUN-WOO, M.: Analysis and Design of Wireless Power Transfer System with an Intermediate Coil for High Efficiency, *ECCE Asia Downunder (ECCE Asia)*, 2013 IEEE , pp.1034-1040, June 2013

[2] HEE-SEUNG, K., DO-HYUN, W., BYUNG-JUN, J.: *Simple Design Method of Wireless Power Transfer System Using 13.56MHz Loop Antennas,* Industrial Electronics (ISIE), 2010 IEEE Intern. Symposium, pp. 1058-1063, July 2010

[3] ZHEN NING, L., CHINGA, R. A., RYAN, T., JENSHAN, L.: Design and Test of a High-Power High-Efficiency Loosely Coupled Planar Wireless Power Transfer System, Industrial Electronics, *IEEE Transactions*, vol. 56, No. 5, pp.1801-1812, May 2009

[4] YIMING, Z., ZHENGMING, Z.: Frequency Splitting Analysis of Two-Coil Resonant Wireless Power Transfer, *Antennas and Wireless Propagation Letters, IEEE* , vol.13, No., pp. 400-402, 2014

[5] ZHANG, Y.; LU, T.; ZHAO, Z.; HE, F.; CHEN, K.; YUAN, L.: Selective Wireless Power Transfer to Multiple Loads Using Receivers of Different Resonant Frequencies, *Power Electronics, IEEE Transactions*, No. 99.

[6] KIANI, M., GHOVANLOO, M.: The Circuit Theory Behind Coupled-Mode Magnetic Resonance-Based Wireless Power Transmission, Circuits and Systems I, Regular Papers, *IEEE Transactions*, vol. 59, No. 9, pp. 2065-2074

[7] KUSAKA, K.; ITOH, J.-I.: *Experimental Verification of Rectifiers with SiC/GaN for Wireless Power Transfer Using a Magnetic Resonance Coupling, Power Electronics and Drive Systems (PEDS)*, IEEE Ninth Intern. Conference, pp.1094-1099, Dec. 2011

[8] TOOLEY, M, TOOLEY, M. H.: Electronic Circuits: Fundamentals and Applications, *Newnes*, pp. 77-78, ISBN 978-0-7506-6923-8

[9] CHUNLI, W, ZHIMING, B, JINGKUI, X, JINXING, W.: *Simulation Analysis on Quality Factor of RF Receiving Coil for an MRI System,* Control and Decision Conference, CCDC '09, Chinese, pp. 4652-4655, June 2009

[10] BABIC, S. I., SIROIS, F., AKYEL, C.; Validity Check of Mutual Inductance Formulas for Circular Filaments With Lateral and Angular Misalignments, *Progress in Electromagnetics Research M*, vol. 8, pp. 15-26, 2009

[11] BABIC, S. I., AKYEL, C.: Calculating Mutual Inductance between Circular Coils with Inclined Axes in Air, *Magnetics, IEEE Transactions*, vol. 44, No. 7, pp. 1743-1750, July 2008

[12] BABIC, S., AKYEL, C.: Improvement in Calculation of the Self- and Mutual Inductance of Thin-wall Solenoids and Disk Coils, *Magnetics, IEEE Transactions*, vol. 36, No. 4, pp. 1970-1975, July 2000

[13] HOCKICKO, P., BURY, P., MUNOZ, F.: Analyses of Dielectric Properties of Lithium Phosphate Glasses, *Communications - Scientific Letters of the University of Zilina*, No. 2A, 2013

[14] RADIL, R., JANOUSEK. L.: Yeast Growth Influenced by Parallel Combination of Time-Varying and Static LF EMF, *Communications - Scientific Letters of the University of Zilina*, No. 2A, 2013.

Milan Stork *

SINUSOIDAL AND RELAXATION WIDE RANGE VOLTAGE CONTROLLED OSCILLATORS

This paper presents a sinusoidal Wien-bridge and square wave wide range voltage controlled oscillators. The square wave oscillator is based on relaxation (Schmitt trigger) topology. All described oscillators have potential use in different applications, e.g. phase locked loops, modulation and detection. The frequency changing is based on optically coupled resistor with 100 dB dynamic range. The oscillators were constructed and measured. The new method for amplitude control for quadrature oscillator is also described.

Keywords: *Wien-bridge oscillator, relaxation oscillator, phase locked loop, voltage controlled oscillator, photoresistor, quadrature oscillator.*

1. Introduction

A voltage controlled oscillator (VCO) is one of the important basic building blocks in analog and digital circuits. For example, a VCO is the main building block in phase locked loop (PLL) and clock generator circuits [1]. This paper presents the design of 2 types of oscillators that are continuously voltage tunable. The frequency changing for all oscillators is based on optically coupled photoresistor (Vactrol) with 100 dB dynamic range [2]. The first is Wien-bridge oscillator with frequency range from approx. 0.1 Hz to 250 kHz with sinusoidal output. The Vactrol is used also for amplitude stabilization. The second oscillator is relaxation oscillator based on digital circuit with frequency range from 10 Hz to 9 MHz with square wave output. It is important to note that the control voltage and oscillator part are optically coupled.

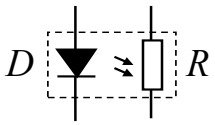

Fig. 1 The optically coupled photoresistor - Vactrol

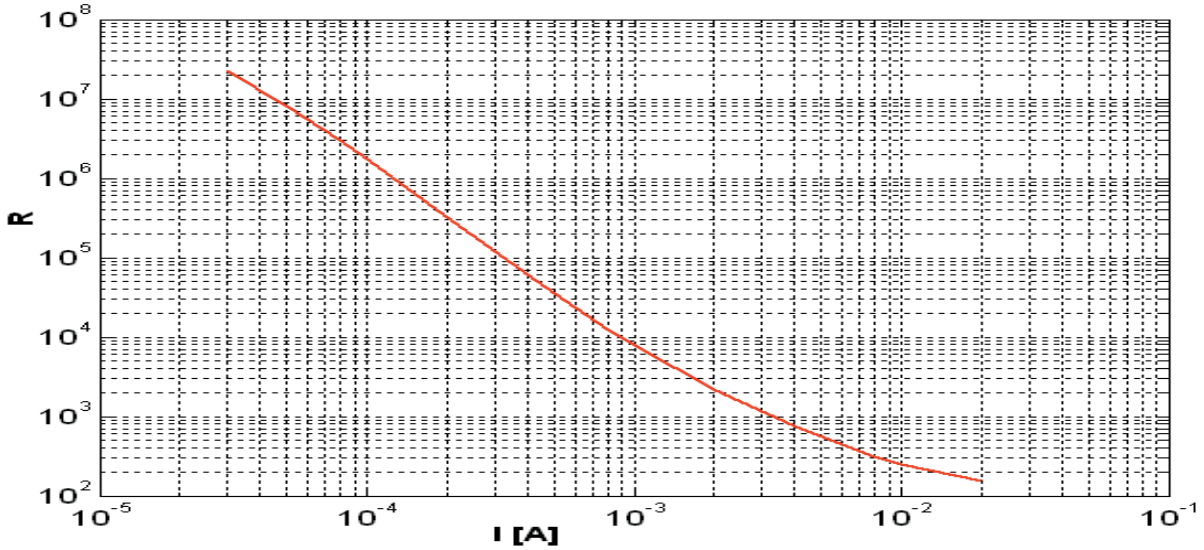

Fig. 2 Output resistance vs. input current for VTL5C1

* **Milan Stork**
Applied Electronics and Telecommunications/RICE, University of West Bohemia, Plzen, Czech Republic
E-mail: stork@kae.zcu.cz

2. Optically coupled photoresistor characteristic

Vactrol consists of a LED diode and photoresistor (Fig. 1). A photoresistor or light-dependent resistor (LDR) or photocell is a resistor whose resistance decreases with increasing light intensity. Optically coupled photoresistor (OR), also called photoresistive opto-isolator or Vactrol (after a trademark introduced by Vactec, Inc.) offers 100dB dynamic range, fast response time, and very high dark resistance. Some technical parameters for VTL5C1 [2] are: Min. isolation Voltage @ 70% Rel. humidity: 2500 VRMS; Max. resistor power: 175 mW; Max. resistor voltage: 100 V; Max LED current: 40 mA; Response time to 63% final R_{ON} 2.5 ms. The measured output resistance vs. input current is shown in Fig. 2 (logarithmic scales are used for both the X and Y axes).

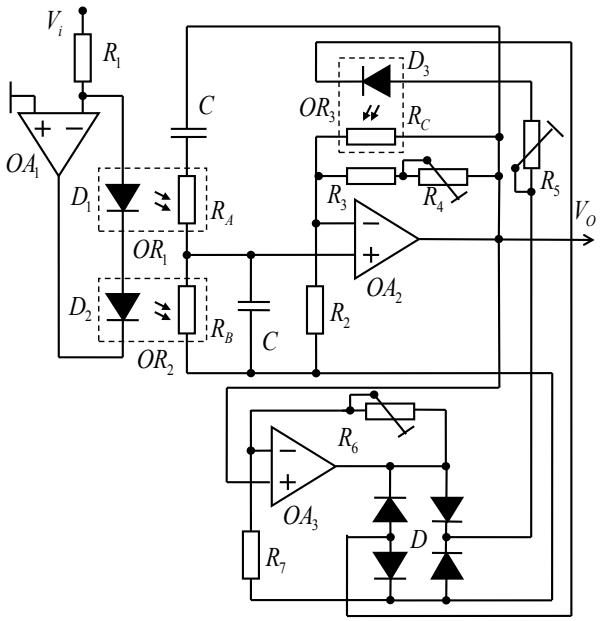

Fig. 3 The Voltage controlled Wien-bridge oscillator with buffer amplifier. R_1=1k; C=1n; R_2=10k; R_3=15k; R_4=10k; R_5=1k; R_6=R_7=10k; OA-TL074; D - 4x Schottky diodes, OR_1-OR_3 optically coupled photoresistors VTL5C1.

3. Wide range voltage controlled Wien-Bridge oscillator

The voltage controlled Wien-bridge oscillator [3 - 5] is shown in Fig. 3. The operational amplifier OA_1 is used to form voltage controlled current source. The current i_D, flows through diodes D_1 and D_2 of the OR_1 and OR_2. The output current is

$$i_D = \frac{V_i}{R_1} \qquad [\text{A, V, } \Omega] \qquad (1)$$

where V_i is input voltage and R_1 is resistor connected to inverting input.

The Wien-bridge oscillator consists of OA_2 where C; R_A; R_B are in positive feedback. The buffer OA_3 and diode bridge D, R_3, R_4, R_5 and OR_3 are used for automatic gain control. The output frequency is given as

$$f_o = \frac{1}{2\pi C\sqrt{R_A R_B}} \qquad [\text{Hz, F, } \Omega] \qquad (2)$$

Resistance of OR is approximately

$$R \approx \frac{k_{OR}}{i_D} = \frac{k_{OR}}{V_i / R_1} = \frac{k_{OR}}{V_i} \qquad [\text{A, V, } \Omega] \qquad (3)$$

where k_{OR} is OR constant and i_d is current through OR LED diode. Suppose that the R_A=R_B=R in this case the output frequency is given by

$$f_o = \frac{1}{2\pi C\sqrt{R_A R_B}} = \frac{1}{2\pi CR} \approx \frac{V_i}{2\pi CR_1 k_{OR}} \text{ [Hz, F, } \Omega] \qquad (4)$$

Measured output frequency vs. input voltage is shown in Fig. 4. The frequency spectrum is shown in Fig. 5 (spectral quality is better than 50 dB).

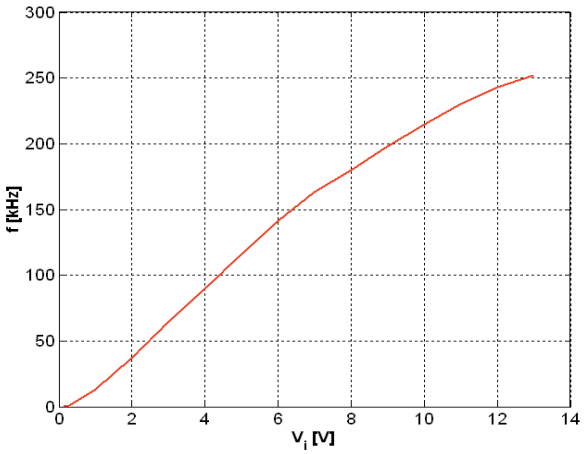

Fig. 4 Output frequency vs. input voltage for Wien-bridge oscillator

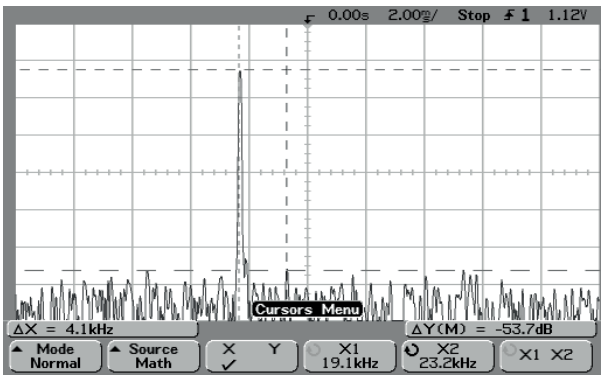

Fig. 5 The frequency spectrum of voltage controlled Wien-bridge oscillator

4. Amplitude control in quadrature sinusoidal oscillator

In this part another principle of the amplitude control of the quadrature sinusoidal oscillator is used. The block diagram of the quadrature oscillator with amplitude (energy) stabilization is presented in Fig. 6. The method is based on compensation of the parasitic dissipation parameters $-\alpha_1$ and $-\alpha_3$ by the multipliers connected in parallel along the dissipation blocks [6 and 7]. Desired value of the amplitude A of the oscillator signals is fed into the amplitude control block. The quadrature outputs of the oscillator (x_1 and x_2) are also connected to the amplitude control block. Amplitude control is based on eq. (5) where ideal steady state is

$$x_1^2 + x_2^2 = \left(V_1 \sin(2\pi ft)\right)^2 + \left(V_1 \cos(2\pi ft)\right)^2 = V_1^2 \underbrace{\left(\sin(2\pi ft)^2 + \cos(2\pi ft)^2\right)}_{} = V_1^2 = A \tag{5}$$

The amplitude is affected by means of PI (Proportional-Integrated) controller and multipliers controlled by x_3.

$$x_3 = k_p\left(A - x_1^2 - x_2^2\right) + k_1 \int \left(A - x_1^2 - x_2^2\right) dt \tag{6}$$

and block k_B (in Fig. 6) is used for the balancing of different values of α_1 and α_3. In Fig. 7 the block diagram of compensated integrator is shown (top) and compensated integrator with OA (bottom). The compensated integrator with OA can be described by eq. (7) where $R_4(i_d)$ is photoresistor controlled by current i_d.

$$\frac{V_i}{R_i} = -C\frac{dV_O}{dt} - \frac{V_O}{R_D} + \frac{R_3 R_4(i_d) V_O}{R_2\left(R_3 + R_4(i_d)\right)R_5} \tag{7}$$

For ideal compensation of R_D

$$\frac{1}{R_D} - \frac{R_3 R_4(i_D)}{R_2 R_5\left(R_3 + R_4(i_D)\right)} \tag{8}$$

therefore,

$$R_4(i_D) = \frac{R_2 R_3 R_5}{R_D R_3 - R_2 R_5} \tag{9}$$

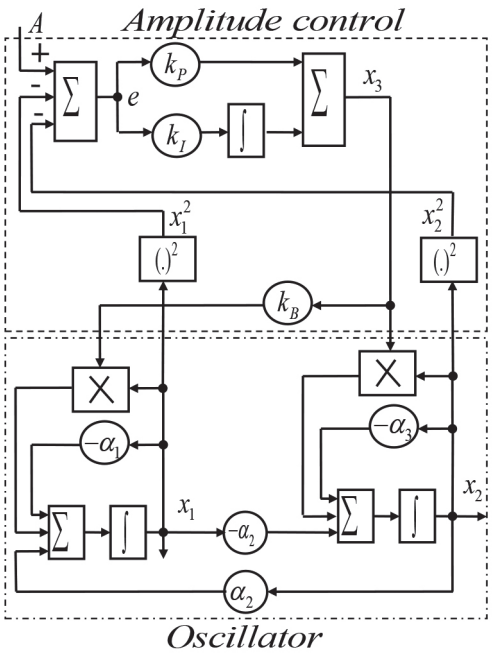

Fig. 6 Block diagram of the amplitude control for quadrature oscillator with compensation of dissipations α_1 and α_3. Controller for amplitude control is based on PI controller

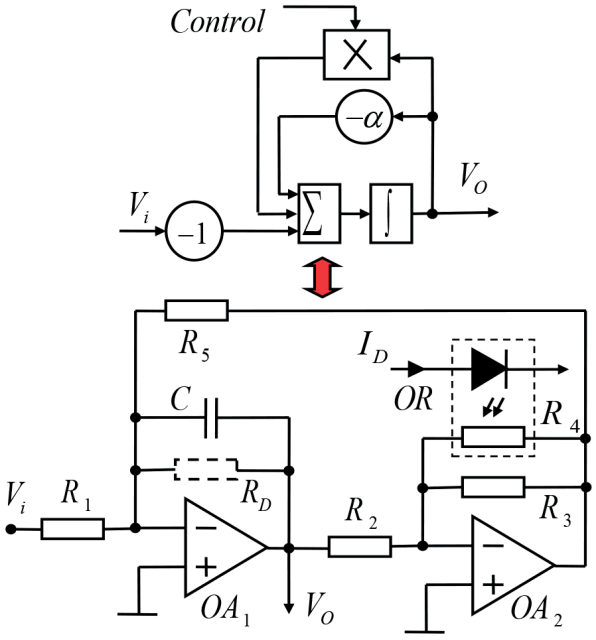

Fig. 7 The block diagram of amplitude control (top) and construction with optically coupled photoresistor (parasitic resistor R_D is compensated)

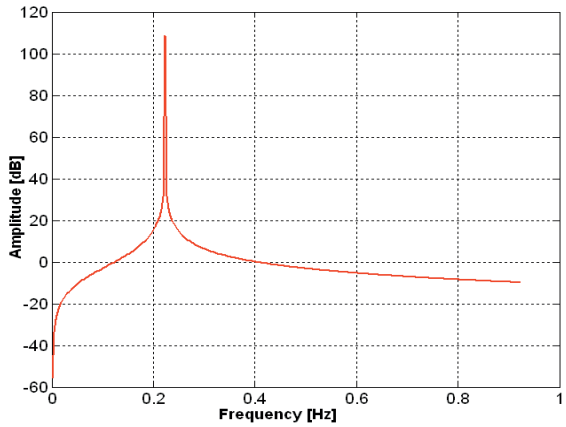

Fig. 8 Frequency spectrum of proposed oscillator (with compensation of the dissipation)

The frequency spectrum of quadrature oscillator with dissipative parameters compensation is shown in Fig. 8.

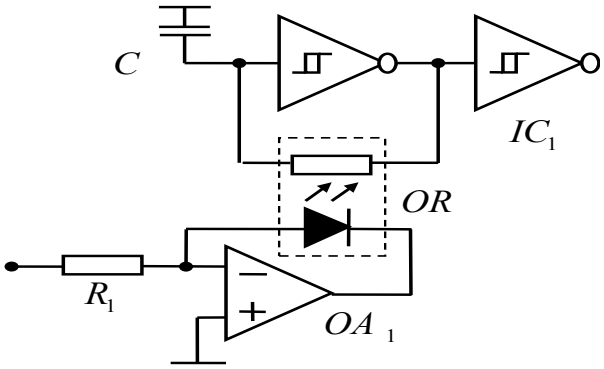

Fig. 9 The circuit diagram of relaxation oscillator with output buffer. R_1=1k; C=56 pF; OA-TL071; IC_1- CD40109, OR - optically coupled photoresistors VTL5C1

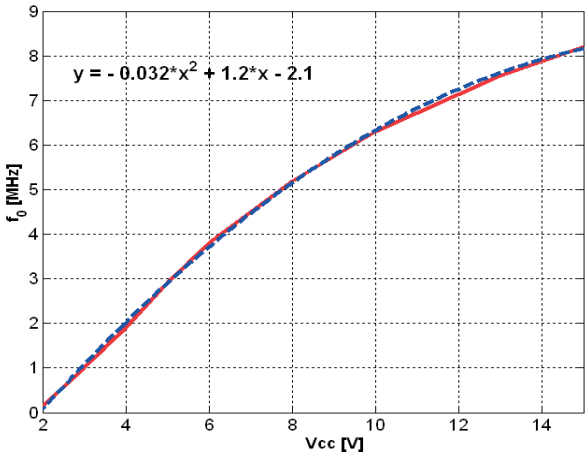

Fig. 10 Output frequency vs. supply voltage for relaxation oscillator with constant V_i=13 [V] (solid line), approximation – dash line

5. Wide range voltage controlled relaxation oscillator

The relaxation oscillator uses one Schmitt trigger capacitor and resistor [8 - 11]. The circuit diagram of voltage controlled relaxation oscillator with output buffer is shown in Fig. 9.

The output frequency vs. supply voltage (with fixed V_i=13 [V]) is shown in Fig. 10. The output frequency vs. input voltage (with fixed V_{CC}=15 [V]) is displayed in Fig. 11.

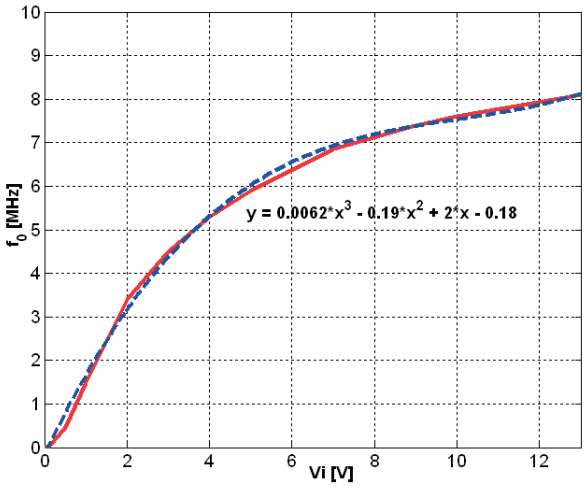

Fig. 11 Output frequency vs. input voltage for relaxation oscillator with Vcc=15 [V] (solid line), approximation – dash line

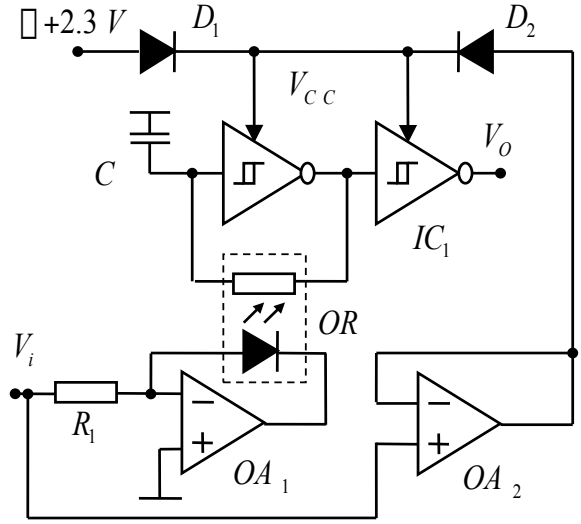

Fig. 12 The circuit diagram of linearized, relaxation oscillator with output buffer. R_1=1k; C=56 pF; OA_2, OA_2-TL072; IC_1- CD40109, D_1, D_2 - Schottky diodes, OR - optically coupled photoresistors VTL5C1

Measured values of output frequency versus input voltage for linearized relaxation oscillator Table 1

V_i[V]	2	3	4	5	6	7	8	9	10
f_o[MHz]	0.12	0.9	1.7	2.6	3.5	4.3	5	5.8	6.4

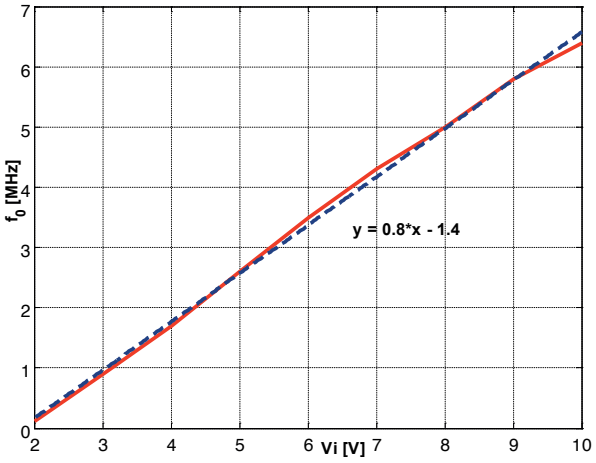

Fig. 13 Output frequency vs. input voltage for linearized relaxation oscillator (see Fig. 12). Measured values – solid line, approximation – dash line

The circuit diagram of linearized relaxation oscillator with output buffer is shown in Fig. 13. Linearization is based on supply voltage increasing together with input voltage. The OA_2 is used as power source for $V_i \geq 2.3$ V. The supply voltage is given by eq. (10):

$$V_{SS} = \begin{cases} \approx 2.3 & if \quad V_i < 2.3 \\ V_i & if \quad V_i \geq 2.3 \end{cases} \quad [V] \qquad (10)$$

Output frequency vs. input voltage of the linearized oscillator is displayed in Fig. 13. Measured values are in Table 1.

6. Conclusion

In this paper the *2* wide range simple V-f oscillators were described. For frequency control, the optically coupled photoresistor was used. The first is Wien-bridge oscillator with sinusoidal output with spectral quality greater than 50 dB. The second is linearized relaxation oscillator. All oscillators were constructed and measured. It is important to note that these oscillators can be used in different applications including PLL, frequency locked loop and low cost frequency synthesizers. The new method for amplitude control of sinusoidal quadrature oscillators with high spectral quality based also on optically coupled photoresistors and PI controller was also described.

Acknowledgment

This research has been supported by the European Regional Development Fund and the Ministry of Education, Youth and Sports of the Czech Republic under the Regional Innovation Centre for Electrical Engineering (RICE), project No. CZ.1.05/2.1.00/03.0094 and by the Grant Agency of the West Bohemia in Pilsen, grant No. SGS-2015-002.

References

[1] POPENDA, A.: The DFM Control System Based on PLL, *Communications - Scientific Letters of the University of Zilina*, No.1, pp. 53-57, 2009.
[2] VTL5C1, 5C2, Low Cost Axial Vactrols, PerkinElmer Optoelectronics, www.perkinelmer.com/opto.
[3] LI, A.: *Programmable Oscillator Uses Digital Potentiometers*, Application note, AN-580, Analog Devices, 2002.
[4] MANCINI, R., PALMER, R.: *Sine-Wave Oscillator*, Application Report SLOA060 - March 2001, Texas Instruments, 2001.
[5] LINDBERG, E.: *Oscillators - An Approach for a Better Understanding,* Proc. of the 2003 European Conference on Circuit Theory and Design, Krakow, 2003.
[6] OLIVEIRA, L. B., FERNANDES, J. R., FILANOVSKY, I. M., VERHOEVEN, C. J. M., SILVA, M. M.: *Analysis and Design of Quadrature Oscillators*, ISBN: 978-1-4020-8515-4, Springer, 2008.
[7] JAIKIA, W., PROMMEE, P.: Electronically Tunable Current-mode Multiphase Sinusoidal Oscillator Employing CCCDTA-based Allpass Filters with Only Grounded Passive Elements, *Radioengineering*, vol. 20, No. 3, pp. 594-599, September 2011.
[8] LINSAY P.S., WANG, D. L.: Fast Numerical Integration of Relaxation Oscillator Networks Based on Singular Limit Solutions, *IEEE Trans. Neural Net*., 9: 523-532, 1998
[9] WEIGANDT, T. C, BEOMSUP, K., GRAY, P. R.: *Analysis of Timing Jitter in CMOS Ring Oscillators,* Proc. of IEEE Int. Symp. Circuits and Systems, vol. 4, pp. 27-30, London, June 1994.
[10] *Accurate and Efficient Frequency Evaluation of a Ring Oscillator*, Application Note 4070-3, Agilent Technologies 2000.

[11] YUCHI, NI: *Low-power CMOS Relaxation Oscillator Design with an On-chip Circuit for Combined Temperature-compensated Reference Voltage and Current Generation,* Northeastern University, Electrical and Computer Engineering Master's Theses. Paper 127, 2014 http://hdl.handle.net/2047/d20004909.

Petr Bernat - Petr Kacor *

OPERATIONAL NON-CONTACT DIAGNOSTICS OF INDUCTION MACHINE BASED ON STRAY ELECTROMAGNETIC FIELD

Paper deals with one new method of testing and operational diagnostics of induction machines using a stray electromagnetic field. This leakage field on the surface or on surroundings of machine frame is the carrier for diagnostic information and we can make simultaneous comparisons of utility, advantages and disadvantages of the existing and most common methods of diagnostics performed using the measurement of the machine supply current. This method is patented as Czech Patent CZ 303 470, UPV 2012.

Keywords: *Induction machine, asynchronous motor, functional testing, technical diagnostics, frequency spectrum, current spectrum, stray electromagnetic field, leakage electromagnetic field.*

1. Introduction

Operational diagnostics of electric machinery represents a field of diagnostics using information associated with operating values of particular machinery to draft final diagnostic results [1 and 2]. Historical development of asynchronous machinery as the most common type of rotary machines in general is fairly long and headed towards a definite objective - maximum utilization of particular design assemblies. That makes the current machinery substantially less bulky and lighter while their mechanical and electrical parameters have improved [3 and 4]. Manufacturers strive to comply with the laws of economics to deliver their production at the minimum cost possible; users pursue the same reasons and seek for the cheapest equipment with the best reliability and durability characteristics feasible [5]. The main objective of technical equipment must not always lie in the maximum reliability, this is due to various reasons (mostly economic or the so called "environmental" ones nowadays), the equipment may show threshold values for utilization of certain materials in particular assemblies rising the potential breakdown risk of particular components, which may lead to numerous alternatives and serious consequences [6]. This further emphasizes the significance of technical diagnostics that may eliminate some deficiencies to a certain extent in a suitable manner to help the equipment operators increase the reliability of their machinery as well as the entire system, where it is integrated. Economic objectives followed by the operator can therefore be met at a much higher level [7].

2. Asynchronous machine as a mechanical/electric system

Asynchronous machines are ranked among electric rotary machinery, the potential breakdown risks are then based on the machine layout as well as the relevant design and operating assemblies comprising the following:

- Electric circuits – i.e. machine wiring with the relevant accessories (conductors, insulating system, outlets and terminals)
- Magnetic circuits of stator and rotor
- Mechanical parts, especially a shaft and bearings, frame, vent.

Reliability of certain assemblies of particular machines can be determined either by analytical or model means, even the so called defect records (defect analysis log - breakdowns and causes) kept at servicing organisations can be a fairly accurate source of data.

Statistics show that electric circuit tends to be the part of machinery most prone to breakdowns; it is mainly the insulating system of stator wiring and the integrity of rotor wiring, which corresponds to the load exerted on these components and potential risks arising from their design. Failures of electric circuit bring fatal impact on machine operability and result in serious interference with all the operating characteristics and values of machinery even when in "smaller" extent (torque, noise, vibrations, temperature increase).

* **Petr Bernat, Petr Kacor**
Department of Electrical Power Engineering, Faculty of Electrical Engineering and Computer Science,
VSB - Technical University of Ostrava - Poruba, Czech Republic
E-mail: petr.bernat@vsb.cz

Failures of electric circuit are less common, these are mainly caused by another defect in the electric or mechanical system of the machine. This type of failure is often due to incorrect maintenance. Failures of the electric circuit would mostly have a low impact on the overall machine characteristics only, as the machine generally remains operable even in such case.

The statistics also show that most breakdowns would not occur individually, several of those are mutually linked in terms of contingencies, some of which may be causative. Diagnostics and servicing of machinery must be based on clear knowledge of these contingencies to ensure accuracy of conclusions reached by diagnostics and correct servicing outcome. This event would result in repeated occurrence or further development of the same or similar failures.

To achieve a clear diagnosis, the particular diagnostic value must be free from any impact brought by changes inside the machine irrelevant to the initial change of conditions or failure or to create an opportunity to confirm or refute such impact using another method or value. One of the options to describe the method for obtaining diagnostic information comprises a detailed analysis of the energy flow inside machine, i.e. a procedure following genuine physical basic principles of the machine operation in relevance to all the physical processes taking place inside the machine in operation.

Rotary electric machine operates with dominant energy flow (depending on the machine operation mode) along the power supply axis (current supply) and the machine shaft (mechanical work). Electric circuits integrated within are defined by the design and type of machine to control the energy flow – wiring, magnetic circuits and air gap. Electromagnetic field plays a key role in transmission of energy between the stator and rotor, Fig. 1.

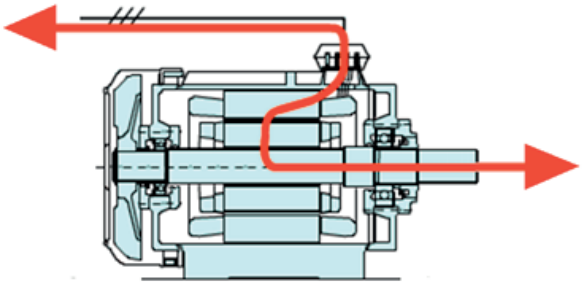

Fig. 1. Dominant way of energy transformation in asynchronous machine as motor or generator

The energy flow through the machine is subject to several effects, some of which are parasitic. The background of dominant transformation of energy is abound with various events, some of which affect the flow of energy. This impact is generally periodic and off the sequence of essential harmonic frequencies. Focusing on any design or failure asymmetry, for example, will reveal its distortion effect on energy flow in the machine by characteristics means. Such distortion will then produce a characteristic projection into other operation values. When proven by measuring or even changed by further electric or mathematical alteration of the signal produced, the distortion can be separated from the main energy flow to obtain the actual diagnostic value required as the information leading towards diagnosis.

3. Diagnostic methods based on frequency analysis of operation parameters of asynchronous machine

Our laboratory has been dealing with development or improvement of diagnostic methods applicable to asynchronous machines for several decades. Research activities conducted by our team have been always aimed at simple obtaining of diagnostic values and applicability of methods even under complex conditions (hazardous areas, e.g. mining environment). The most common failure is represented by breach of rotor cage bars resulting in infringement of symmetry in rotor circuit proven by contravention of current density in particular bars – rotor phases - with subsequent change to the course of electromagnetic field along the rotor perimeter. The rotary field of machine will develop new fields the rotary speed of which is no longer synchronous and these cause cyclic distortion of the main field. The distortion is further transferred via field distortion inside the air gap to enter the stator field to affect the course of current fed to the machine. The main harmonic will be accompanied by lateral bands – frequency lines in reflective layout corresponding to the machine slip frequency:

$$f_x = f_1\left(1 \pm 2s\right) \tag{1}$$

Where: f_x - is the frequency of lateral bands expressing asymmetry, f_1 - is the frequency of machine supply voltage ("i.e. the first one – dominant harmonic"), s - is the slip.

Our measurements have proven direct proportion between amplitudes of these characteristic frequencies and the supply frequency and the magnitude of failure; this ratio can therefore be employed as a diagnostic value to determine presence of asymmetry and for optional benchmark measurements to define the extent of asymmetry. Any asymmetry of machine will show the current spectrum with further - the so called speed - frequencies to be derived using our formula below:

$$f_n = \frac{n}{60} + s \cdot f_1 + i\frac{n}{60} \tag{2}$$

Where: n - is the machine shaft revolution per min., f_1 - is the supply voltage frequency, n_s - refers to synchronous speed. Further frequencies present within the machine current are generated by fluting of stator and rotor slots and potential mechanical asymmetry – most often eccentricity:

Stator slots frequency:

$$f_v = f_1\left(\frac{Q_s}{p} \pm 1\right) \quad (3)$$

$$f_v = f_1\left(\frac{Q_R(1-s)}{p} \pm 1\right) \quad (4)$$

Rotor slots frequency:

$$f_v = \frac{f_1}{p}(1-s)(Q_r \pm p) \quad (5)$$

$$f_v = f_1\left(\frac{Q_S(1-s)}{p} \pm 1\right) \quad (6)$$

Frequency generated by dynamic eccentricity:

$$f_v = f_1\left[(kQ_r \pm n_d)\frac{1-s}{p} \pm \nu\right] \quad (7)$$

$$f_d = f_1\left[\pm\nu \cdot \frac{1-s}{p} + 1\right] \quad (8)$$

Frequency generated by static eccentricity:

$$f_v = f_1\left[kQ_r\frac{1-s}{p} \pm \nu\right] \quad (9)$$

where: Q_r or Q_s - is the number of rotor (stator) slots, f_1 - is the basic harmonic frequency of supply current, p - is the number of pairs of poles, s - is the slip, k= 1,2,3..., ν - is the grade of harmonic being sought.

Knowledge of these frequencies helps use the frequency analysis of current flow to perform diagnostics with both the electric asymmetry of rotor as well as other failures, typically the mechanical asymmetry (eccentricity and incorrect alignment). Figure 2 shows typical spectrums of currents for various severity levels of motor failure.

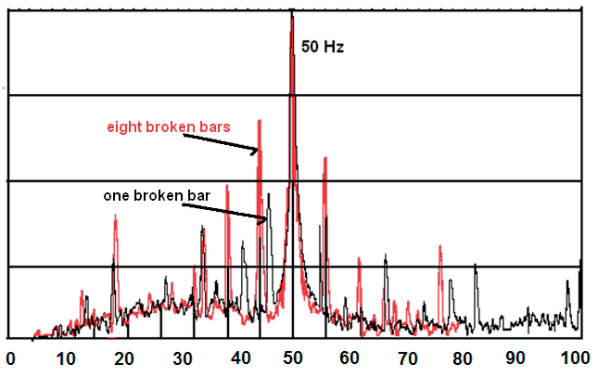

Fig. 2. Standard demonstration of motor failure with various severity levels within the supply current spectrum.

Apart from harmonic analysis, filtration is another method employed to assess a diagnostic value. One of the famous examples is the characteristic proof of asymmetry in motor that becomes evident as an additional frequency appearing in the machine supply current around the 50% speed level. This frequency is lower, compared to the frequency of basic harmonic; and it can be shown by simple filtering off applied to frequencies above approx. 20% f_1.

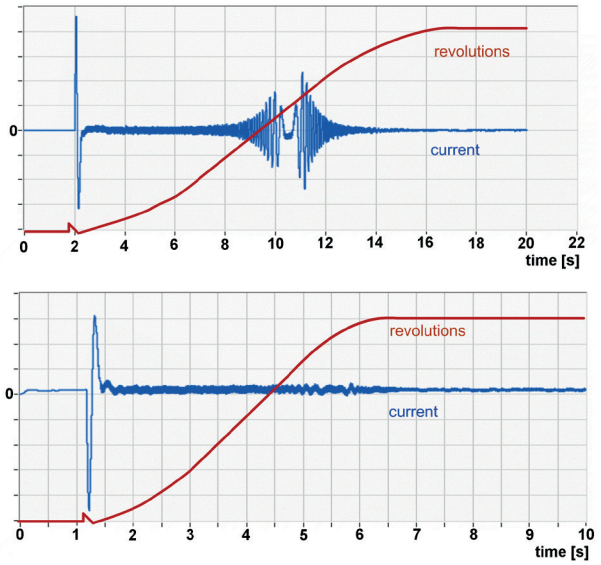

Fig. 3. Filtered record of current during launch on faultless machine and another one with faulty rotor showing a typical demonstration of failure proven by behaviour of the diagnostic value.

Practical application of this method focuses on monitoring of current during motor start-up; this is why it is also called “start-up method”. Its benefit lies in the option to diagnose the starting cage in machine rotor which cannot be diagnosed by any other methods provided within the on-line diagnostic. Figure 3 shows a typical demonstration of motor failure illustrated as a diagnostic value from launch method.

The dominant flow of energy will be accompanied by a whole range of other power effects in case of machine supplied from a frequency converter. If these can be defined, identified or even eliminated, they will not affect the assessment of diagnostic as such, this fact has been proven before [2]. The basic principle of diagnostics conducted on asynchronous machines based on supply current analysis and derived for machinery powered from the mains can be even applied to machinery powered from indirect frequency converters directly and without any substantial alterations or problems. Noise and parasitic frequencies developing due to non-sinusoidal supply can be eliminated efficiently during measurement using analogous or digital filtering and anti-aliasing filters. Any asymmetries will create characteristic frequency lines developed on frequencies that can be determined using the formulas above where the dominant - first harmonic value is the frequency preset at the frequency converter for this machine, so it does not have to be the regular 50Hz. The essential electromagnetic principle of energy transformation remains in the assembly comprising converter-motor-mechanical work, the

stray electromagnetic field then also carries information suitable for diagnostics. The initial worries concerning potential impact of interference on the field measuring chain by occurrence of powerful spurious fields created due to steep initiating processes in the vicinity of such supplied machine and its supply line have not been confirmed. The main portion of switching interference energy is further demonstrated at higher frequency levels only, whereas the diagnostic information is concentrated at the lower end of spectrum close to the dominant harmonic or even between the latter and the zero frequency.

These methods represent a mere fraction of methods already common and developed to a regularly usable level. For the summary of other methods applicable to complex - overall on-line and testing diagnostics of asynchronous machine refer to examples in [2 - 9].

4. Obtaining diagnostic value

The above mentioned diagnostics has been performed using the value allowing to separate the diagnostic information and machine current up until now. Machine current is relatively easy to measure, although there are machines and situations where current as the value measured is hardly available, e.g. on machinery operated in environment with various hazards, e.g. mining areas. Safe performance of diagnostics in this case therefore requires a different value.

Looking at the machine principle and flow of energy throughout its individual components, one would see the role played by electromagnetic field here. It is the field, subject to characteristic distortion by occurring failure that carries such distortion into the supply current as a corresponding image. If we are to obtain the diagnostic value right from the electromagnetic field, the results obtained should match the results achieved by diagnostics based on current. The electromagnetic field is concentrated rather inside the machine and performs the desired work within. However, there is a certain part of electromagnetic field closed outside the frame as a stray field even due to parasitic ways thanks to the design and materials used. Its behaviour over time corresponds with the behaviour of field inside the machine, as well as during the flow of current in machine supply on reciprocal basis.

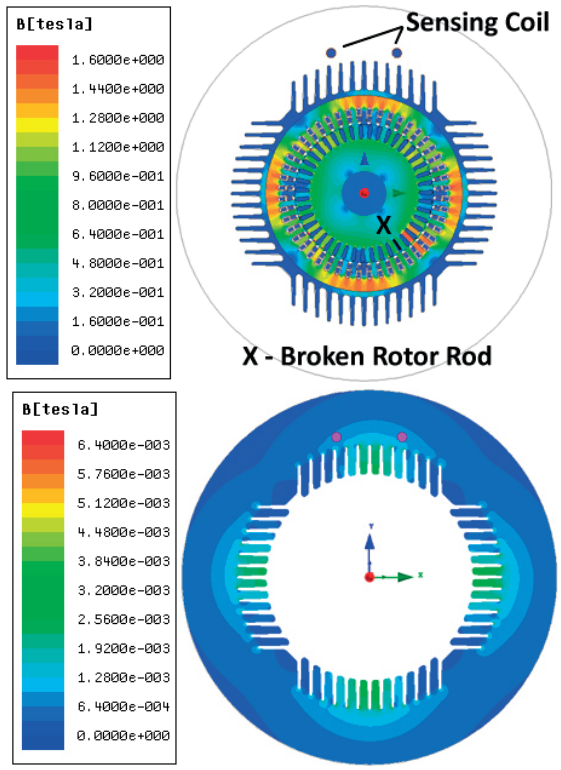

Fig. 4. Distribution of electromagnetic field inside and outside of induction motor with one broken rotor rod at notation X

Figure 4 shows the distribution of electromagnetic field inside and outside – on the surface of asynchronous motor stopped over time – rotation of this field still actually matches rotation of the resultant vector of field inside the machine. Distribution of magnetic flux density is analysed by the help of FEM transient simulation on common design of 2p= 4 poles induction machine. The simulation also comprises the influence of the one broken rod in rotor on total distribution of magnetic flux density.

Values of electromagnetic induction on the machine frame surface and its close vicinity range within units of mT, this value is still three grades below the value of induction inside machine but it still suffices as the information carrier. Monitoring the behaviour of field changes at one specific surface spot produces a time image corresponding with the current, Fig. 5.

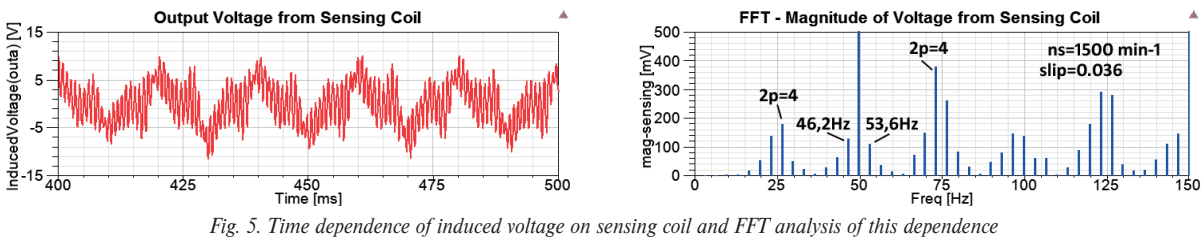

Fig. 5. Time dependence of induced voltage on sensing coil and FFT analysis of this dependence

The stray field of electric machine, as an existing objective value, had been subject to research in the past, most often with respect to electromagnetic compatibility as a matter of fact. Its effects during current induction performed within conductive design elements are also known. Direct measurement of stray field in the machine vicinity as a source of additional information has been utilised in the patent No. DE3722805, for example, providing a description of the method for determination of slip in asynchronous motors used for mining, by measuring of speed with respect to torque characteristic of the particular machine. The rotor current frequency in this method has been determined using the stray magnetic flow outside the motor frame and the frequency signal obtained was then assessed together with the mains voltage of motor subject to measurement. The signal measured was filtered to separate the speed frequency only, corresponding with the mechanical frequency of rotor rotation; this frequency, corresponding to the speed numerically, was the only resultant informative value. Its authors conducted measurement of the magnetic field for non-contact establishment of radial or axial positions of the machine rotor, mostly a synchronous one.

If the stray field and the image of its behaviour over time refer to the field inside machine, the facts above can be followed to perform its diagnostics as its informative value and diagnostic potential are much higher! The bond of machine diagnostic image performed from the stray field using various procedures applicable to diagnostics of behaviour of the supply current with respect to specific machine failures has been clearly proven by contingencies defined above. The contingency between frequency anomalies in the current behaviour with individual typical failures has been proven before by means of many measurements on machines with simulated or actual failures in our laboratory as well as right at industrial sites; that was the reason for repeating these measurements even to prove congruent relations between failures and the behaviour of stray electromagnetic field outside the machine. Monitoring of the diagnostic value was conducted from both the current and field simultaneously with joint assessment producing a clear result – characteristic values of current and field are illustrated by similar means, diagnostics based on the field is therefore not just an accessory, yet rather an equivalent diagnostic method.

The measurement can be conducted using any sensor - decoder for high fidelity conversion of the time path of field changes at a specific spot into another value measurable by regular means (i.e. voltage or current most often). There are two types of sensors applicable in practice; the field probe using Hall Effect or the air-core coil (no regular core coil can be used as the reading could be distorted due to non-linearity and such effect is very hard to predefine). Another benefit of the sensor employed is, besides other, the low internal impedance and parasitic capacity bond, the resultant interference effect caused by electric fields is therefore low when linked to the measuring chain properly. The number of turns on core has no significant impact on measurement; regular machinery can achieve voltage with amplitude around 1V and usual intensity level of approx. one using a thousand coils. The real absolute value of conversion provided by decoder, i.e. the scale for imaging of certain values in the magnetic field associated with the voltage monitored is not important for diagnostics, most of the frequency (Fourier Fast Transform - FFT) diagnostic methods process the diagnosis using comparative values, usually related to the values measured for some of the dominant harmonic frequencies.

The measuring (sensing) coil is linked to the supply input on upstream gauge or analyser directly. The only substantial aspect is to comply with essential conditions applicable for any diagnostic measurement – the conversion must be independent from frequency within a required scope of monitoring focused on diagnostic value, the measurement process must be also run without over-saturating or overloading of input on the decoder or another gauge used respectively; that also applies to peaks entering the measurement chain through a capacity bond, e.g. due to interference when supplied from a frequency converter.

Application of this method has been verified even in hazardous environment for diagnostics of failures on winding of cutter-loader rotor assembly, it can therefore be considered fit for machinery posing certain trouble or even obstacles when obtaining the diagnostic value with regard to safety matters.

5. Conclusion

The method for relatively easy sourcing of diagnostic information from the stray electromagnetic field is under further development and it has been used as basis for a whole range of diagnostic methods focused on diagnostics of particular assemblies within an asynchronous motor. The progress concerns further development of methods and methodology applicable for diagnostics of other failures, especially on stator winding assemblies. Evolving these methods and making them available to experts allow performance of diagnostics of asynchronous motors more efficiently at lower costs, which improve operation economy. Further important benefits arising from the said method include reduction of safety risks associated with diagnostics, which supports extension of its applicability to machinery hard to diagnose due to potential hazards.

Acknowledgment

This work was supported by project No: SP2014/187, VSB – Technical University of Ostrava, Czech Republic.

References

[1] CHMELIK, K., CECH, V., BERNAT, P.: *Method for Determination of Status of Electric Machine, Especially Asynchronous Electric Motors,* Patent CZ 303 470, UPV 2012.

[2] BERNAT, P.: *Negative Impacts of Frequency Converters on Asynchronous Motors*, Dissertation work, VSB-TU Ostrava, 2006

[3] KACOR, P.: *Axial Generator for Small Wind Power Plant*, Proc. of the 13th Intern. Scientific Conference Electric Power Engineering 2012, EPE 2012, May, 2012, VUT Brno, pp.1149-1153, ISBN 978-80-214-4514-7

[4] MIKOLAJ, J., SCHLOSSER, F., REMEK, L.: Life-cycle Cost Analysis in Pavement Management System, *Communications - Scientific Letters of the University of Zilina*, vol. 15, No. 3, 2013, pp. 102-106, ISSN 1335-4205

[5] BERNAT, P., MISAK, S.: *Induction Machine Diagnostics*, Proc. of the 12th Intern. Scientific Conference Electric Power Engineering 2011, EPE 2011, May, 2011, Kouty nad Desnou, VSB-TU Ostrava, pp. 179-182, ISBN 978-802482393-5

[6] KACOR, P., MISAK, S., PROKOP, L.: *VAWT - Modification of Wind Turbine with a Vertical Rotation Axis*, Proc. of the 12th Intern. Scientific Conference Electric Power Engineering 2011, EPE 2011, May, 2011, Kouty nad Desnou, VSB-TU Ostrava, pp. 282-286, ISBN 978-802482393-5

[7] BAUER, P., SITAR, J.: Analysis of Electromechanical Actuator Based on FEM - Circuit Simulator Coupling, *Communications - Scientific Letters of the University of Zilina*, vol. 9, No. 1, 2007, pp. 8-16, ISSN 1335-4205.

[8] KACOR, P., BERNAT, P.: *Analysis of Force Characteristic of Short-circuit Release in Low Voltage Circuit Breaker*, Proc. of 15th Intern. Scientific Conference on Electric Power Engineering, EPE 2014, art. no. 6839414, pp. 515-519, ISBN: 978-147993806-3.

[9] BERNAT, P.: *Operational Diagnostics of Induction Machines*, *Carried out the Stray Electromagnetic Fields (in Czech)*, Proc. of 14th Intern. Scientific Conference on Electric Power Engineering 2013, EPE 2013, pp. 411-415, ISBN: 978-80-248-2988-3.

Lorand Szabo - Mircea Ruba - Daniel Fodorean - Pavol Rafajdus - Peter Dubravka *

TORQUE SMOOTHING OF A FAULT TOLERANT SEGMENTAL STATOR SWITCHED RELUCTANCE MOTOR

The relatively high torque ripples are one of the main disadvantages of the switched reluctance motors. By smoothing their torque they can become more competitive for variable speed drives used in automotive and industrial applications. One of the most promising approaches to reduce the torque ripples of a SRM is the use of a direct instantaneous torque controller. In the paper the effectiveness of this type of control will be proved for a fault tolerant segmental stator SRM. By advanced simulation techniques the working principle of the direct instantaneous torque controlled drive system is illustrated, and its performances are demonstrated.

Keywords: *Switched reluctance motor, segmental stator construction, direct instantaneous torque control, simulation.*

1. Introduction

Beside high electrical and mechanical performances the fault tolerance is the main issue for electrical machines used in diverse safety-critical applications, as aerospace, automotive, military, medical, etc.).

The switched reluctance motor (SRM) due to its robust and simple construction and to the magnetic independence of its phases is inherently one of the most fault tolerant motors on the market [1]. Combining the fault tolerance increasing solutions cited in the literature [2], [3] and [4] with an innovative modular construction of its stator a novel SRM was developed, which is very reliable and quickly repairable. Its performances were improved by minimizing its torque ripples by estimating and controlling the developed instantaneous torque.

2. The segmental stator SRM

The stator of the proposed segmental stator SRM is built up of independent modules. Each one has an E-type iron core and a coil wound on its yoke. The modules corresponding to a phase are placed diametrically opposed in the stator. Between the neighboring modules a non-magnetic spacer is placed to assure the adequate shift of the modules and a good magnetic separation (see Fig. 1).

The four-phase variant has 8 stator modules. The entire segmental stator construction is tightened by 16 rods, 2 passing through each module. The stator is placed between two end shields. The conventional SRM rotor has 14 poles and it is built of laminations. The construction of the segmental stator SRM is given in Fig. 2.

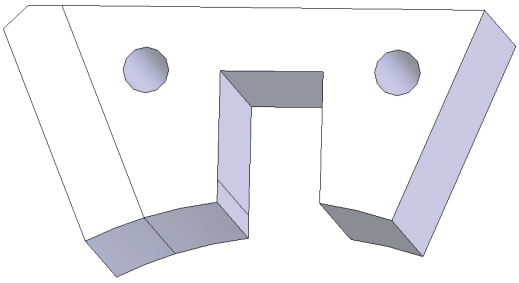

Fig. 1 The iron core of one module together with a spacer

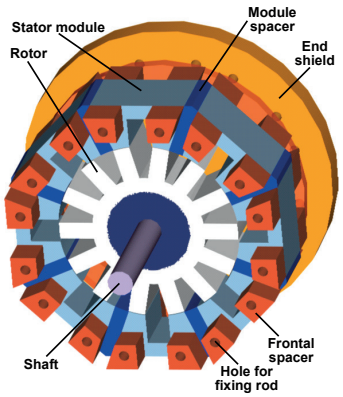

Fig. 2 The segmental stator SRM

* [1]Lorand Szabo, [1]Mircea Ruba, [1]Daniel Fodorean, [2]Pavol Rafajdus, [2]Peter Dubravka
[1]Faculty of Electrical Engineering, Department of Electrical Machines and Drives, Technical University of Cluj-Napoca, Romania
[2]Faculty of Electrical Engineering, Department of Power Electrical Systems, University of Zilina, Slovakia
E-mail: Lorand.Szabo@emd.utcluj.ro; pavol.rafajdus@fel.uniza.sk

The flux lines in the motor obtained by means of finite elements analysis (FEA) for unaligned and aligned positions are shown in Fig. 3 [5].

As it can be seen, the magnetic flux is closed between the two poles of a single module hence they are not passing through the central part of the rotor. Therefore, due to the shorter flux paths the losses in the machine are less than in a classical 4-phase SRM. Also due to this novel design the forces are better balanced in the machine [6].

One of the common fault tolerance increasing solutions is the division of the phases into individual coils, called channels [4], [7] and [8]. This way a fault of a channel will not influence the operation of the other channels of the same phase or of other phases. This solution was used also in the case of the segmental stator SRM in study. Hence, one phase of the machine is compound of two coils from diametrically opposed modules, connected in series or in parallel.

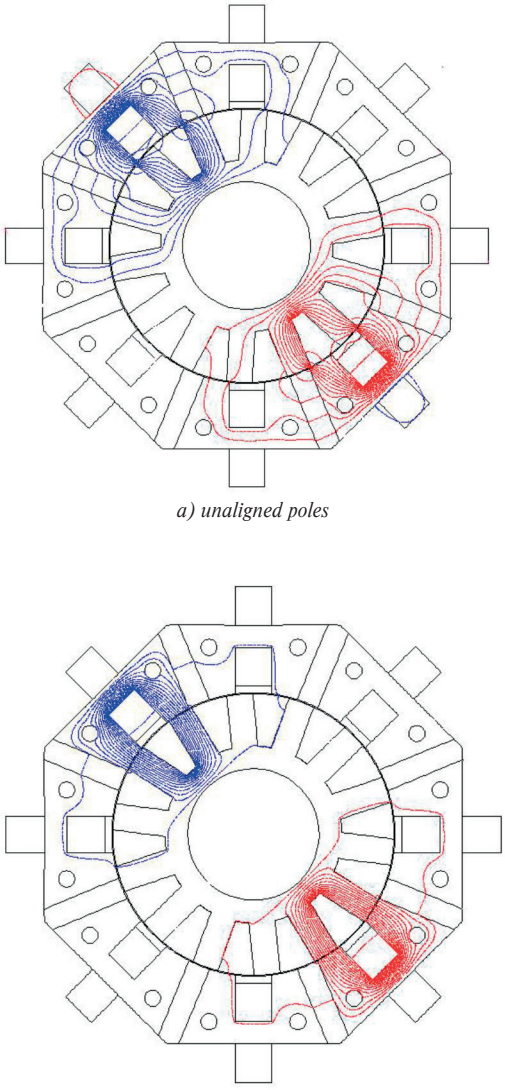

a) unaligned poles

b) aligned poles

Fig. 3 The flux lines in the SRM in study obtained by means of numeric field computations

Due to the specific construction there is no mutual coupling between adjacent coils [6]. The drawback of this solution is that a more complex power converter is required, having as many converter legs as channels [9] and [10].

The adopted modular stator topology allows for an easy and quite low cost manufacturing, and assures the possibility of a fast replacement of a damaged module in case of a coil failure [5].

The main rated specifications of the sample segmental stator SRM taken into study are:

- power: 350 W;
- current: 6 A;
- average torque: 5 Nm.

3. The direct instantaneous torque control

One of the main disadvantages of the SRMs, and also of the particular segmental stator SRM in study, is their high torque ripple. These can generate significant undesired vibrations and noises.

In the literature several methods of SRM torque smoothening methods are cited [11] and [12] and [13]. These all require complex control [14] and [15], accurate torque and rotor position measurement [16], and complex current regulation techniques [17]. Current profiling [18] and [19] and torque sharing [20] and [21], methods are just two solutions that can be used for minimizing the SRM torque ripples.

A common conclusion can be drawn upon studying these methods, namely that as the complexity of the control strategy is increased, the losses in the SRM are also higher [22]. Therefore, a novel method was applied, the direct instantaneous torque control (DITC) [23], [24] and [25]. This has to be used where the losses have to be as low as possible, the system response has to be fast and accurate, and the generated torque must be very smooth [26].

The main advantage of the DITC is the lack of minor current loops, and of the precise tuning requirements of the PI or PID controllers. The torque is controlled directly by using a specific digital hysteresis controller. On the other hand, as the phase currents are not controlled, overheating of the power switches can occur. At high speeds, and when the currents are very high, the falling to nil of the current could be not enough fast and negative torques could be generated by a phase.

The instantaneous torque developed by the SRM needs to be known at each time step. Its precise measurement is difficult and expensive. A more effective approach is the estimation of the torque. In the literature basically four methods are cited for torque estimation. These methods are based on look-up tables, interpolation, analytical approach and artificial neural networks

(ANN) [27], [28] and [29]. For the DITC method, the look-up table approach seems to be the best solution [23], [30] and [31].

For estimating the torque from the measured current and rotor position the static torque versus current and angular position is required. The values of this characteristic are stored in a 2D look-up table which can be obtained via measurements or FEA of the SRM [30] and [31]. Knowing at each time step the actual current and the rotor position, the torque of the SRM can be found by a simple looking in the table. It should be mentioned that separate look-up tables have to be computed for each SRM variant. The simplified block scheme of the DITC system of a SRM under study is given in Fig. 4 [13].

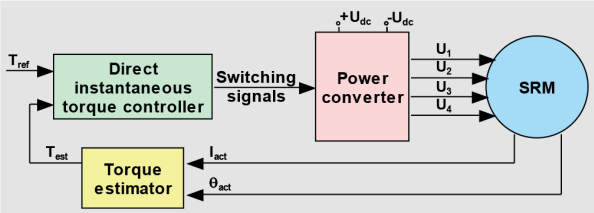

Fig. 4 The block scheme of the DITC system of a SRM [13]

4. The DITC of the modular SRM

The block diagram of the proposed DITC is given in Fig. 5 [32].

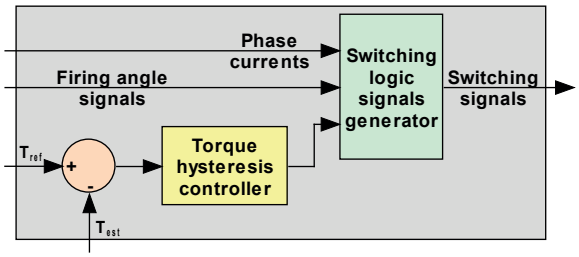

Fig. 5 The block scheme of the DITC [32]

The firing angles compared with the actual rotor position only indicate the conduction zones of the SRM. The main control tasks are performed by the torque hysteresis controller and the generator of switching logic signals. The torque controller uses two different hysteresis bands, one larger than the other. The control strategy follows the following rules:

1. while a single motor phase is active, the torque is controlled inside the main (the wider outer) hysteresis band;
2. during the phase commutation the torque control is performed as follows:
   - for the formerly conducting phase the thinner hysteresis band is imposed;
   - for the next phase the larger outer hysteresis band is prescribed;
3. after the end of the commutation period the torque will be again controlled within the outer hysteresis band.

Upon the actual value of the torque relatively to the two hysteresis bands the voltages of the phases are commutated by soft chopping between three values: $+V_{dc}$, 0, and $-V_{dc}$.

To simulate the DITC system an advance SRM model was built up. The simple, voltage equations based mathematical models [1] cannot be applied here, because of the necessity to integrate also the converter model and the DITC strategy. Therefore a more complex, FEA results based model was applied. For the sample SRM two look-up tables were built up upon the previously obtained FEA results [5], [33] and [34]. They contain the magnetic flux and the torque, respectively, versus the phase current and the rotor position. Upon the values from the two look-up tables two 3D static characteristics for one phase of the segmental stator SRM were plotted (see Fig. 6). The static characteristics of the magnetic flux are required only by the simulation program while that of the total torque both by the control strategy implementation and the DITC system model.

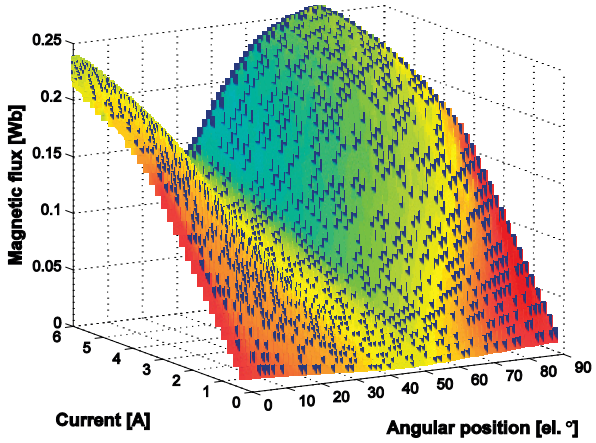

a) magnetic flux vs. phase current and rotor position

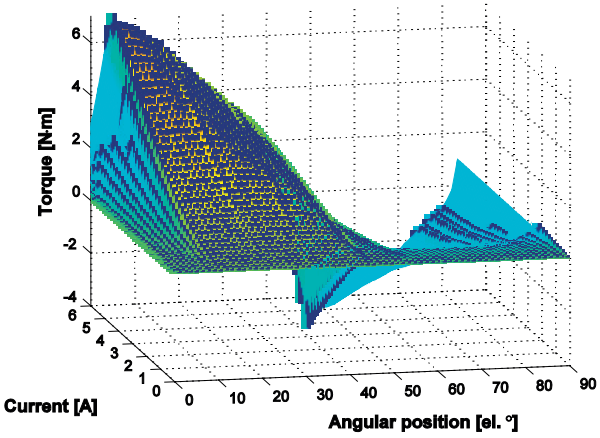

b) phase torque vs. phase current and rotor position

Fig. 6 *The static characteristics of the segmental stator SRM*

The model of the DITC system controlled modular SRM was built up in the MATLAB®/Simulink® environment [34]. The main window of the simulation program is given in Fig. 7.

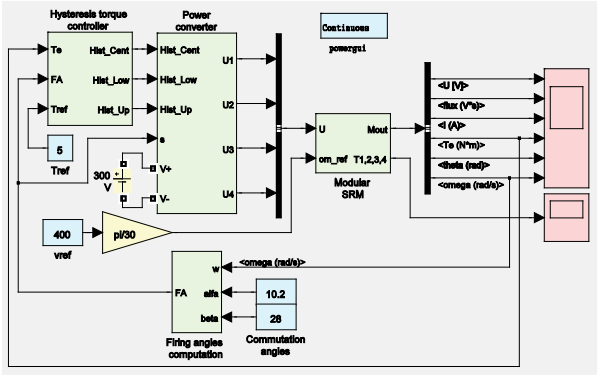

Fig. 7 The main window of the simulation program

The blocks modeling the hysteresis torque controller, the four-phase power converter, the modular SRM and the firing angle computation unit all can be easily distinguished in the modularly built up model.

The *Hysteresis torque controller* subsystem is using three *Relay* type blocks, as shown in Fig. 8. The maximum achievable frequency of the current controllers is 20 kHz.

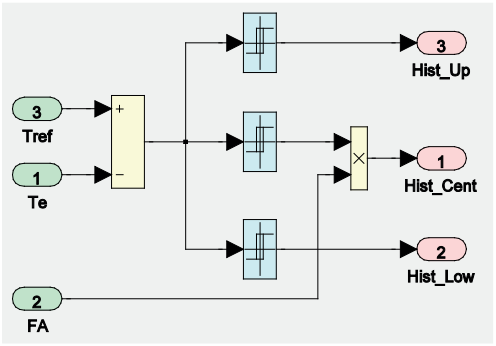

Fig. 8 The Hysteresis torque controller subsystem

The H-bridges of power converter were modeled by using blocks from the *SimPowerSystems* library of Simulink®, as *IGBT/Diode*, etc. [35].

The model of the motor is based mainly on the two 2D look-up tables, built up upon the static characteristics given in Fig. 6.

The simulations were performed under diverse conditions. Here some significant results obtained for the reference torque and speed of 4.5 N·m and 400 r/min are given.

In Fig. 9 the total torque, the imposed one and those developed by the four phases of the segmental stator SRM are given. As it can be seen the developed total torque is very close to the imposed 4.5 N·m reference value. The torque ripples (of 12.45%) are much smaller than those obtained in the case of a classical controlled modular SRM (near 30% [6]).

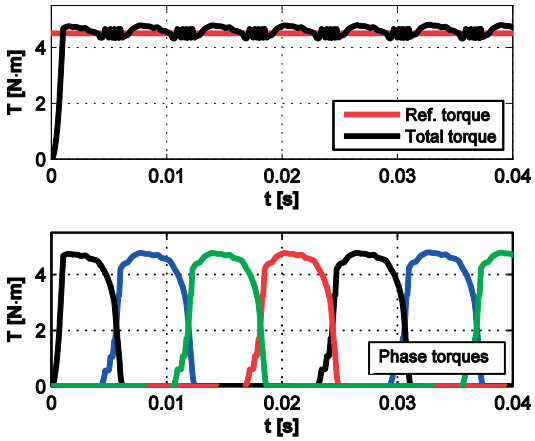

Fig. 9 Results of simulation: the total, the imposed and the phase torques developed by the segmental stator SRM

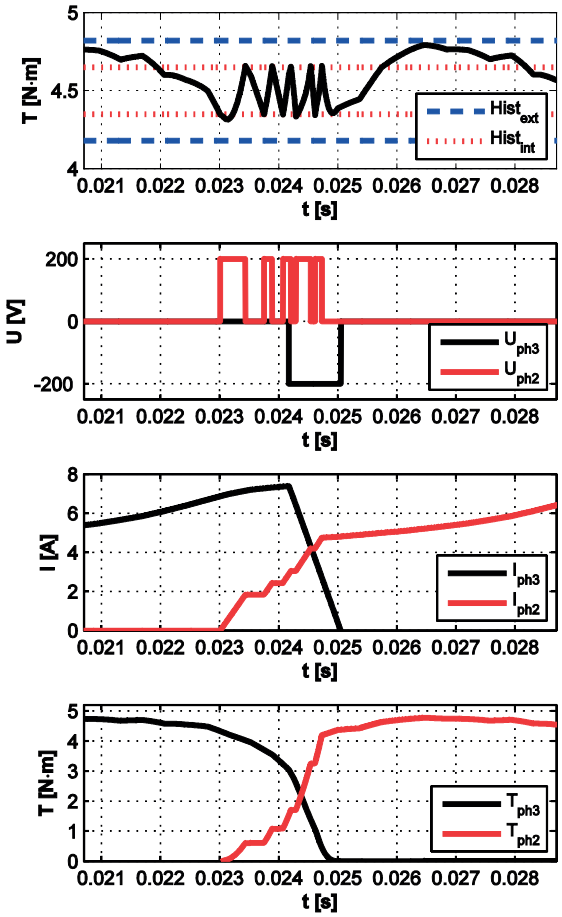

Fig. 10 Zoom of the results given in Fig. 9 showing the two hysteresis bands and the two phase voltages, currents and torques during a commutation

In Fig. 10 a zoom of the results from Fig. 8 during a commutation are given. It can be clearly observed how the instantaneous torque is kept within one of the two (inner and outer) hysteresis bands, upon the developed control strategy. Also the way as the dc voltage is soft chopped between three values ($+V_{dc}$, 0, and $-V_{dc}$) can be followed.

Before approximately 0.023 s, while only phase 3 is in conduction, the torque is controlled inside the main (the outer) hysteresis band. During the phase commutation when usually the torque drops, the torque control is more severe since it is partially performed upon the thinner inner hysteresis band. For the period of commutation also the higher frequency of the voltage soft chopping is clearly visible. After the commutation took place, the torque is kept again within the outer inner hysteresis band.

During the commutation, due to the higher commutation frequency imposed, also the losses in the motor are higher. This is the reason for which the torque is controlled inside the inner hysteresis band only during the phase commutation, the most critical period for a low torque ripple.

5. Conclusions

The paper deals with the control of a fault tolerant SRM having a segmental stator specially designed for safety-critical applications.

The modular construction of the SRM simplifies both its manufacturing and repairing. The independent stator segments can be manufactured separately, and the entire stator can be easily assembled. The SRM can be quickly repaired if winding faults occur, without removing it from the load.

The fault tolerance of this SRM was proven in several previous papers [5] and [6]. Therefore, it can be used in diverse safety-critical applications in the fields of advanced automation systems, automotive, medical, aerospace, military, etc. [36], [37] and [38].

In such high demanding systems also the relatively great torque ripples of the SRMs could be an important drawback. Therefore a simple, but yet effective control approach was taken into study: the DITC technique. The principles of this strategy are detailed in the paper.

The control method has several advantages, as smooth torque generation, direct compensation of the inherent torque ripple during phase commutation, good steady state torque control accuracy, simplification of sets of control variables and reduction of tuning control variables. All these are emphasized in the paper by advanced simulations performed via a MATLAB®/ Simulink® model of the machine. The model was developed by using the static magnetic flux and torque characteristics versus current and rotor position, fetched from the FEA of the machine. The converter model was built up by using blocks from the *SimPowerSystems* library of Simulink®.

The presented results prove the effectiveness of the proposed control method, and hopefully will help the specialists working in this field to deepen their understanding in advanced control of the SRMs.

Future works will include the fault tolerance study of the segmental stator SRM with the proposed DITC. The control strategy will be implemented on an advanced *DSpace* system for the laboratory model of the SRM. A real-time turn ON and OFF angle optimization will be also investigated, which hopefully will more smooth the torque. This way, the DITC method will be applicable on the entire speed range of the machine, even with the possibility to work at speeds above the rated one.

Acknowledgment

This work was supported in part by the Romanian National Authority for Scientific Research, CNDI-UEFISCDI, under PCCA project No. 191/2012 and under bilateral grant No. 647/2013 (in the framework of the "Romanian-Slovak Intergovernmental S&T Cooperation Programme for 2013-2014").

References

[1] HENNEBERGER, G., VIOREL, I. A.: *Variable Reluctance Electrical Machines*. Aachen : Shaker Verlag, 2001.

[2] GOPALAKRISHNAN, S., OMEKANDA, A. M., LEQUESNE, B.: Classification and Remediation of Electrical Faults in the Switched Reluctance Drive, *IEEE Transactions on Industry Applications,* vol. 42, No. 2, pp. 479-486, 2006.

[3] RUBA, M., SZABO, L.: Fault Tolerant Electrical Machines. State of the Art and Future Directions, *J. of Computer Science and Control Systems,* vol. 1, No. 1, pp. 202-207, 2008.

[4] SCHRAMM, A., GERLING, D.: *Evaluation and Comparison of Fault Tolerant Switched Reluctance Machines for a Specific Application,* Proc. of the 9thSpanish Portuguese Congress on Electrical Engineering (9 CHLIE), Marbella, 2004.

[5] RUBA, M., VIOREL, I. A., SZABO, L.: Modular Stator Switched Reluctance Motor for Fault Tolerant Drive Systems, *IET Electric Power Applications,* vol. 7, No. 3, pp. 159-169, 2013.

[6] SZABO, L., RUBA, M.: Segmental Stator Switched Reluctance Machine for Safety-critical Applications, *IEEE Transactions on Industry Applications,* vol. 48, No. 6, pp. 2223-2229, 2012.

[7] HUSAIN, I., RADUN, A., NAIRUS, J.: Fault Analysis and Excitation Requirements for Switched Reluctance-generators, *IEEE Transactions on Energy Conversion,* vol. 17, No. 1, pp. 67-72, 2002.
[8] DING, W., LOU, J., LIU, L.: Improved Decoupled Model of Mutually Coupled Dual-channel SRM with Consideration of Magnetic Saturation in Dual-channel Operation, *IET Electric Power Applications,* vol. 7, No. 6, pp. 427-440, 2013.
[9] MARTÍNEZ, E., ANDRADA, P., BLANQUE, B., TORRENT, M., PERAT, J., SANCHEZ, J.: *Environmental and Life Cycle Cost Analysis of a Switched Reluctance Motor,* Proc. of the 18thIntern. Conference on Electrical Machines (ICEM '2008), Vilamoura, 2008.
[10] SZABO, L., RUBA, M., FODOREAN, D.: *Study on a Simplified Converter Topology for Fault Tolerant Motor Drives,* Proc. of the 11th Intern. Conference on Optimization of Electrical and Electronic Equipment (OPTIM '2008), Brasov, 2008, pp. 197-202.
[11] EVANGELINE, S. J., KUMAR, S. S.: *Torque Ripple Minimization of Switched Reluctance Drives - A Survey,* Proc. of the 5thIET Intern. Conference on Power Electronics, Machines and Drives (PEMD '2010) Brighton, 2010.
[12] HUSAIN, I.: Minimization of Torque Ripple in SRM Drives, *IEEE Transactions on Industrial Electronics,* vol. 49, No. 1, pp. 28-39, 2002.
[13] SOZER, Y., HUSAIN, I., TORREY, D. A.: *Advanced Control Techniques for Switched Reluctance Machine Drives in Emerging Applications,* Proc. of the 2013 IEEE Energy Conversion Congress and Exposition (ECCE '2013), Denver, 2013, pp. 3776-3783.
[14] BAOMING, G., XIANGHENG, W., JINGPING, J.: Nonlinear Internal-model Control for Switched Reluctance Drive with Torque Ripple-free, *Automatika,* vol. 43, No. 1, pp. 2-13, 2002.
[15] NAVARDI, M. J., BABAGHORBANI, B., KETABI, A.: Efficiency Improvement and Torque Ripple Minimization of Switched Reluctance Motor using FEM and Seeker Optimization Algorithm, *Energy Conversion and Management,* vol. 78, No. 2, pp. 237-244, 2014.
[16] ISLAM, M. S., HUSAIN, J.: Torque-ripple Minimization with Indirect Position and Speed Sensing for Switched Reluctance Motors, *IEEE Transactions on Industrial Electronics,* vol. 47, No. 5, pp. 1126-1133, 2000.
[17] GOBBI, R., RAMAR, K.: Optimisation Techniques for a Hysteresis Current Controller to Minimise Torque Ripple in Switched Reluctance Motors, *IET Electric Power Applications,* vol. 3, No. 5, pp. 453-460, 2009.
[18] PETRUŞ, V., POP, A., MARŢIŞ, C., IANCU, V., GYSELINCK, J.: *Direct Instantaneous Torque Control of SRMs Versus Current Profiling - Comparison Regarding Torque Ripple and Copper Losses,* Proc. of the 12thInternational Conference on Optimization of Electrical and Electronic Equipment (OPTIM '2010), Moieciu, 2012, pp. 366-372.
[19] MITRA, R., UDDIN, W., SOZER, Y., HUSAIN, I.: *Torque Ripple Minimization of Switched Reluctance Motors using Speed Signal Based Phase Current Profiling,* Proc. of the 3rdAnnual IEEE EnergyTech Conference, Cleveland, 2013, pp. 1-5.
[20] DOWLATSHAHI, M., NEJAD, S. M. S., AHN, J.-W.: Torque Ripple Minimization of Switched Reluctance Musing Modified Torque Sharing Function, Proc. of the 21stIranian Conference on Electrical Engineering (ICEE '2013), Mashhad, 2013, pp. 1-6.
[21] SUN, J., BAI, F., LOU, W., SUN, F.: *Direct Instantaneous Torque Control Combined with Torque Sharing Function Strategy for Switched Reluctance Drive,* Proc. of the 3rdIntern. Conference on Intelligent Control and Information Processing (ICICIP '2012), Dalian, 2012, pp. 386-389.
[22] SZABO, L., TEREC, R., RUBA, M., RAFAJDUS, P.: Reconfigurable Fault Tolerant Control System for Switched Reluctance Motors, *Electrical and Power Engineering Frontier,* vol. 1, No. 1, pp. 1-7, 2012.
[23] FUENGWARODSAKUL, N. H., DE DONCKER, R. W.: *Instantaneous Torque Controller for Switched Reluctance Vehicle Propulsion Drives,* Proc. of the 20thElectric Vehicle Symposium (EVS-20), Long Beach, 2003.
[24] SUN, J., WANG, Y., BAI, F., SUN, F.: *Simulation of the Direct Instantaneous Torque Control of SRM using MATLAB,* Proc. of the Automatic Control and Artificial Intelligence Conference (ACAI '2012), Xiamen, 2012, pp. 1850-1853.
[25] SURYADEVARA, R., FERNANDES, B.G.: *Modified Direct Instantaneous Torque Control of Switched Reluctance Motor with High Torque per Ampere and Reduced Source Current Ripple,* Proc. of the 7thIntern. Power Electronics Conference (IPEC-Hiroshima 2014 - ECCE-Asia), Hiroshima, 2014, pp. 2433-2437.
[26] RUBA, M., FODOREAN, D.: *Design, Analysis and Torque Control of Low Voltage High Current SRM for Small Automotive Applications,* Proc. of the IEEE Region 8 EUROCON Conference (EUROCON '2013), Zagreb, 2013, pp. 1498-1503.
[27] HUSAIN, T., ELRAYYAH, A., SOZER, Y., HUSAIN, I.: *An Efficient Universal Controller for Switched-reluctance Machines,* Proc. of the 28thAnnual IEEE Applied Power Electronics Conference and Exposition (APEC '2013), Long Beach, 2013.
[28] LIN, Z., REAY, D. S., WILLIAMS, B. W., HE, X.: *On-line Torque Estimation in a Switched Reluctance Motor for Torque Ripple Minimisation,* Proc. of the 2004 IEEE International Symposium on Industrial Electronics (ISIE '2004) Ajaccio, 2004, pp. 981-985.
[29] ST MANOLAS, I., KLADAS, A. G., MANIAS, S. N.: Finite-element-based Estimator for High-performance Switched Reluctance Machine Drives, *IEEE Transactions on Magnetics,* vol. 45, No. 3, pp. 1266-1269, 2009.

[30] INDERKA, R. B., DE DONCKER, R. W., KREHENBRINK, M.: *On-line Estimation of Instantaneous Torque in Switched Reluctance Machine Control,* Proc. of the 2000 IEEE International Symposium on Industrial Electronics (ISIE '2000), Cholula, 2000, pp. 385-389.

[31] DUBRAVKA, P., RAFAJDUS, P., MAKYS, P., PENIAK, A., HRABOVCOVA, V., SZABO, L. et al.: *Design of Fault Tolerant Control Technique for SRM Drive,* Proc. of the 16th European Conference on Power Electronics and Applications (EPE '2014-ECCE Europe), Lappeenranta, 2014, pp. 1-6.

[32] CASTRO, J., ANDRADA, P., BLANQUÉ, B.: *Minimization of Torque Ripple in Switched Reluctance Motor Drives Using Direct Instantaneous Torque Control*, Proc. of the Intern. Conference on Renewable Energies and Power Quality (ICREPQ '2012), Santiago de Compostela, 2012.

[33] JEONG, B., LEE, K., NA, J., CHO, G., BAEK, H.: *Direct Torque Control for the 4-phase Switched Reluctance Motor Drives,* Proc. of the 8thIntern. Conference on Electrical Machines and Systems (ICEMS '2005), Nanjing, 2005, pp. 524-528.

[34] RAFAJDUS, P., SEKERAK, P., KALAMEN, L., HRABOVCOVA, V., CHEN, H.: Static and Dynamic Analysis of Linear Switched Reluctance Machine, *Communications - Scientific Letters of the University of Zilina,* vol. 4, pp. 6-11, 2011.

[35] SZABO, L., RUBA, M., FODOREAN, D., RAFAJDUS, P., DUBRAVKA, P.: *Direct Instantaneous Torque Controlled Modular Switched Reluctance Motor Designed for Automotive Applications,* Proc. of the 10thIntern. Conference ELEKTRO 2014, Rajecke Teplice, 2014, pp. 239-244.

[36] HRABOVCOVA, V., RAFAJDUS, P., LIPTAK, M., SZABO, L.: Performance of Converters Suitable for Switched Reluctance Generator (SRG) Operation, *J. of Electrical Engineering,* vol. 64, No. 4, pp. 201-211, 2013.

[37] RAFAJDUS, P., DUBRAVKA, P., PENIAK, A., SAITZ, J., SZABO, L.: *Design Procedure of Switched Reluctance Motor used for Electric CAD Drive,* Proc. of the 22nd Intern. Symposium on Power Electronics, Electrical Drives, Automation and Motion (SPEEDAM '2014), Ischia, 2014, pp. 112-117.

[38] DUBRAVKA, P., RAFAJDUS, P., MAKYS, P., HRABOVCOVA, V., SZABO, L.: Analysis of Switched Reluctance Behavior under Electrical Fault Conditions, *Communications - Scientific Letters of the University of Zilina*, vol. 2A, pp. 60-66, 2013.

Mario Cacciato - Giuseppe Scarcella - Giacomo Scelba - Pavol Spanik *

SINE WAVE FILTERS DESIGN FOR AC MOTOR DRIVES WITH GENETIC ALGORITHMS

This paper proposes a suitable design methodology of the filter used at the output of inverters for AC motor drives. While it allows to achieve the best tradeoff among different design constraints that are difficult to include in standard design methods, such an approach is able to simultaneously consider several technical issues such as losses and voltage drops of the filter, total harmonic distortion of currents and voltages as well as economic aspects. Accordingly, the proposed procedure determines the optimal values of the filter parameters by exploiting simulations of accurate model of the electrical drive and genetic algorithms. Hence, no rough approximations or complex analytical calculations are performed to suitably design the inverter output filter. The method was validated by means of various tests performed on two different induction motor drives, considering some significant design constraint scenarios.

Keywords: *Power filters, variable speed drives, genetic algorithms, design optimization.*

1. Introduction

Nowadays, the use of electrical drives is becoming more and more pervasive because of considerable price fall while their technical performance has largely increased [1]. On the other hand, if the electrical machines are fed by power converters because of their high switching frequency, additional stresses and drawbacks are experienced in comparison with line frequency powered motors [2 and 3], such as:

- Overvoltage to stator motor windings;
- Bearing currents;
- Acoustic noise;
- Electromagnetic emissions;
- Additional Losses.

The above mentioned effects are strictly related to very fast commutation of inverter power devices which, in some applications, can lead to unacceptable consequences as they cause premature failure of the motor, especially when a long cable is used to connect the inverter and the motor. In those cases, additional filters connected between the inverter and electrical machine could be required [4 and 5].

Various filter typologies have been suggested, depending on desired system performance and cost constraints. The cheapest solution able to reduce the dV/dt applied to motor windings is given by the use of simple output chokes or dV/dt filters; both of them are able to reduce the stress on motor winding insulation but only when a short cable length is used to connect the inverter to the motor. In fact, due to reflection phenomena of the voltage and current waves along the cable, also related with high dV/dt values of inverter power devices, an overvoltage up to twice the DC bus value could be applied to motor terminals if a critical cable length is overtaken. Moreover, as the waves reflection phenomena along the cable occurs at its own frequency, they can interact with PWM pulses of similar period causing the increase of voltage stress, theoretically, up to four times the DC bus voltage value. Furthermore, such kinds of filters are not effective in terms of reduction of bearing currents, acoustic noise, and do not change the drive EMI emission.

Unlike the above solutions, more sophisticated but expensive products are used to provide a nearly sinusoidal phase to phase voltage to motor terminals, thus the negative effects related to the square-wave voltage impulses are significantly reduced. They are normally known on the market as sine wave filters (SWF) [6 and 7].

Other technical solutions have been proposed to further reduce the effects of the high frequency common mode currents. The most popular ones act by modifying the PWM switching pattern while others use three phase coupled magnetic circuits and/or additional power electronic devices to create a preferential common mode current path to the DC bus [8, 9 and 10]. The effectiveness of each solution was qualitatively summarized as reported in Table 1.

As regards the standard analytical filter design methods, most of them exploit the filter transfer function and a simplified model of the electrical motor to compute the system frequency response [11, 12 and 13]. Basically, these procedures establish the filter technical constraints as the rising time, settling time, overshoot

* [1]Mario Cacciato, [1]Giuseppe Scarcella, [1]Giacomo Scelba, [2]Pavol Spanik
[1]Department of Electrical, Electronics and Computer Science, University of Catania, Italy
[2]Department of Mechatronics and Electronics, Faculty of Electrical Engineering, University of Zilina, Slovakia
E-mail: giacomo.scelba@dieei.unict.it

and other properties; then, the filter parameters are calculated by solving a mathematical system of equations obtained using the filter transfer function. As a consequence, the design issues that are not directly related to the filter transfer function, such as losses, harmonic distortion of the currents (THD_I) and voltages (THD_V), voltage drop, costs, EMI and acoustic noise, cannot be taken into account.

In order to consider at the same time all the previously mentioned issues, a design procedure is proposed in this paper, able to determine the optimal value of the SWF components, by combining the attitude of Genetic Algorithms (GA) to simultaneously evaluate a population of many sets of filter components solutions, with the capability to verify the fulfillment of the design constraints using a Graphical Simulation Tool (GST) to model and simulate the electrical drive [14 and 15]. This procedure is able to reach the optimal filter design with a reasonably low computation effort while including system nonlinearities of the drive model. Moreover, this methodology can be easily extended to different filters and drive configurations in many operating conditions, only by modifying the electrical circuit, loads and speeds used in the GST [16]. The effectiveness of the algorithm was verified by considering two different AC drive systems, as it is reported in the following sections.

Behavior of filter topologies Table 1

	Filter type		
Filter effect	*Output chokes*	*dv/dt*	*Sine wave*
Motor insulation	-	+	++
Bearing stress	–	-/+	+
EMI	–	–	-
Leakage current	–	–	–
Acoustic noise	–	–	++

2. Design technique of SWFS based on GA

The design procedure is described in the following subsections and it can be applied to all filter topologies in principle. In order to consider a useful real case, the most common filter topology used in industrial applications was studied; its scheme is shown in Fig. 1 and its transfer function is given by:

$$H(s) = \frac{1 + sRC}{s^2 LC + s(R + R_L)C + 1} \quad (1)$$

This filter is connected between the terminals of the three phase inverter and the electrical machine; a three phase induction machine is considered in this analysis. The filter inputs (A_1, B_1, C_1) are electrically connected to the inverter output terminals while the filter outputs (A_2, B_2, C_2) are coupled to motor terminals. The block diagram of the analyzed AC drive is shown in Fig. 2; it is worth noting that a standard industrial electrical drive is considered, consisting of a diode rectifier, a DC bus capacitive filter, a three phase voltage-source inverter, a RLC filter and an induction motor. The GST used in this study is the SymPowerSystem library of the graphical programming language Simulink, but other GST could be also used to implement the proposed filter design method [17].

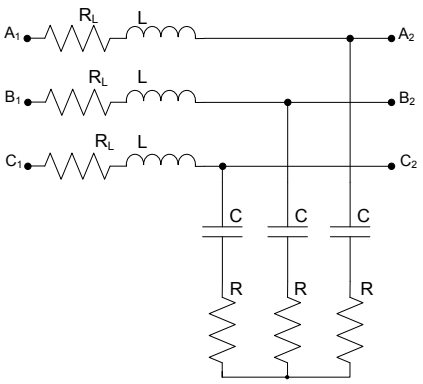

Fig. 1 Scheme of considered filter topology

(a) Design Constraints

In order to optimize the filter size, some additional blocks shown in Fig. 2 are specifically used to compute additional parameters necessary to the GA and used to verify the design specifications. In particular, according to the filter constraints, the values of the resistance *R*, capacity *C* and inductance *L* are set by monitoring the following variables:

The total harmonic distortion of the phase current and line to line voltage labeled THD_I and THD_V, respectively. High THD values would end up with the increase of iron and copper losses as well as torque and speed ripples of the electrical motor. These quantities are calculated in simulation, by means of eqn. 2, where S_h and S_1 are the rms amplitude values of the *th* and first harmonics, respectively.

$$THD\% = \frac{\sqrt{\sum_{h=2}^{\infty} S_h^2}}{S_1} \cdot 100 \quad (2)$$

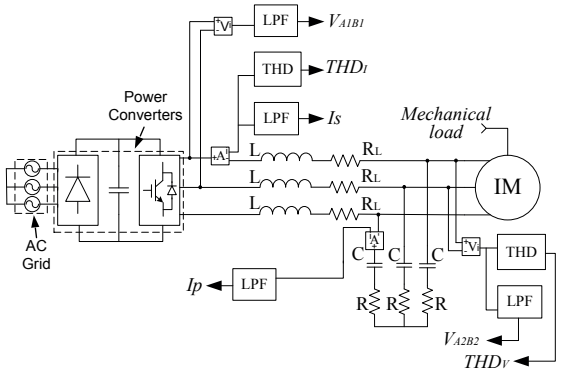

Fig. 2 Block diagram of the electrical ac drive implemented in the GST

The voltage drop *DV* on longitudinal elements of the filter is another key issue that must be minimized by design to avoid a significant reduction of maximum voltage capability of the drive.

In percentage, such a quantity is given by:

$$\Delta V\% = \frac{V_{A_1B_1} - V_{A_2B_2}}{V_{A_1B_1}} \cdot 100 \quad (3)$$

where V_{A1B1} is the amplitude value of the line to line voltage measured at the filter input terminals, while V_{A2B2} is the equivalent voltage value measured at the filter output.

Filter efficiency plays a very important role as it affects the performance of the whole drive. The filter losses P_{loss}, of elements R_L and R, can be calculated as:

$$P_{loss}\% = \frac{3 \cdot \left(R_L \cdot I_s^2 + R \cdot I_p^2\right)}{P_n} \quad (4)$$

where R_L is the parasitic resistance of the inductance L and R is the damping resistor added for control reasons, while P_n is the drive rated power.

Another important design issue considered in the following analysis is the investment cost *IC*, evaluated by considering the linear relationship (5), as a function of the capacity C and inductance L values. The values of C_{L0}, c_L, C_{C0}, C_C are related to components technologies and technical specifications required to L and C [18]. Mainly depending on the voltage class of the drive considered in this study, the following coefficient values were settled on the basis of commercial data C_{L0}=33.3 €, c_L=1.47 €/*mH*, C_{C0}=6.3 €, C_C=0.48 €/μ*F*.

(5)

The parameter R is purposely not included in eqn. 5 because low power resistors are normally used and their cost is negligible compared to other passives. Finally, IC term provides the cost per phase of the filter, thus the total cost is given by *3·IC*.

(b) Genetic Algorithm

Generally speaking, GAs are widely used to solve many optimization and synthesis problems, and work evaluating the previously defined target function that must be optimized, starting from some randomly selected points of the definition domain. They are used recursively to generate a new set of points. Gradually, the points in the generated population will approach local maxima and minima of the target function. Since information from many different regions is used, a GA can move away from a local maximum or minimum if the population finds better function values in other areas of the definition domain, avoiding to remain trapped in a local maximum or minimum of the target function.

In order to identify the best filter configuration, a suitable GA of characteristics listed in Table 2 is exploited to minimize the target function f_{ob} including a linear combination of the aforementioned technical constraints. It can be noted that the domain of f_{ob} is defined by the adopted minimum and maximum values of filter parameters. These limits depend on the rated voltage and current of the drive while the weights associated to each design constraint are strictly related to the importance given to such constraints by the designer. In this paper, three different target functions were taken into consideration as reported in Table 3. Considering the target functions expressions, the constant k was chosen on the basis of the experience. In particular, k was fixed in the range 3 ÷ 7 to achieve the most suitable filter configurations for AC drives with a rated power lower than 20kW.

Technical specification of the GA adopted in the filter design procedure. Table 2

Population Size	100 individuals
Max number of generations	15
Selection function	Stochastic Universal Sampling
Crossover function	Single Point
Mutation function	Uniform
Resolution	41 bit
Elitism	10%
Number of parameters	3
Resistance Variation	$0.1\Omega < R 100\Omega$
Inductance Variation	$0.1\text{mH} < L < 100\text{mH}$
Capacity Variation	$0.1\mu F < C < 100\mu F$
Stop Criteria	max generation

Target functions Table 3

$f_{ob}^{\ A}$	$THD_1\% + THD_V\% + \Delta V\% + kP_{loss}\%$
$f_{ob}^{\ B}$	$THD_1\% + THD_V\% + \Delta V\% + kP_{loss}\% + IC/10$
$f_{ob}^{\ C}$	$THD_1\% + THD_V\% + \Delta V\% + kP_{loss}\% + IC$

As it is shown in Table 3, the first target function $f_{oa}^{\ A}$ does not include the filter costs while the other two functions $f_{ob}^{\ B}$ and $f_{ob}^{\ C}$ combine this economic constraint with different weights.

(c) Design Procedure

The design procedure suitably exploits the two tools GST and GA in order to minimize f_{ob}. A schematic representation of the method is depicted in the flow chart of Fig. 3 and can be explained as follows. Initially, a first random generation of *(R, L, C)* candidates is provided; then, the GST is exploited to simulate the motor drive adopting the above filter parameter sets. The simulation provides the corresponding value of filter performance that is used to evaluate the objective function f_{ob}. Soon after, the Stop Criteria is evaluated and if it is not satisfied, a next generation *of R, L, C* values is provided to the GST, repeating the simulation with new set of components.

In order to have a fixed execution time of the algorithm, in the proposed method the Stop Criteria was fixed equal to the max number of generations.

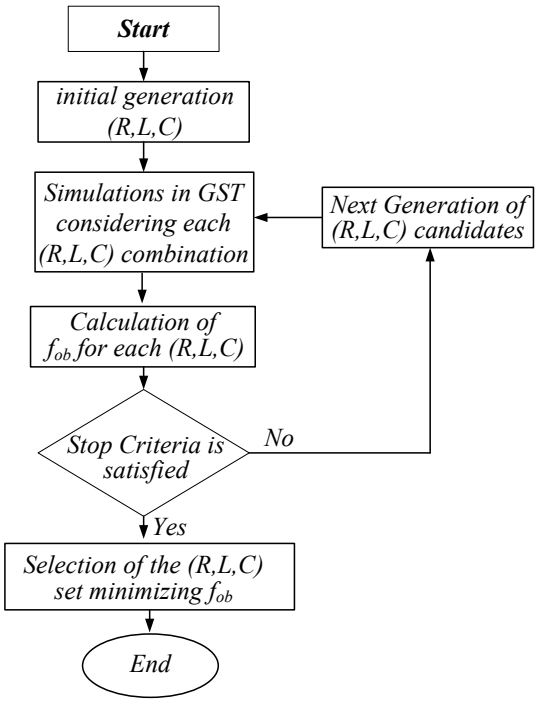

Fig. 3 Flow chart of optimal filter sizing procedure

3. Case study

The design method was validated by considering two induction motor drives whose motor specifications are listed in Table 4. In order to simplify the calculation, power device losses and magnetic saturation of the induction machine were neglected [19, 20 and 21].

The reliability of the design method was verified by running it numerous times considering the same AC drive configuration, but modifying the initial population of *(R, L, C)* candidates. In spite of the initial set of R, L, C, its final values calculated at the end of the procedure are very close. As a matter of fact, considering three different initial values of filter parameters with Motor I and using the objective function f_{ob}^{A}, the trajectories followed and final values achieved of set (R, L, C) are shown in Fig. 4. The drive operating conditions are: rated frequency, amplitude modulation index m_a=0.5, load torque 20Nm and inverter switching frequency equal to 5 kHz. As it is shown in Fig. 4, depending on the initial values the procedure follows different trajectories and converges to very close values of the filter parameters, confirming the consistency of the method. In this case, considering the approximation due to the commercial components, the values are R=1.0Ω, C=3.5 μF and L=6.0 mH. The performances of the SWF are reported in Table 5.

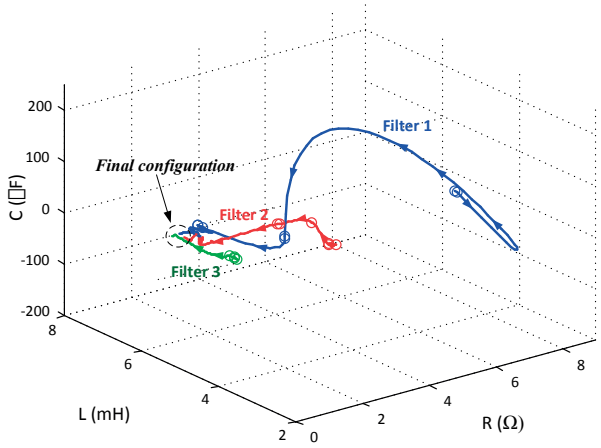

Fig. 4 Trajectories of elaborated sets of R, L, C values

Technical specifications of Motors I and II — Table 4

Rated Power	4000 W	15000 W
Rated Voltage	400 V	400 V
Stator Resistance	1.405 Ω	0.2147 Ω
Stator Leakage Inductance	5.839 mH	0.991 mH
Rotor Resistance	1.395 Ω	0.2205 Ω
Rotor Leakage Inductance	5.839 mH	0.991 mH
Magnetizing Inductance	0.1722 H	0.06419
Mechanical Inertia	0.0131 kg · m^2	0.102 kg · m^2
Pole Pairs	2	2

The proposed method can be also used to analyze the impact of the drive operating conditions on the filter performance. Hereafter, the influences of switching frequency, partial load, power rating and investment cost on the determination of the optimal filter design were studied.

Technical performances of the filter with commercial components — Table 5

	THD_V%	THD_I%	ΔV%	P_{loss}%	f_{ob}^{A}
Filter	2.943	6.889	3.527	1.270	17.060

(a) Switching frequency

Generally speaking, performance, cost and size of sine wave filter are strongly related to the switching frequency f_{sw} of the inverter power devices. In fact, addressing the same filter performance, at higher inverter switching frequencies, the cutoff frequency of the filter can be broadened thus smaller filter elements are required with some positive consequences, mainly in terms of size and cost.

The second test was carried out considering a 4kW drive operating at the same conditions of the previous tests but with different m_a=0.9 and switching frequency. In this case, by applying the proposed method, different values of the filter parameters are calculated as reported in Table 6. It is worth noting that modifying the amplitude of the fundamental phase voltage (m_a=0.9), R value needs to be increased to maintain limited filter losses. Moreover, as the switching frequency increases, the capacitor value C is considerably reduced while the inductance value L is not subjected to significant variations leading to a considerable reduction of the THD_I.

After determination of the best filter parameters set for a specific switching frequency, the filter performance of such filters related with possible variations of the switching frequency were evaluated. The results of this study are summarized in Tables 7 - 9 addressing that no significant differences are detected among the three filter arrangements operating at different f_{sw} except for the cutoff frequency F_c which is higher for the filter designed for the highest f_{sw}.

(b) Load torque

The drive always operates at partial loads or at overload conditions. The maximum load torque considered during the filter design procedure influences the final *(R, L, C)* set because it is strictly related with the phase current amplitude. In fact, the voltage drops on the inductive reactance and R_L increases with the amplitude of the phase current, hence, it is necessary to reduce the L value when the maximum allowed load is increased.

Moreover, as it is obvious, it is convenient to increase the section of the wires used to form the inductance to drop the stray parameter R_L, thus reducing the conduction losses. In order to evaluate how the optimal configuration of the SWF is affected by the load conditions, the proposed design procedure was applied to the same operating conditions of previous tests, with m_a=0.9, f_{sw}=5 kHz in correspondence with three different load conditions. The results are listed in Table 10. From the calculations, the resulting performances are similar for the three cases and they are matching good technical specifications.

The three *(R, L, C)* component sets listed in Table 10 were considered to compute the filter performance with the drive operating in different load conditions; the results are reported in Tables 11 - 13. It is worth noting that the filter design procedure confirms the aforementioned assumptions, i.e., filters designed for lower phase current amplitudes present higher losses and voltage drops when they operate at high current amplitudes, considerably affecting the performance of the drive. Fig. 5 shows a drive

Optimal filter configurations achieved considering different switching frequencies — Table 6

f_{sw} [kHz]	R [Ω]	L [mH]	C [μF]	THD_V %	THD_1 %	ΔV %	P_{loss} %	f_{ob}^A
5	7.8	4.3	7.5	3.3	9.0	3.8	1.30	22.7
10	15.4	5.1	4.3	3.9	5.0	3.7	1.17	18.5
15	13.9	4.3	1.8	5.3	4.3	4.0	1.19	14.0

Technical specifications of the filter R=7.76 Ω, L=4.33 mH, C=7.52 μF designed for f_{sw}=5 kHz — Table 7

f_{sw} [kHz]	THD_V %	THD_1 %	V%	Fc [Hz]	P [W]	P_{loss} [%]	f_{ob}^A
5	3.32	9.04	3.77	1394	52.94	1.32	22.7
10	4.09	5.60	3.23	1394	48.42	1.21	19.0
15	2.48	3.92	3.54	1394	53.00	1.33	17.0

Technical specifications of the filter R=15.32 Ω, L=5.08 mH, C=4.30 μF designed for f_{sw}=10 kHz — Table 8

f_{sw} [kHz]	THD_V %	THD_1 %	ΔV%	Fc [Hz]	P [W]	P_{loss} [%]	f_{ob}^A
5	5.64	7.57	4.40	1730	53.15	1.32	24.2
10	3.88	5.04	3.71	1730	46.88	1.17	18.5
15	2.72	3.22	4.13	1730	46.86	1.17	15.9

Technical specifications of the filter R=13.88 Ω, L=4.26 mH, C=1.75 μF designed for f_{sw}=15 kHz — Table 9

f_{sw} [kHz]	THD_V %	THD_1 %	ΔV%	Fc [Hz]	P [W]	P_{loss} [%]	f_{ob}^A
5	9.66	9.78	3.96	2902	51.46	1.29	29.8
10	5.01	5.84	3.27	2902	46.67	1.17	19.9
15	5.27	4.28	3.98	2902	47.98	1.20	14.0

Optimal filter configurations achieved considering different loads Table 10

T_L [Nm]	R [Ω]	L [mH]	C [μF]	THD_V %	THD_1 %	ΔV %	P_{loss} %	f_{ob}^A
0	1.2	14.2	8.0	0.43	7.69	6.5	0.17	15.5
10	25.5	9.0	4.2	4.95	6.58	5.3	0.6	19.9
20	7.7	4.3	7.5	3.32	9.04	3.8	1.32	22.7

Technical specifications of the filter $R = 1.23\,\Omega, L = 14.26\,mH, C = 8.01\,\mu F$ designed for *Load* = 0 *Nm* Table 11

T_L [Nm]	THD_V %	THD_1 %	ΔV %	F_C [Hz]	P [W]	P_{loss} %	f_{ob}^A
0	0.44	7.65	6.53	731	6.76	0.17	15.4
10	0.63	6.50	9.35	731	17.74	0.44	18.7
20	0.86	0.93	51.77	731	420.84	10.52	106.2

start-up with a *V/f=const.* control strategy, with different load values and filter sets. It can be observed that filters sized for lower loads cannot be adopted at high currents because they produce significant voltage drops, which affects the torque capability of the motor. As a matter of fact, the first two filter sets affect the maximum motor torque, excluding the possibility to run the drive at rated load.

(c) Power Rating

In order to confirm the general validity of the proposed design technique regardless drive power ratings, a 15kW induction motor drive was also taken into consideration, operating at different switching frequencies and loads, with m_a=*0.9* and rated motor frequency. The calculated filters are listed in Table 14 together with the corresponding performance.

In order to limit the THDs, voltage drops and losses, the capacitor *C* value provided by the designed procedure is increased

Technical specifications of the filter $R = 25.52\,\Omega, L = 9.07\,mH, C = 4.16\,\mu F$ designed for *Load* = 10 *Nm* Table 12

T_L [N×m]	THD_V %	THD_1 %	ΔV %	F_C [Hz]	P [W]	P_{loss} %	f_{ob}^A
0	4.89	10.98	4.60	1338	11.30	0.28	21.9
10	4.92	7.07	5.34	1338	21.69	0.54	20
20	7.81	1.19	40.31	1338	634.65	15.87	128.6

Technical specifications of the filter $R = 7.76\,\Omega, L = 4.33\,mH, C = 7.51\,\mu F$ designed for *Load* = 20 *Nm* Table 13

T_L [N×m]	THD_V %	THD_1 %	ΔV %	F_C [Hz]	P [W]	P_{loss} %	f_{ob}^A
0	3.28	24.20	2.17	1395	10.90	0.27	31
10	3.30	15.47	2.74	1395	20.70	0.52	24.1
20	3.34	9.02	3.77	1395	52.96	1.32	22.8

Filter specifications for different loads and switching freq. Table 14

f_{sw} [kHz]	T_L [N×m]	R [Ω]	L [mH]	C [μF]	THD_V %	THD_1 %	ΔV %	P_p %	f_{ob}^A
5	0	1.04	7.1	42.9	0.4	6.6	7.5	1.2	20.5
5	40	5.23	2.3	16.3	3.9	9.1	5.4	4.7	42.3
5	60	10.3	1.9	8.5	9.5	7.0	6.4	9.7	71.5
15	0	4.18	4.2	10.7	0.4	6.6	6.0	1.6	22.0
15	40	5.57	2.5	16.0	1.9	6.2	6.2	5.1	22.0
15	60	15.2	1.8	4.9	5.6	4.5	5.9	8.9	60.5

while the inductor L values are decreased with respect to those used for the 4kW motor drive. Moreover, similar results regarding the switching frequency and load dependence are confirmed also in these cases.

(d) Investment cost

In the previous analysis the investment costs were not included in the object function, thus excluding the economic aspect from the filter design. The results reported in Table 15 were achieved by using the object functions f_{ob}^{B} and f_{ob}^{C} and considering a 4kW motor drive operating at rated conditions and f_{sw}=5kHz. It is adequate to note that as the weight associated to IC (f_{ob}^{C}) is increased a considerable reduction of the capacitor value C is pointed out, yielding to an increment of voltage drop and THDV. On the contrary, the bandwidth of the filter is increased.

4. Conclusions and future works

In this paper, the filter design method based on GA and recursive simulations was proposed. Such a technique can be assumed as a valid alternative to standard design procedures as it allows to provide high performance filter arrangement without exploiting complicated analytical studies while contemporarily consider design constraints of both technical and economic nature.

The method was also used as a tool to analyze the impact of each technical constraint on filter parameters and it also allows evaluating the effects of parameter variation on filter performance.

Although the proposed methodology was tested adopting a simple filter topology, it can be suitably applied to more complex filtering systems, thus represents a very useful tool especially in the case of complex filter topologies. Moreover, many design constraints can be also included, such as high frequency common mode currents and overvoltage at motor terminals which are really difficult to manage with standard methods at the same time with all other constraints.

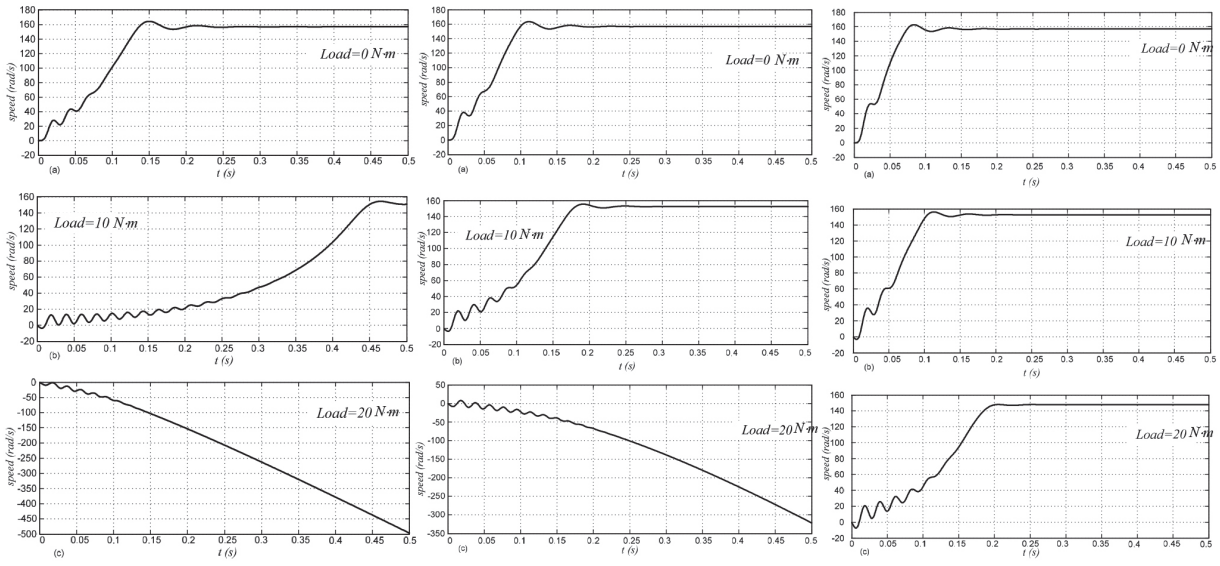

Filter of Table 11 Filter of Table 12 Filter of Table 13

Fig. 5 Speed transition during the start-up of the drive at different loads using three filter configurations

Technical specifications of the filters including investment cost Table 15

	THD_V%	THD_I%	ΔV %	R [Ω]	L [mH]	C [μF]	P_{loss}%	F_c [Hz]	IC [€]
f_{ob}^{B}	3.50	7.42	4.4	9.2	5.21	5.22	1.3	1.52	67
f_{ob}^{C}	4.46	6.75	5.0	7.3	5.82	2.52	1.3	2.05	64

References

[1] VITTEK, J., FTOREK, B.: Energy Efficient Speed and Position Control of Electric Drives with PMSM, *Communications - Scientific Letters of the University of Zilina*, 16 (1), 2014, pp. 64-71.

[2] CACCIATO, M., CONSOLI, A., FINOCCHIARO, L., TESTA, A.: *High Frequency Analysis and Modeling of Bearing Currents and Shaft Voltage on Electrical Motors*, Proc. of the IEEE Eighth Intern. Conference on Electrical Machines and Systems, ICEMS 2005, Nanjing, pp. 27-29 September 2005, pp. 2065-2070.

[3] SERPORTA, C., TINE, G., VITALE, G., DI PIAZZA, M. C.: *Conducted EMI in Power Converters Feeding AC Motors: Experimental Investigation and Modelling*, Proc. of the 2000 IEEE Intern. Symposium on Industrial Electronics, ISIE 2000, 2000, Cholula : Puebla, pp. 359-364.

[4] CACCIATO, M., CAVALLARO, C., SCARCELLA, G., TESTA, A.: *Effects of Connection Cable Length on Conducted EMI in Electric Drives*, Proc. of IEEE Intern. Conference on Electric Machines and Drives, IEMDC '99, 1999, Seattle, pp. 428-430.

[5] MOREIRA, A. F., SANTOS, P. M., LIPO, T. A., VENKATARAMANAN, G.: Filter Networks for Long Cable Drives and their Influence on Motor Voltage Distribution and Common-mode Currents, *IEEE Transactions on Industrial Electronics*, vol. 52, No. 2, 2005, pp. 515-522.

[6] SALOMAKI, J., HINKKANEN, M., LUOMI, J.: *Cost-Effective Design of Inverter Output Filters for AC Drives*, IEEE 33rd Annual Conference of the Industrial Electronics Society, IECON 2007, pp. 1220-1226.

[7] HANIGOVSZKI, N., LANDKILDEHUS, J., BLAABJERG, F.: *Output Filters for AC Adjustable Speed Drives*, Proc. of Twenty Second Annual IEEE Applied Power Electronics Conference, APEC 2007, 2007, Anaheim, pp. 236-242.

[8] CACCIATO, M., DE CARO, S., SCARCELLA, G., SCELBA, G., TESTA, A.: Improved Space-Vector Modulation Technique for Common Mode Currents Reduction, *IET Power Electronics*, vol. 6, No. 7, 2013, pp. 1248-1256.

[9] DI PIAZZA, M. C., LUNA, M., VITALE, G.: *EMI Reduction in DC-Fed Electric Drives by Active Common-Mode Compensator IEEE Transactions on Electromagnetic Compatibility, early access,* 2014, pp.1-10.

[10] CACCIATO, M., CONSOLI, A., SCARCELLA, G., SCELBA, G., TESTA, A.: *Modified Space-Vector-Modulation Technique for Common Mode Currents Reduction and Full Utilization of the DC Bus*, Proc. of Twenty-Fourth Annual IEEE Applied Power Electronics Conference and Exposition, APEC 2009, Feb. 2009, Washington DC, pp. 109-115.

[11] VON JOUANNE, A., ENJETI, P. N.: Design Considerations for an Inverter Output Filter to Mitigate the Effects of Long Motor Leads in ASD Applications, IEEE Transactions on Industry Applications, vol. 33, No.°5, 1997, pp. 1138-1145.

[12] LEE-HUN K., HWAN-KYUN Y., CHUNG-YUEN W., YOUNG-REAL K., GI-SU CH.: *Output Filter Design for Conducted EMI Reduction of PWM Inverter-fed Induction Motor System*, IEEE International Conference on Power Electronics and Drive Systems 2001, pp. 252-258.

[13] SOZER, Y., TORREY, D. A., REVA, S.: New Inverter Output Filter Topology for PWM Motor Drives, *IEEE Transactions on Power Electronics*, vol. 15, No.°6, 2000, pp. 1007-1017.

[14] ZUBI, H. M., DUNN, R. W., ROBINSON, F. V. P., EL-WERFELLI, M. H.: *Passive Filter Design Using Genetic Algorithms for Adjustable Speed Drives*, Proc. of IEEE Power and Energy Society General Meeting 2010, pp. 1-7.

[15] NORAINI, M. R., GERAGHTY, J: *Genetic Algorithm Performance with Different Selection Strategies in Solving TSP*, Proc. of the World Congress on Engineering, vol. II, WCE 2011, July, 2011, London

[16] LISERRE, M., DELL'AQUILA, A., BLAABJERG, F.: Genetic Algorithm-based Design of the Active Damping for an LCL-filter Three-phase Active Rectifier, *IEEE Transactions on Power Electronics*, vol. 19, No. 1, pp. 76-86, 2004.

[17] DRGONA, P., PRIKOPOVA, A., FRIVALDSKY, M., PRIECINSKY, M.: Simulation Based Method for Design and Application of Digital Control System, *Communications - Scientific Letters of the University of Zilina*, vol. 13 (2A), 2011, pp. 32-37.

[18] SALOMAKI, J., HINKKANEN, M., LUOMI, J.: Influence of Inverter Output Filter on Maximum Torque and Speed of PMSM Drives, *IEEE Transactions on Industry Applications*, vol. 44, No. 1, pp. 153, 160, 2008.

[19] CACCIATO, M., CONSOLI, A., SCELBA, G., SCARCELLA, G.: An Effective Energy-saving Scalar Control for Industrial IPMSM Drives, *IEEE Transactions on Industrial Electronics*, vol. 60 (9), 2013, pp. 3658-3669.

[20] FRIVALDSKY, M., DOBRUCKY, B., SCELBA, G., SPANIK, P., DRGONA, P.: Bidirectional Step-up/step-down DC-DC Converter with Magnetically Coupled Coils, *Communications - Scientific Letters of the University of Zilina*, 15 (3), 2013, pp. 21-25.

[21] CACCIATO, M., CONSOLI, A., SCARCELLA, G., SCELBA, G.: Indirect Maximum Torque per Ampere Control of Induction Motor Drives, *EPE J. (European Power Electronics and Drives J.)*, 18 (4), pp. 34-41.

COMMUNICATIONS – Scientific Letters of the University of Zilina
Writer's Guidelines

1. Submitted papers must be unpublished and must not be currently under review for any other publication.
2. Submitted manuscripts should not exceed 8 pages including figures and graphs (in Microsoft WORD – format A4, Times Roman size 12, page margins 2.5 cm).
3. Manuscripts written in good English must include abstract and keywords also written in English. The abstract should not exceed 10 lines.
4. Submission should be sent: By e-mail – as an attachment – to one of the following addresses: komunikacie@uniza.sk or holesa@uniza.sk (or on CD to the following address: Zilinska univerzita, OVaV – Komunikacie, Univerzitna 1, SK-10 26 Zilina, Slovakia).
5. Uncommon abbreviations must be defined the first time they are used in the text.
6. Figures, graphs and diagrams, if not processed in Microsoft WORD, must be sent in electronic form (as JPG, GIF, TIF, TTF or BMP files) or drawn in high contrast on white paper. Photographs for publication must be either contrastive or on a slide.
7. The numbered reference citation within text should be enclosed in square brackets. The reference list should appear at the end of the article (in compliance with ISO 690).
8. The numbered references (in square brackets), figures, tables and graphs must be also included in text – in numerical order.
9. The author's exact mailing address, full names, E-mail address, telephone or fax number, the name and address of the organization and workplace (also written in English) must be enclosed.
10. The editorial board will assess the submitted paper in its following session. If the manuscript is accepted for publication, it will be sent to peer review and language correction. After reviewing and incorporating the editor's comments, the final draft (before printing) will be sent to authors for final review and minor adjustments
11. Submission deadlines are: September 30, December 31, March 31 and June 30.

COMMUNICATIONS

SCIENTIFIC LETTERS OF THE UNIVERSITY OF ZILINA
VOLUME 17

Address of the editorial office:
Zilinská univerzita
Office for Science and Research
(OVaV)
Univerzitna 1
SK 010 26 Zilina
Slovakia

E-mail: komunikacie@uniza.sk

Each paper was reviewed by two reviewers.

Journal is excerpted in Compendex and Scopus.

It is published by the University of Zilina in
EDIS – Publishing Institution of Zilina University
Registered No: EV 3672/09
ISSN 1335-4205

Published quarterly

Single issues of the journal can be found on:
http://www.uniza.sk/komunikacie

ICO 00397 563
April 2015